Universiteit Gent
Faculteit Ingenieurswetenschappen en Architectuur
Vakgroep Informatietechnologie

Actieve en Passieve Golflengtefilters voor Geintegreerde Spectrometers in Siliciumfotonica

Active and Passive Wavelength Filters for Silicon Photonic Integrated Spectrometers

Alfonso Ruocco

Proefschrift tot het bekomen van de graad van
Doctor in de Ingenieurswetenschappen: Fotonica
Academiejaar 2015-2016

Universiteit Gent
Faculteit Ingenieurswetenschappen en Architectuur
Vakgroep Informatietechnologie

Promotoren: Prof. Dr. Ir. Wim Bogaerts

Examencommissie:

Prof. Dr. Ir. Hendrik Van Landeghem (voorzitter)	Universiteit Gent
Prof. Dr. Ir. Wim Bogaerts(Promotor)	Universiteit Gent, INTEC
Prof. Dr. Ir. Dries Van Thourhout	Universiteit Gent, INTEC
Prof. Dr. Ir. Pieter Rombouts	Universiteit Gent, ELIS
Dr. Ir. Ananth Subramanian	Universiteit Gent, INTEC
Dr. Ir. Thijs Spuesens	IMEC
Dr. Ir. Martin Fiers	LUCEDA Photonics
Dr. Ir. Peter J. Harmsma	TNO Afdeling Optica

Universiteit Gent
Faculteit Ingenieurswetenschappen en Architectuur

Vakgroep Informatietechnologie
Sint-Pieternieuwstraat 41,B-9000 Gent, België B-9050 Gent, België

Tel.: +32-9-264.33.16
Fax.: +32-9-331.35.93

Proefschrift tot het behalen van de graad van
Doctor in de Ingenieurswetenschappen: Fotonica
Academiejaar 2015-2016

Acknowledgment

Wow, where do I start....A special thanks goes to Wim, more than a supervisor, he is the mentor of my research and the promoter of my ideas. He was the catalyzer that helped to convert a rough thought into an innovative research activity. Although I worked in close collaboration with Wim, Dries gave me precious and very much appreciated inputs during my research. The acknowledgement extends to all the senior academic staff: Roel, Geert, Peter B., Gunther, Nicolas and Bart. It is difficult to couple the idea of such a relevant research group with a so pleasant family environment. Thanks to Andrea for the guidance he provided in the beginning: he taught me a lot.

I really enjoined to broaden my knowledge, this would not have been possible without the constant and precious support of Michael, Jeroen and Steven. These guys have always been there to satisfy my thirst for software/hardware/processing knowledge, and when the topic was too hard....they were there to help, thanks.....

A special thank you to the thesis readers and translators: Aditya, Paolo, Bart, Sarah, Michael, Pieter W., Alex and Frederic. These guys translated form Alfonsish to English and sometimes to Dutch and gave relevant feedback to the hard work of preparing a thesis.

I'd like to thank all the people that in these years brought some fun into my life: Sarvagya, Tovarish Anton, Frederic, Muneeb, Bendix, Utsav, Kasper, Amin, Andreas the big, Alejandro, Sören (quit it...), Sourav, Ananth, Ashim, Andrew. You guys let me feel at home.

A special section goes for the big office fellowship: Antonio, Aditya, Leila, Alex, Paul, Jing, Sulakshna, Ruijun, Haka, Daan, Chen (eheee..eeh?), JanWillem, and the atypical Chinese Ang and Yufei. Thanks to them I learned a lot of technical stuff (due to the continuous talking) and I trained myself to work with 120 dB of noise (due to the continuous talking).

I'm glad I had loooong and helpful technical (and not only) discussions with Muneeb (the guy with big knowledge and patience), Andrew and Bendix (people big large reservoir of info), Antonio (my linux reference), Aditya (my personal processing adviser), JanWillem and Daan (my bio-teammate), Pieter D. and Haka.

A special thanks to Shibnath, Sarvagya and Muneeb my professional partners and friends.

I'd like to thank also the "glWhocare"team: Ananth and Paolo for their priceless and brotherly advices, you were a reference point for me. Thanks also to Wouter, Danaë, Thij, Eva, Kristien and Ilses for your constant support.

A large group like ours always sees people coming and leaving, but this is not a

good reason to only look at the present when it comes to acknowledgement. So I'd like to thank also people that left: Dorian, Oscar, Stefania, Kristinn thanks for all the good memories I have. You represent (together with Haka) the best outgoing group....

For sure I forgot people, It always happens, but thanks to everyone to make Belgium my second home for these years.

I'll switch to Italian for the final part.

Grazie ai miei genitori Luigi ed Esterina che hanno creduto in me quando per farlo bisognava essere o completamente folli o completamente fiduciosi, mi piace pensare che lo abbiano fatto per la seconda: i miei traguardi, non sono mai solo i miei.... Grazie a mio fratello Antonio, da sempre un immancabile sostegno per me. Grazie a miei suoceri Franco e Lucrezia, da quasi due decadi posso sempre contare su di loro. 'Dulcis in fundo' un grazie a quella che è la compagna di mia vita Luisa, quando ho bisogno di te, ci sei e ci sei sempre stata. In fine il mio pesiero va a mia figlia Isabella che ha riscritto l'ordine delle priorità, tu sei la nuova luce che mi illumina il cammino.

Gent, February 2016
Alfonso Ruocco

Table of Contents

List of Figures

List of Tables

List of Acronyms

A

AC	Alternating current
AWG	Arrayed waveguide grating
ARMA	Auto regressive moving average
AR	Auto regressive

B

BG	Bragg grating
BPM	Beam propagation method

C

CDF	Cumulative distribution function
CDMA	Code division multiple access
CMA	Covariance Matrix Adaptation
CMOS	complementary metal-oxide semiconductor
CT	Cross-talk
CW	Continuous wave
CWDM	Coarse wavelength division multiplexing

D

DBR	Distributed Bragg grating
DC	Directional coupler
DC	Direct current

DE	Differential Evolution
DOE	Design of experiment
DUT	Device under test
DWDM	Dense wavelength division multiplexing

E

EME	Eigenmode expansion
EO	Electro-optic
ES	Evolutionary strategy

F

FBG	Fiber Bragg grating
FDM	Frequency division multiplexing
FDTD	Finite-difference time-domain
FFT	Fast Fourier transform
FPR	Free propagation region
FTIR	Fourier transform infrared spectroscopy
FWHM	Full width at half maximum

I

IL	Insertion loss
IR	Infrared

L

LOD	Limit of detection

M

MA	Moving average

MMR	Micro-ring resonator
MMI	Multimode interference
MZI	MachZehnder interferometer
MZM	MachZehnder modulator
MPA	Guided-mode propagation analysis
MPW	multi-project wafer

O

OR	Operative range
OSA	Optical spectrum analyzer

P

PCG	planar concave grating
PDF	Probability density function
PIC	Photonic integrated circuit

R

RIU	Refractive index unit
RMS	Root-mean-square
ROIC	Readout integrated circuit

S

SC	Star coupler
SHS	Spatial heterodyne spectrometers
SLED	Superluminescent diode
SNOBFIT	Stable Noisy Optimization by Branch and Fit
SOI	Silicon on insulator

T

TE	Transverse electric
TDM	Time division multiplexing
TIA	Transimpedance amplifier
TO	Thermo-optic

W

WDM	Wavelength-division multiplexing
WS	Wave shaper

X

XT	Cross-talk

Nederlandse samenvatting –Summary in Dutch–

Inleiding

Geminiaturiseerde geïntegreerde spectrometers and golflengtemeters zijn belangrijke componenten toepasbaar in een breed gamma van applicaties. Enkel voorbeelden van toepassingsdomeinen zijn optische netwerken, gezondheidszorg, en milieu sensoren. Hoge resolutie, hoge nauwkeurigheid en een groot meetbereik zijn in de meeste gevallen gewenst. In de meeste gevallen kunnen niet-geïntegreerde meettoestellen gemakkelijk voldoen aan de vereisten. Deze functionele vereisten worden meestal gerealiseerd ten koste van andere aspecten. Meetinstrumenten zoals spectrometers en golflengtemeters zijn vaak groot en duur en bevatten bewegende onderdelen. Ten gevolge van de fysische afmetingen is het vaak onmogelijk deze toestellen te gebruiken in nieuwe technologische toepassingen. Het is ondoenbaar om een Yokogawa spectometer in te bouwen in de Mars Rover of te implanteren in het menselijk lichaam. Geïntegreerde fotonische circuits in silicium kunnen een antwoord bieden op de vereisten van afmeting, kostprijs en integratie. Siliciumgebaseerde fotonica beschikt reeds over een ruim gamma van functionele bouwblokken. Essentiële componenten zoals golflengtefilters, modulatoren en modeomvormers hebben voldoende maturiteit bereikt om exploratie van meer complexe on-chip functionaliteit mogelijk te maken.

Figuur 1: Yokogawa optical spectrum analyzer : $\sim 20\ Kg$

Silicium-op-isolator geïntegreerde spectrometers

Geïntegreerde fotonische spectrometers zijn uitvoerig beschreven en aangetoond in de literatuur. Het merendeel van de voorgestelde implementaties voor spectrometers berust op geïntegreerde optische filters. Meer specifiek maken de meeste ontwerpen gebruik van *arrayed waveguide gratings* (AWG), planaire diffractie-

roosters (*Planar concave gratings* of PCG) en Mach-Zehnder interferometers (MZI). AWG's en PCG's zijn algemeen gebruikte WDM (*Wavelength division multiplexing*) filters. In spectrometer toepassingen worden AWG's en PCG's gebruikt om een vast aantal optische golflengtes te demultiplexeren in verschillende fysieke kanalen. De resolutie en het operatiebereik van de spectrometer is direct gecorreleerd met de plaatsing van kanalen en het vrij spectraal bereik (FSR) van de WDM filters. Spectrometers gebaseerd op een reeks MZI's maken gebruik van de sinusoïdale transmissie van de individuele componenten. Door de fasevertraging van de MZI's correct te schalen bereikt men een transmissie die de fouriergetransformeerde is van de input. Voor dit type spectrometer bestaat er een trade-off tussen resolutie en operatiebereik, bepaald door het aantal MZI's in de circuit. De diverse oplossingen die hier beschreven staan bieden de typische voordelen van silicium-op-isolator (SOI) fotonica: kleine afmeting, beperkte kostprijs en afwezigheid van bewegende onderdelen.

Uitdagingen van het huidig onderzoek: actieve en passieve optische filters

In de literatuur wordt gewag gemaakt van verschillende, hoog performante geïntegreerde spectrometers, die zijn ontwikkeld voor het silicium-op-isolator (SOI) materiaalplatform. Echter,de performantie van al deze spectrometers is gelimiteerd door de fabricagekwaliteit van het huidige materiaalplatform. In plaats van te proberen om de limieten van de huidige fabricatie-technologie te verleggen, gebruiken we in dit werk een combinatie van verschillende optische filters en modulatietechnieken om de beperkingen opgelegd door de SOI fabricatie te omzeilen.

Optische filters: ontwerp en analyse

De studie van de optische filter focust zich op technieken om de filter te ontwerpen, te simuleren en te karakteriseren. Een andere uitdaging ligt in het ontwerpen van een gesloten cyclus voor het volledige siliciumfotonica engineering proces: eerdere meetresultaten worden gebruikt als input voor het filterontwerp om op die manier op maat te kunnen ontwerpen voor het platform. Met dit doel hebben we een geïntegreerd softwareframework ontwikkeld dat gebruikt wordt voor het ontwerp en de simulatie van eindige impulsrespons (*finite impulse response* - FIR) en oneindige impulsrespons (*infinite impulse response* - IIR) optische filters. De uitdaging is om te kunnen starten van abstracte designparameters (zoals de filter transmissie) en het hele process te kunnen opvolgen tot en met de analyse van de meetresultaten. Dit werd bereikt door het combineren van verschillende Python-gebaseerde software pakketten.

Dit wordt geïllustreerd in Fig. 2. Links, in het gele kader, wordt een algemene simulatie getoond waarin de filter wordt behandeld als een abstract element: op basis van de vereiste transmissie worden de polen en nullen van de filter gedefinieerd. Vervolgens worden deze polen en nullen omgezet naar fotonische ont-

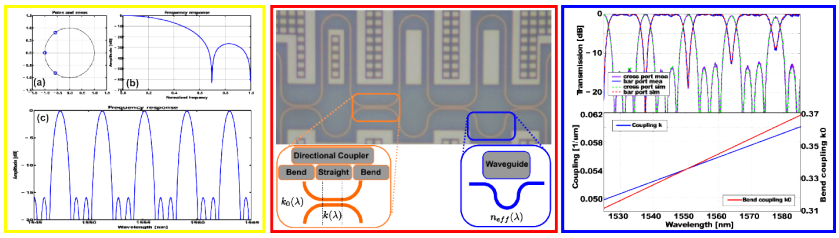

Figuur 2: Framework voor optische filters: van functionele parameter design tot extractie van optische parameters door meting

werpparameters. Daarop volgt het ontwerp en de simulatie van de lay-out van de fotonische component. De fabricage van de chips gebeurt in in de CMos pilootlijn van IMEC in Leuven. In het rode kader wordt een microscoopbeeld getoond van de filterchip. Voor het opmeten van de filter wordt hetzelfde softwareframework gebruikt als voor het ontwerp. Slimme data-analyse methodes worden gebruikt om de optische eigenschappen van de component af te leiden uit de meetdata. In het blauwe kader staat een voorbeeld van een meting met bijhorende data fitting. Door de metingen te analyseren met behulp van hetzelfde fotonische simulatiepakket als werd gebruikt voor het ontwerp van de componenten, verkrijgen we zeer accurate informatie over de optische eigenschappen van de individuele subblokken van het fotonisch geïntegreerde circuit. Het softwarepakket is getest op verschillende filters, meer bepaald op FIR en IIR architecturen. Uit de data zijn de optische koppeling en de groepsindex van de verschillende designs afgeleid. Deze optische parameters kunnen vervolgens gebruikt worden bij de simulatie en het ontwerp van een volgende generatie filters.

Spectrometers op basis van actieve, afzonderlijke filters

Actieve modulatie en afstelling van de filters wordt gebruikt om de performantie van individuele filters te optimaliseren. De focus ligt op enkelvoudige ringfilters en Mach-Zehnder interferometers (MZI). De ring resonator wordt gemoduleerd door gebruik te maken van het thermo-optisch (TO) effect. Gedopeerde silicium verwarmingselementen zijn aangebracht aan beide kanten van de optische ringgolfgeleider. Vanuit het thermisch standpunt zijn het optisch en het thermisch silicium sterk aan elkaar gekoppeld, maar optisch gezien is er geen beïnvloeding. De filter wordt opgemeten aan de *drop* poort. Fig. 3(b) toont een microscoop beeld van de ringfilter. Aangezien we de filter uitmeten aan de drop poort kunnen we de transmissie benaderen door een Lorentziaan. De Lorentziaanse transmissie kan worden gebruikt om het onbekende inputspectrum te scannen in het tijdsdomein. Het werkingsgebied is beperkt tot het vrij spectrale bereik (FSR) van de ring, in dit geval $\sim$ 10 nm. De metingen zijn uitgevoerd zowel met discrete als conti-

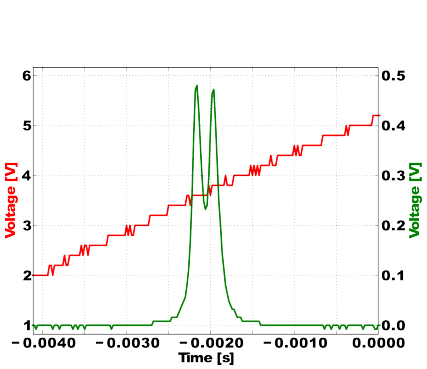

(a) Resolutiemeting: 300 pm

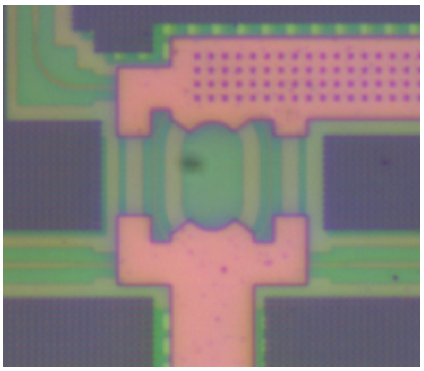

(b) Thermo-optische ring gezien onder de microscoop

Figuur 3: Scanning spectrometer: karakteristiek van de resolutie en uitzicht

nue aansturing in het tijdsdomein. Beide experimenten leiden tot goede resultaten. De limieten van de component zijn getest door middel van continue aansturing. In dit geval, konden we een resolutie meten van 300 pm over de volledige FSR. Fig. 3(a) geeft de resolutiemeting weer. Twee instelbare lasers, 300 pm van elkaar verwijderd, worden gescheiden door een uitdovingsverhouding van ~ 3 dB in het tijdsdomein. De MZI golflengtemeter steunt op ladingsdragersdispersie voor de modulatie. Fasemodulatoren op basis van ladingsdepletie worden aangebracht op beide armen van de asymetrische interferometer. Germanium fotodetectoren zijn geïntegreerd in het circuit, dus een aparte optische output is overbodig. Het werkingsprincipe van deze golflengtemeter is gebaseerd op de convolutie van de ingangsgolflengte en de transmissie van de asymmetrische MZI. In Fig. 4(b) wordt een microscoopbeeld van de MZI golflengtemeter getoond.

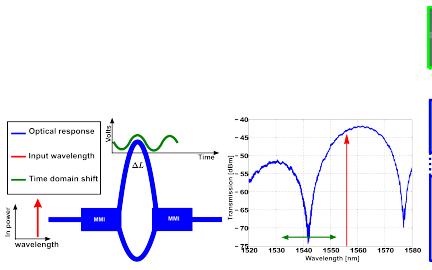

(a) Werkingsprincipe van asymmetrische MZI golflengtemeter

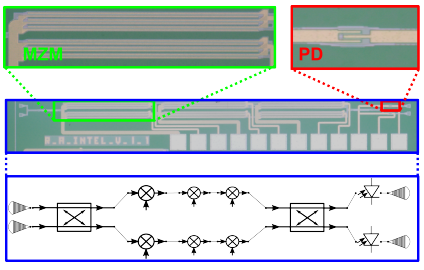

(b) Microscopisch beeld en schema van de MZM

Figuur 4: Werkingsprincipe en microscopisch beeld van de volledig geïntegreerde fazeverschuiving golflengtemeter

Als we de interferometer moduleren met behulp van een sinussignaal, dan bevat de uitgang in het tijdsdomein informatie over het golflengteverschil tussen de ingangsgolflengte and het dal (of de piek) van de MZI transmissie. Het werkingsprincipe is kort uitgelegd in Fig. 4(a). De blauwe curve geeft het passieve antwoord van de MZI weer, de rode lijn duidt de ingangsgolflengte aan en de groene lijn duidt de sinusoïdale modulatie aan. De gemiddelde precisie die we konden bereiken met deze golflengte meter was $\sim 64\ pm$ over de volledige FSR van $\sim 30\ nm$.

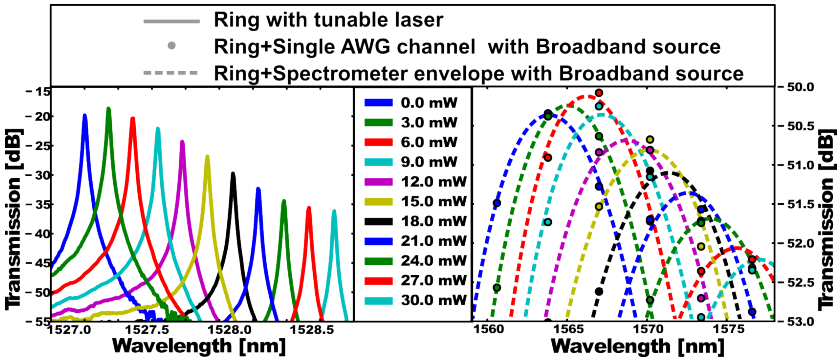

Figuur 5: Vergelijking van de fazeverschuiving van de ring sensor (links) and het ring-AWG cascadesysteem (rechts)

Gecascadeerde optische filters en spectrometers

Om de intrinsieke limitaties van individuele AWGs en ringen te overstijgen, worden beide gecombineerd in meer complexe architexteren. Hiertoe wordt de ring gemoduleerd door het thermo-optisch effect. De basisarchitectuur gaat uit van een enkelvoudige ring die een AWG voedt. Dit concept wordt onderzocht voor verschillende toepassingen.

Eerst wordt het geïntegreerd optisch circuit gebruikt als een sensor voor de effectieve brekingsindex, waar de ring als sensor dient en de AWG gebruikt wordt als geïntegreerde spectrometer. De Vernier-schaling tussen de vrije spectrale breedte van de ring en de spatiëring van de uitgangskanalen van de AWG zorgen ervoor dat de spectrale verschuiving van de uitgangsenveloppe een winstfactor heeft in vergelijking met de verschuifing van een eenvoudige ring. Fig 5 vergelijkt de verschuiving van een enkelvoudige ring (links) en de envelope-verschuiving van het gekoppeld ring-AWG systeem (rechts) bij hetzelfde elektrisch vermogen. Hoewel een winstfactor in detectielimiet van 16 wordt verwacht, ligt deze in het experiment lager ten gevolge van fabricage-variaties. Bijgevolg werd een winstfactor van ~ 9 gemeten. Het gebruik van dezelfde architectuur als scannende spectrometer wordt experimenteel aangetoond: als de vrije spectrale breedte van de ring groter is dan

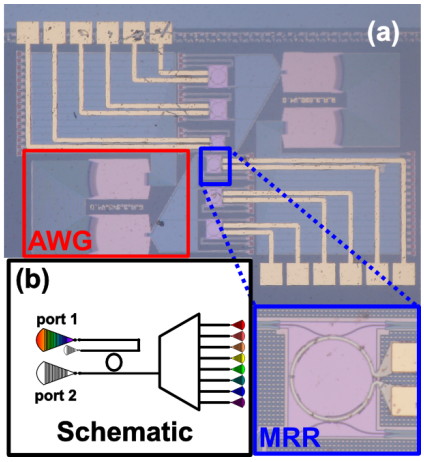

Figuur 6: Schema en microscopisch beeld van de ring-AWG cascadespectrometer

de bandbreedte van de AWG ligt er slechts n resonante piek in het golflengte-bereik van de AWG. De periodieke respons van de ring wordt gemoduleerd met het thermo-optisch effect. Elke resonante piek scant de kanaal-bandbreedte van de AWG waarmee die geassocieerd is. In dit experiment wordt een resolutie bereikt van 50 pm in een werkingsgebied van 48 nm, overeenkomstig met de vrije spectrale breedte van de AWG. Fig. 6 geeft een schematische voorstelling en een microscopiebeeld van het circuit.

Tijds-gemultiplexte spectrometers gebaseerd op optische filters.

Het concept van multidomein-multiplexing wordt toegepast op golflengte detectie. Door het verdelen van golflengtes in verschillende fysische kanalen, doet een AWG die als spectrometer gebruikt wordt reeds aan golflengte-multiplexing. Het toestel heeft meerdere ingangen; deze worden zodanig geplaatst dat hun spectraal antwoord aan de uitgang verschoven wordt volgens een Vernier-schaal. Aangezien deze aanpak de kanaal-equivalente spatiëring vermindert, wordt de ”dode zone”tussen de uitgangskanalen van de AWG verwijderd. Elektrische modulatie wordt gebruikt om aan de ingangen een label toe te kennen , wat nodig is omdat verschillende ingangen nzelfde fysisch uitgangskanaal delen.

Het label bestaat uit een tijds-domein multiplexing (TDM) of frequentie-domeim multiplexing (FDM) met behulp van MZI modulatoren. Via deze benadering wordt een resolutie van 12 pm getoond, gebruik makend van een AWG met een kanaalspatiëring van 4 nm en een vrije spectrale breedte van 20 nm. Fig. 7 toont de gemeten nauwkeurigheid wanneer de ongekende ingansgolflengte die van de aanpasbare laserlijn is.

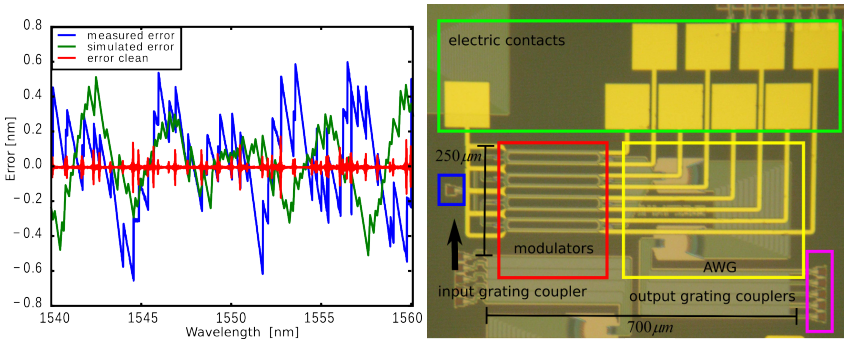

(a) Simulatie en meting van de locale nauwkeurigheid

(b) Vernier gemultiplexte spectrometer

Figuur 7: Microscopisch beeld en meting van de locale nauwkeurigheid van de Vernier gemultiplexte spectrometer

Conclusie

We hebben een aantal nieuwe concepten voor geïntegreerde spectrometers aangetoond, gebaseerd op gemoduleerde en/of gecascadeerde golflengtefilters. Met behulp van modulatietechnieken konden we het uitleesproces vereenvoudigen en de resolutie van de spectrometer of golflengtemeteropdrijven. Door meerdere filters in een cascade te plaatsen konden we ook het werkingsbereik drastisch vergroten. Verschillende concepten zijn experimenteel aangetoond.

English summary

introduction

Miniaturized integrated spectrometers and wavelength meters are key components for a wide variety of applications, ranging from optical networking to health, and environmental sensing, space instruments, etc. High resolution, high accuracy, and a large operation range are in most of the cases highly desirable, and non-integrated devices are usually capable of delivering the needed specifications in term of resolution and operation range. The functional objectives are often achieved at the expense of other features. Indeed, instruments like spectrometers and wavelength meters are often bulky, costly and with movable parts. The drawback of these physical aspects is the impossibility for them to be used in cutting edge technology fields. For instance it is quite cumbersome to send a bulky spectrum analyzer (cf. Fig. 8) to Mars and impossible to implant it in a human body. Silicon integrated photonics can be the answer to the quest for size, costs, and integration. Silicon photonics platforms nowadays count a large variety of demonstrated photonic integrated devices. Essential building blocks such as wavelength filters, modulators, mode converters are reaching a sufficient maturity level and yield to move forward and it becomes now possible to look at more complex functionalities on-chip.

Figure 8: Yokogawa Optical spectrum analyzer: $\sim 20\ Kg$

SOI integrated spectrometers

Different implementations of photonic integrated spectrometers have already been proposed and demonstrated. Most of the proposed architectures rely on integrated passive optical filters. More specifically, most of the integrated spectrometers have been demonstrated using AWGs(Arrayed waveguide grating), PCGs(Planar concave gratings) and MZI(Mach-Zehnder interferometer) arrays. AWGs and PCGs are are commonly used WDM (Wavelength division multiplexing) filters. When

they are deployed as spectrometers, AWGs and PCGs are used to de-multiplex a number of optical wavelengths into different physical channels. Hence, the resolution and the operation range of the spectrometers are directly correlated with the channel spacing and free spectral range of the WDM filters. MZI arrays spectrometers make use of the periodic sinusoidal transmission of the individual device. Scaling the proper incremental delay of the MZIs in the array, the output can be considered as the Fourier transform of the input spectrum. The integrated FT spectrometer suffer from a trade-off between the resolution and the operation range dictated by the number of MZIs in the array. The approaches proposed offer the advantages of SOI photonics. Thus small footprint, contained costs and absence of movable parts.

Challenges of the present work: active and passive optical filters

The literature counts several high-end performance integrated spectrometers developed on SOI platform, but all of them suffer from the current platform limitations, and the resolution cannot be scaled much beyond 1 nm. Instead of pushing the limits of the current fab technologies, in the present work a combination of different optical filters and modulation techniques are used to overcome the limitations imposed by the SOI fabrication process.

Optical filters: design and analysis

Our optical filter studies focus on the techniques to design, simulated and characterize optical filters. Closing the loop of the silicon photonics engineering workflow is also a challenge: we feed the characterization results to our filter framework with the intention to modify our next generation designs on the platform. To suprt this work we developed an integrated software framework for the design of FIR and IIR optical filters. The challenge is to start from functional abstract parameters (such as filter transmission) and follow up the whole process until the measurement analysis. This has been achieved combining different Python-based software tools.

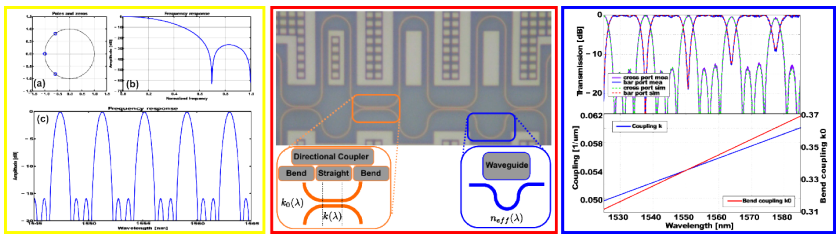

Figure 9: Optical filter framework: from functional parameter design to optical parameter extraction by measurement

Fig. 9 shows an example of the this work. Starting from the left in the yellow box, there is the general purpose simulation where the filter is handled as an abstract device: the poles and zeros are defined starting from the required transmission. The zeros and poles are then converted into photonic design specifications. Then follows the photonic simulation and the layout associated to the device. The fabrication is done by the CMOS pilot line in IMEC (in the red box a microscope image of the filter). The measurement of the device is then coupled back into the same framework as used for the design. Smart evolutionary strategies are used for the optical parameter extraction from the device measurements. In the blue box an example of the measurement and its fitting is given. The fitting of the measurement uses the same photonic simulation tool as used for the design, and it returns accurate information about the optical properties of the individual sub-blocks of the photonic integrated circuits. The tool is tested on different filters: in particular on FIR and IIR architectures, from which optical couplings and group indices are extracted. The extracted optical parameters are fed again into the simulation for the design of the following device generation.

Active single filters spectrometers

Active modulation and tuning techniques are applied to single stage filters to enhance their performances as wavelength interrogation devices. The focus is on single stage rings and MZIs. The ring resonator is modulated with the TO(Thermo-optic) effect. Doped silicon heaters traveling on both side of the ring photonic wire: the photonic and the thermal silicon strip are optically uncoupled, but thermally strongly coupled. The device is measured at the drop port. Fig. 10(b) shows a microscope image of the device.

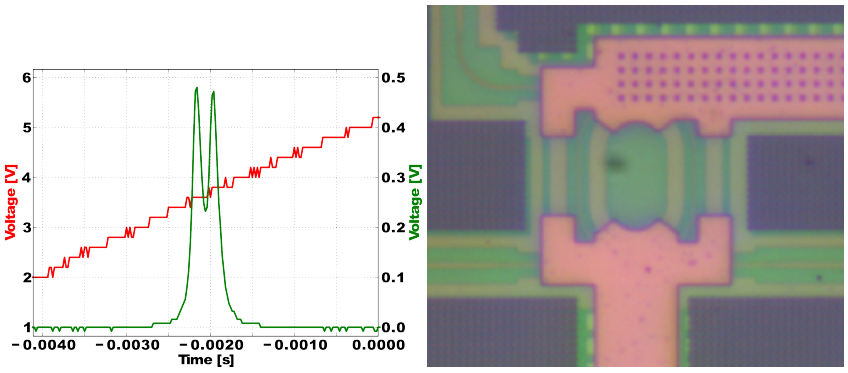

(a) Resolution measurement: 300 pm

(b) Microscope image of the thermo-optic modulater ring

Figure 10: Scanning ring spectrometer: resolution characterization and microscope image

Since the drop port is used, the transmission is Lorentzian. The Lorentzian

transmission is used to scan in the time domain the unknown input spectrum: thus the operation range is limited to the FSR of the ring, in this case, $\sim 10\ nm$. The measurement is carried out with discrete and continuous time domain driving. Both the experiments deliver good results. The limits of the device are tested with continuous driving. In this case, a resolution of 300 pm is measured across the whole FSR. Fig. 10(a) represents the resolution measurement. Two tunable lasers spaced 300 pm and an extinction ratio of $\sim 3\ dB$ separates them in a time domain.

We also implemented a wavelength meter based on a single modulated MZI. The MZI wavelength meter uses the carrier-dispersion effect for the modulation. In particular, carried depletion phase shifters are realized on both the arms of the asymmetric interferometer. Germanium photodiodes are integrated into the circuit, thus no optical output is needed. The principle behind this wavelength meter is based on the property of the convolution between the input wavelength and the transmission of the asymmetric MZI. Fig. 11(b) shows a microscope image of the device.

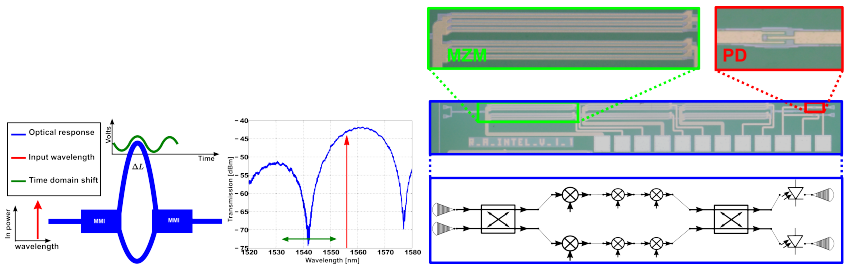

(a) Working principle of the asymmetric MZI wavelength meter

(b) Microscope image and schematic of the MZM

Figure 11: Working principle and microscope image of the fully integrated phase shift wavelength meter

Modulating the response of the interferometer with a sinusoidal carrier, the time domain output carries information about the wavelength offset between the input wavelength and the dip (or the peak) of the MZI transmission. The working principle is briefly introduced in Fig. 11(a) where the blue curve represents the passive response of the MZI, the red line represents the input wavelength and the green line is the modulating sinusoidal carrier. The achieved accuracy of this wavelength meter was $\sim 64\ pm$ average accuracy and $\sim 200\ pm$ worst case, on the whole FSR of $\sim 30\ nm$.

Cascaded optical filters spectrometers

To increase both the operation range and the resulation, we combine multiple filter elements together. AWGs and rings are combined into more complex architectures, where the TO effect is used to modulate the ring. The main architecture is

based on a single ring fed to an AWG. The same concept is explored for different purposes. First the PIC is measured as an effective index sensor, where the ring operates as the sensor and the AWG operates as the integrated spectrometer.

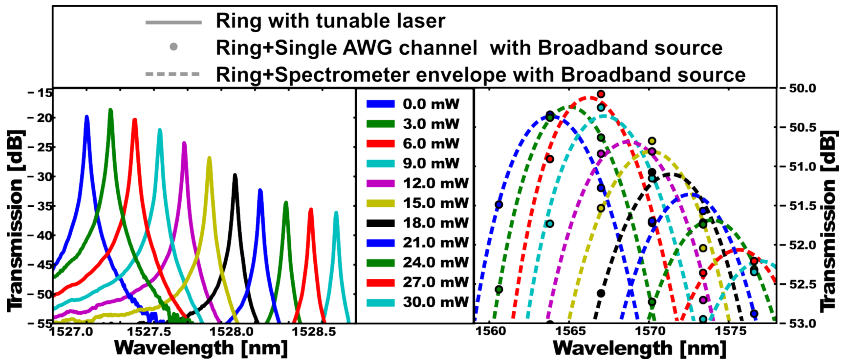

Figure 12: Shift performance comparison of the ring sensor(left) and ring+AWG cascaded system(right)

The Vernier scaling between the FSR of the ring and the output channel spacing of the AWG allows the shift of the output envelope to have a gain factor compared to the shift of the ring in stand-alone configuration. Fig. 12 shows the comparison of the ring shift (on the left) and the envelope shift of the ring/AWG system (on the right) when the same electrical power is applied. The expected gain factor of the *limit of detection* LOD is 16, but due to fabrication variations it is lower. The measured gain of the LOD is ~ 9.

The same architecture is experimentally demonstrated as a scanning spectrometers: if the FSR of the ring is larger than the AWG channel bandwidth, only one resonance peak is in the AWG channel wavelength range. Using TO effect, the comb response of the ring is modulated. Each resonance peak scans the AWG channel bandwidth with which it is associated. The resolution achieved with this experiment is 50 pm on the operation range of 48 nm, corresponding to the FSR of the AWG. Fig. 13 represents the schematic and the microscope image of the device.

Time multiplexed optical filters spectrometers

The concept of multi-domain multiplexing is applied to wavelength detection. An AWG used as spectrometer already performs wavelength division multiplexing, dividing different wavelengths into different physical channels. The device used has multiple inputs; these are positioned such that their spectral response at the outputs is shifted according to a Vernier scale. This approach reduces the equivalent channel spacing, thus removing the ”dead zone” between the AWG output channels. Since multiple inputs share the same physical output channel, electrical modulation is used to label the inputs.

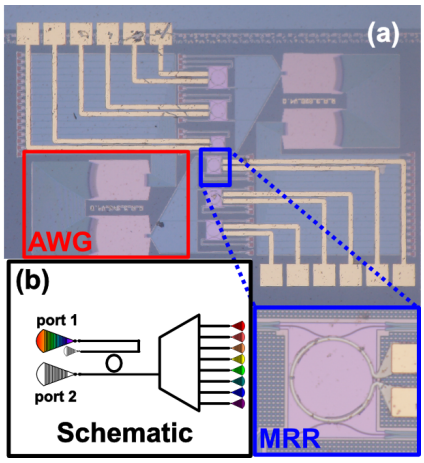

Figure 13: Schematic and microscope image of the ring-AWG cascaded spectrometer

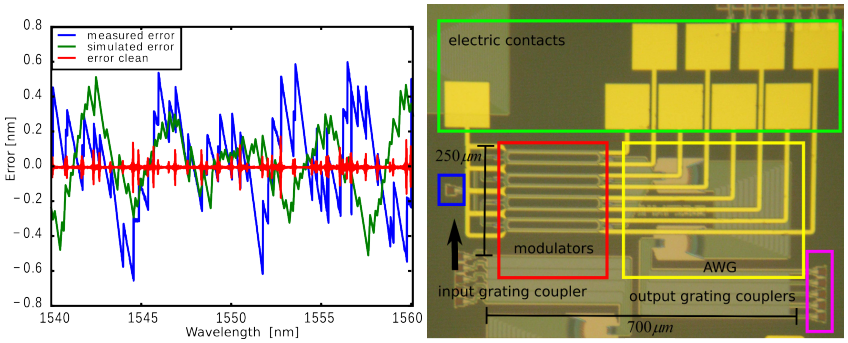

(a) Simulation and measurement of the local accuracy

(b) Microscope image of the Vernier multiplexed spectrometer

Figure 14: Microscope image and local accuracy measurements of the Vernier multiplexed spectrometer

The labeling is realized using TDM (Time division multiplexing) or FDM (Frequency division multiplexing) with MZI modulators. With this approach, a resolution of 12 pm is demonstrated using an AWG with 4 nm channels spacing and an FSR fo 20 nm. Fig. 14 shows the measured accuracy when the unknown input wavelength is the tunable laser line.

Conclusion

We demonstrated a number of novel integrated spectrometer concepts based on modulated and cascaded wavelength filters. Using modulation techniques, we

could facilitate the read-out and increase the resolution of the spectrometer or wavelength meter. By cascading multiple filters, we could increase the operation range. Several concepts were experimentally demonstrated.

1 Introduction

The goal of this work is to combine passive and active silicon integrated photonics to make near-infrared spectrometers with high wavelength resolution. Spectrometers, or the devices capable of separating a multiwavelength spectrum into its constituent wavelength components, have many applications. They range from biomedical diagnostics, environmental and chemical sensing, networking, microwave photonics and so on. High-resolution spectrometers are typically relatively bulky and sensitive components. For this reason, they are difficult to be integrated into low-cost devices such as integrated sensors or point-of-care diagnostic tools. This we intend to overcome by integrating the spectrometer functionality onto a single chip, and by using active modulation and signal processing techniques.

1.1 Optical spectrometers

Optical spectrometers are devices capable of measuring the spectral properties of the light. Information such as intensity as well as other characteristics of light such as the polarization state can be mapped as a function of the wavelength. The name ”spectrometer” itself is a general term used to indicate a device that resolves the different wavelength/frequency components of light, but depending on the particular application and on the range of wavelengths to be analyzed, the implementation of a spectrometer can be very different. This is because the techniques used to characterize different wavelength ranges are different, and so are the particular requirement dictated by the application. Spectrometers can be divided into three

different types according to their working principle.

1.1.1 Spectrometers: working principles

A first type of spectrometers is *dispersion based*. For this effect to take place, one can use a dispersive media or a dispersive device, for which the phase velocity depends on the wavelength. An example of such a device can be a prism or a grating. The analysis of the spectrum can be either serially or in parallel. In the first case the device is called monochromator, since only one detector is used and through a tunable slit the wavelength intensities are serially selected and recorded. In the latter case an array of detectors is used to reveal the wavelength contributions in parallel, in this case the device is often called a spectrograph.

Another kind of spectrometers is *filter-based*. The key element of such a family of spectrometers is a wavelength filter, as the name suggests. One can use an optical filter, either based on absorption or interference to transmit only the desired component of the spectrum. Using an array of filters with different transmitted wavelength, one can obtain a filter-based spectrometer, however the resolution is limited by the properties of the filters themselves (i.e its line width and free spectral range). Other approaches use the correlation between the incident angle of the beam onto the filter and the wavelength.

Fourier transform based spectrometers are a less intuitive way of characterizing spectra. Fourier Transform based spectrometers work in a different domain, the Fourier domain. The unknown input light source is split into two paths, where one is addressed to a stationary mirror, the second is addressed to a movable mirror. The movable mirror is used to modulate the incoming light in the time domain, as function of the displacement of the movable mirror. What is collected by the photodetector is the interferogram. Performing an inverse Fourier transform on the time domain recorded response, the wavelength domain spectrum can be reconstructed.

1.2 Application for spectrometers

In this paragraph, we list some of the main applications that suffer from the size and cost discrepancy between the DUT and the interrogator. A first example can be bio-sensing. Applications in *internet of things* and *point-of-care* diagnostics are driving toward extreme miniaturization of sensing components. In some cases, even human implantation is considered for continuous and non-invasive monitoring of bio-agents. Often such sensors are fabricated in CMOS compatible fabs, leading to a substantial reduction of the fabrication costs. But on the other hand, the interrogating device can still be extremely bulky and costly.

Another example is represented by structural sensors such as FBGs (Fiber

Bragg gratings). These sensors are embedded in optical fibers that can be embedded in the structures to be monitored (e.g. buildings and bridges). An example of practical application is structural health monitoring. Also in this case the sensor itself offer several advantages such as compactness, light weight and contained costs. But again the read-out spectrometer can be quite unwieldy.

Spectrometers are also relevant for spectroscopy applications. In that case, the interaction of light and matter is used to obtain information about the content of the sample. A small quantity of a certain substance is, in general, placed in the path of the light and the transmission spectrum carries information about the matter content. Besides the absorption spectroscopy, emission spectroscopy is also a common technique to analyze the matter. This can be used to identify biological materials, or gases.

Integrated spectrometers are also required for networking application where the knowledge of the on-chip wavelength is required for example to dynamically drive the feedback circuitry responsible for the on-chip sources.

1.3 SOI integrated spectrometers

These different kinds of spectrometers are in general extremely bulky, and thus it is extremely difficult to integrate them with the sensor itself. If the absence of movable part is not a strict requirement, some MEMS (Microelectromechanical systems) based solutions have been proposed using a CMOS compatible manufacturing platform [1]. In applications (such as space) where no movable parts can be used, other approaches have to be investigated.

Integrated photonics, and especially silicon photonics, can bring a solution here [2]. Silicon photonic waveguides can be used to make extremely small optical circuits. Besides, these can be made with CMOS mass fabrication technology. The working principles used to implement non-integrated spectrometers can be implemented in an SOI integrated waveguide platform. Silicon photonics research has built a strong track record of realizing a wide variety of passive wavelength filters, which perform the wavelength-selective functions needed to realize integrated spectrometers. However, compared to some other (bulkier) photonic technologies, the control of the waveguide dimensions is not (yet) extremely accurate. The lack of accuracy has a direct effect on the quality of the wavelength filters: only relatively coarse wavelength channels are possible, and the number of channels is limited. **The goal of the present work is to overcome these limitations using a combination of techniques.**

1.3.1 Wavelength demultiplexers filters

Silicon-on-insulator spectral filters are used for multiplexing/demultiplexing functions: many wavelengths can be combined into a single waveguide or conversely, multiple wavelengths sharing the same waveguide can be separated into different waveguides. The kind of filters often used for this purpose are image-based devices: in particular AWGs (Arrayed waveguide gratings) and PCGs (Planar concave gratings). These filters lever on interference concept. Multiple light paths interfere at the focal path, and output waveguides collect different wavelengths within a certain bandwidth. MZIsMachZehnder interferometers and microring resonators also rely on interferometry concept: in their simplest configuration (one stage) only two light paths interfere for the MZI or a singe light path interfere with itself for the ring. The wavelength interrogation properties of these two filters are limited, but their are suitable to be cascaded and combined to obtain more compels structures capable of re-addressing the wavelengths in different photonic wires.

1.3.2 Existing filter based spectrometers

Many solutions to realize integrated, SOI-based spectrometers have been proposed. Most of the are based on integrated WDM (*wavelength division multiplexing*) filters. In particular, depending on the range of operations and on the required resolution, AWGs and PCGs are often capable of delivering the proper specification. When the target resolution is comparable to the achievable channel bandwidth, a passive integrated WDM filter is often used in stand-alone configuration. A compact device which has no active power consumption can be sufficient to meet the requirements. Sub-nanometer channel spacings and therefore resolution can be achieved [3]: in this case fabrication related limitations impose a compromise between the resolution and the dynamic range performances. Other applications where the requirements on the resolution are less stringent allow more flexibility in term of filter selection [4]: the resolution of the passive filters can again be sufficient for the application. To compensate for the raw resolution limitations of the integrated optical filters, numerical postprocessing of the read-out data can often be a viable solution for on-line or off-line spectrum measurements [5, 6] . Other approaches that do not use image based filters have also been proposed, as in [7]. An array of resonators filters the wavelengths sequentially. This strategy pays the consequence of SOI-based photonics fabrication variations, in particular the SOI fabrication variability does not allow passive grid alignment of the rings.

1.4 Thesis objective and outline

The objective of the present work is to make use of the building blocks available on the silicon photonics platform to develop integrated spectrometers with a reso-

lution that exceeds that of the passive filter component. The target is to combine passive photonic filters with ”active” components, where active refers to the capability of changing the optical transmission dynamically. The active components used are modulators and, in general, phase shifters.

1.4.1 Passive filters exploration

We compare the main performance indicators of four different kinds of optical filters, namely Mach-Zehnder interferometers, microring resonators, AWGs, and PCGs. Once the strengths and the weakness of each are listed, we develop an integrated software framework for the design and analysis of FIR (Finite impulse response) and IIR (Infinite impulse response) filters. The same tool is used for the extraction of the optical parameters from the measurement of the fabricated devices. The challenge there is to build a reliable photonic engineering framework capable of design and analyze the FIR and IIR filters based on their functional specifications, and to compare their performances with the same modeling tool. For instance, we can apply the same phase noise for the waveguiding structures of all the filters. The techniques and the tools used for the filter design and analysis are the same used for electrical filter design. This work is presented in Ch. 2.

1.4.2 Active single stage filters spectrometers

In a first step, we applied active modulation techniques to single stage filters. A ring based thermo-optic modulator is used as a scanning spectrometer. The operation range is the FSR of the device. We apply a similar concept to an asymmetric MZI modulator, but in this case a faster carrier depletion modulator is used. The challenge is to improve or add wavelength interrogation capabilities to optical filters that otherwise have only limited features. This work is presented in Ch. 3. The first part of the chapter explores the different modulation techniques, also providing practical implementations, while in the second part of the chapter, we apply these techniques to the device under test.

1.4.3 Multi-device spectrometers

To improve the resolution and operation range beyond that of a single filter, we combine different filters topologies to enhance their performances compared to the stand-alone configuration. In particular, we used rings and AWGs: the first offer high wavelength selection properties while the second has a larger operation range. The challenge is to achieve a high resolution and large operation range spectrometer. These devices are also dynamically tuned or modulated with active thermo-optic tuning. This work is presented in Ch. 4.

1.4.4 Multi-domain multiplexing

In this part of the work, we combine the WDM technique with time domain multiplexing techniques. The target is to enhance the performance of the WDM filter, taking advantage of its flexibility to admit multiple inputs as well. The used WDM filter is an AWG. Each input of the AWG is fed by an MZI modulator. The modulator is used for labeling of the inputs since they share the same physical output channels. The challenge consists in the proper design of each sub-element of the PIC (Photonic integrated circuit) and to build the mathematical algorithms for the wavelength recovery. This work is presented in Ch. 5.

1.5 Conclusion

In this work we have explored a number of novel spectrometer concepts based on combinations of integrated wavelength filters with active modulation. With these techniques, we can overcome resolution limits of passive filters and achieve a larger operation range than with the individual filters. To enable this, we have developed a number of characterisation tools, which are described in detail in App. A, and App. B.

1.6 List of publications

1.6.1 Journal Publications

- **A. Ruocco**, A. Ribeiro, W. Bogaerts (Manuscript in preparation), Digital to analog optical component driving
- **A. Ruocco** and W. Bogaerts (Manuscript in preparation), Integrated Wavelength Meter in Silicon based on Phase Shifting
- **A. Ruocco**, M. Fiers, W. Bogaerts (Manuscript in preparation), Robust Universal Optical Circuit Characterization and Optimization
- M. Muneeb, **A. Ruocco** , A. Vasiliev, A. Malik, H. Chen, M. Nedeljkovic, L. Cerutti, et al.,(submitted) Heterogeneousn integration of InAsSb p-i-n photodiodes on a 3.8um wavelength range SOI arrayed waveguide grating spectrometer,*Photonics Technology Letters*
- S. Dwivedi, **A. Ruocco**, M. Vanslembrouck, T. Spuesens, P. Bienstman, P. Dumon, T. Van Vaerenbergh, W. Bogaerts, Experimental Extraction of Effective Refractive Index and Thermo-Optic Coefficients of Silicon-On-Insulator Waveguides using Interferometers,*Journal of Lightwave Technology*

- A. Subramanian, E.M.P. Ryckeboer, A. Dhakal, F. Peyskens, A. Malik, B. Kuyken, H. Zhao, S. Pathak, **A. Ruocco** et al., Silicon and silicon nitride photonic circuits for spectroscopic sensing onachip ,*Photonics Research (invited)*
- Y. Xing, T. Ako, J. George, D. Korn, H. Yu, P. Verheyen, M. Pantouvaki, G. Lepage, P. Absil, **A. Ruocco**, C. Koos, J. Leuthold, K. Neyts, J. Beeckman, W. Bogaerts, Digitally Controlled Phase Shifter using an SOI Slot Waveguide with Liquid Crystal Infiltration,*Photonics Technology Letters*
- M. Muneeb, **A. Ruocco**, A. Malik, S. Pathak, E.M.P. Ryckeboer, D. Sanchez, L. Cerutti, J.B. Rodriguez, E. Tournie, M. Smit, G. Roelkens,Silicon-on-insulator shortwave infrared wavelength meter with integrated photodiodes for on-chip laser monitoring, *Optics Express*
- **A. Ruocco**, D. Van Thourhout, W. Bogaerts, Silicon Photonic Spectrometer for Accurate Peak Detection using the Vernier Effect and Time-Domain Multiplexing,*Journal of Lightwave Technology*

1.6.2 Conference Publications

- A. Ribeiro, **A. Ruocco**, L. Van Acker, W. Bogaerts, Demonstration of a 4x4-port Universal Coupler,*12th International Conference on Group IV Photonics* **post-deadline** *(GFP 2015)*
- **A. Ruocco**,W. Bogaerts", Fully Integrated SOI Wavelength Meter Based on Phase Shift Technique,*12th International Conference on Group IV Photonics (GFP 2015)*
- **A. Ruocco**, José Juan Colás,W. Bogaerts, Microring Resonator Refractive Index Sensor with Integrated Spectrometer,*12th International Conference on Group IV Photonics (GFP 2015)*
- D. Delbeke, A. Subramanian, P. Cardile, W. Woestenborghs, **A. Ruocco**, J.W. Hoste, D. Martens, A. Dhakal, P. Bienstman, G. Roelkens, N. Le Thomas, R. Baets, **Submitted**, Silicon photonics for on-chip spectrophotometry,*12th International Conference on Group IV Photonics (GFP 2015)*
- S. Dwivedi, T. Van Vaerenbergh,**A. Ruocco**, T. Spuesens, P. Bienstman, P. Dumon, W. Bogaerts **Accepted**, Measurements of Effective Refractive Index of SOI Waveguides using Interferometers, *Integrated Photonics Research (IPR 2015)*
- **A. Ruocco**, M. Fiers, M. Vanslembrouck, T. Van Vaerenbergh, W. Bogaerts, Multi-parameter extraction from SOI photonic integrated circuits using circuit simulation and evolutionary algorithms,*Photonics West 2015*

- W. Bogaerts, S. Pathak, **A. Ruocco**, S. Dwivedi, P. De Heyn, P. Dumon, D. Van Thourhout, J. Van Campenhout, P. Absil, Silicon photonics non-resonant wavelength filters: comparison between AWGs, echelle gratings and cascaded Mach-Zehnder filters, *Photonics West 2015*

- **A. Ruocco**, D. Van Thourhout, W. Bogaerts, Silicon Photonic Accurate Wavelength Detection using an AWG and Time-Domain Multiplexing,*11th International Conference on Group IV Photonics (GFP 2014)*

- **A. Ruocco**, D. Van Thourhout, W. Bogaerts, SOI Lattice Filters Design Framework: from Functional Parameters to Layout,*Proceedings of the 18th Annual Symposium of the IEEE Photonics Society Benelux Chapter 2013*

- W. Bogaerts, Y. Li, S. Pathak, **A. Ruocco**, M. Fiers, A. Ribeiro, E. Lambert, P. Dumon, Integrated design for integrated photonics: from the physical to the circuit level and back,*Proceeding SPIE 8781, Integrated Optics: Physics and Simulations May 2013*

References

[1] R F Wolffenbuttel. *MEMS-based optical mini- and microspectrometers for the visible and infrared spectral range*. Journal of Micromechanics and Microengineering, 15(7):S145, 2005.

[2] Ananth Z. Subramanian, Eva Ryckeboer, Ashim Dhakal, Frédéric Peyskens, Aditya Malik, Bart Kuyken, Haolan Zhao, Shibnath Pathak, Alfonso Ruocco, Andreas De Groote, Pieter Wuytens, Daan Martens, Francois Leo, Weiqiang Xie, Utsav Deepak Dave, Muhammad Muneeb, Pol Van Dorpe, Joris Van Campenhout, Wim Bogaerts, Peter Bienstman, Nicolas Le Thomas, Dries Van Thourhout, Zeger Hens, Gunther Roelkens, and Roel Baets. *Silicon and silicon nitride photonic circuits for spectroscopic sensing on-a-chip, Invited*. Photon. Res., 3(5):B47–B59, Oct 2015.

[3] P. Cheben, J. H. Schmid, A. Delâge, A. Densmore, S. Janz, B. Lamontagne, J. Lapointe, E. Post, P. Waldron, and D.-X. Xu. *A high-resolution silicon-on-insulator arrayed waveguide grating microspectrometer with sub-micrometer aperture waveguides*. Opt. Express, 15(5):2299–2306, Mar 2007.

[4] E. Ryckeboer, A. Gassenq, M. Muneeb, N. Hattasan, S. Pathak, L. Cerutti, J.B. Rodriguez, E. Tournié, W. Bogaerts, R. Baets, and G. Roelkens. *Silicon-on-insulator spectrometers with integrated GaInAsSb photodiodes for wide-band spectroscopy from 1510 to 2300 nm*. Opt. Express, 21(5):6101–6108, Mar 2013.

[5] M. Nedeljkovic, A.V. Khokhar, A. Delage, P. Cheben, and G.Z. Mashanovich. *Mid-infrared silicon-on-insulator Fourier-transform spectrometer chip*. Photonics Technology Letters, IEEE, PP(99):1–1, 2015.

[6] Charles G. Askins, Martin A. Putnam, and E. J. Friebele. *Instrumentation for interrogating many-element fiber Bragg grating arrays*, 1995.

[7] Zhixuan Xia, Ali Asghar Eftekhar, Mohammad Soltani, Babak Momeni, Qing Li, Maysamreza Chamanzar, Siva Yegnanarayanan, and Ali Adibi. *High resolution on-chip spectroscopy based on miniaturized microdonut resonators*. Opt. Express, 19(13):12356–12364, Jun 2011.

2
Wavelength filters

This chapter gives an introduction to the different types of optical wavelength filters. Before going into detail on the individual filter types, we will give a general overview of the model adopted for optical filters and the general modeling approach. The duality of optical and digital filters is then proposed, and the main common tools and techniques for photonic engineers are explained. The model adopted for the analysis of the basic building blocks in the optical filters is discussed, including some simulations of the most complex elements.

With this knowledge, the different families of optical filters are analyzed in more detail, and the peculiarity of particular design approaches are discussed. The chapter continues with the description of the standard performance indicators used for all the optical filters, also giving a brief introduction to the parameters that affect the performance. We then perform a comparative study of these parameters with our simulation tools based on a general model behavior for the different filters. The focus is on *moving average* (MA) filters and the parameters of interest are the *insertion loss* (IL) and the *cross-talk* (XT). The following section describes in detail the *auto-regression moving-average* (ARMA) filter framework. The method and the software tool we present are capable of designing ARMA filters starting from the general purpose functional specification of the filters and step by step create the photonic simulation and layout. This way, we close the photonic engineering loop: measurements of the fabricated filter devices are fed into the design framework and the optical specifications are then extracted and compared with the outcome of the simulation used in the design phase. Moreover, using the extracted optical parameters, complex filter architectures are designed and simulated.

2.1 Optical filters

An optical filter is a device that separates different wavelengths or colors in an optical beam [1]. The filtering process is performed on a spectrum with a broader, more complex wavelength content. The response of optical filter devices can be designed to fulfill the requirements of the particular application of interest. This can be a bandpass filter for an optical communication channel, a wavelength sampler for a spectrometer, a wavelength meter for a Bragg filter, or a pulse shaper for optical signal processing.

The working principle behind most optical filters is interference. Optical interference is the phenomenon in which at least two optical waves are combined into a single optical wave. Because both waves have a phase, the resulting amplitude can be different from the pure sum of the individual waves' amplitudes. Fig. 2.1 represents graphically the concept of interference between analytical harmonics and thus sinusoidals with different phases relations.

A required property for interference to occur is the coherency of the waves. In the case of optical filters, a coherent optical wave generated by the source, is handled is such way it is divided over different propagation paths; these are then recombined to obtain the interference. The interference can be made wavelength dependent by introducing optical delays between the paths that have a wavelength dependent phase delay. The wavelength dependence of the interference makes it possible to shape the transmission of the filter to select or exclude the desired wavelengths.

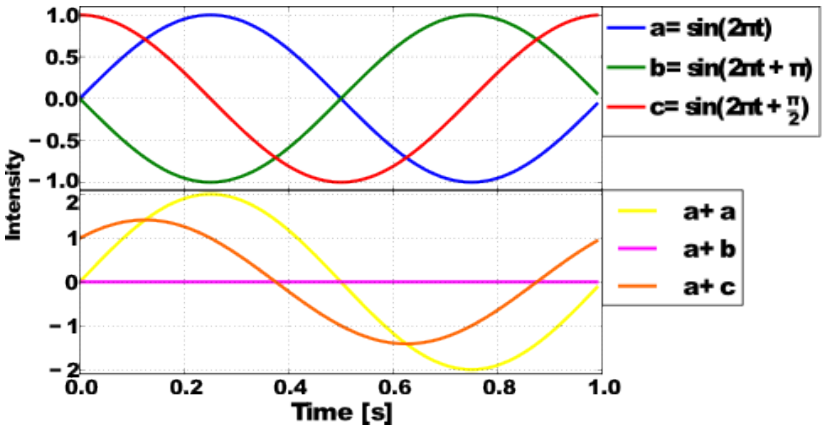

Figure 2.1: Representation of the interference phenomena in case of space coherence: constructive and destructive interferences are represented

2.1.1 Optical filters general behavior

The main mechanism which is used to manipulate the optical interference is the optical path length difference between each two coherent optical beams. The optical path is determined by both the optical and physical properties of the used waveguide. A waveguide is a structure capable of guiding an optical wave. In SOI such component is realized with a rectangular cross-section of silicon as represented in Fig. 3.1. Both these quantities can be engineered according to the requirements [2]. One of the possible approaches is to use the same waveguide structure and use the physical length as a design parameter. We keep the cross-section is fixed and therefore also the effective index. While this could be considered a simplification of the design space for optical filters, it is sufficiently general for the explanations in the rest of this chapter.

We assume each physical delay path to be a multiple of a unit delay length. The light beams traveling through different optical paths accumulate a phase delay ϕ thus, each of these phase delay can be expressed as an integer multiple of $L_{unit}2\pi n_{eff}/\lambda$.

In dispersive as well as in non-dispersive media, the phase will be wavelength dependent ($\phi(\lambda)$); the platform in use in the present work is highly dispersive [3]. Eq. 2.1 and Eq. 2.2 represent two consecutive resonance orders m and $(m+1)$: solving the system of these two equations replacing $\lambda_{m,(m=1)} = \lambda_0 \pm \Delta\lambda_{FSR}/2$ we obtain the relation in Eq. 2.3 expressing the Free Spectral Range.

$$\frac{\phi(\lambda_m)}{2\pi} = \frac{n_{eff}(\lambda_m)L_{unit}}{\lambda_m} = m \tag{2.1}$$

$$\frac{\phi(\lambda_{m+1})}{2\pi} = \frac{n_{eff}(\lambda_{m+1})L_{unit}}{\lambda_{m+1}} = (m+1) \tag{2.2}$$

We reformulate the Eq. 2.1 and Eq. 2.2 in terms of the wavelength λ_m at a resonance peak (m^{th}) and using Eq. 2.5 to model the dispersion of the photonic wire. Each of the Eq. 2.1 and Eq. 2.2 gives instead the absolute position of the resonance peaks representing individually Eq. 2.4.

$$FSR = \frac{\lambda_0^2}{n_g \Delta L} \tag{2.3}$$

$$\lambda_m = \frac{n_{eff}\Delta L}{m} \tag{2.4}$$

Eq. 2.3 represents the relation between the *free spectral range* (FSR) and the physical delay path length δL of the two waveguide carrying the interfering waves. The group index n_g (in Eq. 2.5) is assumed to be wavelength independent, and this statement is true if the range of interest is relatively small compared to the central wavelength λ_0.

Note that in literature Eq. 2.3 often refers to effective index instead of group index, and this approximation is usually valid for low index contrast waveguides. However, high dispersion platforms such as SOI instead require the group index to be used, which incorporates the first-order wavelength dispersion [4].

$$n_g = n_{eff}(\lambda_0) - \lambda_0 \frac{dn_{eff}}{d\lambda}|_{\lambda_0} \tag{2.5}$$

Eq. 2.4 and Eq. 2.3 dictate respectively the order and the periodicity of the filter response and are used for the design of most of the filters architectures. The determination of the order remains challenging due to the multiple solutions of Eq. 2.4 [5].

Another non-ideality that is worth to add to our model is the phase coherency [6]. The optical phase delay introduced in the previous section in not constant. It has a variation that depends on the cross-section variations of the photonic wire.

$$< |E^2| >= \frac{1}{2}\left(1 + cos\left(\frac{2\pi < n_{eff} > \Delta L}{\lambda}\right) e^{-((2L+\Delta L)/L_{coh})}\right) \tag{2.6}$$

The transmission of two optical paths interference (cf. 2.2.3) with a certain delay ΔL, exhibits a sinusoidal response [6] as represented in Eq. 2.6, where the physical length of the two delay lines are respectively (L) and $(L + \Delta L)$. L_{coh} is coherence length of the photonic wire. Fluctuations induced by the term $\Delta L/L_{coh}$ will shift the resonance position of the sinusoidal curve.

2.1.2 Duality of optical and digital filters

When using a fixed optical delay between consecutive optical paths, we can easily observe the duality between optical filters and digital electrical filters. This means we can use many of the digital filtering techniques for the design of optical filters.

The path delay generating the filter response is an integer multiple of a unit delay length. This property allows us to use describe the filter in the Z-transform domain. Eq. 2.7 represents the Z-transform for a discrete signal where $h(n)$ is the impulse response of the discrete signal or in our case of the filter. Being z a complex number, this function is evaluated on the unitary circle. Comparing the Z-transform with the general case of optical filters, Eq. 2.8 represents the relation between the z coefficient and the optical parameter; the ΔL corresponds to the fixed physical delay between two paths in the device.

$$H(z) = \sum_{n=-\infty}^{+\infty} h(n) z^{-n} \tag{2.7}$$

$$z = e^{\frac{j2\pi\Delta L}{\lambda}} \tag{2.8}$$

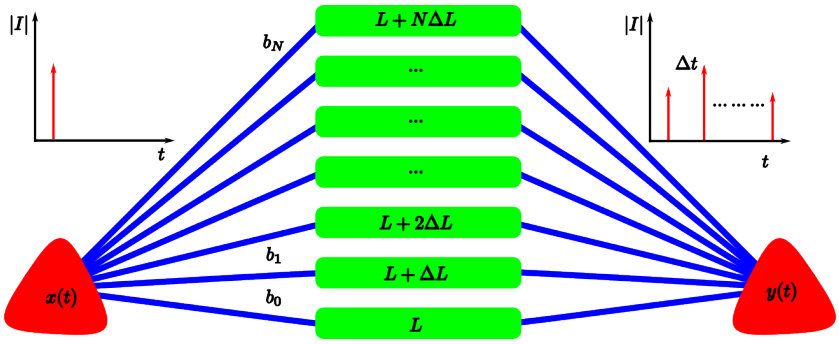

Figure 2.2: The image shows a basic representation of a finite impulse response device based on constant delay lines increment: the general purpose image represents the time domain behaviour of the device when the input is a single time domain pulse

$$y(t) = b_0 x(t) + .. + b_{N-1} x(t-(N-1)\Delta t) + b_N x(t - N\Delta t) \tag{2.9}$$

A practical example is represented by the general purpose FIR device in Fig. 2.2, where we see its time domain behavior. Different paths are addressed to different path lengths, at the output, these are recombined again, resulting in a series of impulses, one for each delay line and according to their individual Δt. The concept is formalized in Eq. 2.9.

The output of the filter relates to the input through weighted contributions of inputs and inputs with feedback. The concept is generalized in Eq. 2.10, the weight of the contributions are provided by a_n and b_m. The Z-transform of the previous relation is represented by a ratio of a polynomial transfer function as in Eq. 2.11. The roots of such polynomial relations are complex numbers and their names depend on their position in the equation: the roots of the numerator are called zeros while the roots of the denominator are called poles. The polynomials allow a number of solutions equal to its order, some of them can be multiple. In the case of passive filters the relation $\Gamma < 1$ remains since Γ sets the gain.

$$y(n) = b_0 x(n) + .. + b_M x(n-M) - a_1 y(n-1) - .. - a_N y(n-N) \tag{2.10}$$

$$H(z) = \frac{\sum_{m=0}^{M} b_m z^{-m}}{1 + \sum_{n=1}^{N} a_n z^{-n}} = \frac{\Gamma z^{N-M} \prod_{m=1}^{M} (z - z_m)}{\prod_{n=1}^{N} (z - p_n)} \tag{2.11}$$

If only feed-froward configuration is adopted, Eq. 2.11 admits only zeros, while if also feedback is present, the equation also admits poles. In the case of optical filters, the aforementioned conditions correspond respectively to MA (Moving

Average) and AR (Auto-Regressive) filter. If both poles and zeros are present, we can talk of ARMA filters. Another set of definitions can be adopted for these filters: MA filters can also be defined as FIR (Finite Impulse Response) while the AR and ARMA filters can be defined as IIR(Infinite pulse response) filters. The IIR definition includes both AR and ARMA filters since this classification is more general; if the system admits feedback, it can have an infinitive response to a finite input. Thus, FIR/IIR definition is strictly system oriented, while MA/AR/ARMA is more mathematical oriented.

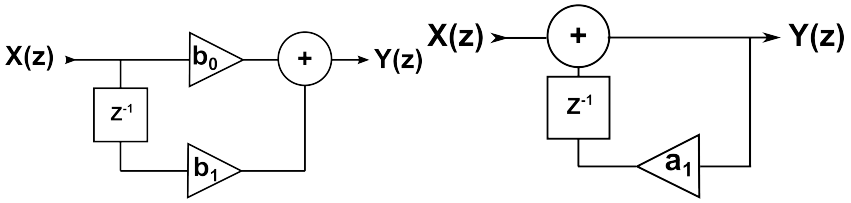

(a) Block diagram of a single stage moving average filter

(b) Block diagram of a single stage auto-regressive filter

Figure 2.3: Representation of a single stage moving average and auto regressive filter: the schematic block diagram is not linked to photonics, but has general validity

Fig. 2.3 shows the block diagram of a single pole(MA) and a single zero(AR) digital filter, respectively on the left and on the right. An optical equivalent of AR and MA filters are a single stage ring resonator and MZI respectively. The first exhibits a single pole transfer function, while the latter exhibits a single zero transfer function. These basic building blocks of Fig. 2.3 can be combined in more complex networks to realize more complex transfer functions. The blocks in Fig. 2.3 are schematic diagrams not strictly connected to optical filters. Indeed they can be for example electronic devices or pure mathematical operators.

2.2 Optical filters architectures

The transfer function of a filter is realized by selecting the most suitable topology. Depending on the particular requirement, for example, MA, AR or ARMA can be the best candidate: while MA filters always exhibit a stable response and linearity of the phase, AR filters can achieve better performances of cross-talk and narrow band with a lower number of stages. A basic example of an optical filter is a *Mach-Zehnder interferometer* (MZI), single stage or multistage: in such devices two light paths interfere with feed-forward architecture. Another kind of architecture is represented by microring resonators (MRR) where a single light path interferes with itself and hence makes a feedback architecture. The MZI or MRR architectures can be combined to generate more complex architectures [7, 8]: by increasing the

complexity, it is possible to achieve better performance (crosstalk, roll-off, ...) and to meet certain application requirements. By generalizing the concept of multiple coherently interfering light paths, other topologies can be obtained. Examples of such devices are the *Arrayed Waveguide Gratings* (AWG) and the *Planar Concave Grating* (PCG). The main difference between AWGs [9] and PCGs [10] lies in the implementation of the path delays: in the AWGs the different paths are represented by individual waveguides while in the PCGs the path delay is implemented in a free propagation region. Another common operation required by both the devices is the light splitting: when the light enters the filters, it is distributed over the different paths while maintaining their phase relation. A point worth to mention about both the AWGs and PCGs is that they have a combination of guided and free propagation regions, and thus, these devices also embed an imaging system. Fig. 2.4 schematically represents these four main types of filters.

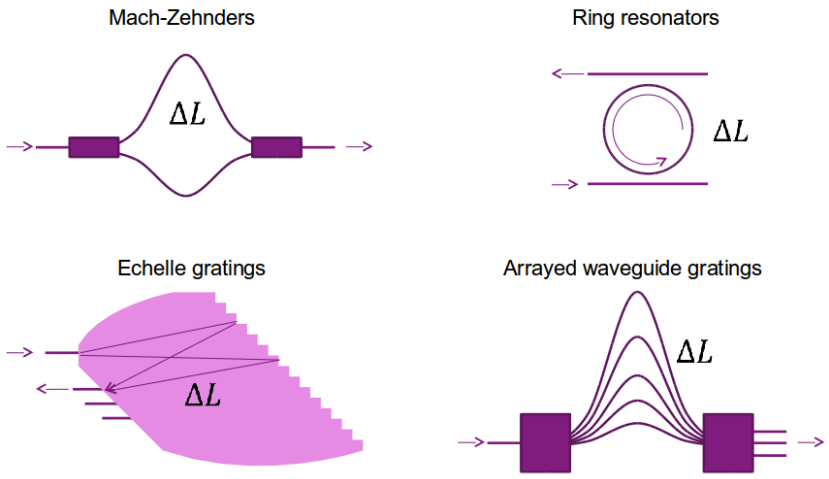

Figure 2.4: Representation of different optical filters implementation (from [11])

2.2.1 Common building blocks for optical filters

All the optical filters treated in this chapter share the same basic photonic building blocks: delay lines and power splitters. In this section, we introduce those basic building blocks as stand-alone devices. We expose the mathematical relations used for their modeling and the simulation approach used for their design. The target of this device modeling is to build a set of building blocks that can then be used in more complex structures. Discussing the modeling now allows us to use a higher level of abstraction in the larger photonic circuits, and the focus can be on the

circuit design and performance instead of device simulation and optimization.

2.2.1.1 Material system: Silicon on insulator

For this work we mainly use *silicon on insulator* (SOI) as a base material for our photonic integrated circuits. The SOI material stack we use has a 220 nm (for some application 400 nm) thick crystalline silicon layer on top of a 2 μm buried thermal silicon dioxide (*buried oxide* or BOx). The BOx layer separates the silicon device layer from the silicon substrate. On top of the photonic layer, different cladding materials can be used: two of the most commonly used are air or silicon dioxide (usually called *oxide* in this work).

Keeping in mind that the mathematical formalism adopted for the modeling of the photonic wires is suitable for a large variety of platforms, in this work we consider only high index contrast photonic wires and slabs assumed to be single mode TE like mode [12].

2.2.1.2 Delay lines and photonic wires

The key optical building block in a photonic integrated circuit is the waveguide. It transports light on the surface of the chip, but also introduces an optical delay that can be used to implement wavelength filters. The optical properties of a waveguide (n_{eff}, n_g, ...) are largely dictated by its cross section.

In SOI, we can use waveguides with different cross sections. We mostly use so-called *photonic wires*. These are fully etched submicron waveguides with a very high index contrast, which allows for a very tight bend radius [13]. .

The optical simulation of the photonic wires can be carried out with a different software tool: we use mode solvers. The results of such simulation are the optical properties of the guiding structure, in particular, the effective index and its wavelength dependency. Depending on the platform, particular cross-section, and wavelength range, the Taylor-like expansion terms of the effective index are also taken into account. In silicon photonic wires, with their high index contrast and subwavelength dimensions, these higher-order terms are non-negligible. Remember that the group index is related to the first Taylor-like expansion term of the effective index, and it is this exactly group index that controls some essential filter properties like the FSR.

Eq. 2.12 describes the analytical model used to evaluate the effective index of the photonic wire.

$$n_{eff}(\Delta\lambda) = \sum_{n=0}^{N} f^n n_{eff}(\lambda_0)\Delta\lambda^n \tag{2.12}$$

In Eq. 2.12 the first term $\frac{\delta n_{eff}}{\delta\lambda}$ is proportional to the group index. Eq. 2.13

expresses the relation between the group index as presented in Eq. 2.5 and the Taylor expansion based model in Eq. 2.12.

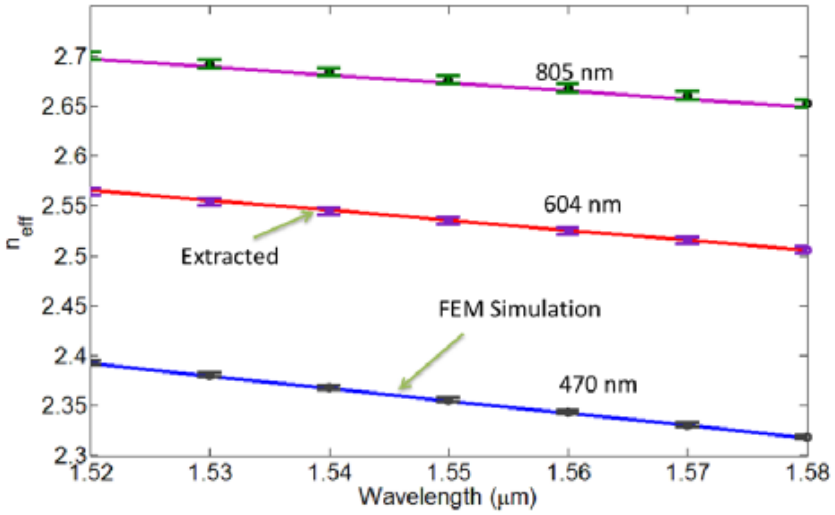

(a) Effective index for three different waveguides cross-sections

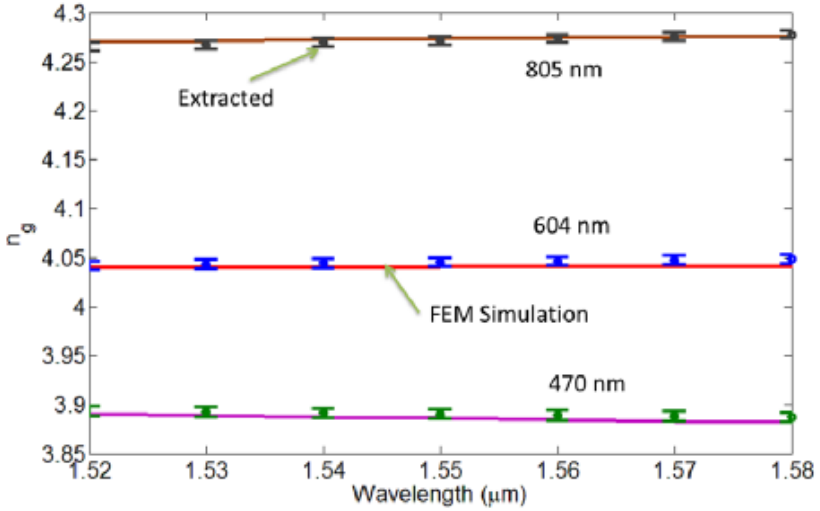

(b) Group index for three different waveguides cross-sections

Figure 2.5: The plots represent effective index (a) and group index (b) for three different photonic wires [5]

The main difference between Eq. 2.5 and Eq. 2.13 lies in the consideration or not of the first derivative of the group index dn_g/d_λ.

$$n_g(\lambda) = n_{eff}(\lambda_0) - \lambda_0 \frac{dn_{eff}}{d\lambda} - \lambda_0 \Delta\lambda \frac{d^2 n_{eff}}{d\lambda^2} \tag{2.13}$$

The effective index is a complex number, with the real part proportional to the propagation constant, and the imaginary part proportional to the propagation loss of the waveguide. For the platform used in this work, 220 nm thick SOI and operation at wavelengths around 1550 nm, three Taylor terms are included: the *effective index* and two derivatives, which describe the *group index* and the *group velocity dispersion*. During the design only first Taylor term is considered. For the analysis also the derivative of the group index can be extracted [5].

The simulation and the extraction of $n_{eff}(\lambda)$ and $n_g(\lambda)$ are shown in Fig. 2.5, respectively in (a) there is the effective index and in (b) there is the group index for three strip waveguides: namely 470, 604,805 nm width. These widths come from SEM images of the cross-section.

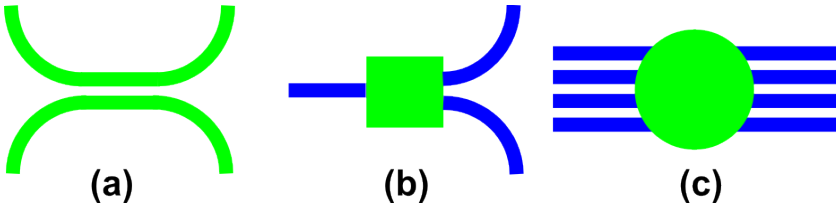

Figure 2.6: Schematic representation of the power splitting devices: (a) symmetric DC, 3 dB MMI splitter and a NxN starcoupler, in green the coupling part, in blue the photonic wires

2.2.1.3 Power splitters

Power splitters are needed for optical filters to distribute the light over two or more delay lines, but also to combine these different contributions together. Because of reciprocity, passive power splitters can be used for both functions.

Different power splitting devices are available in integrated photonics, but for the present work we use three types in particular: *directional couplers* (DCs), *multi-mode interferometers* (MMIs) [14] and *star couplers* [15]. Fig. 2.6 represents the splitting devices discussed in this paragraph: (a), (b) and (c) represents schematically respectively a symmetric DC, a 1×2 MMI and a 4×4 starcoupler: the green sections are the power splitters/combiners.

DCs are realized by placing two parallel waveguides close together. These waveguides, even if physically isolated, are optically connected since the evanescent fields exponentially decay out of the waveguide cores and have a non-zero overlap: the coupling strength is proportional to the product of this field overlap in the coupler cross-section, integrated along the propagation direction.

We can describe a DC with the following simple functional model. The waveguides composing the DC are considered identical, but the model can be extended for asymmetric waveguides [4], and could actually be useful for some specific applications [16]. Assuming the specific coupling strength to be constant along the longitudinal direction, the total power coupling can be obtained multiplying the specific coupling strength k with the length of the coupling section. The contribution of the bent section to the total coupling is also relevant. Assuming this contribution to is not dependent on the length of the coupler, it is represented by the term k_0.

$$\mathcal{K}(\Delta\lambda) = sin(\kappa_0(\Delta\lambda) + \kappa(\Delta\lambda).L_c)^2 \tag{2.14}$$

$$\kappa = \sum_{n=0}^{N} -f^n \kappa(\lambda_0)\Delta\lambda^n \tag{2.15}$$

$$\kappa_0 = \sum_{n=0}^{N} -f^n \kappa_0(\lambda_0)\Delta\lambda^n \tag{2.16}$$

All of the contributions included in the DC behavioral model are wavelength dependent. As with the waveguide properties, we also use a Taylor expansion model of the coupling properties. Eq. 2.14 represents the power coupling associated with a DC of length L, 2.15 represents the coupling strength of the straight section with a given gap and 2.16 represents the coupling associated with the bend with given gap and bend radius.

Simulation tools such as FDTD can be used for the simulation of the DCs. The bend section and the straight section can be simulated individually and then combined in a comprehensive functional model of the DC, according to Eq. 2.14. As expressed by Eq. 2.14, DCs are wavelength dependent: the longer is the coupler the more severe the wavelength dependence. Several approaches to have colorless DCs have been proposed [17, 18].

In contrast to DCs, MMIs are made of a waveguide that supports a larger number of guided modes. Waveguides can launch and collect light at both ends of the multi-mode region. An MMI can have any number of inputs and outputs so that we can talk about a NxM MMI coupler. Full modeling of MMI devices can be done with different techniques, but the most common for this device are Eigenmode expansion and propagation (EME) and the beam propagation method (BPM) and (guided-mode propagation analysis) MPA.

The simulation technique used for the 1×2 MMI of which the result is in Fig. 2.7 is EME (EigenMode Expansion) method. The main target of our MMI is to have an ideal balanced 1×2 or 2×2 splitter, but other application can have different requirement [20].

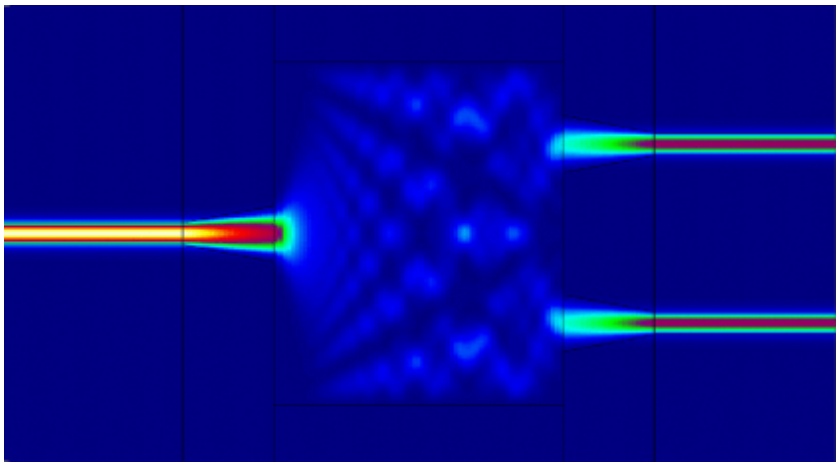

Figure 2.7: The image represents the filed distribution in a 1×2 MMI simulated with the eigenmode propagation tool FIMMPROP [19], the purpose of such device is to split the input power in two output evenly and so 3 dB for each output.

An important aspect of the couplers that we use is the phase relation that persists between the outputs. Concerning the DCs, assuming the device to be lossless, the two output modes are in quadrature of phase, thus, a phase difference $\Delta\phi\frac{\pi}{2}$ characterizes the optical signals the outputs. For the MMIs, we have to distinguish between the 1×2 and the 2×2: in the first case, the two outputs are in phase due to the symmetry of the device along the propagation direction. While concerning the MMIs 2x2, the outputs are in quadrature(as for the DCs), due to the phase relation of the modes in the multimode region.

A brief comparison between the MMIs and DCs is required. The MMIs are very tolerant in case they are designed for a particular splitting ratio. A notable example is the 3 dB (50/50) splitter: it provides a splitting ratio of 50% over a wide range of wavelengths and with a higher tolerance to fabrication compared to DCs, that on the other hand provide design flexibility. It is indeed possible to define arbitrary splitting ratios, just using the proper length of the DC (cf. Eq. 2.14).

A *star coupler* consists of two arrays of waveguides facing each other, one of them can be considered as the input side and the other as the output side. These are separated by an unpatterned slab region, which acts as a *free propagation region* since the light is no longer restricted in the horizontal plane. The incoming light from an input is injected into the slab, diffracts and propagates towards the output array grating. This diffraction distributes the incoming light over the array of output waveguides. Because the angular profile of the diffraction is Gaussian-like, the power distribution over the outputs will also be Gaussian if all the waveguides are designed identical (a uniform star coupler). Typically, the angular spread of the

star coupler is chosen to capture 95-98% of the optical power. Because the outputs are arranged in a circle, the waves in the output waveguides are also in phase.

It is also possible to engineer the power splitting ratios in the outputs. For instance, in a $1 \times N$ power splitter, the purpose is to split the power evenly over the output waveguides. Due to the Gaussian-like profile of the diffraction pattern, the position and the size of each output waveguide has to be tailored to capture the same amount of power [21].

When a splitting device is needed, we have to select the proper building blocks according to the requirements in term of wavelength dependency, tolerance, splitting ration flexibility and number of outputs. A first selection can be made according to the number of outputs required: for instance, high output counting device can be achieved either with a tree of 1x2 MMIs or with a non-uniform star coupler. The first approach is lossier but can guarantee more power splitting homogeneity, while the star coupler power splitter can be less lossy, but it exhibits a larger outputs power intensity inhomogeneity. For few output channels (1x4 for instance) a single MMI is also a valuable solution. When in comes to design flexibility, directional couplers are the best choice, since they can be designed to have an arbitrary splitting ratio according to their length, and also they are extremely low loss. Of course, the number of outputs is limited. Star couplers can also be designed to have arbitrary power splitting ratios. If the main requirement is wavelength and fabrication tolerance, MMIs remains the best alternative compared to DC.

2.2.1.4 Conclusion: basic blocks

Now we have introduced the basic blocks and their essential parameters required for the design of optical filters. We have formulated a standard model for each type of block so we can reliably design filters with a similar formal model by cascading individual building blocks. These can then be simulated with a circuit simulation tool, such as CAPHE [22].

2.2.2 Photonic circuit simulator

A photonic circuit tool is used to model the behavior of the basic building block just introduced. We use CAPHE [22]: it is a scattering matrix based simulation tool. All the building blocks are modeled as NxN matrix, each of the element is the particular scattering coefficient of the i^{th} port when the j^{th} port is stimulated. Each port is assumed to carry only one mode. If multiple modes are allowed into a physical port, each of them is described by an individual scattering element. The limited capabilities of the scattering matrix description for photonic components are expanded combining the scattering approach with more suitable tools. For instance, a relation between the geometrical and behavioral parameters of a waveguide can be built, revealing the optical parameters of the device with an FDTD

simulator and linking them to the scattering element.

2.2.3 MZI based filters

The first type of optical filters that we introduce are on-chip MZI (Mach-Zehnder interferometer). Integrated MZIs are extremely flexible and can be applied for different optical functions. They can be used for broadband [23] or narrow-band modulators or as the building block of complex wavelength filters [24], which can be designed for an arbitrary wavelength transmission response, since in theory every transmission can be replicated by its Fourier series. A specific implementation example of such higher order filters are optical lattice filters. These similar to lattice filters in the electrical domain, consisting of a cascade of DCs and delay stages. Techniques for digital filter design can be used to calculate the coupling coefficients and delays required for a given spectral response [25].

2.2.3.1 MZI working principle

In its simplest configuration, an MZI is composed of a 1×2 splitting section, two delay lines, and a 2×1 combiner.

$$I_{out}(\lambda) = \frac{1}{2}(1 + 2k\sqrt{1-k^2}sin(\Delta L(\frac{n_{eff}2\pi}{\lambda})))I_{in} \tag{2.17}$$

Eq. 2.17 represents the theoretical output of an MZI where the splitter is a directional coupler with a cross-coupling ratio κ and a bar transmission of τ. These quantities should satisfy the condition $\sqrt{\kappa^2 + \tau^2} = 1$. This relation is valid when the DC is reciprocal and loss-less. The transmission of this device depends on the properties of the DC and of the delay ΔL of the waveguides. The overall wavelength response has a sine-like response, with peaks and dips respectively where full constructive and destructive interference takes place. We should also mention that MZI based structures are always stable since there is no feedback and thus no poles.

The simulation of MZI structures is carried out with the circuit simulator CAPHE using models described earlier for the waveguides and power splitters. The scattering matrix of the sub-blocks are then combined in a scattering matrix for the entire circuit, and a wavelength sweep is performed. The non-idealities originating from fabrication tolerances are added to the scattering models of the power splitter and waveguides [26].

Fig. 2.8 shows an example of the simulation of a single-stage MZI. The couplers used are directional couplers (DCs), the MZI has a non-zero coupling length. By choosing the proper length (based on k and k_0 obtained from FDTD simulation), the DC has a power coupling of 3 dB (50/50), which results in a very strong

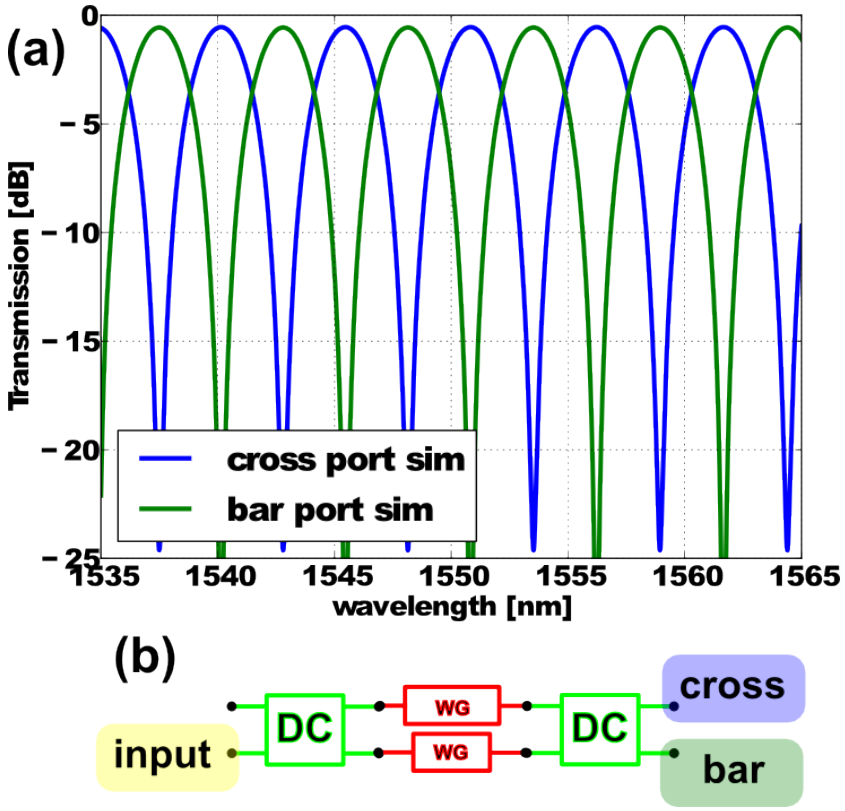

Figure 2.8: Example simulations of an asymmetric MZI (a) and the schematic block diagram used for the simulation (b)

extinction ratio between the constructive and destructive wavelengths. In this chapter, we will discuss how we use MIZs to build high order and more complex filters. MZI based devices will be used in Ch. 3 and Ch. 5 to achieve more complex functions. In Ch. 3 we used an asymmetric MZI modulator for wavelength interrogation, while in Ch. 5 symmetric MZI are used to switch and modulate the optical power.

2.2.4 MRRs based filters

Microring resonators consist of a waveguide folded back onto itself, creating a feedback path where light interferes with a delayed copy of itself. Hence, MMRs can be classified as AR filters. MRRs are extremely appealing for many photonic applications: from sensing [27] to networking [28]. They can have an extremely narrow-band response in a compact device with a low order [29].

2.2.4.1 Properties of microring resonators

The basic configuration of microring resonators consists of a looped waveguide and a directional coupling section to connect the loop and the carrier bus. This architecture with a single bus line is called an *all-pass* ring filter. When a second coupling section is added, the architecture of the ring has an *add-drop* configuration. The transmission spectrum of a simple add-drop ring resonator is described by Eq. 2.18: τ is the transmission of the directional couplers, and a is the absorption of the ring.

$$I_{out} = \frac{\tau_2^2 a^2 - 2\tau_1\tau_2 a cos(\phi) + \tau_1^2}{1 - 2\tau_1\tau_2 a cos(\phi) + (\tau_1\tau_2 a)^2} \tag{2.18}$$

The general Eq. 2.3 for the FSR is valid also in this case, where the delay ΔL is equal to the round trip length of the ring resonator. An important condition for the operation of the MMR is called *critical coupling* when the power coupled with the DC is equal to the internal loss in the cavity. In this case, the transmission at the resonance drops to zero [30]. With non-negligible loss, the critical coupling condition is met for $r_2 a = r_1$.

Other important parameter to characterize MMRs are the *finesse* and the *Q-factor*, which both relate to the line width of the ring resonances [29]. From Eq. 2.19 and Eq. 2.20 it is also possible to obtain the relation between these two important parameters.

$$Finesse = \frac{FSR}{FWHM} \tag{2.19}$$

$$Q_{factor} = \frac{\lambda_{res}}{FWHM} \tag{2.20}$$

FWHM is the full width at half maximum of the ring resonance. The physical meaning of these two quantities is related to the number of round-trips made by the photonics in the looped cavity before it has leaked out due to losses or coupling to the buses. Similar to MZIs, the MMRs require only a few basic element for the simulation: waveguides and power splitters. These elements are modeled with scattering matrices. We have to mention that in this case more attention has to be given to the modeling of the parasitic effects, such as back reflection. This can cause the clockwise and counterclockwise mode to couple, significantly affecting the performance of the ring [31].

Fig. 2.9 shows a simulation of a single stage ring. The couplers used are DCs with zero length, and a bend coupling factor k_0=0.4(cf. Eq. 2.16). The values are obtained by FDTD simulation of the bent section.

In this chapter, we will discuss how the rings can be used in more complex filter architectures (ARMA filters). Moreover, ring will be used in Ch. 3 and Ch. 4 to

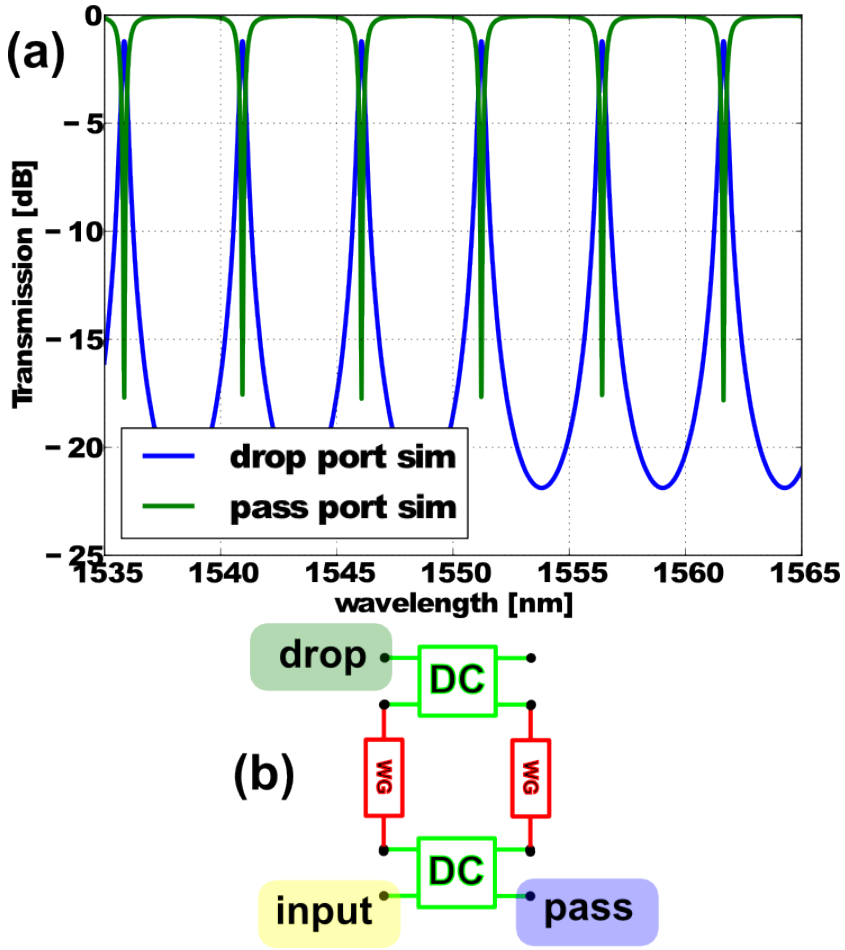

Figure 2.9: Example simulations of a MRR (a) and the schematic block diagram used for the simulation (b)

selectively filter narrow-band optical windows: the selectivity will be implemented using thermo-optic modulation.

2.2.5 Planar concave gratings

PCGs or echelle gratings are the combination of an integrated staircase reflection grating that is curved to obtain focusing. In operation, it is similar to a Czerny-Turner interferometer [32]. A PCG simultaneously separates/combines the wavelength contents of the input light, focusing the output wavelength channels into different output waveguides. It is used in many applications such as network-

ing [33, 34], spectrometry [35] among the others. PCGs are comparable in operation to AWGs (discussed in the next section), but the two types of devices perform optimally for different sets of functional parameters (number of wavelength channels, channel spacing, ...) [36].

2.2.5.1 PCG working principles

A PCG is composed of free-propagation slab area in which a grating is etched. Opposite to the grating are the input and output waveguides. The input waveguide injects light into the FPR (Free Propagation Region). The light that reaches the grating will have a different (wavelength dependent) phase delay for every reflecting facet. The light is refocused back towards the output waveguides, but with a constant, but wavelength dependent, phase delay between the contributions of subsequent facets. As a result, the refocusing point is wavelength dependent, coupling different wavelength channels into different outputs. Simply etching the reflecting facets into the FPS gives rise to high losses since the reflection of a single interface is only 35%. This reflection can be improved with metal deposition, but we use a distributed Bragg grating reflector (DBR) on each facet. This approach is compatible with the standard silicon photonics fabrication platform, and does not require extra processing steps. With such technique reflectivity above 80% can be achieved [37]. One of the most common mounting used in PCG design is the Rowland configuration [38]. In this mounting technique, the input and output apertures are placed along a Rowland circle with a fixed radius R. The facets of the grating are positioned on a circle with radius $2R$. Both this circumferences are tangent in the center of the grating, this is called pole (P). With such configuration, all the points of the Rowland circle are imaged on the same focal circle with a reflection angle determined by Eq. 2.21 [37]. In Eq. 2.21 d is the grating period while Θ_i Θ_d are the angles between the grating normal at the pole and the incident and diffracted beams respectively. m is the diffraction order. Since the coupling from input to output involves an imaging process, the modeling of the PCG requires a higher level of complexity.

$$d(sin\Theta_i + sin\Theta_d) = m\frac{\lambda}{n_{eff,slab}} \tag{2.21}$$

The used approach is a hybrid solution involving scalar diffraction methods for the FPR propagation and rigorous coupled-wave analysis for the estimation of the diffraction of the gratings. The simulation procedure can be divided into three individual parts: the grating incident field calculation, the diffracted field calculation and the overlap of the diffracted fields at the output apertures. The incident field at the center of the grating facets is calculated according to the Kirchhoff-Huygens diffraction formula, assuming the waveguide mode profile to be Gaussian. The diffracted field is calculated in a similar way, considering the incident

and diffracted angles. The output spectrum is calculated by integrating the contributions of all the grating facets [37]. Fig. 2.10(b) shows the schematic representation of the simulation diagram and (a) the simulation of a $8 \times 3.2nm$ channel PCG.

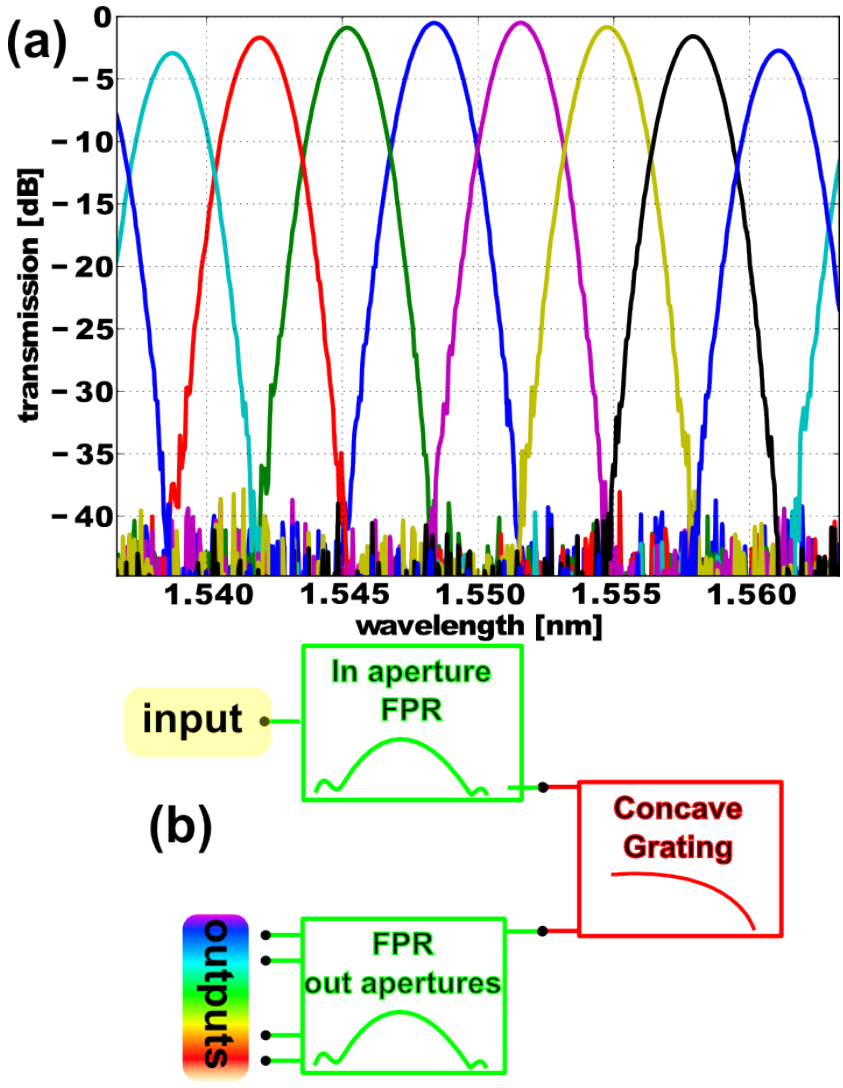

Figure 2.10: Example simulations of an eight channels PCG (a) and the schematic block diagram used for the simulation (b)

2.2.6 Arrayed waveguide gratings

AWGs are among the most flexible optical integrated filters: they are extremely suitable for multiplexing and routing of high counting in/out optical channels device [39, 40]. The AWG can be considered as a combination of three sub-blocks: an input star coupler, an array of delay waveguides, and an output star coupler. The star couplers diffract the light toward the array of waveguides; these add a wavelength-dependent phase delay, and the contributions are combined in the second star coupler. [9].

2.2.6.1 AWGs working principles

The array grating is the basic building block of an AWG. It provides the phase difference between the optical waves [9]. There are multiple conditions that have to be simultaneously satisfied. The first design equation is the relation between the physical delay ΔL and the FSR, given in Eq. 2.3. The ΔL in this case is the incremental length difference between two consecutive waveguides in the grating. The group index n_g is that of the photonic wires used in the array. If there are imbalances between the waveguides (e.g. between straight and bent sections) [41], these have to be corrected. This can be achieved by using the same number of bends on each photonic wire of the array. The star coupler, as briefly introduced in the sec. 2.2.1.3, divides the input power among all the waveguides of the array. An important requirement, in this case, is the phase relation between the light coupled to the array waveguides: the apertures of the array of waveguides connected to the FPR are identical and placed on the focal circle, with such design approach we preserve the phase homogeneity.

$$m'\lambda + n_{eff,wires}\Delta L - n_{eff,slab}R\Delta\alpha(sin\Theta_i + sin\Theta_o) = 0 \qquad (2.22)$$

The input and output waveguides can be mounted confocal or on a Rowland circle [41]. We define the grating line and the focal line, respectively as the path where the grating lines are placed and path where the input or output waveguides are placed. The delay between the waveguides of the array is designed to be an integer of the unit delay length ΔL. This quantity is combined with the optical delay length introduced by the star couplers to obtained the wavelength of maximum transmission according to the Eq. 2.22.

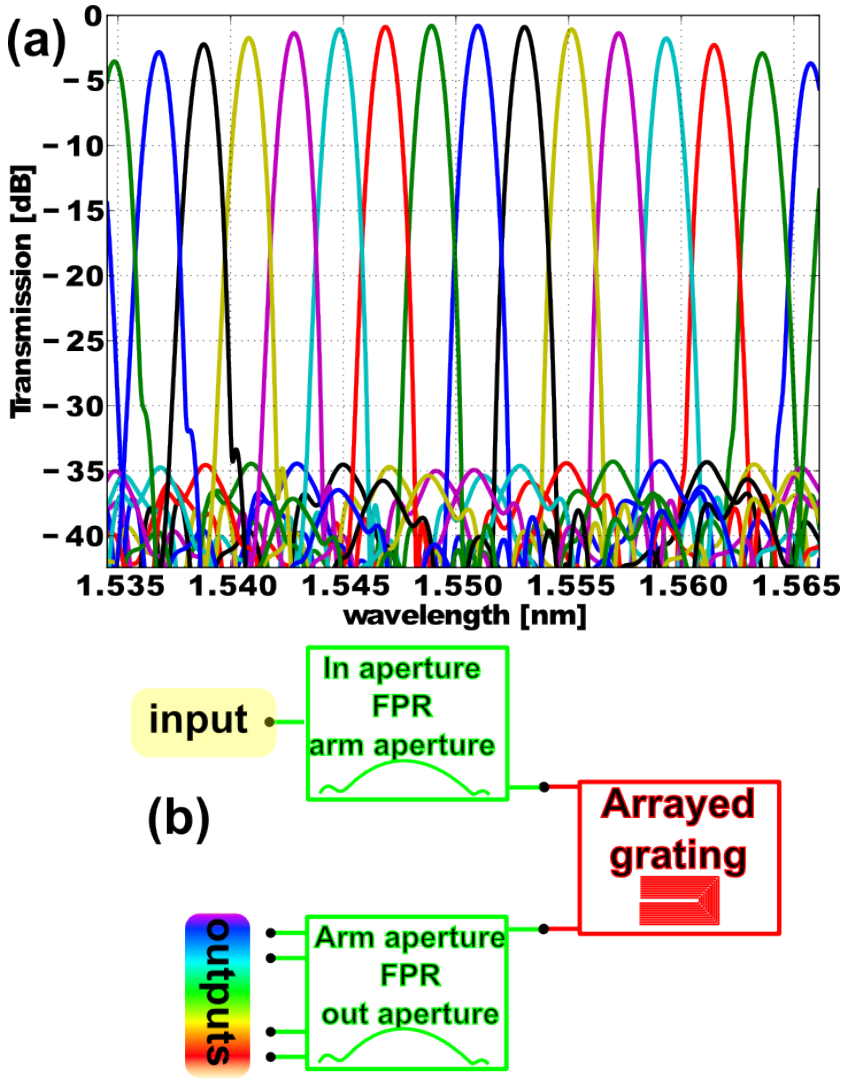

Figure 2.11: Example simulations of a sixteen channels AWG (a) and the schematic block diagram used for the simulation (b)

In Eq. 2.22 m' is an integer multiple of ΔL, $n_{eff,slab}$ is effective refractive index of the FPR while $n_{eff,wires}$ is the effective index of the photonic wires. The optical path is calculated using both these effective indices along the respective lengths in the slab ($R\alpha$) and the photonic wires(ΔL).

Similar to the PCGs, the simulation of AWGs is carried out with a hybrid technique. Each of the sub-blocks (star couplers and delay lines) is simulated individually and then the transmission matrices are combined to obtain the cumulative

transmission of the device [42].

The CAMFR eigenmode solver is used to obtain the field profile that will propagate in the FPR. A semi-analytical Fresnel-diffraction scheme is used for the calculation of the FPR propagation. The procedure is repeated for all the in/out apertures and arms apertures. It is then repeated for the in and out star couplers. Each waveguide of the arrayed grating is modeled with a the model already proposed since it is a standard single mode waveguide. The three matrices, corresponding to the FPR, arrayed grating and output FPR, are multiplied to obtain the transmission of the AWG. Fig. 2.11 represents the building block schematic in (b) and the result of an AWG 16 channels and 2 nm channels spacing AWG [42].

In the present work the AWG is used in Ch. 4 and Ch. 5. It is used as a wavelength selective filter. In Ch. 4 the AWG is combined with a ring resonator of which only a resonance peak is addressed to an AWG channel. In Ch. 5 the AWG is the only wavelength selective filter used, but using multiple inputs and time-domain multiplexing the equivalent channel spacing is reduced, thus, higher resolution is achieved.

2.2.7 Conclusion

In these paragraphs, we introduced four different kinds of optical filters: MZI, microring resonators, PCGs and AWGs. They can all be described with the same methodology of zero/poles diagrams, but while AWGs and PCGs are image-based devices, in ring and MZI no image is involved, and the light never leaves the photonic wire. Thus, the first two types are intrinsically lossy, while the other are (in theory) lossless. On the other hand the AWGs and PCGs are more prone to large channel counting, hence more suitable to be used as spectrometers. The ring and the MZI can achieve higher resolution and wavelength selective properties. Moreover, they are more suitable for tuning. In the following part, these devices will be combined to combine their strengths. In Ch. 3 we use the high wavelength selectivity of the rings and the modulation capability of ring and MZI to realized integrated spectrometers. In Ch. 4 the high resolution of the ring is combined with large channel counting of the AWGs. In Ch. 5 the AWG capability of having multiple inputs and outputs with custom channel spacing is used to enhance the wavelength resolution limited by fabrication.

2.3 Performance Metrics for Optical Filters

Depending on the application, different specifications are imposed on an optical filter. In this section, we introduce a number of common metric to characterize the performance of wavelength filters. In particular, we introduce the concept of *insertion loss* (IL) and *cross-talk* (CT). We also describe the main mechanisms that

influence these metric in the different optical filter architectures. Fig. 2.12 gives a graphical interpretation of the IL and CT for a general filter transmission [43].

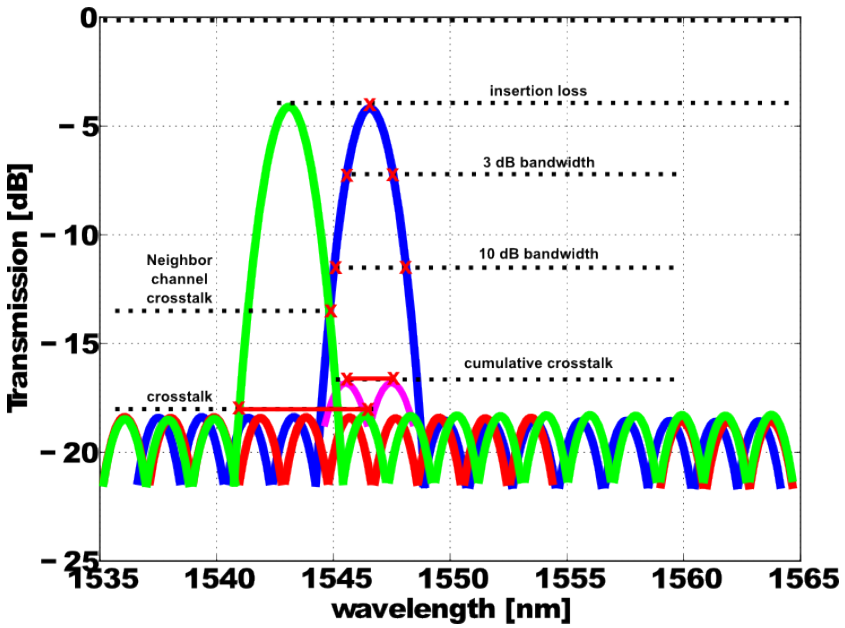

Figure 2.12: Graphical representation of the insertion loss and different cross-talks for a general purpose filter

2.3.1 Insertion loss

The IL is the loss of power when a filter is inserted into the optical path at a wavelength where maximum transmission is required. IL is usually expressed in dB. In integrated optical filters the IL is influenced by different mechanisms, depending on the architecture adopted [44].

2.3.1.1 Waveguide loss

The source of loss that is common to all types of filter is the intrinsic propagation loss of the photonic wires and slabs [45]. This propagation loss is itself associated to different mechanisms. The loss in crystalline silicon is, in general, negligible at 1550 nm, but due to the fabrication process, the upper silicon layer of the wafer is slightly boron-doped to have a reproducible P-concentration, but this doping introduces some bulk loss [46].

Unsatisfied bonds or other element bonds at the interface Silicon/Oxide or Silicon/Air also introduce absorption as the photons get absorbed [46], and can intro-

duce surface doping due to band shifting [47]. For submicron photonic wires and high optical power density, non-linear absorption can also affect the propagation loss [48]. In general, this effect can be neglected for most of the devices, except when the device has resonances which induce a hight local power density, such as in microring resonators [29]. Substrate leakage is also present in SOI waveguides: When the buried oxide is too close, the evanescent tail of the mode will feel the high-index silicon of the substrate.

Another contribution to propagation loss is scattering. Rayleigh scattering arises from sub-wavelength perturbations in the bulk of the waveguide core [49]. Scattering at the sidewall roughness is also present at the waveguide core interfaces, and because of the semiconductor processing, it is actually a predominant contributor to the propagation loss. Improvements in fabrication quality can dramatically affect the sidewall scattering loss [50].

All the contributions are dependent on the optical field distribution inside the waveguide, and, therefore, wavelength dependent and cross-section dependent. Apart from non-linear loss, all of the phenomena depends linearly on the length of the waveguide, and are expressed as the specific absorption constant α. What we obtain is the product of the loss and the length of the photonic wire.

For bends, we can use a loss parameter as a function of the bending angle, for a fixed bend radius. [51].

2.3.2 Loss in couplers

DCs are affected by non-idealities such as loss and scattering. The losses are mainly induced by the same cause introducing losses in the waveguides since these are the main constituent of the DCs. An additional element is the modal conversion losses caused by the cross-section mismatch between the eigenmodes at the transition region (bend section of the DCs) and the DC straight section [52]. Another source of non-ideality in DCs is the scattering at the discontinuity [53].

2.3.2.1 Imaging related loss

In AWGs and PCGs, but also MMIs, an additional source of insertion loss is due to imaging non-idealities. The FPRs used in both AWGs and PCGs act as an imaging system, refocusing diffracted light. The first mechanism of loss in FPRs is the incomplete power capture by the grating array. A portion of the Gaussian-like field radiated by the input aperture is outside of the collection cone of the array. There are also losses due to reflection and scattering inside the star coupler.

In the case of the AWG, most of this reflection is caused by the narrow separation between the grating apertures, which is limited by lithography minimum feature size. In the case of the PCG scattering and losses are caused by imperfect grating reflectors, which at the edges scatter light outside of the collection

cone of the waveguides [36]. Because both AWGs and PCGs are periodic grating structures, they will couple some light to different diffraction orders. This effect is predominant at the central channel. Loss non-uniformity is the loss due to the far field envelope of the array aperture. This effect is more pronounced in the outer channels, which can suffer up to $3dB$ power penalty compared to the center channel.

2.3.3 Crosstalk

The crosstalk is, in general, the ratio between the target signal and the unwanted contributions in the same physical channel [54]. In regard to optical filters, there are few definitions for the crosstalk depending on the application. Crosstalk can be defined relative to the center channel, or the 3 dB and 10 dB bandwidth: the reference power is estimated, respectively at the center of the channel, inside the 3 dB bandwidth and inside the 10 dB bandwidth.

2.3.3.1 Crosstalk in optical filters

The crosstalk of optical filters can be a design parameter, as in the case of window based design [25], or a parasitic effect [55]. In the first case, the cross-talk level is a specification, which is included in the design algorithm, to which parasitic effects have to be added. In the second case, the ideal cross-talk is zero, but non-idealities affect it. An example of design specifics where the crosstalk is a design parameter is the Chebyshev window approach: the crosstalk level is imposed by properly selecting zeros and poles. Whether the CT is a design parameter or purely a parasitic consequence, it is always an issue to minimize the unwanted effects which make the CT worse. In filters where no imaging system is used, the crosstalk is mainly influenced by the phase errors introduced by the waveguide imperfections: the tolerances affect the local variability of the photonic wire's effective index, and, therefore, exact optical length. One of the direct consequences of this effect is the phase correlation variations between the different light contributions at the interference sections. For imaging based systems the crosstalk is a function of the image quality at the output waveguide. The image quality itself is influenced by the star coupler or facet fabrication tolerances. On top of this, phase errors from the FPR are also present, but typically less pronounced due to the robustness to the fabrication of the slab regions. The FPRs are more robust against phase errors than strip waveguides [56], since no side-wall roughness affects the propagation constant. When we have multiple channels filters, we can have two definitions of cross-talk: standard crosstalk and cumulative crosstalk. They are the difference between the peak power of the passband and respectively the worst case of the power coupled from other channels and the sum of the power coupled from all the other channels [41]. For a graphical representation of the cross-talk in the filter

response refer to Fig. 2.12.

2.3.3.2 IL and CT comparison in optical filters

We perform a simulated comparison of the insertion loss and the crosstalk in different types of filters, but limited to feed-forward architecture, i.e. MZI lattice filters, arrayed waveguide grating and planar concave gratings. To perform such comparison, an equivalent coherence length L_c is attributed to the waveguides and from this quantity random phase errors are estimated [46] according to the Eq. 2.23 [57], where L is the physical length of the waveguide. The same model is used for the waveguide of the array grating and the waveguides of the lattice filters. Different approaches are used for the grating of the PCG where coherence length of the phase error is defined in a different way: the main phase error contribution does not arise from waveguides, but from the fabrication tolerances of the facets of the gratings, since the imperfect edges of the facets scatter incoherent light. We have to mention that a substantial lower contrition to phase non-idealities arise from the slab region, and thus it is neglected in the following discussion.

$$< \Delta\phi(dL)^2 >= \frac{2L}{L_c} \tag{2.23}$$

Fig. 2.13 represent the results of the CT and IL trends of different FIR filters as a function of filter stages and for different phase error variances. In the filters under test the channel properties are the same, except for the PCG, which has a channel spacing of 20 nm instead of 8nm. The insertion loss reaches an optimum point when the number of arms is 3 times the number of outputs; the same assumption is valid for PCGs as well using a number of facets 40 times the number of outputs. This condition comes from the fact that fewer arms and reflectors, do not supply enough contributions to create a proper image of the field. The lattice filters instead reach a minimum IL when the number of stages is 2 times the number of equivalent [25] outputs, since with lower order filters, we do not have the minimum amount of Fourier contribution for the description of the filter. The behavior of the crosstalk follows similar trends, giving an optimal value of arms of twice the number of outputs for the AWG. The PCGs needs a number of facets 60 times the number of outputs. The lattice filters need instead a number of stages 2 times the number of equivalent channels [25].

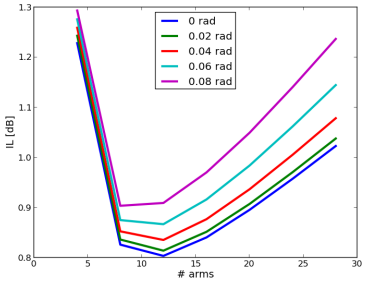

(a) IL of AWG 8 nm channels spacing vs number of arms

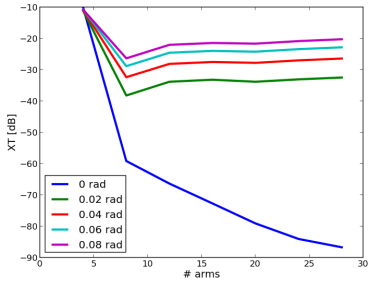

(b) XT of AWG 8 nm channels spacing vs number of arms

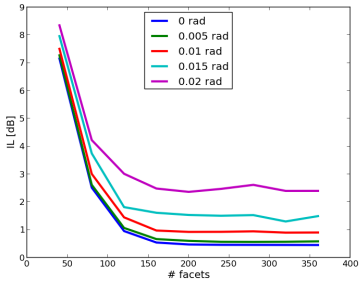

(c) IL of PCG 20 nm channels spacing vs number of facets

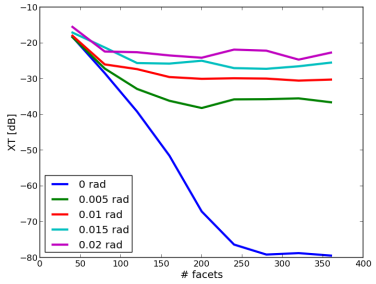

(d) XT of PCG 20 nm channels spacing vs number of facets

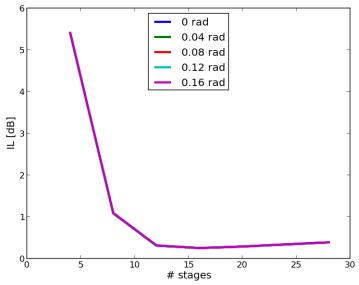

(e) IL of lattice filter 8 nm channels spacing vs number of stages

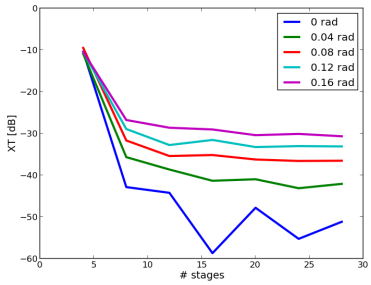

(f) XT of lattice filter 8 nm channels spacing vs number of stages

Figure 2.13: The plots represent on the left and on the right respectively the crosstalk and the insertion loss behaviours when increasing the order of the filters. They are listed in the order AWGs, PCGs and lattice filters

This is due to the same condition of the IL where few stage filters do not have enough Fourier components for the description of the filter shape. This experiment is limited to the simulation models adopted for the waveguides taking into account

waveguide losses and phase noise. The results are in agreement with experiments reported in literature [37, 41, 46].

2.4 ARMA filter design framework

Auto-regressive Moving Average (ARMA) optical filters comprise a very useful class of filters. First of all, they are made of basic photonic sub-blocks, and can be implemented with just photonic wires and directional couplers. The advantage of ARMA filters lies in the flexibility of using both *auto-regression* (AR) and *moving average* (MA) mechanisms, and thus leveraging both architectures: lower order ARMA filters can be used instead of higher order AR or MA filters [4]. Moreover, as introduced in 2.1.2, the duality between Z-transform and optical ARMA filters give to the designer a full set of established mathematical and design tools already developed for electronics. We developed a full framework for ARMA filters design starting from the general purpose filter simulation [58], as in Fig. 2.14(b). After the design and simulation of the normalized filter response, we proceed with the analysis of the zero-pole diagram in Fig. 2.14(a). Levering on these tools and on the functional parameters of the basic building block we obtain the photonic circuit simulation in Fig. 2.14(c) using CAPHE [22, 59]. The layout is then obtained with IPKISS [60].

2.4.1 Generic digital filter tools for ARMA optical filters design

We approach the study of optical filters with methodologies developed for digital general purpose filters, making use of the duality introduced in Par. 2.1.2. The reason we do it lies in the fact that a lot of algorithms already developed for digital filters can be directly adopted for optical filters design. Moreover, if we treat optical filters like digital/analog LTI (Linear time-invariant) systems, we can increase the level of abstraction compared to the use of electromagnetic theory. A higher level of abstraction enables efficient and straightforward scalability of the elementary devices. The result of such fast scalability is proposed in the coming paragraph where a general purpose design and simulation framework for MA and AR filters is proposed.

Defining the desired transmission spectrum is the first step in a filter design. Any known filter window can be used, which include Butterwood, Chebyshev, ideal box window, elliptical etc [58]. The design of the general purpose filter starts with the definition of its parameters such as the stop-band, the pass-band and attenuation.

Since we are working with a general digital filter, the parameters are expressed as normalized quantities: the frequency(wavelength) range is normalized between 0 and 1, and the cut-off frequency is expressed accordingly. Fig. 2.14(a) represents

the zero-pole diagram of a fourth order Chebyshev lattice filter.

The transmission T as in Fig. 2.14(b) is specified by the attenuation in the pass band and the stop band. These specifications are converted into the series of Fourier components and the relative zero-pole diagram, shown in Fig. 2.14(a). Most of these filter design windowing have been tested through simulation, but the focus is on Chebyshev filters. This choice is made since the Chebyshev filter design procedure minimizes the error between ideal and filter response and provide steep roll-off and good ripple properties [4].

2.4.2 ARMA filters photonic design and simulation

The filter parameters from such calculations are general purpose. They can be seen as a theoretical solution for the Z-transform correlated to the zero-pole diagram2.11 or as power coefficients and phase relation to be used for a filter design: it can be in principle either electronic or photonic. Our particular case is of integrated photonic filters: the power coefficients and the phases information corresponds to optical power splitting and optical phase delays. The ARMA filter, in their simpler configuration, can be realized with only directional couplers and waveguides. For calculating the length of the directional couplers,we invert Eq. 2.14 evaluated at the wavelength of interest, which gives us Eq. 2.24.

$$L_c = \frac{sin^{-1}\sqrt{\mathcal{K}} - k_0}{k} \tag{2.24}$$

Another important parameter is the FSR that can be estimated with the Eq. 2.3. This parameter is not related to the general purpose filter, but it is used to shift the base transmission spectrum at the wavelength of interest. As for the coupling coefficients: when a large phase shift ($> \pi$) is needed, one can think of using a long directional coupler, but a more attractive solution is to manage the phases on the waveguide of the delay lines by adding a length to the delay stage according to the Eq. 2.25, where the mentioned ΔL_{phase} gives a 2π shift corresponding to one FSR.

$$\Delta L_{phase} = \frac{\lambda_0}{n_{eff}} \tag{2.25}$$

The simulation of ARMA filters is carried out with the CAPHE photonic circuit simulator in which our elaborate model for directional coupler and waveguide is implemented. To a very good approximation, we can consider ARMA filters to be passive and linear components (i.e. for operations where the optical power is not excessive), and we can limit the simulation of interest to wavelength response. This approximation is valid if optical power density in resonant structures such as rings does not lead to non-linear effects. If this condition is not valid, the hypothe-

sis of passivity is not valid and the simulation will require additional time domain simulations at different input power levels.

2.4.3 MA devices: lattice filters

Lattice filters belong to a sub-category of ARMA filters, as there is no feedback (AR), but only feed-forward (MA) [61]. Basically, lattice filters are composed of cascaded MZIs. They are exclusively composed of n 2×2 power splitters, in our case DCs, and $n - 1$ delay stages, where n represents the order of the filter. In this case the order n represents the number of the cascaded stages and does not have to be confused with resonance order defined in Eq. 2.4. The Higher order adds more Fourier components to the filter and, therefore, corresponds to better performances. As a consequence, there will be less error in the replication of the desired response. However, the higher order allows for the accumulation of more non-idealities and, therefore, requires a much better control on the design parameters such as the power splitting for each stage. Satisfying the trade-off between these requirements in correlation with the capabilities of the platform in use, gives the optimal filter.

Once the design specifications are converted into photonic layout properties, the photonic circuit simulator tool can solve the equivalent scattering matrix associated with the device, taking into account the full models and physical parameters. In the case of the lattice filters, and for analytical calculation, the directional coupler stage can be modeled as Eq. 2.26 and the delay stage is modeled as Eq. 2.27. Remember that the 4×4 matrix describing the 4 ports sub-blocks is reduced to a 2×2 transmission matrix neglecting the reflections at all the optical ports. We opt for transmission matrices instead of scattering matrices, since the first can be directly multiplied for cascaded components.

$$T^i_{cou} = \begin{bmatrix} \tau_i & -j\kappa_i \\ -j\kappa_i & \tau_i \end{bmatrix} \tag{2.26}$$

$$T^i_{del} = \begin{bmatrix} e^{-j\beta\Delta L} & 0 \\ 0 & 1 \end{bmatrix} \tag{2.27}$$

With the previous assumption, the full system can be described by Eq. 2.28, which analytically solve the scattering matrix of any lattice filter. Of course, we prefer to use the photonic circuit simulator software, since it allows in a more straightforward way to define complex models for optical properties of the sub-block that in the Eq. 2.28 are scalar quantities. Each sub-block used in the photonic circuit simulator has well established optical properties that the software converts into a scattering matrix. Moreover, the same block can be re-used for any circuit that adopts the same sub-device. In our case the software embeds the circuit simulator and the layout edit as well, so during the simulation phase, we also define the

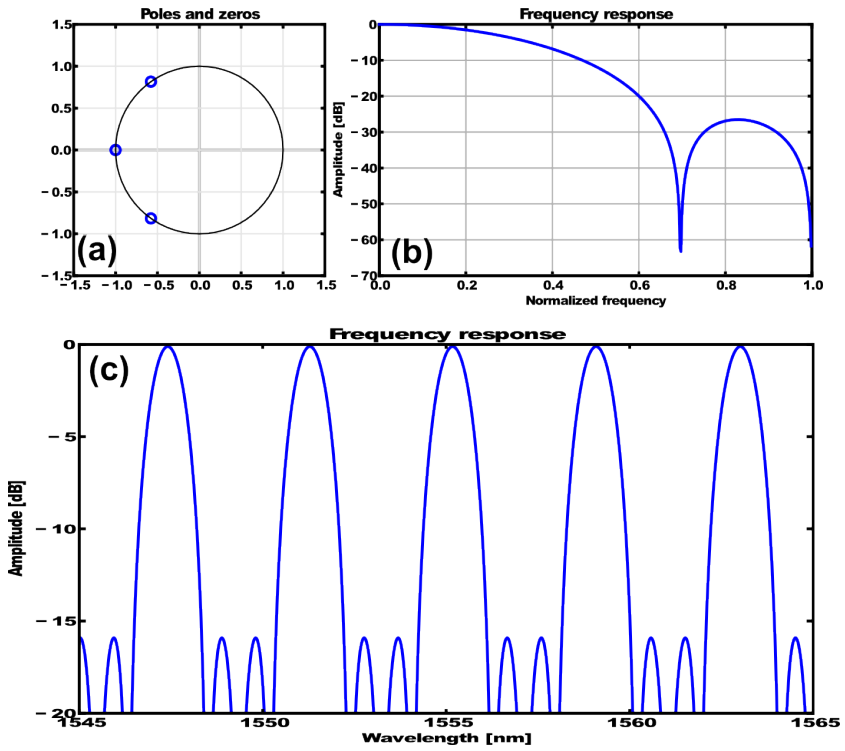

Figure 2.14: Three different steps of ARMA filter design: (a) is the zero-pole diagram of a fourth order lattice filter, (b) is the general purpose digital filter simulation and (c) is the optical equivalent of the digital filter previously simulated

layout of the structure ready for fabrication. The result of such approach is that the device sent out for fabrication is the same for which we run the simulation.

$$T = T_c^{n+1} \prod_{i=1}^{n} T_{del}^i T_{cou}^i \tag{2.28}$$

2.4.3.1 Lattice filters design of experiments

Chebyshev windowing filter design approach is used. In order to design them, we need at least three specification parameters: the order of the filter n, the cut-off frequency and the attenuation in the stop-band. The extra required parameter is FSR: this will be used when the general purpose filter becomes an optical filter.We fix the FSR to 1600 GHz, 12 nm around 1550 nm. The cut-off frequency is set to 0.250 and 0.125 normalized frequency, this corresponds respectively to 400 and 200 GHz. The specification for the stop-band attenuation is set to 15 dB. Differ-

ent orders n are designed, from the fourth to the twentieth. This is an aggressive experiment and is meant to explore the limit of the model and technology.

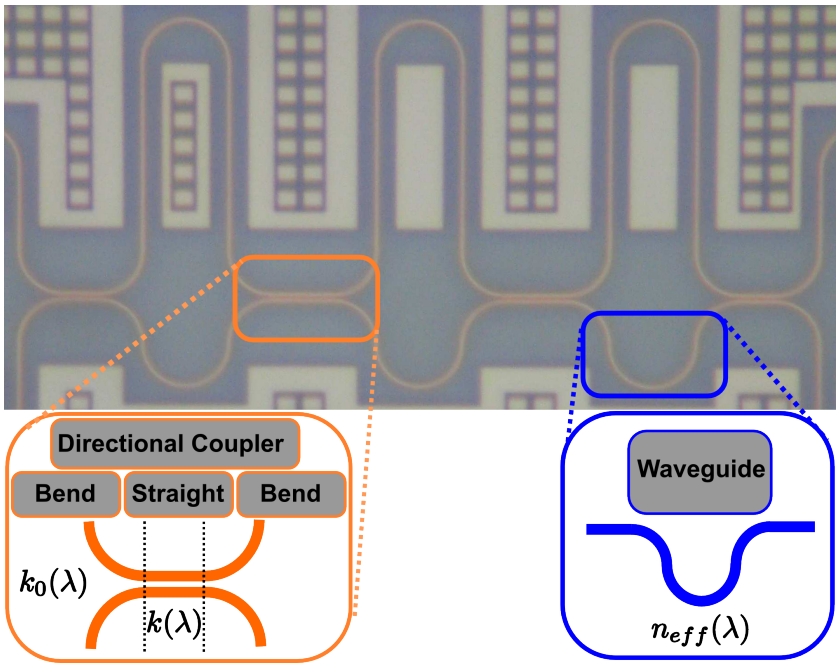

Figure 2.15: Microscope image of a fourth order lattice filter designed with Chebyshev window: the sub-blocks contains the directional coupler and the photonic wires as highlighted

Fig. 2.15 is a microscope image of a fourth order lattice filter, and the sub-blocks of waveguides and directional coupler can be clearly distinguished. The layout is realized with IPKISS. For the straight section, the waveguide is tapered to a wider width to reduce the contribution of sidewall variations the phase errors [46]. A wider waveguide is much more tolerant to the side wall roughness since the optical mode is better confined.

2.4.3.2 Lattice filters experimental results

Fig. 2.16 represents the crosstalk and insertion loss for different orders (cascaded stages) in function of the wavelengths. We see discrete points since the quantities are measured at the wavelength of the passband and thus where there is constructive interference for the different orders. As expected, the best performance is only at one wavelength since the DCs are wavelength dependent. The best performances should be at the wavelength used as the reference for the design, but due to processing variations, the point of optimal performances has shifted. Fig. 2.16(a)

and (b) represent the cross-talk in function of the wavelength, while Fig. 2.16(c) and (d) represent the insertion loss in function of the wavelength: left images and right images are respectively for 0.250 and 0.125 normalized cut-off frequency corresponding to 400 and 200 GHz.

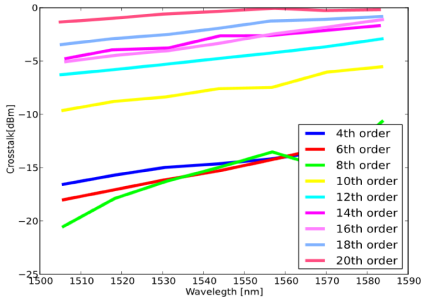

(a) CT of 400 GHz lattice filter in function of the wavelght for different orders

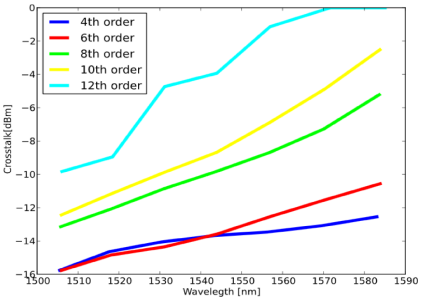

(b) CT of 200 GHz lattice filter in function of the wavelght for different orders

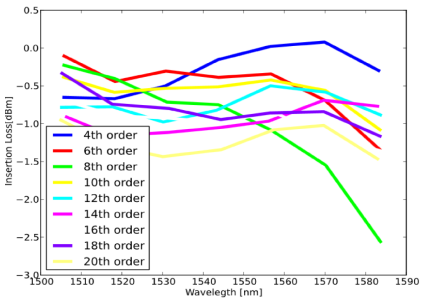

(c) IL of 200 GHz lattice filter in function of the wavelght for different orders

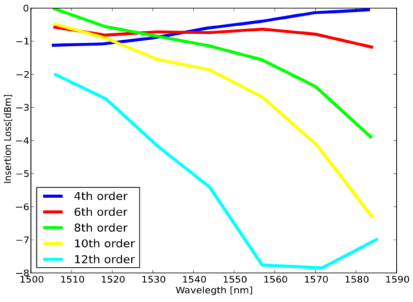

(d) IL of 400 GHz lattice filter in function of the wavelght for different orders

Figure 2.16: The four plots represent the performance of 4000 and 200 GHz lattice filters with 1600 GHz FSR: on the left 400 GHz and of the right 200 GHz

Fig. 2.17 shows the cross-talk as a function of the lattice filters stages. Fig. 2.17(a) regards lattice filters with cut-off frequency of 250 Ghz, while Fig. 2.17(b) regards the lattice filters with cut-off frequency of 125 Ghz; until the 8^{th} stage, the behaviours follows the simulation in Fig. 2.12 for the same device, beyond this limit the measured device suffer from decreasing of performances. The reason lies in the tolerances of the DC for which we did not account in the simulation analysis.

In Fig. 2.17 we see that after a preliminary improvement from increasing the number of cascaded stages, very high order filters start to show a decrease in performance due to imperfections in the coupling coefficients of the directional couplers. For high order filters we need control down to a few percent of the power with high accuracy and due to the cascaded nature of the filter, the error increases

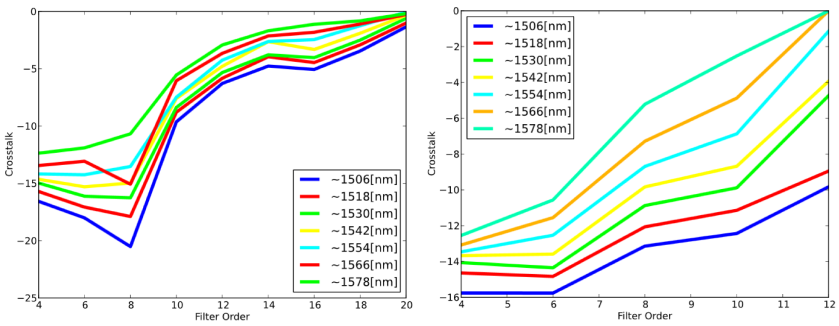

(a) CT of lattice filters cut-off 250 GHz *(b) CT of lattice filters cut-off 125 GHz*

Figure 2.17: Cross-talk of lattice filters as a function of the order (number of stages). The upper plot and the lower plot represent respectively the CT of 0.250 and 0.125 normalized cut-off frequency. The plots represent the performance evaluated at the different order of the passband channels

significantly when increasing the order. The 125 GHz normalized frequency requires smaller couplings compared to the 250 GHz, and this is the reason why the latter still performs better than the first. In the case of a lattice filter, we should also consider that the crosstalk improvement in ideal conditions saturates to the value used as the target for the design of the Chebyshev window as shown in Fig. 2.12. Tab. 2.1 represent the performances summary for the described DOE. Notice that the ratio of 1/10 dB of such filters is extremely high compared to other kinds of filters, since with lattice filters we can reach a nice box shape.

		IL [dB]	CT [dB]	1/10dB BW	area[μm^2]
4^{th} order	4X400GHz	-0.66	15.7	0.33	4280
	8X200GHz	-1.08	14.6	0.33	4200
8^{th} order	4X400GHz	-0.40	17.9	0.33	7744
	8X200GHz	-0.55	12.1	0.32	7808
12^{th} order	4X400GHz	-0.77	5.8	0.57	11172
	8X200GHz	-2.72	8.9	0.38	11336

Table 2.1: Main outcome of the lattice filters measurements including IL, CT, 1/10dB and footprint

2.5 Parameter extraction and optimization

In order to reliably design filters, the exact model parameters for the basic blocks need to be known. While simulation can already give a good estimate, the actual values need to be extracted from measurements. Classic techniques for the

characterization and parameter extraction for photonic devices and PICs in general include the use of inverse formulas already deployed for the design phase. An example is the inverse use of Eq. 2.3 and Eq. 2.4. The inverse formulas as follow in Eq. 2.29 and Eq. 2.30 can be used for extraction of group index and effective index [3, 62].

$$n_g = \frac{\lambda_0^2}{FSR\Delta L} \tag{2.29}$$

$$n_{eff} = \frac{\lambda_0 m}{\Delta L} \tag{2.30}$$

The problem with this inverse formula for the effective index is that the exact interference order m is usually unknown, so other techniques are needed to accurately extract the index from the measurements. These were developed by Sarvagya Dwivedi in his Ph.D. [5].

One of the possible way to extract the group index and (when possible) the effective index is to fit the peaks or dips of the transmission spectrum, through them we can quantify the n_g and the n_{eff} according to Eq. 2.3 and Eq. 2.4. With this methodology, the accuracy is limited by the fitting procedure including only a few points; indeed, the peaks and dips are limited in number to the resonance orders of the filter in the measured range. This is only one example of the weakness in parameter extraction from optical filters, but the concept extends to all PICs and both to wavelength domain and time domain. Often in the case of complex circuits, the characterization techniques include the use of testing stand-alone blocks replicating the device in the PIC. Measuring the test devices, we assume that they have the same performance of the blocks embedded in the photonic integrated circuit. In SOI, this assumption is not generally true, since local variations of optical properties across the die lead to different performances of the same optical device but in a different position [26, 63].

The perspective changes when more information needs to be extracted such as wavelength dependencies of the group index and thus the variations of FSR across the spectrum. Then it is no longer possible to define an inverse formula in closed form from which the parameters can be directly calculated. In that case, the parameter extraction becomes a non-trivial inverse problem that requires an iterative optimization algorithms. We developed an extraction technique that allows us to use the CAPHE circuit simulation tool to extract the technology parameters from measured devices.

Fig. 2.18 represents the schematic block diagram flow for the optimization procedure used for the parameter extraction. The opaque boxes represent the starting point for the procedure: the measured spectrum and the optical technology parameters used to create the layout. CAPHE is used for the simulation of the

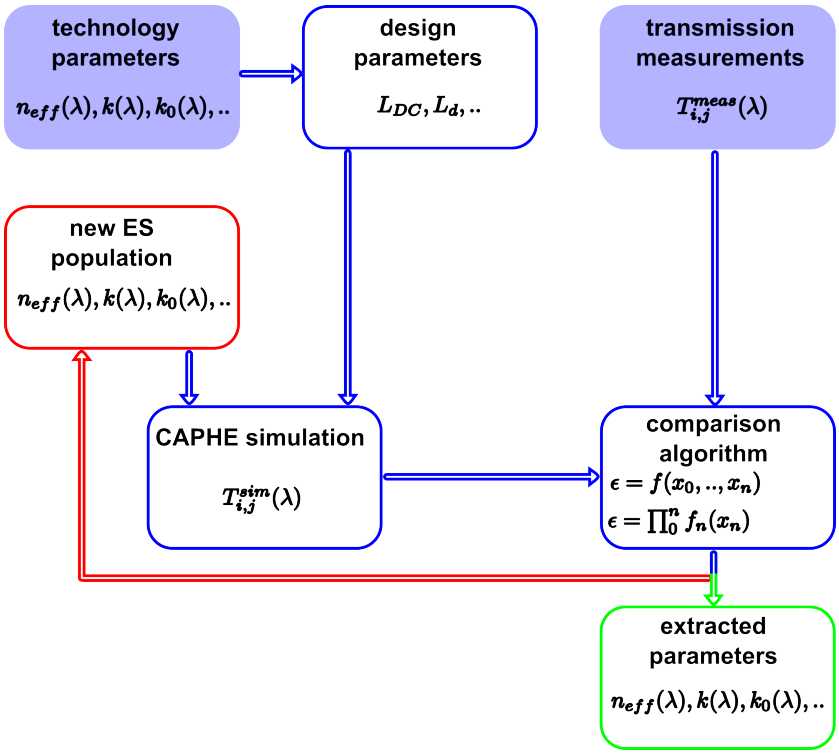

Figure 2.18: Parameter extraction process: opaque box are the starting steps. Red and green paths represent respectively the next iteration required and the end of the loop due to meet on not-meet of the converging parameter. The comparison algorithm represents the two main convergence conditions:fully simultaneous and fully sequential, or a hybrid between the two.

device. We used a comparison algorithm to estimate the error between the measurement and the simulation. If the convergence criteria are not met, evolutionary strategies [64] generate new technology parameters and the resulting simulation is again compared to the measurements.

2.5.1 Full spectrum fitting

While the traditional method uses only a few data points to calculate the circuit's parameters (e.g. the distance between the transmission minima can be used to calculate the FSR, and then the group index), we propose to use the entire measured spectrum for the extraction of the optical parameters. This should increase the accuracy and reliability, as the entire spectrum contains much more information than only a few data points. As an example, we apply our approach to the extrac-

tion of the FSR and the group index. If we would only consider the separation of the minima or maxima in the spectrum, the extraction accuracy is limited by the measurement resolution. The position of an individual peak needs to be calculated, and measurement noise and ripple can easily affect the result of a peak fitting algorithm:

$$\Delta FSR_{acc} = \Delta\lambda_{m,res} + \Delta\lambda_{(m-1),res} \tag{2.31}$$

$$\Delta n_{g,acc} = \frac{n_g \Delta\lambda_{m,res}}{FSR} \tag{2.32}$$

The error on the FSR is Eq. 2.31 and its correlation with the extraction of the group index is Eq. 2.32. With our proposed approach, which fits a complete parametric circuit model to the complete measurement spectrum, the error is largely determined by the fitting error, and the effect of measurement noise is less pronounced. The fitting error can be estimated with a stochastic approach and using a re-sampling technique [65].

$$E_{RMS} = \sqrt{\frac{\sum_{t=0}^{n}(T_t - T(\lambda_t))^2}{n}} \tag{2.33}$$

Eq. 2.33 expresses the RMS error due to fitting, and this quantity can be used as the standard deviation of a stochastic random Gaussian noise affecting the measurement for a repetitive FSR extraction.

2.5.2 PIC simulator used for parameter extraction

Further improvement can be done to the characterization procedure. Often analytical models are used for the individual building block composing the PIC. In our approach, we model the circuit with the specialized CAPHE photonic circuit simulator in which each node has N bidirectional ports. The block is then reduced to a $N \times N$ scatter matrix made of $S_{i,j}$ elements. The linear, instantaneous response can be used for wavelength domain simulation. An advantage connected to the use of a photonic circuit simulator rather than pseudo-analytical models comes from the fact that it is straightforward to characterize the sub-blocks without using testing structures. Each port of the device, for instance, auxiliary ports of 2×2 MMIs and DCs or extra auxiliary ports on multiplexing filters such as AWGs and PCGs is used for full characterization of the scattering matrix element. To avoid an explosion of the number of model parameters, we do introduce some assumptions: we only work with reciprocal, linear components, and assume that the known loss corresponds to $S_{n,m} = S_{m,n}$ and $I - S^H \cdot S^H = L_{loss}$. For many devices, we also assume zero reflections such that the scattering matrix is populated by more zeros [44].

2.5.3 Use of global optimization strategies

When using an evolutionary optimization strategy, we can choose to use either local or global optimization techniques. We opted for a global technique because that allows for a more explicit decoupling of the fitting process and the circuit description. In the case of relatively simple PICs, the optimization algorithm is quite robust against convergence problems, multiple solutions or non-linearity [66].

An example of a low-complexity circuit for which the fitting technique is very robust is an MZI with a dispersive model for both waveguides and splitters. The MZI consists of 4 devices: 2 waveguides and 2 splitters, but we can reduce the two waveguides to a single device: a differential delay. Because the expected transmission of an MZI is a cosine-like function, we can use a simple linear least-square error as the cost function for the optimizer [67]. For more complex PICs with more pronounced spectral features (e.g. resonance peaks) other cost functions are needed, that emphasize the importance of the spectral features.

Black-box optimizations are often more effective and robust. The RMS is basically an indicator of the "distance" between the measured and the simulated transmission. Using the RMS (in Eq. 2.33) as the parameter to minimize, corresponds to the optimization (extraction) of the scattering parameters of the individual blocks. More in detail the parameters are the effective index, the group index for the waveguides while for the DCs we optimize the coupling κ and the transmission τ. The optimization of these quantities includes their derivatives as well.

Alternative, we can use the RMS in a logarithmic scale: its meaning is then no longer physical, but at the same time it is helpful for a better fitting since optical filters carry important information at the noise floor level, and sharp spectral features carry more weight. The noise floor level is better qualified by a logarithmic fitting, and has a relatively larger impact. To balance the result of the fitting when different objective functions need to be simultaneously satisfied as in the case of linear/logarithmic convergence, we explore multi-objective convergence. Both the criteria have to be minimized simultaneously with the "weight" decided by the user: for instance, we can minimize the quantity $(E_{rms,lin} + E_{rms,log})$.

We test and compare different global optimization techniques. We propose the results of the algorithm that delivers the best results. The techniques we test are Differential Evolution (DE) [68], Stable Noisy Optimization by Branch and Fit (SNOBFIT) [69] and Covariance Matrix Adaptation (CMA) [70] Evolutionary Strategy(ES) [70].

2.5.3.1 The CMA Evolutionary strategy

According to our experimental results, the best global optimization algorithm for a black box filter is the *covariance matrix adaptation* CMA [70]. The CMA method

allows facing objective functions which are non-linear, non-separable, nonconvex, noisy and with a high condition number. Moreover, CMA allows overcoming typical problems faced by other evolutionary algorithms such as bad performance with small populations and premature convergence. These properties make the method very suitable for parameter extraction from optical transmission measurements, as measurement noise and phase errors can complicate the convergence with other methods. Fig. 2.19 gives an example of the first step CMA evolution on a 2D variable and 1D target function. A disadvantage of the CMA algorithm is that it requires a fairly large number of simulations to converge.

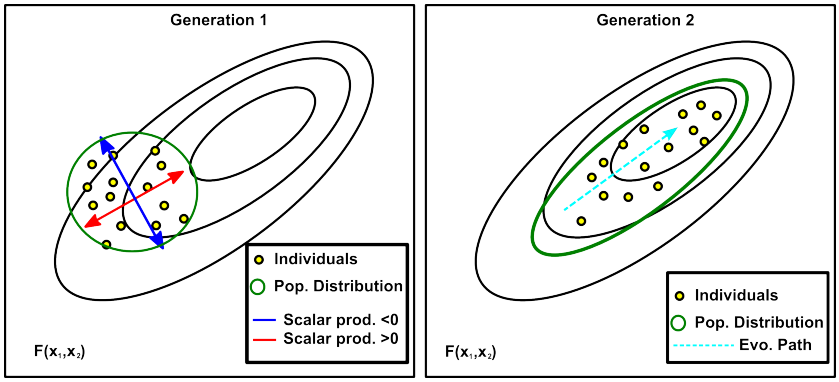

Figure 2.19: Covariance Matrix Adaptation evolution: graphical representation of the evolution between first and second generation in the case of two variable space with real single dimension target function

The CMA procedure starts with a population of parameters as in Fig. 2.19 left. Multivariate Gaussian distributions are used to generate new individuals. The starting covariance matrix estimate of the first population is then cumulatively enhanced evaluating an evolution path over a number of generations as shown in Fig. 2.19 right. The same concept of self-adaptation based on the evolution path and cumulative adaptation is applied to the step size and the overall scale of the Gaussian distributions. If the scalar product of the selected mutations is positive, the next generation of the population takes larger steps in the same direction; if the scalar product of selected mutations is negative, the steps cancel out and the step-size is reduced [70].

Fig. 2.20 represents the comparison of the performances obtained with the three optimization algorithms adopted when fitting the measurement of a MZI. As we see the CMA is the first method to converge and it also results in the smallest residual RMS, as shown in the detail in Fig. 2.20.

The different methods all include stochastic phenomena, so the number of iterations as well as the final extraction are not unique, but will vary between each

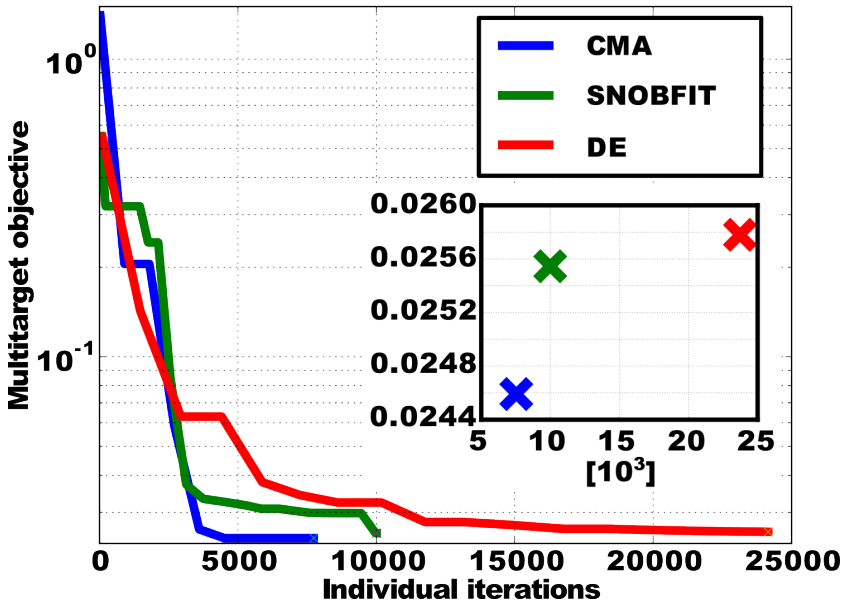

Figure 2.20: Comparison of the three black-box algorithms tested on a single stage MZI: in th box the zoom on the converging point to underline the converging value

optimization run. Overall, the best performing algorithms remain the CMA for all the tests performed. In this analysis the algorithm internal calculation time for the generation of the feed-forward test parameters is neglected. This is because it is comparable for all the algorithms and negligible compared to the PIC simulation time.

2.5.4 Parameter extraction for AR and MA optical filters

Our parameter extraction procedure is tested for the characterization of AR and MA filters fabricated on IMEC's silicon photonic platform. The model parameters used for the DCs and waveguides include wavelength dependencies in the second order of the Taylor series. The effective index is included in the model, but as we already discussed, the actual response of optical filters is not very dependent on the exact value of the effective index, but rather on that of the group index. Therefore, we consider the effective index a 'floating' parameter and the extracted value as not reliable nor relevant.

In addition to the functional parameters, we introduce a number of imbalance factors which express local variation within the device. For instance, the effective index of the delays can slowly vary across the device because of local fabrication variations. Similarly, the coupling coefficients of the directional couplers can be

slightly different between for instance in Fig. 2.15 between the first and third stage, even though they have been designed to be identical. Due to the symmetry of the device along the propagation direction, is not possible to extract the direction of this imbalance. For instance, if there is an imbalance in n_{eff}, we cannot know the larger value of n_{eff} corresponds to the first or last stage.

Fig. 2.21 represent the transmission spectrum of the cross ports of a fourth order lattice filter. The "cross port sim" curve shows the original spectrum, as simulated after the design based on our dispersive model of n_g, $_0$ and k. The "cross port mea" curve shows the measured result. The insets in Fig. 2.21 represent the direct consequences of fabrication variations: n_g variations cause variations of the free spectral range, n_{eff} variations produce a shift of the resonance peaks. Variations of coupling coefficient and unbalancing coupling and delay stages produce cross-talk non-ideality both in absolute value and non-homogeneity.

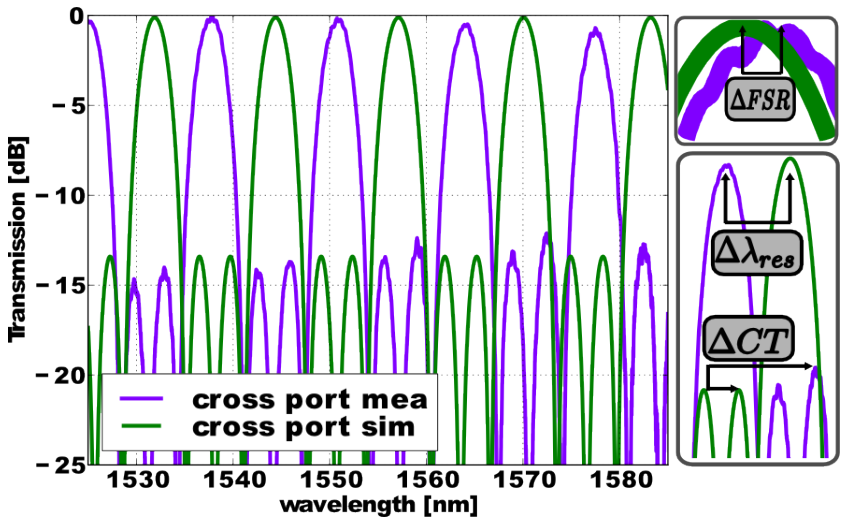

Figure 2.21: Spectrum of a single 4th order MZI lattice filter: the main non-idealities due to fabrication tolerances between the simulation before the optimization and the measured circuit are represented

Fig. 2.22 shows the convergence of the unknown optical parameters. The variables are normalized to their original design value, so the starting value is 1.0 for all of them. We see a very rapid convergence for the group index n_g within 100 simulations, this is due to the strong linear correlation of group index and free spectral range. The first order derivatives of the optical parameters are the last to converge since the starting value have a strong perturbation. The other variables stabilize after almost 2000 simulations. Fig. 2.22 refers to the first order FIR filter and thus, there are seven variables to be optimized.

The upper plot in Fig. 2.24 represents the fitting and the measurement of the

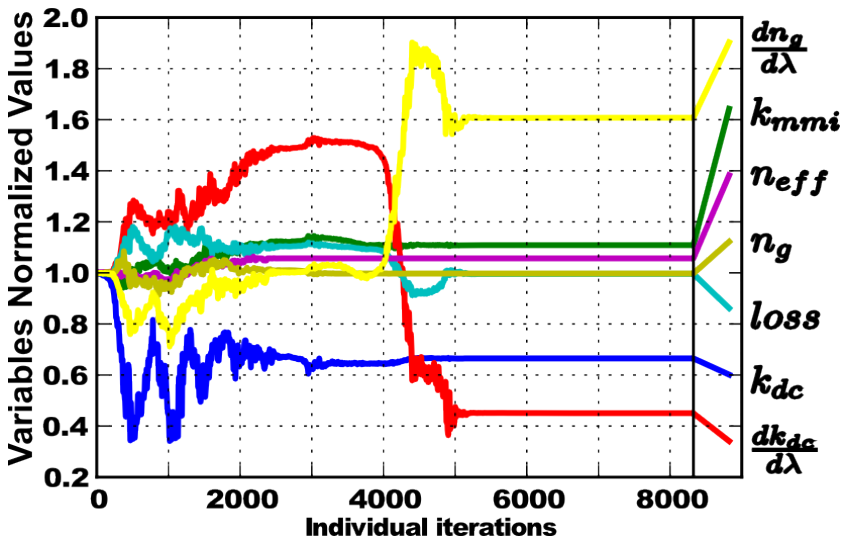

Figure 2.22: Convergence of the 7 most relevant normalized variables in the CMA algorithm in case of first order FIR filter. The variable are normalized to the first guess values

of the device in Fig. 2.23(a), thus a single stage MZI with two different coupling devices: a MMI and a DC. The lower plot in Fig. 2.24 represents the extracted optical parameters: the group index and the coupling coefficient k of the straight section of the DC (see Eq. 2.15). Since in this single structure, it is not possible to uncouple the coupling for the straight and the bent section, the coupling due to the bends k_0 is taken from the simulation. The MMI splitter, which has at least one order of magnitude of splitting and wavelength dependency stability, is assumed to be an ideal 3 dB splitter. Since there is only one DC in involved in the characterization, k and k_0 of Eq. 2.14 cannot be uncoupled. The gap between the waveguide is 200 nm while the length of the straight section is 8.0 um, the radius of the bend section is $5um$. The extracted coupling k is 0.082 $[um^1]$, in this case, we assume the value of the simulation for the coupling due to bending k_0.

In Fig. 2.25 we see the same experiment performed on a fourth order lattice filter: its architecture is represented in Fig. 2.23(c). Fig. 2.25 also collects the most relevant optical parameters extracted from the analysis of the structure: in particular the couplings of the bend and straight section, as well as the group index. All the coupling stages use directional couplers with the same cross section but different length. A balancing factor is added along the symmetry plane of the device to capture slow, location dependent parameter variations. The coupling structures account for the contribution of the two bend sections and the straight section. The bend radius is the same for all the stages while the straight sections

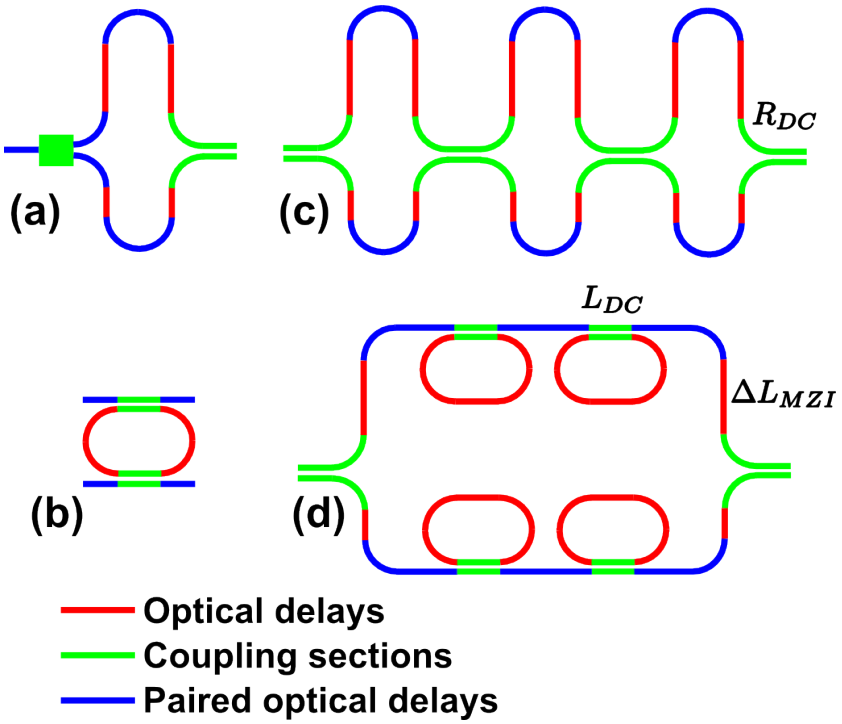

Figure 2.23: The images represent the schematic of the different filter used for parameter extraction (a),(b) and (c) and for parameter optimization (d)

are used to control the splitting factors. The bend radius is 5 um and the gap is 220 nm.

Fig. 2.26 represents the application of the method on a circular silicon micro-ring resonator. The device was fabricated in another fabrication run, so the extracted optical parameters are substantially different from the results of the other experiments. The directional couplers do not have a straight section, so the model only includes a fixed (but wavelength dependent) contribution. The group index extracted from this device includes the perturbation introduced by the coupling section [71]. The topology of this AR filter does not allow to distinguish between the optical path of the waveguide and the equivalent optical path of the directional coupler included in the feedback loop of the interfering paths. The ring under test has both an add and drop ports, so the critical coupling condition is achieved with asymmetric directional couplers [29]: design-wise, this condition is exploited using two different gaps of the DCs, this to keep symmetry in the shape of the ring itself. The radius of the bend section is 5 um, while the gaps are 180 nm for the pass and 200 nm for the drop port, in both cases the straight section is zero.

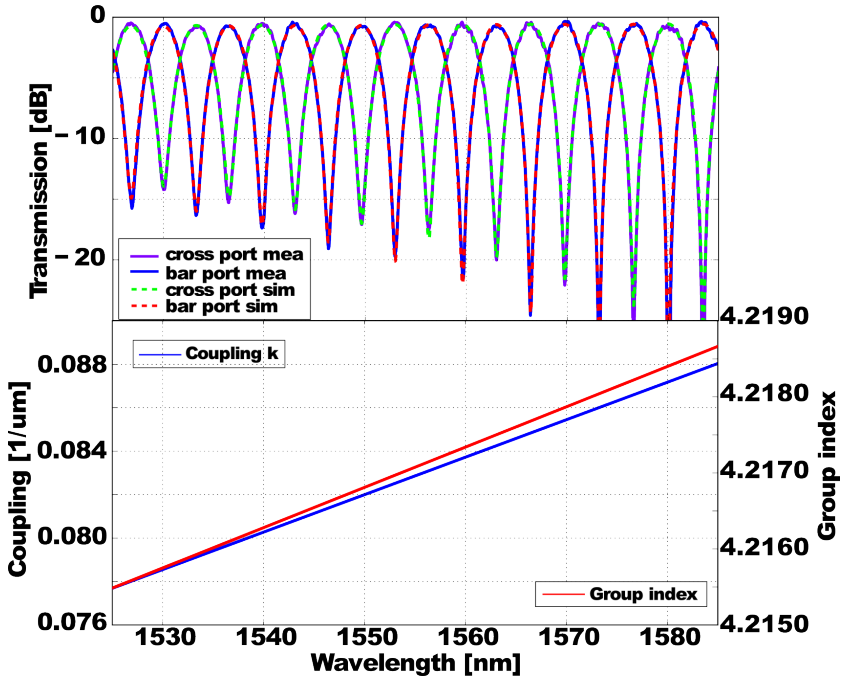

Figure 2.24: Mach-Zehnder filter fitting with multi-objective approach and the most relevant extracted technological parameters: coupling strength and group index. The coupling coefficient implies an ideal coupling of the bend section, since the topology does not allow the uncoupling of bend and straight section couplings

2.5.5 Parameter optimization for ARMA complex optical filters

We also applied the same approach for design optimization of the complex ARMA filter, with an ideal band-pass target function. Often computer assisted design algorithms are not possible with complex topologies [72, 73]. We chose the topology presented in Fig. 2.23(d): a MZI with four rings. Using the same waveguide type for all the delays, including the rings, the delay of the loading rings can be set to twice the delay of the main MZI: this corresponds to poles the roll-off region of the MZI. The target is the pointwise convergence of the simulated photonic circuit toward an ideal band-pass filter. After choosing the topology, an initial value of ΔL based on the desired value of the FSR and the known group index n_g are determined. The unknown layout parameter target of the optimization are the lengths of the DCs, while the optical properties are assumed to be known since they are extracted from the previous parameter extraction of the other filters. The optimization procedure is, therefore, the same, but the set of parameters is comple-

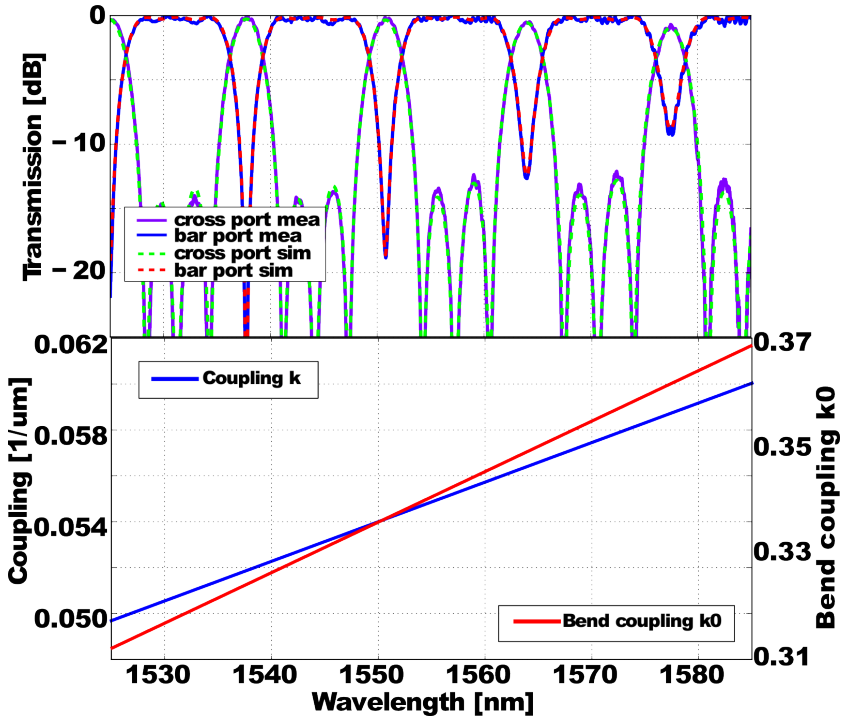

Figure 2.25: Fourth order FIR filter fitting with multi-objective approach and the most relevant extracted technological parameters: coupling due to straight and bend section

	n_g	κ	κ_0	die	DC gap
1_{st} ord. FIR	4.2178	0.082*	n/a	a	200 [nm]
4_{th} ord. FIR	4.2134	0.054	0.335	a	220 [nm]
1_{st} ord. IIR	n/a	n/a	0.395	b	180 [nm]

Table 2.2: Extracted parameters for the filters under test at 1550 nm, some parameters are not applicable because not present in the topology. Where the k is associated with (*) expresses that for the extracted value, the assumption of ideal k_0 is adopted

mentary to the set used for the extraction from the measurement. Fig. 2.27 shows the simulated transmission of the two outputs of the PIC with the optimized coupling coefficients, together with the target function. Tab. 2.3 collects the obtained lengths for the directional coupler of the rings in Fig. 2.23(d) where the arrows down and up represent respectively the ring up and down in the schematic.

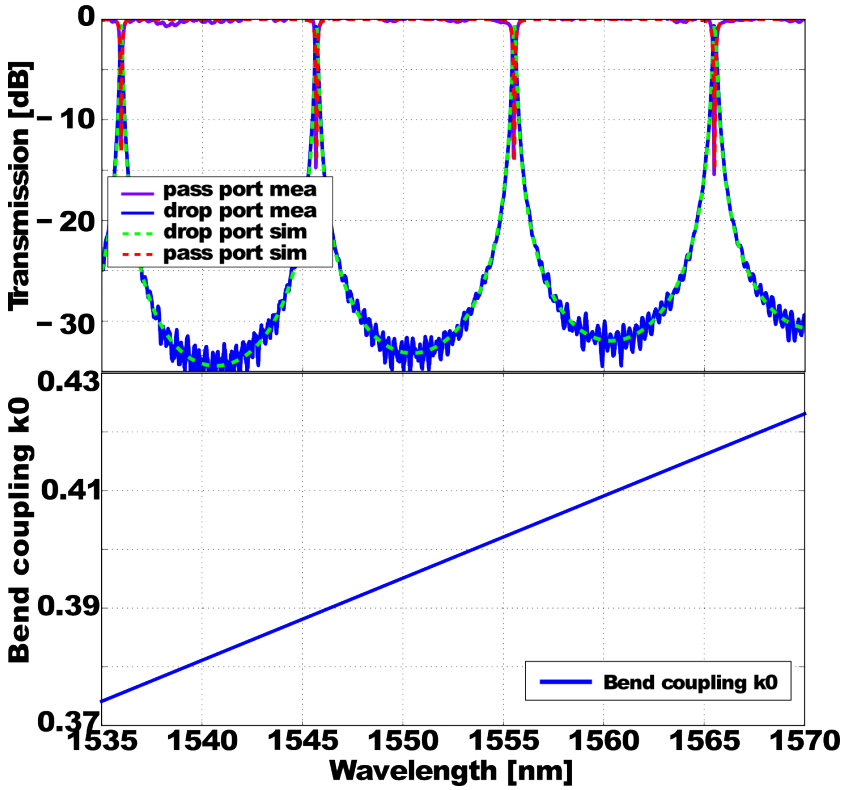

Figure 2.26: Ring filter fitting with multi-objective approach and the most relevant extracted parameter: the coupling due to bend section since there is no straight section is present in the device

2.5.6 Wafer scale parameter extraction

The procedure is also applied to extract wafer scale information. The results of such extraction can be used to obtain relevant information about processing uniformity across the wafer. The device used for this experiment is represented in Fig. 2.23(c): a fourth order lattice filter with Chebyshev window design. The fabrication was done through the ePIXfab MPW (multi-project wafer) service in IMEC, Belgium and the processing is done in a 200mm CMOS pilot line. Our dies are replicated multiple times across the wafer. The full wafer is measured with an automated setup that can collect the transmission as a function of wavelength between different inputs and outputs [66]. The automation without interruption, in a clean room environment, keeps the measuring conditions stable for all the dies on the wafer. For each die, a reference structure is measured prior to the lattice filters of interest. The reference structure consists of a straight waveguide of

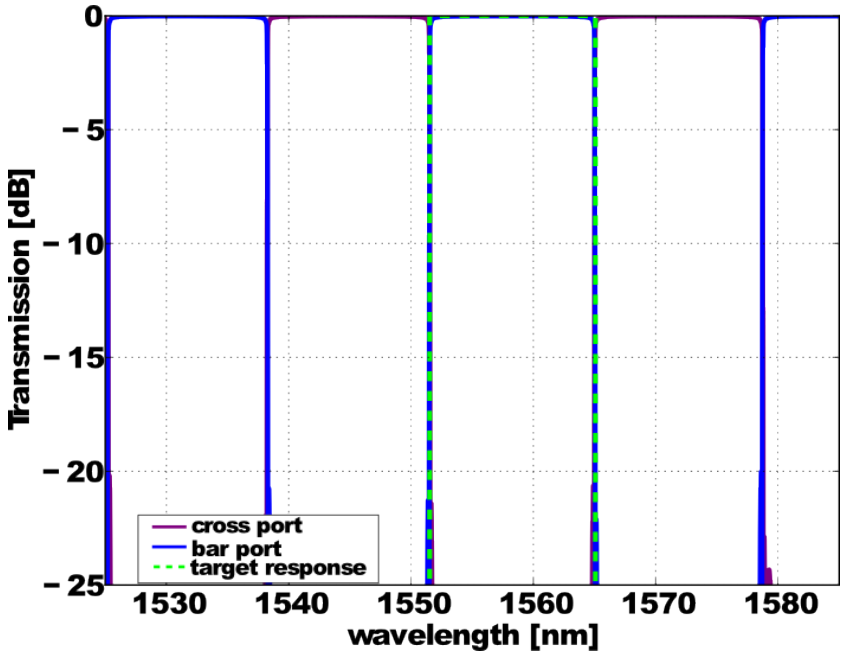

Figure 2.27: Design optimization or complex IIR filter. The device is a four ring assisted MZI interferometer as shown in Fig. 2.23(d). The green dashed line is the target box-like response.

	$DC \uparrow L\mu m$	$DC \uparrow L\mu m$	$DC \downarrow L\mu m$	$DC \downarrow L\mu m$
DC lengths	7.64	10.53	12.09	3.63

Table 2.3: Design specifications for the coupling lengths expressed in um of the four rings in the ring-assisted MZI in Fig. 2.23(d), using a fixed gap for the couplers of 220 nm and the coupling values obtained with the extraction procedure.

a well-known length connected to two grating couplers. The same vertical coupling device is used for the coupling of the lattice filter. The grating coupler has a wavelength-dependent response, but we normalize all our measurements to the response of the reference to eliminate most of the grating coupler effects.

Fig. 2.28 shows the main outcome of the full wafer analysis and statistics. In detail Fig. 2.28(a) shows the statistical results of the group index extracted from the filter. Except for the values on the wafer edges, the extracted values come close to the results of the simulations represented by the red dot. Also for the coupling coefficients of the straight section k and the coupling due to bending section $_0$ the extracted values match the results of the simulation, also in this case represented by the red dot. Fig. 2.28(b) represents the group index over the whole wafer. The

obtained results can be correlated with the physical characteristics of the processed waveguides. Since no full information on linewidth and thickness across the whole wafer are known, it is not straightforward to reconstruct the correlation between optical parameters and the cross-section of the photonic wire.

2.6 Passive integrated filters comparison

The filters treated in this chapters can all be used as a spectrometer for various applications. They all are capable of providing information on the wavelength content of the input light. However, depending on the functional specification, it could be better to select MZI lattice filters, rings, or AWGs or PCGs. In this section, we compare the relative merits of the different filters.

2.6.1 AWG or PCG?

The same working principle of the diffraction is used for PCGs and AWGs. The direct consequence of this is that while the main parameter influencing the insertion loss of the PCG is the reflectivity of the grating, for the AWG this parameter is dominated by the transmission loss of the waveguides.

The array of waveguides in the AWGs is the equivalent of the FPR+facets in the PCG. The consequence of this difference is that the crosstalk is dominated by the waveguide fabrication variation in the AWGs and by the reflective facets (the DBR) in the PCGs. Also, the FPR has an influence on the CT of the PCGs, but this influence is less dominant since the slab regions are more fabrication tolerant. This is intuitive if we consider that the optical properties of a waveguide depend on thickness and width, while, in first approximation, for a slab they depend only on the thickness.

Comparing AWGs and PCGs, we can conclude that since the diffraction happens in the slab for the PCGs and in the waveguides for the AWGs, the footprint of the PCGs is larger than the AWGs for the same FSR. The reason for this is the significantly lower dispersion of the slab compared to waveguides. On the other hand, PCGs do not suffer from layout limitations in the case of small delay ΔL (larger FSR). An intrinsic limitation affecting the PCGs is the fabrication imperfection of DBRs of the facets: the imperfect edges of the facets creates scattered light.

In conclusion, PCGs are the best choice for low channels counting and large FSRs for applications such as CWDM. When smaller FSR and smaller channel spacing is needed, AWGs are the best option. For AWGs with large channel spacing, other layout strategies can be used: an example is provided by the box-shaped AWG [36].

2.6.2 Rings or MZI filters?

Ring and MZI based devices offer better performances in term of insertion loss since the guided light never leaves the photonic wires, and no imaging mechanism is needed. This assumption is valid in the case of the use of DCs as the splitting device, in case MMIs are used, image losses are present. Rings suffer from layout limitations imposed by the minimum bend radius, according to Eq. 2.3, while MZIs do not have this limitation. Thus, the FSR of the ring has a smaller upper limit compared to the MZI(cf.Ch. 3). These two filters can be combined and cascaded to obtain high order filters. Worth to mention is that in rings since there is feedback is more likely to have non-linear effects.

Some basic property, valid in general for FIR and IIR filters, can be extended to ring and MZI based filters: FIR are always stable while IIR can be unstable. The instability is due to the presence of poles in the case of IIR. FIR filters can have linear phase.

Rings have a higher wavelength selectivity: fewer order ring based filters can achieve small FWHM and thus, higher resolution. Rings are also suitable to be cascaded on the same optical bus and thus, interrogate the input spectrum serially. In SOI, aligning multiple rings to a wavelength grid is still challenging [74].

MZIs exhibit a sinusoidal response, hence, a single stage MZI does not provide high wavelength selectivity. However, high order MZI filters can have an arbitrary optical transmission. Moreover, the sinusoidal response can be used for FT analysis of the input spectrum: this approach requires an array of parallel MIZs [75].

2.6.3 Conclusions: filter comparison

Fig. 2.29 represents a qualitative comparison of WDM filters where some of the relevant specifics are listed. To each kind of filter is attributed a value from 0 to 1 for the different performance indicator listed. The outcome of such comparison is that there is no unique answer to the question: which is the best WDM filter? When coarse channels are needed the optical choice are the PCGs, in opposition we find dense division multiplexing application in which AWGs are the best alternative. This is a rough statement, but between the two extremes, there are operation requirements in which the selection of the proper image based filter is not straightforward. If few channels but with narrow-line response are needed, rings are a viable solution because suitable for cascaded architectures. With few channels, broad bandwidth and large FSRs, MZI based architectures are the best solution. They are suitable for very small ΔL, thus, very large FSRs(at the limit theoretically infinitive). MZIs can be cascaded to realize lattice filters. In the case of rings and MZI, thanks to the size and relatively simple architecture, active tuning is possible.

2.7 Conclusion

The study of WDM filters proposed in this chapter has been carried out for the purpose of selecting the best devices to be used as spectrometers. Wavelength selective filters are required to make spectrometers, but the selection of the device in not always trivial. Moreover, a reliable engineering design flow is needed to be able to meet the expectations.

We developed an integrated framework capable of simulating and designing FIR and IIR filters based on microring resonators and MZIs. The measurement of the device is then used as feedback for the design framework with the purpose of optimizing the layout parameters to the fabrication platform used. Accurate optical parameter extraction is performed, such as effective index and coupling coefficients and their wavelength dependencies. Such analysis is done combining a photonic circuit simulator for the modeling of the components involved. We compared the different filter typologies to obtain a clear idea of their pros and cons and their trade-offs.

In the next chapters, we are going to realize integrated spectrometers using the filters studied and compared in this chapter. In particular in Ch. 3 we explore tuning and modulation techniques applied to single stage rings and MZIs. In Ch. 4 we cascade rings and AWGs to make use of their strengths: in particular we lever on the high wavelength selectivity of the ring and the large FSR of the AWG. In Ch. 5 we make use of the AWGs capability of allowing multiple inputs and outputs. The inputs are labeled in the time domain such that they can be multiplexed in the same outputs, in this way we reduce the channel spacing of the pure passive AWG, overcoming the intrinsic channel spacing limitations of the device.

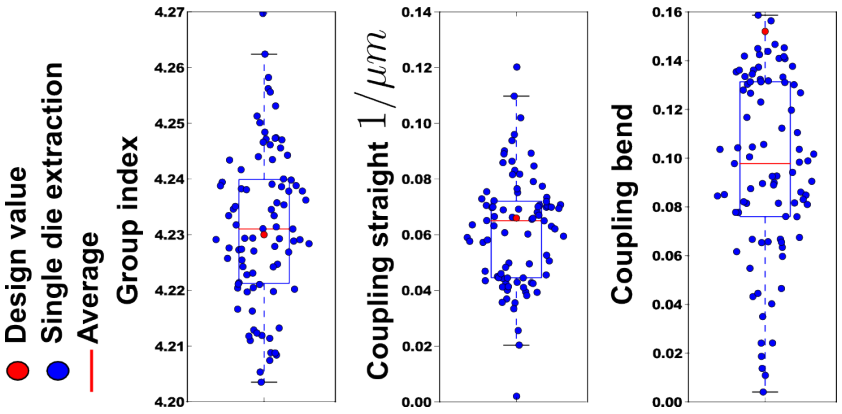

(a) Statistical results on the wafer parameter extraction for group index, coupling of the straight and the bend section

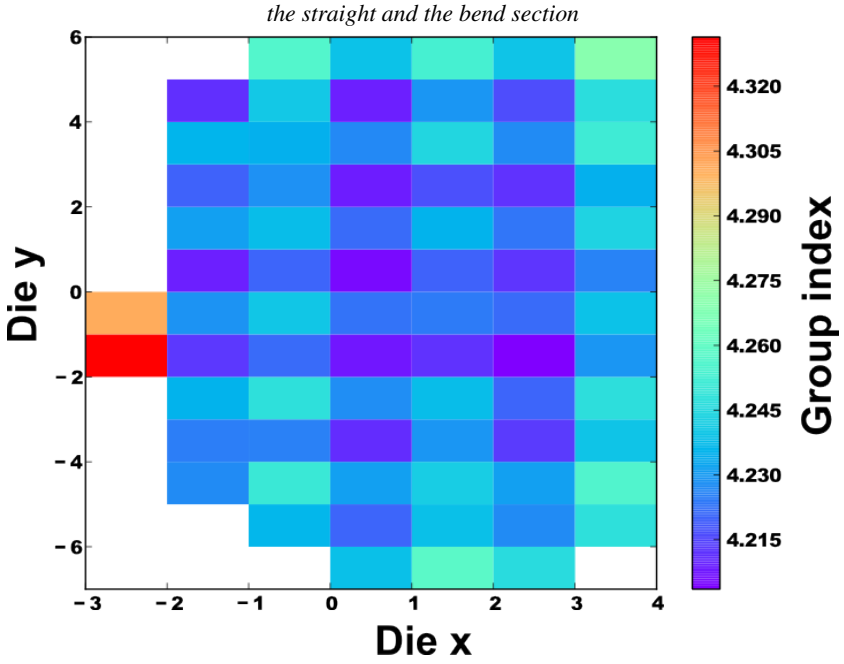

(b) Wafer map of group index in function of the (X,Y) die position

Figure 2.28: Statistical data and wafer maps of the parameter extracted on wafer scale

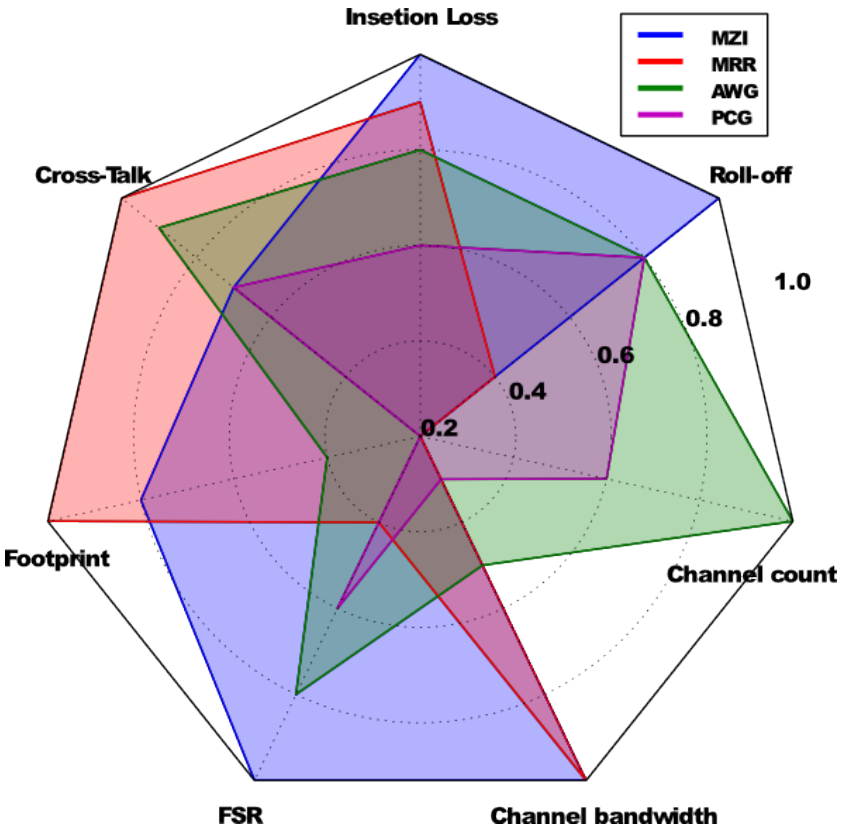

Figure 2.29: The star-plot represents a qualitative comparison of the optical filters treated in this chapter

References

[1] W. Bogaerts, S.K. Selvaraja, P. Dumon, J. Brouckaert, K. De Vos, D. Van Thourhout, and R. Baets. *Silicon-on-Insulator Spectral Filters Fabricated With CMOS Technology*. Selected Topics in Quantum Electronics, IEEE Journal of, 16(1):33–44, Jan 2010.

[2] Swagata Samanta, Pallab Banerji, and Pranabendu Ganguly. *Effective index-based matrix method for silicon waveguides in $\{SOI\}$ platform*. Optik - International Journal for Light and Electron Optics, 126(24):5488 – 5495, 2015.

[3] Eric Dulkeith, Fengnian Xia, Laurent Schares, William M. J Green, and Yurii A. Vlasov. *Group index and group velocity dispersion in silicon-on-insulator photonic wires*. Opt. Express, 14(9):3853–3863, May 2006.

[4] Christie K. Madsen and J.H. Zhao. *Optical Filter Design and Analysis: A Signal Processing Approach*. John Wiley & Sons, Inc., New York, NY, USA, 1st edition, 1999.

[5] Sarvagya Dwivedi, Alfonso Ruocco, Michael Vanslembrouck, Thijs Spuesens, Peter Bienstman, Pieter Dumon, Thomas Van Vaerenbergh, and Wim Bogaerts. *Experimental Extraction of Effective Refractive Index and Thermo-Optic Coefficients of Silicon-on-Insulator Waveguides Using Interferometers*. Jornal Lightwave Technol., 33(21):4471–4477, Nov 2015.

[6] R. Adar, C.H. Henry, M.A. Milbrodt, and R.C. Kistler. *Phase coherence of optical waveguides*. Lightwave Technology, Journal of, 12(4):603–606, Apr 1994.

[7] C.J. Kaalund and Gang-Ding Peng. *Pole-zero diagram approach to the design of ring resonator-based filters for photonic applications*. Lightwave Technology, Journal of, 22(6):1548–1559, June 2004.

[8] Junfeng Song, Q. Fang, S. H. Tao, M. B. Yu, G. Q. Lo, and D. L. Kwong. *Passive ring-assisted Mach-Zehnder interleaver on silicon-on-insulator*. Opt. Express, 16(12):8359–8365, Jun 2008.

[9] M.K. Smit and C. Van Dam. *PHASAR-based WDM-devices: Principles, design and applications*. Selected Topics in Quantum Electronics, IEEE Journal of, 2(2):236–250, Jun 1996.

[10] M.L. Calvo and V. Lakshminarayanan. *Optical Waveguides: From Theory to Applied Technologies*. Optical Science and Engineering. CRC Press, 2007.

[11] Wim Bogaerts, Shibnath Pathak, Alfonso Ruocco, and Sarvagya Dwivedi. *Silicon photonics non-resonant wavelength filters: comparison between AWGs, echelle gratings, and cascaded Mach-Zehnder filters*, 2015.

[12] P. Dumon, W. Bogaerts, V. Wiaux, J. Wouters, S. Beckx, J. Van Campenhout, D. Taillaert, B. Luyssaert, P. Bienstman, D. Van Thourhout, and R. Baets. *Low-loss SOI photonic wires and ring resonators fabricated with deep UV lithography*. Photonics Technology Letters, IEEE, 16(5):1328–1330, May 2004.

[13] W. Selvaraja, S.and Bogaerts, P. Absil, D. Van THourhout, and R. Baets. *Record low-loss hybrid rib/wire waveguides for silicon photonic circuits*. In Group IV Photonics (GFP), 2015 IEEE 12th International Conference on, Sep 2010.

[14] L.B. Soldano and E.C.M. Pennings. *Optical multi-mode interference devices based on self-imaging: principles and applications*. Lightwave Technology, Journal of, 13(4):615–627, Apr 1995.

[15] C. Dragone, C.H. Henry, I.P. Kaminow, and R.C. Kistler. *Efficient multichannel integrated optics star coupler on silicon*. Photonics Technology Letters, IEEE, 1(8):241–243, Aug 1989.

[16] S.P. Dwivedi and W. Bogaerts. *Compact athermal filter in silicon waveguides for WDM and bio-sensing applications*. In Fiber Optics and Photonics (PHOTONICS), 2012 International Conference on, pages 1–3, Dec 2012.

[17] R. Halir, A. Maese-Novo, A. Ortega-Mo nux, I. Molina-Fernández, J. G. Wangüemert-Pérez, P. Cheben, D.-X. Xu, J. H. Schmid, and S. Janz. *Colorless directional coupler with dispersion engineered sub-wavelength structure*. Opt. Express, 20(12):13470–13477, Jun 2012.

[18] Zeqin Lu, Han Yun, Yun Wang, Zhitian Chen, Fan Zhang, Nicolas A. F. Jaeger, and Lukas Chrostowski. *Broadband silicon photonic directional coupler using asymmetric-waveguide based phase control*. Opt. Express, 23(3):3795–3808, Feb 2015.

[19] Photon Design. *FIMMPROP*, 1999.

[20] E.C.M. Pennings, R.J. Deri, R. Bhat, T.R. Hayes, and N.C. Andreadakis. *Ultracompact, all-passive optical 90 degrees -hybrid on InP using self-imaging*. Photonics Technology Letters, IEEE, 5(6):701–703, June 1993.

[21] T. Spuesens, S. Pathak, M. Vanslembrouck, P. Dumon, and W. Bogaerts. *Integrated grating coupler/power splitter for on-chip optical power distribution*.

In Group IV Photonics (GFP), 2014 IEEE 11th International Conference on, pages 141–142, Aug 2014.

[22] Martin Fiers, Thomas Van Vaerenbergh, Ken Caluwaerts, Dries Vande Ginste, Benjamin Schrauwen, Joni Dambre, and Peter Bienstman. *Time-domain and frequency-domain modeling of nonlinear optical components at the circuit-level using a node-based approach*. JOSA B, 29(5):896–900, 2012.

[23] M.R. Watts, W.A. Zortman, D.C. Trotter, R.W. Young, and A.L. Lentine. *Low-Voltage, Compact, Depletion-Mode, Silicon Mach 2013;Zehnder Modulator*. Selected Topics in Quantum Electronics, IEEE Journal of, 16(1):159–164, Jan 2010.

[24] David A. B. Miller. *Self-aligning universal beam coupler*. Opt. Express, 21(5):6360–6370, Mar 2013.

[25] A. Ruocco, D. V. Van Thourhout, and W. Bogaerts. *SOI Lattice Filters Design Framework: from Functional Parameters to Layout*. Proceedings of the 18th Annual Symposium of the IEEE Photonics Society Benelux Chapter, pages 223–226, 2013.

[26] S.K. Selvaraja, W. Bogaerts, P. Dumon, D. Van Thourhout, and R. Baets. *Subnanometer Linewidth Uniformity in Silicon Nanophotonic Waveguide Devices Using CMOS Fabrication Technology*. Selected Topics in Quantum Electronics, IEEE Journal of, 16(1):316–324, Jan 2010.

[27] Tom Claes, Wim Bogaerts, and Peter Bienstman. *Experimental characterization of a silicon photonic biosensor consisting of two cascaded ring resonators based on the Vernier-effect and introduction of a curve fitting method for an improved detection limit*. Opt. Express, 18(22):22747–22761, Oct 2010.

[28] M. Pantouvaki, Hui Yu, M. Rakowski, P. Christie, P. Verheyen, G. Lepage, N. Van Hoovels, P. Absil, and J. Van Campenhout. *Comparison of Silicon Ring Modulators With Interdigitated and Lateral p-n Junctions*. Selected Topics in Quantum Electronics, IEEE Journal of, 19(2):7900308–7900308, March 2013.

[29] W. Bogaerts, P. De Heyn, T. Van Vaerenbergh, K. De Vos, S. Kumar Selvaraja, T. Claes, P. Dumon, P. Bienstman, D. Van Thourhout, and R. Baets. *Silicon microring resonators*. Laser Photon. Rev., 6(1):47–73, 2012.

[30] John M. Choi, Reginald K. Lee, and Amnon Yariv. *Control of critical coupling in a ring resonator–fiber configuration:application to wavelength-selective switching, modulation, amplification, and oscillation*. Opt. Lett., 26(16):1236–1238, Aug 2001.

[31] Brent E. Little, Juha-Pekka Laine, and Sai T. Chu. Opt. Lett., 22(1):4–6, Jan 1997.

[32] J. Brouckaert, W. Bogaerts, P. Dumon, D. Van Thourhout, and R. Baets. *Planar Concave Grating Demultiplexer Fabricated on a Nanophotonic Silicon-on-Insulator Platform*. Lightwave Technology, Journal of, 25(5):1269–1275, May 2007.

[33] Lech Wosinski, Ning Zhu, and B. Jaskorzynska. *Silicon-based integrated multiplexers for WDM systems*. In Transparent Optical Networks, 2009. ICTON '09. 11th International Conference on, pages 1–4, June 2009.

[34] J. Brouckaert, G. Roelkens, S. Selvaraja, W. Bogaerts, P. Dumon, S. Verstuyft, Zon-Qiang Yu, D. Van Thourhout, and R. Baets. *Miniature integrated spectrometer fabricated on a silicon-on-insulator substrate*. In IEEE Lasers and Electro-Optics Society, 2008. LEOS 2008. 21st Annual Meeting of the, pages 55–56, Nov 2008.

[35] Xiao Ma, Mingyu Li, and Jian-Jun He. *Spectrometer-on-a-chip based on echelle diffraction grating in SiON waveguides*. In Communications and Photonics Conference and Exhibition, 2011. ACP. Asia, pages 1–2, Nov 2011.

[36] S. Pathak, P. Dumon, D. Van Thourhout, and W. Bogaerts. *Comparison of AWGs and Echelle Gratings for Wavelength Division Multiplexing on Silicon-on-Insulator*. Photonics Journal, IEEE, 6(5):1–9, Oct 2014.

[37] Joost Brouckaert. *Integration of Photodetectors on Silicon Photonic Integrated Circuits (PICs) for Spectroscopic Applications*. PhD thesis, University of Gent, Department of information technology, 2010.

[38] D. Chowdhury. *Design of low-loss and polarization-insensitive reflection grating-based planar demultiplexers*. Selected Topics in Quantum Electronics, IEEE Journal of, 6(2):233–239, March 2000.

[39] K. Takada, M. Abe, M. Shibata, M. Ishii, and K. Okamoto. *Low-crosstalk 10-GHz-spaced 512-channel arrayed-waveguide grating multi/demultiplexer fabricated on a 4-in wafer*. Photonics Technology Letters, IEEE, 13(11):1182–1184, Nov 2001.

[40] S. Cheung, Tiehui Su, K. Okamoto, and S.J.B. Yoo. *Ultra-Compact Silicon Photonic 512 x 512 25 GHz Arrayed Waveguide Grating Router*. Selected Topics in Quantum Electronics, IEEE Journal of, 20(4):310–316, July 2014.

[41] Shibnath Pathak. *Silicon Nano-Photonics Based Arrayed Waveguide Gratings*. PhD thesis, University of Gent, Department of information technology, 2014.

[42]

[43] Wim Bogaerts, Shibnath Pathak, Alfonso Ruocco, and Sarvagya Dwivedi. *Silicon photonics non-resonant wavelength filters: comparison between AWGs, echelle gratings, and cascaded Mach-Zehnder filters*, 2015.

[44] D.M. Pozar. *Microwave Engineering*. Wiley, 2004.

[45] P. Dumon, W. Bogaerts, V. Wiaux, J. Wouters, S. Beckx, J. Van Campenhout, D. Taillaert, B. Luyssaert, P. Bienstman, D. Van Thourhout, and R. Baets. *Low-loss SOI photonic wires and ring resonators fabricated with deep UV lithography*. Photonics Technology Letters, IEEE, 16(5):1328–1330, May 2004.

[46] Pieter Dumon. *Ultra-Compact Integrated Optical Filters in Silicon-on-insulator by Means of Wafer-Scale Technology*. PhD thesis, University of Gent, Department of information technology, 2014.

[47] L. Alloatti, C. Koos, and J. Leuthold. *Optical loss by surface transfer doping in silicon waveguides*. Applied Physics Letters, 107(3), 2015.

[48] J. Leuthold, C. Koos, and W. Freude. *Nonlinear silicon photonics*. Nat Photon, 4(8):535–544, Aug 2010.

[49] Matthew Borselli, Thomas Johnson, and Oskar Painter. *Beyond the Rayleigh scattering limit in high-Q silicon microdisks: theory and experiment*. Opt. Express, 13(5):1515–1530, Mar 2005.

[50] Matthew Borselli, Thomas J. Johnson, and Oskar Painter. *Measuring the role of surface chemistry in silicon microphotonics*. Applied Physics Letters, 88(13), 2006.

[51] Yurii Vlasov and Sharee McNab. *Losses in single-mode silicon-on-insulator strip waveguides and bends*. Opt. Express, 12(8):1622–1631, Apr 2004.

[52] Fengnian Xia, Lidija Sekaric, and Yurii A. Vlasov. *Mode conversion losses in silicon-on-insulator photonic wire based racetrack resonators*. Opt. Express, 14(9):3872–3886, May 2006.

[53] Ji tyrok, Ivan Richter, and Milan ior. *Dual resonance in a waveguide-coupled ring microresonator*. Optical and Quantum Electronics, 38(9-11):781–797, 2006.

[54] I.T. Monroy and E. Tangdiongga. *Crosstalk in WDM Communication Networks*. The Springer International Series in Engineering and Computer Science. Springer US, 2013.

[55] S. Pathak, M. Vanslembrouck, P. Dumon, D. Van Thourhout, and W. Bogaerts. *Effect of mask grid on SOI arrayed waveguide grating performance*. In Group IV Photonics (GFP), 2013 IEEE 10th International Conference on, pages 31–32, Aug 2013.

[56] Francesco Morichetti, Antonio Canciamilla, Carlo Ferrari, Matteo Torregiani, Andrea Melloni, and Mario Martinelli. *Roughness Induced Backscattering in Optical Silicon Waveguides*. Phys. Rev. Lett., 104:033902, Jan 2010.

[57] Yisu Yang, Yangjin Ma, Hang Guan, Yang Liu, Steven Danziger, Stewart Ocheltree, Keren Bergman, Tom Baehr-Jones, and Michael Hochberg. *Phase coherence length in silicon photonic platform*. Opt. Express, 23(13):16890–16902, Jun 2015.

[58] A.V. Oppenheim and R.W. Schafer. *Discrete-Time Signal Processing*. Pearson Education, 2011.

[59] *http://www.lucedaphotonics.com/en*.

[60] Ghent University - imec. *IPKISS parametric design framework*. http://www.ipkiss.org.

[61] Koji Yamada, Tetsufumi Shoji, Tai Tsuchizawa, Toshifumi Watanabe, Jun ichi Takahashi, and Sei ichi Itabashi. *Silicon-wire-based ultrasmall lattice filters with wide free spectral ranges*. Opt. Lett., 28(18):1663–1664, Sep 2003.

[62] Xi Chen, Zheng Li, Moustafa Mohamed, Li Shang, and Alan R. Mickelson. *Parameter extraction from fabricated silicon photonic devices*. Appl. Opt., 53(7):1396–1405, Mar 2014.

[63] Lukas Chrostowski, Xu Wang, Jonas Flueckiger, Yichen Wu, Yun Wang, and Sahba Talebi Fard. *Impact of Fabrication Non-Uniformity on Chip-Scale Silicon Photonic Integrated Circuits*. In Optical Fiber Communication Conference, page Th2A.37. Optical Society of America, 2014.

[64] R. Horst, P.M. Pardalos, and N. Van Thoai. *Introduction to Global Optimization*. Nonconvex Optimization and Its Applications. Springer, 2000.

[65] B. Efron and R.J. Tibshirani. *An Introduction to the Bootstrap*. Chapman & Hall/CRC Monographs on Statistics & Applied Probability. Taylor & Francis, 1994.

[66] A. Ruocco, M. Fiers, M. Vanslembrouck, T. Van Vaerenbergh, and W. Bogaerts. *Multi-parameter extraction from SOI photonic integrated circuits using circuit simulation and evolutionary algorithms*, 2015.

[67] Sarvagya Dwivedi, Thomas Van Vaerenbergh, Alfonso Ruocco, Thijs Spuesens, Peter Bienstman, Pieter Dumon, and Wim Bogaerts. *Measurements of Effective Refractive Index of SOI Waveguides using Interferometers*. In Advanced Photonics 2015, page IM2A.6. Optical Society of America, 2015.

[68] Rainer Storn and Kenneth Price. *Differential Evolution A Simple and Efficient Heuristic for global Optimization over Continuous Spaces*. Journal of Global Optimization, 11(4):341–359, 1997.

[69] Waltraud Huyer and Arnold Neumaier. *SNOBFIT – Stable Noisy Optimization by Branch and Fit*. ACM Trans. Math. Softw., 35(2):9:1–9:25, July 2008.

[70] N. Hansen and A. Ostermeier. *Adapting arbitrary normal mutation distributions in evolution strategies: the covariance matrix adaptation*. In Evolutionary Computation, 1996., Proceedings of IEEE International Conference on, pages 312–317, May 1996.

[71] W.J. Westerveld, J. Pozo, S.M. Leinders, M. Yousefi, and H.P. Urbach. *Demonstration of Large Coupling-Induced Phase Delay in Silicon Directional Cross-Couplers*. Selected Topics in Quantum Electronics, IEEE Journal of, 20(4):1–6, July 2014.

[72] Lian-Wee Luo, Salah Ibrahim, Carl B. Poitras, Stevan S. Djordjevic, Hugo L. Lira, Linjie Zhou, Jaime Cardenas, Binbin Guan, Arthur Nitkowski, Zhi Ding, S J. Yoo, and Michal Lipson. *Fully Reconfigurable Silicon Photonic Interleaver*. In Conference on Lasers and Electro-Optics 2010, page CFL5. Optical Society of America, 2010.

[73] Zhipeng Wang, Shih-Jung Chang, Chi-Yu Ni, and Yung Jui Chen. *A High-Performance Ultracompact Optical Interleaver Based on Double-Ring Assisted Mach 2013;Zehnder Interferometer*. Photonics Technology Letters, IEEE, 19(14):1072–1074, July 2007.

[74] P. De Heyn, J. De Coster, P. Verheyen, G. Lepage, M. Pantouvaki, P. Absil, W. Bogaerts, J. Van Campenhout, and D. Van Thourhout. *Fabrication-Tolerant Four-Channel Wavelength-Division-Multiplexing Filter Based on Collectively Tuned Si Microrings*. Lightwave Technology, Journal of, 31(16):2785–2792, Aug 2013.

[75] M. Nedeljkovic, A.V. Khokhar, A. Delage, P. Cheben, and G.Z. Mashanovich. *Mid-infrared silicon-on-insulator Fourier-transform spectrometer chip*. Photonics Technology Letters, IEEE, PP(99):1–1, 2015.

3

Spectrometers based on actively modulated filters

This chapter introduces the concept of electro-optic tuning to overcome the limitations of passive optical filters used as spectrometers. When a spectrometer with broadband operative range, high resolution and accuracy is required, passive integrated SOI optical filters fail to deliver the required results, usually because of intrinsic limitations of fabrication. SOI integrated spectrometers are therefore limited by the accuracy and reproducibility of SOI technology. In this chapter, we use active tuning and modulation techniques to dynamically change the filter's response. The advantage of active optical filters spectrometers is the capability to change their transmission spectrum dynamically.

First the physical phenomena which are able to change the filter's response are introduced: in particular the focus is on the thermo-optic effect and electro-optic effect. The former is due to the temperature dependence of the silicon refractive index, while the latter is due to the carrier density dependence of the refractive index, which requires the silicon to be doped. Basic filter structures such as ring resonators and MZIs with active modulation capabilities are used as wavelength interrogation devices. Multiple active driving schemes are tested: in particular stepped and continuous driving. The first consists of sequentially tuning the filters with discrete electrical current and time steps. Continuous driving consists of driving the filters with a time continuous signal (or AC carrier).

3.1 Passive integrated spectrometers: fabrication variations

Optical filters realized in SOI suffer from fabrication uncertainty in all the geometrical properties. Most prominent are width, thickness and sidewall angles of the waveguides and slabs. Fig. 3.1 represents an example of ideal cross-section and the results of the fabrication. In most simulations, the ideal cross-section is used, while this does not necessarily correspond with reality. The geometrical aspect of the waveguide directly influences the optical parameters (in particular effective index and group index) of the device realized with it [1, 2]. How the group index, effective index, coupling, etc. influence basic filter transmission has been treated in Ch. 2.

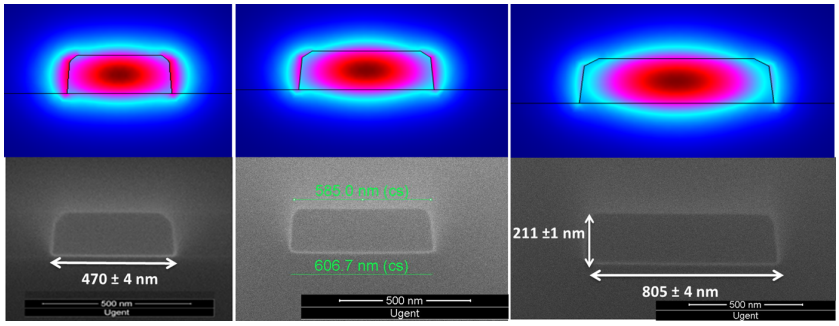

Figure 3.1: Cross-section and mode profile simulation of three different strip waveguide: they were designed to have 450, 600 and 800 nm width. They were designed to have rectangular profiles(from [3]).

3.1.1 Non-idealities compensation for optical filters

There are several practical consequences of the mismatch between ideal and fabricated layout, as shown in Fig. 2.21. First of all, there is a shift of the wavelength transmission resonance peaks. The shift $\Delta\lambda$ is determined by the variation of effective index Δn_{eff}. In addition to that, variations of the group index Δn_g lead to changes in the separation of the resonance orders (or FSR). Post-processing solutions have been used to permanently adjust the filter transmission after fabrication, such as trimming [4, 5], but this is a non-wafer scalable process, and not CMOS compatible in the sense that it cannot be applied to devices which have already been covered by CMOS metallization. In some case, the devices can be calibrated after a detailed characterization. A relevant example are filters designed to be cyclic [6]. The compensation can be done rearranging the association between the physical channel and the wavelength information that it is carrying.

Passive calibration is not possible when it comes to absolute wavelength control of a single device or the alignment of multiple devices on the same die to a wavelength grid. An example is the case of an array of ring filters that need to be aligned to a certain wavelength grid of communication channels, but only using a single, common tuner element [7].

3.1.2 Passive optical spectrometers

When we discuss spectrometer applications, the grid corresponds to the resolution of the spectrometer, or the wavelength 'bins' in which light can be separated.

A spectrometer using imaging-based filters (AWG or PCG) use a single filter with multiple outputs that can split the input in its wavelength contributions. The resolution is defined by the output channel spacing. The minimum channel spacing that can be designed for most of the WDM filters is limited by the precision of the fabrication technology, and this is also the case for AWGs and PCGs [8].

The operation range of a spectrometer is governed by a filter's FSR, i.e. the spacing with which the filter spectrum repeats itself. In the case of AWGs, the FSR is limited by the minimum delay length between every two adjacent waveguides in the array.

The minimum channel spacing is instead limited by the phase on the waveguides, since smaller FSR means longer delay length, thus, larger phase. Moreover, more output channels (higher resolutions) leads to more waveguides in the array, thus, a higher average arm length, which again will increase the phase errors.

In the case of PCGs, higher resolution will require a larger number of facets (DBRs) with a consequent larger FPR. The FPR becomes excessively large with a consequent increase of the phase errors. Furthermore, a higher number of facets also leads to more scattered light at their edges.

In the ring, the FSR is limited (upper limit) by the minimum bending radius that fixes the minimum circumference. The minimum bending radius is limited by the acceptable loss in the in the bend itself(cf. Par. 3.3.1.3). Furthermore, coupling and waveguide roughness limit the performances in term of Q-factor and extinction ratio.

The issues related to MZIs based structures arise mainly when multiple devices need to be cascaded (in lattice filters for example), indeed, in this case the inhomogeneity between the delays of the stages causes degradation of the device performances.

Also in this case, the splitting non-idealities affect the extinction ratio. These are outstanding cases, but not fully exhaustive of the fabrication limits imposed to WDM optical filters.

The SOI platform is also affected by thermo-optical variations. Environmental temperature variations can change the response of the entire PIC at the same time,

but it is also possible to have a temperature gradient across larger circuits [3]. To compensate for this, there have been several approaches: a full passive compensation can limit the thermo-optic parasitic drift, but it is not possible for all types of wavelength filtering devices [9].

On the other hand, the thermo-optic coefficient is not just a source of problems, but can also be used for active manipulation of the circuit, which we will use to our advantage in the work described further in this chapter, both to overcome the limitations of fabrication, but also to improve the functionality of our spectrometers.

3.2 Tunable optical filters

We can influence waveguide parameters to change the transmission of optical filters, effectively creating a tunable filter. Tunable filters are an essential component for applications in telecommunication [10], sensing [11], microwave photonics [12]. The active tuning can be performed with different mechanisms, such as temperature, and silicon has a quite high thermo-optic constant. Another mechanism is the manipulation of the carrier density in the waveguide core. While temperature dependence can be considered to be a weakness of the platform, we use it as a useful a resource in this chapter.

The variation of temperature or carried density affects the effective index of the guided modes of the waveguide by changing the refractive index of the core material. The variation of the effective index of the silicon wire is proportional to the overlap of the integral between the optical mode and the local refractive index change.

$$\Delta n_{eff} = \frac{\iint_s \delta n(x,y) \mid E(x,y) \mid^2 \Delta x \delta y}{\iint_s \mid E(x,y) \mid^2 \Delta x \delta y} \tag{3.1}$$

The integration surface is the waveguide cross-section. $|E(x,y)|$ is the electric field and $\delta n(x,y)$ is the local effective index variation of the material [13]. In the waveguide core this is silicon, which typically has a large change, while outside it is oxide, which usually has a much lower change.

Since we are working with filters, it is worth to talk about the shift of the resonances of the device itself and how it changes with an external agent (temperature, carrier concentration, etc.).In SOI, the dispersion of the photonic wire has to be taken into account. Eq. 3.2 represents the wavelength shift of an interference based filter, when an external agent causes an effective index variation [14, 15].

$$\frac{d\lambda_{res}}{de_{ex}} = (n_{eff}\alpha_{sub} + \frac{dn_{eff}}{de_{ex}})\frac{\lambda_{res}}{n_g} \tag{3.2}$$

In Eq. 3.2 λ_{res} is the resonant wavelength, while e_{ex} is the external agent; α_{sub} is the substrate expansion coefficient. The formula keeps its validity in case of different external agents such as temperature or carrier concentration variations.

This general information on effective index tuning properties apply to different types of optical filters, for tuning and modulation purposes. We will focus on TO and EO effect. The first make use of the thermo-optic coefficient of the silicon dn/dT, while the second make use of the electro-optic coefficient of the silicon $dn/dn_{carrier}$. The following paragraphs provide more detail on the individual tuning mechanism.

3.2.1 Thermo-optic effect for tuning silicon waveguides

The thermo-optic offers a simple and well-controlled modulation and tuning mechanism for photonic components. The refractive index change of Silicon induced by temperature is:

$$\frac{\delta n}{\delta T} = 1.86 \cdot 10^{-4} K^{-1} \tag{3.3}$$

In this work, we use the TO effect to tune the response of filters and devices and to modulate optical signals. The modulation using TO effect is slow [16], so it is suitable only if the required modulation speed is $< 1KHz$.

Fig. 3.2 shows the bode diagram of a symmetric thermo-optic MZI modulator and a microring resonator. There is a good matching of the performances since the same thermo-optic strategy is used. The mismatch arises from the intrinsic response of the devices. The exponential thermal rise/fall behavior is, in this case, modulated by the transmission response of the devices. Thus, a Lorentzian and a sinusoidal for the ring and the MZI, respectively.

The most common use of the TO effect is the tuning of optical filters, and the slow speed of tuning is in the suitable frequency range for many applications.

The variation of the refractive index in Eq. 3.3 produces a variation in the effective index of the photonic wires. As we discussed in the previous section, the thermal tuning efficiency will be dependent on the cross-section [16]. Simulation tools such as COMSOL can be used to calculate the temperature distribution induced by a heater, and the corresponding n_{eff} distribution [3]. Since the refractive index varies linearly with temperature, also the waveguide mode's effective index variation will be linear, at least within a certain ΔT. Moreover, according to

$$\Delta T = Q \cdot R_{therm} \tag{3.4}$$

The general relation between thermal power flow and temperature change is also linear. Eq. 3.4 estimates the temperature variation when the thermal power flow Q is flowing through the thermal resistance R_{therm}. In our case ΔT needs to

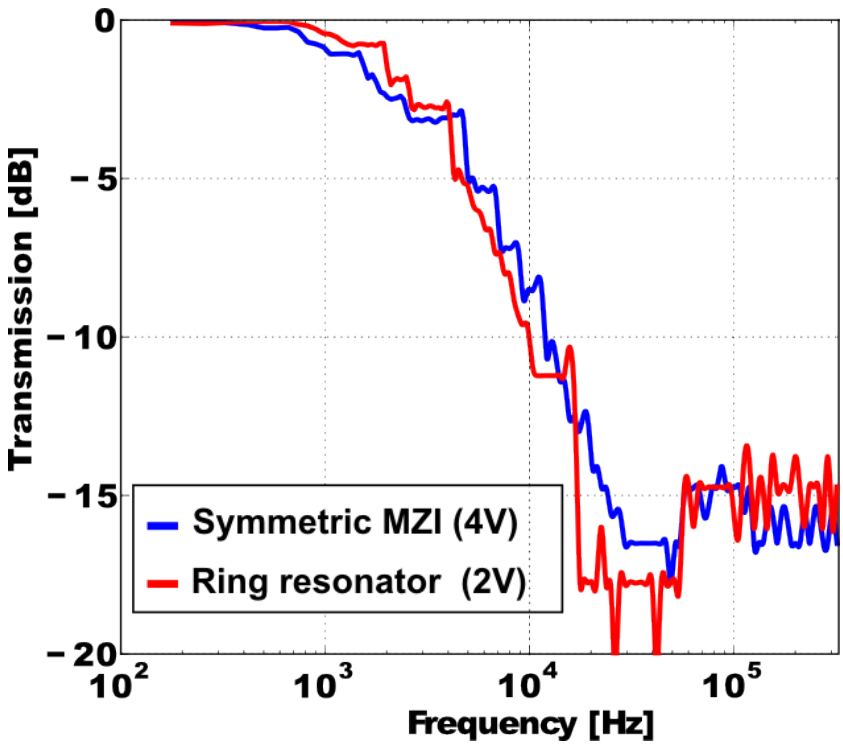

Figure 3.2: The plot shows the bode diagram of the MZI and ring resonator presented in Fig. 3.6 and Fig. 3.12. The output is the voltage level of the output photodiode used as electro-optic transducer for the optical devices.

be integrated across the length of the device. As there is a different thermal path between the heater and the waveguide (heating up) and the waveguide and the substrate (cooling down), there is a different time constant for heating and cooling [16]. This double time constant is qualitatively depicted in Fig. 3.4. A simple way of injecting heat into the structure is to dissipate electric power in the proximity of the photonic wire. The efficiency of the heater as a tuning element can be described as the power needed to induce a π phase shift in a waveguide. This figure of merit is independent of the waveguide length. A certain Δn_{eff} corresponds a phase shift $\Delta\phi$ over the waveguide length. The same power can generate a larger temperature rise, while in a longer waveguide the power will result in a lower temperature rise. But as long as all processes are linear, the accumulated phase shift will be the same, irrespective of the waveguide's length. The power required to reach the Δn_{eff} corresponding to $\Delta\phi = \pi$ is called P_π [17]. This figure of merit is largely dependent on the thermal environment of the heaters. A lower value of P_π indicated a more efficient heater.

First, the electrical power needs to be driven into the heater, which can be a resistor positioned close to a photonic wire. In some cases, the resistor can be the photonic wire itself. Different approaches and optimizations are available in CMOS technology to implement these heaters [16, 18]. In this work, we implemented two different heater strategies and tested and used them for wavelength interrogation purpose: a metallic heater on top of the silicon waveguide and a doped silicon heater at the side of the waveguide. The first type is added at the back end of the wafer processing. The second is fabricated in the front end of the line, in the same layer as the waveguides themselves. Both heater types were fabricated through the MPW of IMEC.

3.2.1.1 Metal heater on top of the waveguides

We use metal heaters to add tuning functionality to standard passive silicon circuits. These chips are made on a simple process that only defines the passive silicon waveguides and covers them with an oxide cladding. We then process metal heaters in the Ghent University clean room.

The heater consists of metal tracks deposited on the oxide cladding. Standard strip waveguide has a silicon oxide cladding of about 1 um. We use different lithographic masks to define multiple levels of metal for the heater resistor and the contacting wires. First of all the pattern of the heater is realized by image reversal lithography and sputtering. The metal stack consists of 100 nm of titanium and 20 nm of gold represented in Fig. 3.3 with red. A lift-off step removes the unwanted metal. With the same technique, a second layer of gold, represented in Fig. 3.3 with blue is realized on the wires and pads.

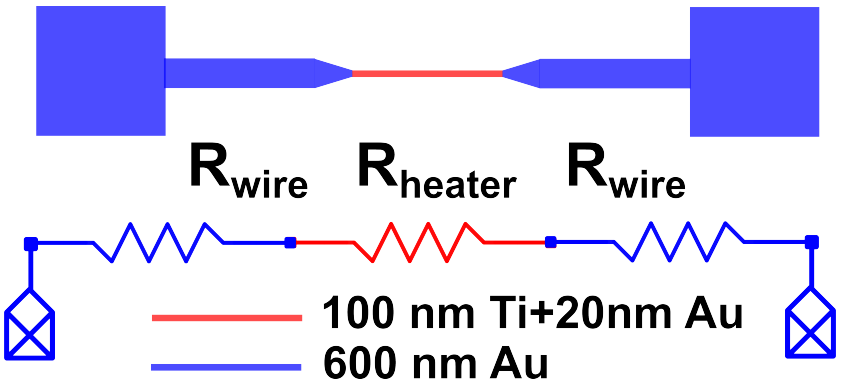

Figure 3.3: Mask layers and schematic representation of metal heater on top of the waveguide: on the top image we see the layout, in the bottom image an electrical schematic of the circuit

When using gold wires, the thickness is about 600 nm. This guarantees the

resistance of the wires to be negligible compared to the resistance of the heaters, so the electrical power is dissipated only in the actual heater on top of the waveguide. Fig. 3.3 shows the top view (top) and the electrical equivalent circuit (bottom) of the top metal heater. The value of R_{wire} is kept in the range of $\sim$20 Ω/mm, while the value of R_{heater} is in the order of $\sim$10 $k\Omega/mm$, thus, in general, the resistance of the wire is neglected.

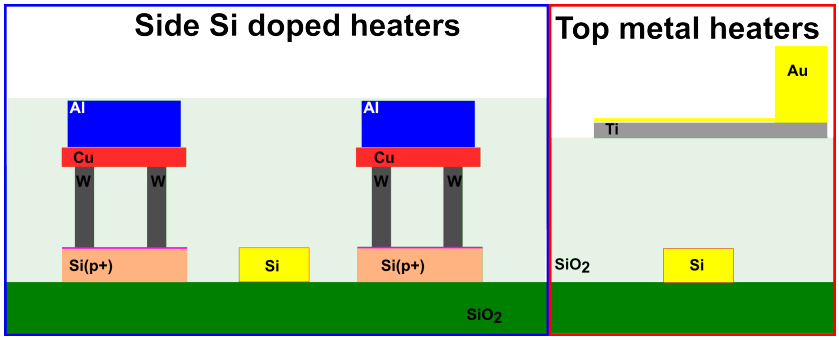

Figure 3.4: The images represent the standard cross-section used for the heaters architectures adopted in this work: left image is the cross-section for side doped heaters, while right image is the cross-section for top metal heaters

Fig. 3.4(right) represents the standard cross-section adopted for metal top heater. With the top metal heaters, the resistivity of the device is experimentally extracted and quantified as 10 $\frac{\Omega}{\square}$. The value of the resistance is obtained by multiplying the resistivity and the serially connected boxes of the heater.

In Ch. 4 the top metal heaters are used to modulate in time domain mirroring resonators, such that a well-defined correlation between electrical driving and wavelength position of the resonance peak is established. The top metal heaters are used in Ch. 5 where we drive an array of MZI symmetric switches. We use them for TDM, and only an ON/OFF switching operation is carried out. The speed used for the switching is compatible with the limitation of the device.

3.2.1.2 Side doped waveguides

When fabricating optical circuits in a CMOS fab such as IMEC, there is also the possibility of a 'full platform'. This process starts from the same passive waveguide devices but adds multiple levels of doping, silicidation, tungsten contacts and a CMOS-like copper metallization. In this process, there are different ways to define a heater, using doped silicon lines, silicides and also metal heaters on top of the waveguide [16].

For this work, we made used of doped silicon strips traveling on both sides of the photonic waveguide. The fabrication was realized with ePIXfab MPW service

in IMEC, Belgium. The resistivity of the bulk silicon is high enough to have acceptable resistance values and acceptable geometrical proportions at the same time. Highly doped silicon will provide a much lower resistance. Because the heaters are placed close to the waveguide, an important design specification is how to avoid any optical coupling between the optical waveguides and the heater. This is done by properly designing the gap between the waveguide and the heater and using different cross-sections to avoid any phase matching [19]. The resistivity for the doped waveguide is fixed by the technology and it has a typical value of 160 $\frac{\Omega}{\square}$. The resistivity of these heaters is, in general, higher than the resistivity of the metal heater, so a single heater line is often split into multiple sections with parallel interdigitated electrical contacts. By playing with the lengths and number of the sections we can tailor the electrical properties to the operating range of the measurement equipment. Interdigitated contacting requires lower voltages and higher current for the same heater absolute length. Remember that rearranging the contacts only adjusts the voltage and current range, but not the heater efficiency: the same amount of power is needed to obtain a π phase shift.

The doped silicon heaters and the waveguides share the same layer of the silicon, thus they are covered by an oxide cladding. The heaters are connected to the copper wires with tungsten vias. Silicide is present at the silicon-tungsten interfaces. The copper, in turn, is connected to the aluminum used for the pads. Fig. 3.4(b) shows an example cross-section.

Fig. 3.5(top) shows the lateral cross-section of the side doped heaters. Fig. 3.5(bottom) shows the equivalent circuit for the used layout, the lumped net of resistances that we find at the connection point is considered as an equivalent resistance$R_{contact}$.

The side doped heaters are used in this chapter, at Par. 3.3 where a thermo-optic ring modulator is used to scan the wavelengths included its FSR. Such device is used as a spectrometer. The heaters are realized on both sides of the ring.

3.2.1.3 Thermo-optic symmetric MZI modulator

A representative example of a thermo-optic filter can be a symmetric MZI modulator. It consists of two 3 dB splitter connected by two waveguides of the same physical length. The power splitters are MMIs while the arms are simple strip waveguide with a width of 450 nm. The length of the arms is designed such that the required temperature to achieve π shift is below the safe working region of the heater itself. The length is 200 um, assuming 50 um as the safe threshold.

The heaters are realized with side doped waveguides on both sides of both arms. Fig. 3.6(a) shows a microscope image of the device. Each section of the heater is contacted multiple times in such way that an interdigitated electrical connection is realized. The base material resistivity is higher than metal, requiring higher voltages for its driving. With the interdigitated architecture, the overall resistance becomes smaller, requiring lower driving voltage to drive the same power.

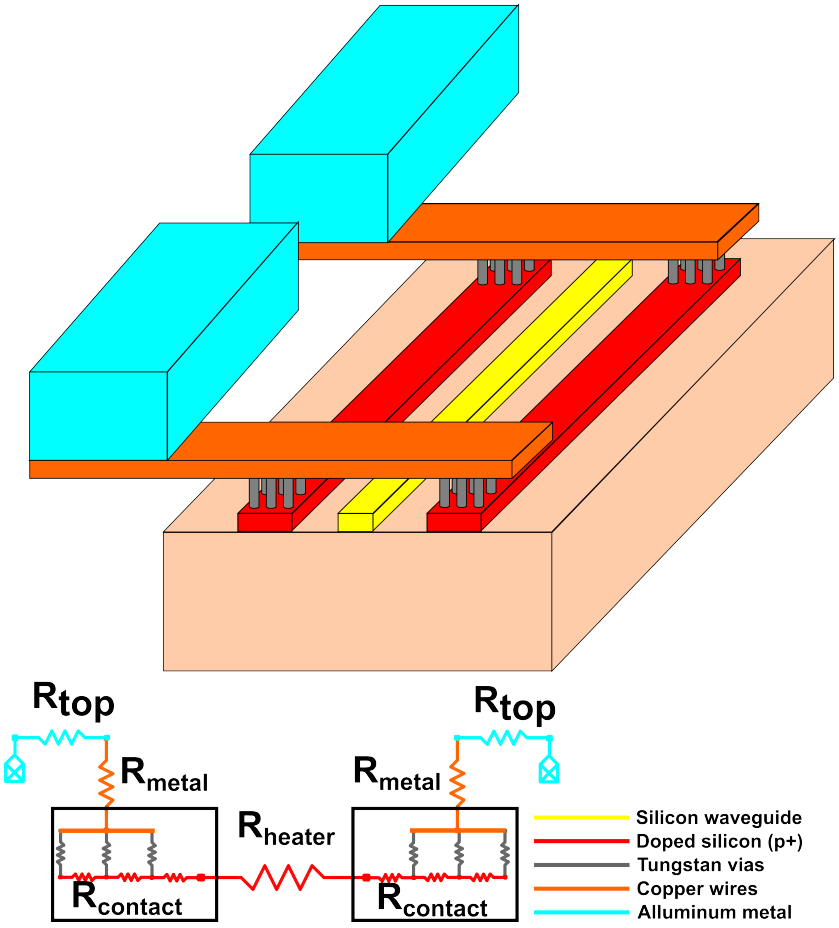

Figure 3.5: Transversely cross-section of the side doped heaters in the top image. The bottom image shows the equivalent electrical circuit.

This is achieved at the expense of a higher driving current. More important is that the electrical properties are compatible with our measurement infrastructure.

Fig. 3.6(b) shows the electro-optic characteristic of the MZI when the voltage is swept, while Fig. 3.6(c) shows the electrical characteristic: IV and RI curves. The figure of merit P_π is $\sim 40\ mW$. An extinction ratio (difference of intensity of constructive and destructive interference) of $>25\ dB$ is measured. This simple but good result is is also an indication of the quality of the passive optical devices.

In Fig. 3.6(c) the strong non-linear coefficient of the resistance as a function of the voltage. The actual dependency of the resistance comes from the relation between the mobility and the temperature. More in detail, we apply a voltage, which causes the conversion of electrical power into thermal power. The increase

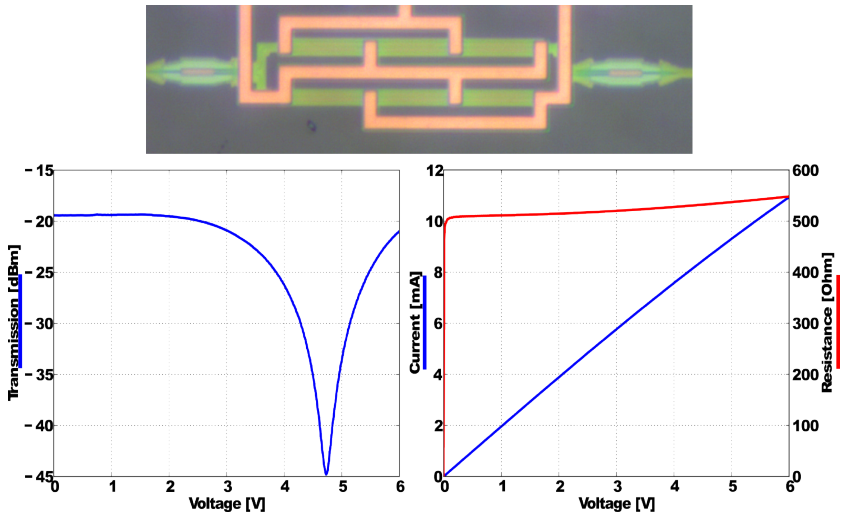

Figure 3.6: The images show the microscope image of a symmetric MZI thermo-optic modulator with side doped heaters: the plots represent the electro-optic and electric characteristic of the device

of the temperature produces our desired optical transmission variation as well as a reduction of the carriers mobility μ. The standard relation between the increment of resistance and the temperature is expressed in Eq. 3.5, a second order Taylor relation is most common model used to model the resistance itself as in Eq. 3.6 [20].

$$\frac{\Delta R(T)}{R(T_0)} = \frac{\Delta \rho(T)}{\rho(T_0)} = \frac{\Delta \mu(N_D, T)}{\mu(T_0)} \tag{3.5}$$

$$R(T) = R(T_0) = [1\alpha(T - T_0) + \beta(T - T_0)^2] \tag{3.6}$$

The non-linearity is represented by the linear slope of the resistance as a function of the voltage. This effect is much more relevant in the doped heaters compared to metal heaters, since the dR/dT is much larger in the doped silicon than in metals [21].

3.2.2 Carrier dispersion effect for modulation in silicon waveguides

A faster, but less efficient tuning mechanism is the modulation of the carrier density in the silicon waveguide. The refractive index of silicon is dependent on the actual concentration of free carriers [13]. The metal contacting the surface of the waveguides induces absorption losses, hence, to apply a voltage to the doped

waveguide we adopt a rib cross-section for the waveguide. The partially etched (150 nm) trench is heavily doped since we want it to be a low resistance section, on the other hand, we need the contact of the metal vias and the trench as far as possible from the waveguide core, and thus, the optical mode.

An efficient way of generating carrier accumulation or depletion is to use a PN junction [22]. The PN junction, also known as diode, is a well-known electronic component [21]. At the PN junction, a depletion region is formed due to the different potential of the Fermi levels. The carrier density and the width of the depletion region can be modulated by biasing the diode with forward of reverse bias. In the case of forward bias, there will be carrier injection and the depletion region will shrink. In the case of reverse bias, the junction is even further depleted of carriers and the depletion region becomes larger [21].

Eq. 3.7 describes the behavior of the diode for the three working regimes: direct, reverse and break-down.

$$J = J_0(e^{\frac{qV}{NkT}} - 1) \tag{3.7}$$

Eq. 3.7 represents the model of a PN junction current density. The working condition for a PN junction as an optical modulator is in reverse bias, since carrier depletion is a faster and more electrically efficient phenomenon. The interest is mainly in the second term that is relevant since it gives information on the breakdown voltage. The breakdown voltage is the maximum voltage with which the device can be driven. The breakdown voltage also fixes the maximum phase shift achievable with the phase shifter using this PN junction. The current is extremely small when in reverse bias condition [21], and for our devices under test it is in the order of $\sim$ 0.6 A/m. The effective index of the waveguide can be modulated by creating an overlap between the depletion region and the optical field. The relation between the carrier density and the voltage is quite linear when used in reverse bias at low voltages. This assumption is valid in first approximation since it is strongly non-linear for bias reverse bias $> 3V$. The drawback of the carrier dispersion effect is the efficiency. The effect is much weaker than the TO effect, and the required footprint to have π shift is, at least, one order of magnitude higher. Another unwanted phenomenon induced by the doping is the increased loss, which is, in general, one order of magnitude higher compared to the undoped strip waveguide. In the first case 2.5 dB/cm are expected, while for doped silicon the loss is in the order of 25.0 dB/cm. Also, the change in carrier concentration for modulating the n_{eff} will also induce a modulation in the waveguide loss.

For our devices, the doping concentration and profile are fixed by the fab. They are optimized for the reverse bias conditions. There is a trade-off condition to choose the right doping concentration: on one hand the Δn_{eff} is proportional to the square root of the doping concentration while the depletion region on the other hand shrinks with doping concentration. A reduced depletion region implies

a reduction of the overlap of the optical mode with the depletion region [22].

Different layouts can be used to realize the PN junction overlap with the optical mode. In this work two of the most common are used: lateral and interdigitated(longitudinal) PN junctions.

The interdigitated junction is realized with P-type and N-type fingers which alternate along the waveguide direction. In this case, the PN junction sections are orthogonal to the waveguide direction. The lateral junction consists of two opposite sides of the optical waveguide doped with P-type and N-type and so the interface of the doping is parallel to the waveguide direction. While the lateral junction architecture shows less IL and is faster, on the other hand, the interdigitated architecture exhibits a higher efficiency expressed regarding the figure of merit $V_\pi L_\pi$. Respectively the $V_\pi L_\pi$ for interdigitated and lateral junction are 0.8 and 0.95 Vcm at 0 V bias. $V_\pi L_\pi$ is the parameter that is usually adopted to design the required length to reach a given Δn_{eff} with a specified operating voltage (smaller than breakdown voltage). The breakdown voltage for these structures is usually $9\ V$, due to the small size of the junction itself.

An Ohmic channel is created after the PN junction on the P and N sides. These Ohmic channels are contacted through tungsten vias to the first level of metal (copper) traces. Silicide is present at the interface of the Ohmic contacts and the vias. Aluminum is then used for the electrical pads. Fig. 3.7 represent the cross-section used for interdigitated (a) and lateral doping patterns (b). The main parameters used for the design also are represented.

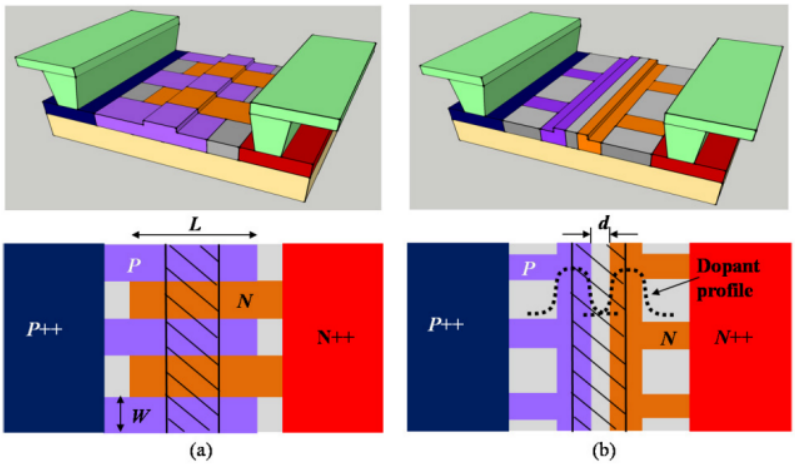

Figure 3.7: The images represent the standard cross-section used for interdigitated and lateral doping patters used for carried depletion based phase shifters, from [23]

The carried depletion phase shifters and thus, modulators are used in Par. 3.3.2

where an asymmetric carrier depletion base MZI modulator is used as a wavelength meter. In Ch. 4 the same device but in symmetric configuration is used as a carrier depletion broadband modulator: it is used in an array of four MZM to label four individual input channel of an AWG.

3.2.2.1 Carrier depletion microring resonator

A peculiar example of a tunable filter based on carrier depletion effect is the microring resonator modulator [24]. The waveguide used is a rib: it is formed by a slab of 70 nm thickness and a strip waveguide of 220 nm thickness. The microring modulator has two directional couplers, thus, both add and drop port are present. In order to achieve critical coupling [25], the directional couplers are designed with different gaps: on the output directional coupler 200 nm and on the input directional coupler 215 nm.

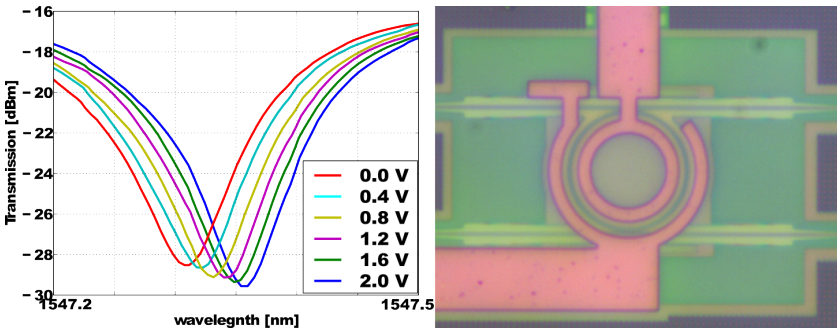

Figure 3.8: The image on the right shows the microscope image of a microring modulator based on carrier depletion effect and lateral junction. The image on the left shows the transmission spectra of a resonance dip for different reverse voltage biases.

Fig. 3.8(b) shows the microscope image of the carrier depletion ring modulator and (a) shows the ring the peak shift in function of the applied voltage. The measured modulation efficiency is of 0.25 pm/V. The radius of the ring is 9.65 um. When this device is designed for high-speed applications, the drop port (the second directional coupler) is not present, while in this case the introduction of the drop port implies the design of another directional coupler. This introduces more inhomogeneity in the doping profiles surrounding the ring. The consequence of this action is a lower modulation efficiency and speed.

3.2.3 Tuning and modulation techniques comparison

In the previous paragraphs, we introduced the different modulation techniques based on the thermo-optic and carrier dispersion effect. For the experiments discussed further, we have used metal on top of the waveguides and doped silicon

wires on the side of the waveguides for thermal tuning. We also use the carrier effect in lateral and interdigitated PN junctions.

In this section we briefly compare these techniques, to motivate our choices of tuning mechanisms when we discuss the applications in this and following chapters.

	Length of π	Electrical eff.*	Cut-off freq.	Loss
Top metal	$>100um$	$>40\ mW/\pi$	$<1\ kHz$	none
Side waveguide	$>50um$	$>30\ mW/\pi$	$<1\ kHz$	none
Interdigitated PN	$>1.5\ mm$	$>10\ uW/\pi$	$>1\ GHz$	$\sim 25\ \frac{dB}{cm}$
Lateral PN	$>1.5\ mm$	$>10\ uW/\pi$	$>1\ GHz$	$\sim 25\ \frac{dB}{cm}$

*Table 3.1: The table collects the main performance indicator of the modulation techniques that are used in this chapter. * The electrical efficiency refers to our particular experiments*

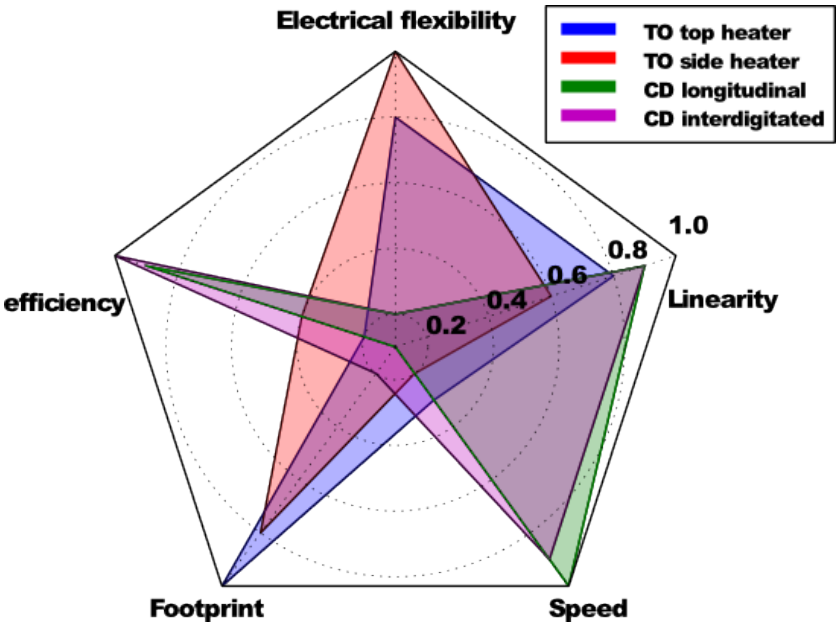

Figure 3.9: The star plot represents a qualitative comparison of the phase shifting techniques used

In Tab. 3.1 a summary comparison of modulation speed, footprint and efficiency are reported. This table is then graphically depicted in Fig. 3.9, where a value from 0 to 1 has been attributed to the different properties of each modulation technique. The main distinction is between the TO and carrier-based devices. TO based devices are more compact, but slow and power hungry. Carrier-based

devices are much faster (several orders of magnitude) and much less power hungry. On the other hand, they require a larger footprint. The first choice is always between heaters and PN-junctions. Then, after the selection of the modulation technique, the sub-category of device can be selected and tailored according to the requirements.

3.3 Spectrometers based on a single modulated filter

Active tuning of an optical filter gives us a known correlation between the wavelength transmission and the electrical drive signal. We can use that correlation to improve the interrogation of filters in a spectrometer. In this paragraph, we construct the relation between the external drive signal (e.g. electrical voltage, current or power) and the transmission spectrum of the filter. When we inject a modulated signal, the resulting time-signal at the output(s) of the filter can then be used to reconstruct the wavelength content of the source. This way, the modulation can give us additional information compared to a static filter.

We demonstrate both TO and carrier modulation effects are used to enhance the wavelength interrogation properties of ring resonators and MZI filters. The drawback of such approach is, of course, the power consumption, but it is paid back by the flexibility and performances. As we will see in following chapters, it can also be used to multiplex read-out signals, which can dramatically reduce the complexity of the read-out electronics (e.g. requiring fewer photodetectors for the same spectrometer resolution).

3.3.1 Ring based spectrometers

The first filter in which we applied modulation is the ring resonator. As mentioned in Ch. 2 Eq. 2.26 the response of the drop port of a microring resonators is a Lorentzian-like curve. The resolution of an individual ring resonator is assumed to be equal or smaller than the FWHM:

$$\lambda_{res} \leq FWHM = \frac{\lambda_0^2(1-ra)}{\pi n_r L\sqrt{ra}} \tag{3.8}$$

Assuming an array of rings aligned to a spectrometer grid as shown in Fig. 3.10, the resolution of the total spectrometer depends on the FSR of the single rings, and the number of rings:

$$\lambda_{res} = \frac{FSR}{N_{ring}} \tag{3.9}$$

The operation range is equal to the FSR of the rings.

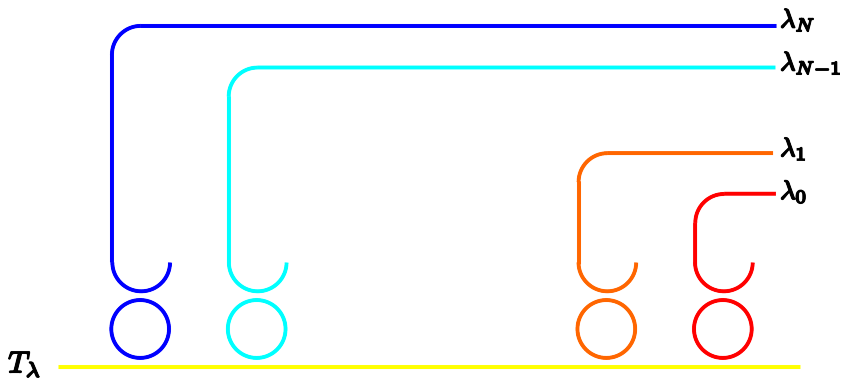

Figure 3.10: Ring array based spectrometer: the wavelengths are sequentially dropped from the main bus by individual rings with regularly spaced wavelength resonance peaks

Each of the rings provides information about the wavelength at which the resonance is centered. In SOI, there is an intrinsic limitation to this approach, as the processing tolerances do not allow to design the ring resonance with arbitrarily high accuracy. The effective index accuracy mismatch translates in the resonance wavelength mismatch. The result is a series of peaks from the array of rings, but not exactly aligned with a wavelength grid, and therefore, the spectrometer is not guaranteed to provide the proper $\Delta\lambda res$.

If we add TO tuning capability to our design, the grid misalignment can be compensated with electrical tuning. The amount of electrical power required to align the ring to the grid is

$$P_{tun} = \frac{P_\pi \cdot N_{ring} \cdot |(\lambda_{grid} - \lambda_{ring})|}{FSR} \tag{3.10}$$

As the TO effect can only increase the effective index, and, therefore, can only redshift the spectrum of the filter, Eq. 3.10 is valid only under the condition that $\lambda_{grid} > \lambda_{ring}$. It is worth to mention that the electrical power is in DC condition. Moreover, overall thermal monitoring is required, because the ambient thermal environment variation can change the boundary conditions of the system, and affect the optical response of the entire circuit.

3.3.1.1 Stepped driven ring spectrometer

A single ring with TO tuning can work as an array of rings aligned to the grid. Depending on the geometrical specifications of the ring, it is possible to span the full FSR using a heater integrated with the ring [26]. The same ring can then sequentially interrogate the wavelengths of the grid. The driving conditions for the stepped microring resonator spectrometer are given by

$$P_n = \frac{P_\pi \cdot \Delta\lambda_{steps}}{FSR} = \frac{P_\pi}{N_{steps}} \tag{3.11}$$

where the operation range is equal to the FSR of the ring, and λ_{steps} and N_{steps} are respectively the wavelength resolution and sampling points. Since the sampling is performed in the time domain, the readout of the wavelength channels is performed sequentially. The stepping is calculated in power since the TO response is linear with the electrical (and thus thermal) power dissipated.

Fig. 3.11 shows the measurement of the drop output port of a single ring resonator, driven with ΔP such that the wavelength step is $\sim 1nm$. The heaters are placed both inside and outside of the ring as shown in Fig. 3.12(b). This particular ring has an FSR $\sim 10.0nm$. The accuracy, in this case, is related mainly to the thermo-optic linearity of the PIC. The overall PIC is kept at a stable temperature of 25 $^\circ C \pm 0.1$ using a temperature-controlled measurement stage. This temperature variation corresponds to $\sim 0.01nm$ assuming $d\lambda/dT = 0.1[nm/K]$. The dynamic range is limited by the crossing point n and $(n+1)$ steps of the ring, in this particular case it is $\sim 15dB$. Reducing the constraints of the dynamic range, higher accuracy can be achieved. Indeed using the boundary conditions of Eq. 3.8, the accuracy can be increased by one order of magnitude.

3.3.1.2 Continuous ring spectrometer

The active driving of the ring can also be done in a continuous way instead of the stepping approach: this improves the resolution and the speed of acquisition. Continuous driving can overcome some of the limitations of stepped driving: the stepped driving approach (in theory) requires calibration for each individual step. It also offers no information of the spectrum in the gap of two neighbor steps, unless a post-measurements data analysis is performed [27].

With continuous driving, this calibration step can be avoided; the tuning is needed only at the beginning of the scanning cycle. Continuous modulation increases the complexity of the electronics and data analysis. For low speed TO tuning, it is possible to work with relatively simple electronics and perform real-time analysis in software.

With continuous driving, we can use a direct correlation between the time domain readout and the wavelength. We know that the narrow line of the ring spans its FSR with a certain time domain relation, and by monitoring the output signal, cross-correlated with the driving signal, we can extract the optical power as a continuous function of wavelength.

In a first approximation, we can assume the response of the ring to be very narrow (at the limit a Dirac pulse). For simplicity, let us also use a constant scanning speed. If these two assumptions are valid, the system can be described by a

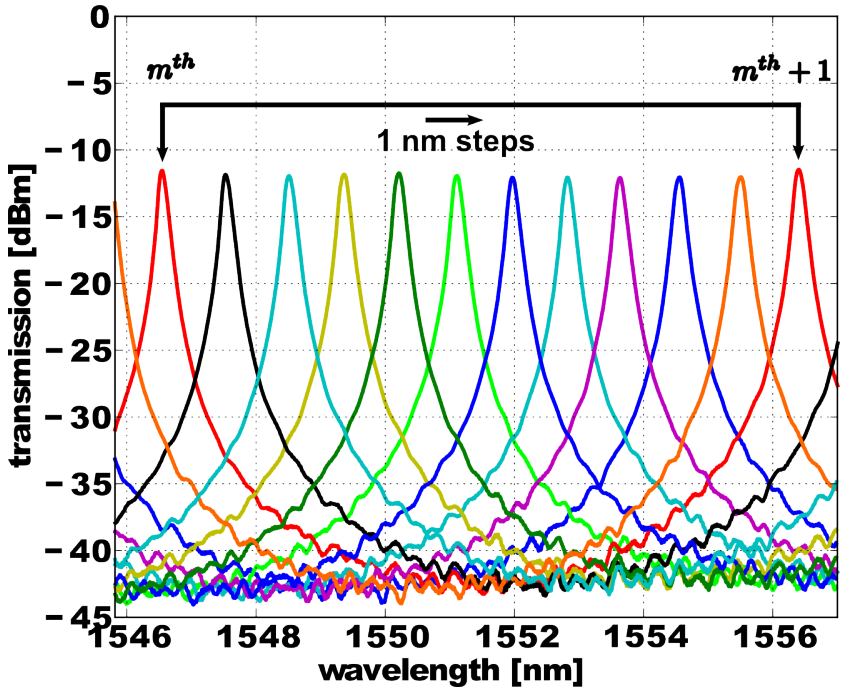

Figure 3.11: Spectrometer response based on a ring with doped side heaters. $\sim 1nm$ steps are provided for the wavelength interrogation

straightforward analytical model. The transmission of the system is the convolution of ring Lorentzian and the unknown spectrum, of course limited to a single FSR of the ring.

To obtain a constant scanning speed, we need to apply a linear signal in electrical power, as the wavelength shift is linear with temperature. However, electrical driving is performed either by applying a voltage or a current. We compensate for this mismatch by using the square root of the voltage carrier. In particular, a sawtooth-like and sinusoidal-like voltage carrier are used. The first offers linearity of time domain vs. wavelength under test. The second offers a sinusoidal relation between the spanned wavelength and the driving carrier.

$$I_{out}(t) = \int_{\lambda_n(t_0)}^{\lambda_{(n+1)}(t_0)} S_{in}(\lambda) L_{ring}(\lambda, t) d\lambda \tag{3.12}$$

Eq. 3.12 represent analytically the response of the system as described: $S_{in}(\lambda)$ is the unknown spectrum. The response of the ring is represented by $L_{ring}(\lambda(t)$: the peak position is a function of time, and, therefore, the output intensity has the same time-wavelength correlation. The extremes of the integration interval are

limited to the instants where the peak of the ring is at the edges of its FSR. These limits are respectively the n^{th} and the $(n^{th}+1)$ resonance orders. The integral limits are fixed by use of optical tunable passband filters.

The device used for the experimental demonstration is a strip waveguide ring with pass and drop ports and it is shown in Fig 3.12.

The thermo-optic shift is achieved with P-doped silicon heaters realized on the sides of the ring waveguide.

The chip is fabricated through ePIXfab MPW ISIPP25G+ service in IMEC, Belgium. The typical nominal resistivity of the used technology of 160 $\Omega/\square$. The FSR of the ring is $\sim 10nm$ and the circumference is $\sim 57um$. The optical coupling between the optical waveguide and electrical wire is negligible. This condition has been verified with Lumerical FDTD simulation, during the design phase of the device [28] and by measurements. The gap between the strip waveguide of the ring and the external and internal heaters are respectively 1.2 and 0.9 um while the width of the heaters is 2.2 um.

Fig. 3.12 shows the microscope image of a thermo-optic shifted ring. The tungsten vias have a nominal current limit of 0.7 mA each @ 100 $°C$. The number of vias is over-dimensioned to take into account possible overheating issue. Keeping in mind that the silicon is a thermal conductor, the area of the DCs is kept as far as possible from the heaters region, in order to reduce thermal coupling variation.

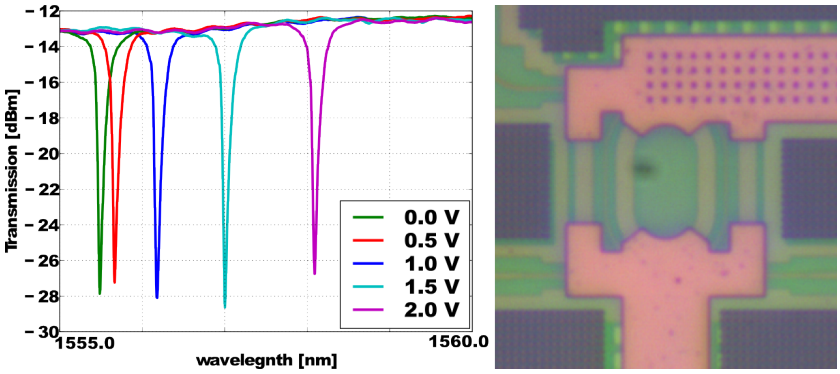

Figure 3.12: Thermo-optic test of ring modulator of different voltage bias. On the left a microscope image of the device.

The resonance peaks are centered around ∼1546 nm and ∼1556 nm for the n and $(n+1)$ orders. The position of the peaks is evaluated when no electrical power is applied, and the chip is kept at a constant temperature of 25 $°C$. We measure the resolution of the spectrometer using two tunable lasers: one of them constantly centered at 1550 nm, the other one is shifted with steps of $\Delta\lambda$ of $\pm$100 pm. The read-out is performed with an oscilloscope, monitoring both the driving and driven signals. The optical signal comes from the analog output of an optical powermeter,

set to have fixed dynamic range. By using two tunable lasers, we can calibrate the correspondence between the time scale and the wavelength. This test gives us an accurate characterization of the resolution of the device. Fig. 3.13 represents two wavelengths spaced of three different $\Delta\lambda_{res}$.

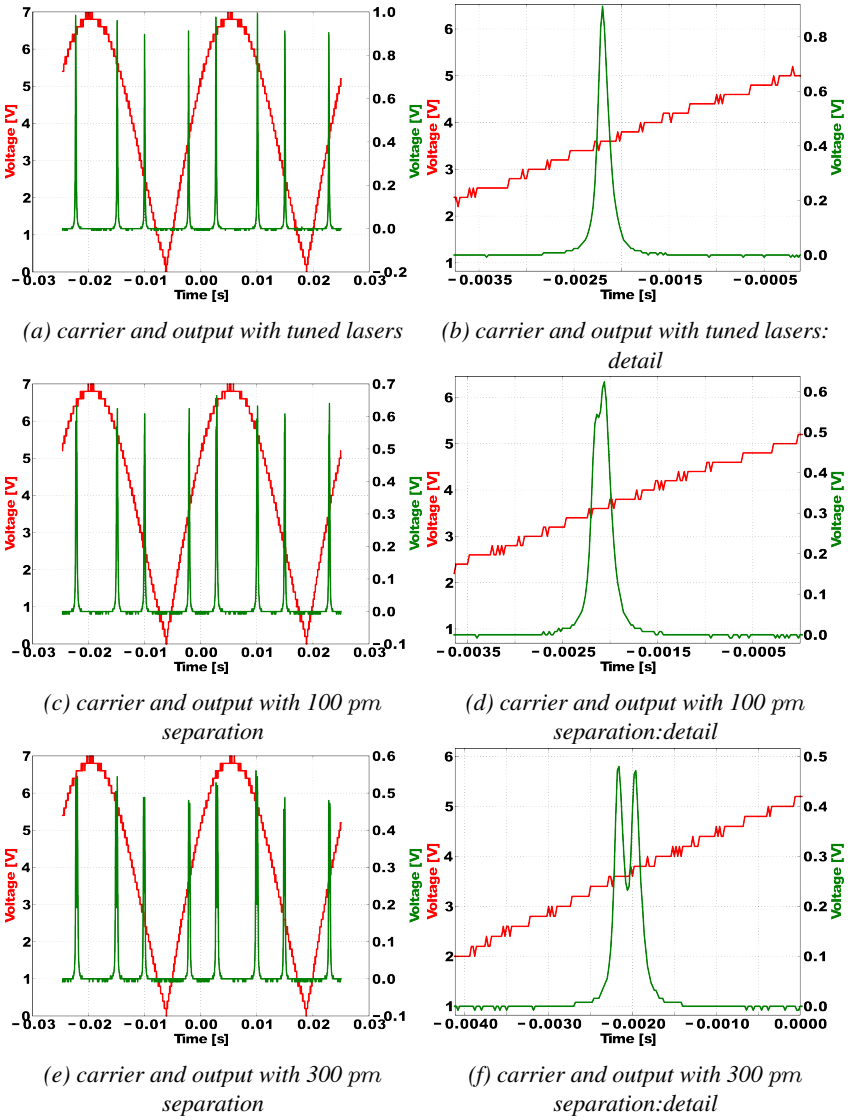

(a) carrier and output with tuned lasers

(b) carrier and output with tuned lasers: detail

(c) carrier and output with 100 pm separation

(d) carrier and output with 100 pm separation:detail

(e) carrier and output with 300 pm separation

(f) carrier and output with 300 pm separation:detail

Figure 3.13: The time response of the output of the ring (in green) and the carrier signal (in red): on the right there is the zoom-in at the position of the peaks. From the top: there are three case with tuned peak , 100 pm and 3000 pm apart

The plots represent the response of the ring in the time domain when the carrier signal is the square root of a sinusoidal carrier at a frequency of 10 Hz. The driving speed is low since thermal transient can limit the resolution of the device. The thermo-optic transient can mask the different wavelength contributions. If driven with signals faster than the thermal response, the circuit acts as a low pass filter, thus masking the fast variations. To avoid this effect, we choose the carrier at least ten times slower than 3τ of the heater response. The cut-off frequency of these structures is ~ 1 KHz.

The device is characterized with the setup shown in Par. A.3: an arbitrary signal generator is combined with an oscilloscope. The time domain trace is recorded by the oscilloscope.

Fig. 3.13(a),(c) and (e) show the case of two lines with different separation between them. Two periods of the carrier signal used for the electrical driving are plotted. Fig. 3.13(b),(d) and (f) show a close-up of the peaks position in the time domain. Fig. 3.13(a) and (b) show the electrical carrier signal (in red) and the electrical output (in green) when the two lasers linewidth have no gap, thus, both of them at 1550 nm. Fig. 3.13(c) and (d) show the case of 100 pm of separation between the two wavelengths of the lasers; the peak separation is visible but is not sufficient to distinguish between the two lines. Fig. 3.13(e) and (f) show the case of 300 pm of separation between the two wavelengths of the lasers; in this case there are 3 dB of extinction. Hence, we can conclude that the resolution of this spectrometer is 300 pm, with an FSR of $\sim$ 10 nm. The last characterization we perform with the ring scanning spectrometer is the recovery of a random spectrum obtained with a broadband source (an SLED) and a tunable optical filter capable of generating random spectrum. In this particular case we generate a triangular passband transmission with a dip and a peak on the rising and fall side, both the bandwidth of dip and peak is on 1 nm. Fig. '3.14 shows the comparison of the input spectrum recovery in linear scale. The green curve is obtained with a commercial optical spectrum analyzer, while the blue spectrum is obtained with the scanning ring spectrometer.

3.3.1.3 Ring spectrometers conclusions

The thermo-optic effect is used to modulate the output signal of a ring resonator spectrometer. The heaters are realized on both sides of the optical waveguide with high doped silicon. We test two different driving strategies have. The stepped driving creates a discrete correlation between the n^{th} step and the λ_n interrogated. The resolution of 1 nm is experimentally demonstrated, but better performances can be achievable using the stepped driving. The continuous driving creates a correlation between the time domain the interrogated spectrum. A more appealing driving procedure has been tested: continuous time domain driving a resolution of 300 pm has been measured across the full FSR.

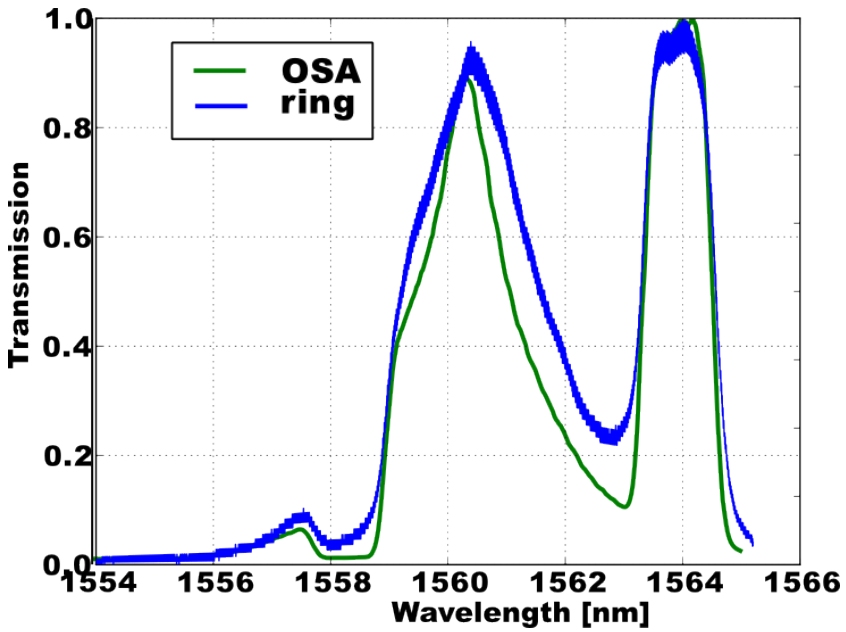

Figure 3.14: Random spectrum reconstruction: comparison of a commercial OSA and of the ring scanning spectrometer

The main limitation that affects such approach is the limited operative range achievable. The FSR is inversely proportional to the round trip length of the ring. Thus, the minimum length of the ring is limited by the reasonable bending radius of a strip waveguide without having too many optical losses [29]. For instance assuming 5 um bending radius as an acceptable design for a strip waveguide, the FSR of the ring is in about 18 nm. Moreover, such a small ring does not suit the thermo-optic requirements for the full FSR coverage. Assuming the same thermo-optic efficiency, the same P_π is required for an FSR shift. Thus for a smaller ring and same P_π, higher thermal power density is required: thus a local higher ΔT is reached. This requirement compromises the integrity of the heaters. The design under test with 7 um bending radius and a total straight section of ~ 15 um proved to be thermally stable and to achieve more than one FSR shift.

3.3.2 MZI based wavelength meter

An asymmetric MZM (Mach-Zehnder modulator) is used to measure an unknown input wavelength. This is achieved by monitoring the electrical phase delay of the optical output while modulating one MZI arm. An MZI in a stand-alone configuration does not provide sufficient information on the wavelength content. This is due to the slow sinusoidal-like transmission spectrum (cf. Ch. 2). The output of

the device is assumed to be the integral of the sinus-like transmission and the input spectrum. This hypothesis is valid considering that the optical output is connected to a photodiode. The PD does not provide any information about the wavelength content of the collected light; it just converts incident photons into electrical current. However, we can translate the wavelength content of the input by actively driving the modulator with a time-dependent signal. A simple asymmetric MZI with phase shifters on both arms combined with a sinusoidal driving voltage is used to extract the input optical wavelength with high accuracy across the whole FSR of the MZI. The information about the input wavelength is contained in the electrical phase delay between the driving and the driven electrical signal.

3.3.2.1 MZI based wavelength meter

The sinusoidal transmission response of a passive asymmetric MZI can already give information of a single input wavelength. This can be done only under stringent requirements. There is a unique relation between input wavelength and the output intensity if the input wavelength is limited to half of the FSR of the MZI transmission spectrum. For this assumption to be valid, the input optical power needs to be known and constant in time and over the wavelengths. The operating wavelength range is limited to half of the FSR (cf. Ch. 2 Eq. 2.17) since the transmission characteristic is injective [30] in this interval. The accuracy of such measurement is also limited by the response stability of the filter, the constant power of the input and the accuracy of the readout of the photocurrent. Moreover, since the sensitivity is defined by Eq. 3.13 the accuracy of the measurement depends on the particular region of the spectrum. The derivative operation in Eq. 3.13 is allowed since we are working not with the theoretical response, but with the actual measured curve corresponding to the transmission of the filter.

$$S = \frac{d \int_{\lambda_{min}}^{\lambda_{max}} I_{out} d\lambda}{d\lambda} \tag{3.13}$$

The sensitivity is proportional to the derivative of the sensor output to the wavelength. The output spectrum I_{out} is assumed to be the integral of the source spectrum and the transmission associated to the MZI. In the case of a single wavelength, the integral degenerates to the transmission sampled at the input wavelength λ_{in}. As this is a sinusoidal curve, the derivative becomes zero close to the minimum and maximum, and near those points, it becomes difficult to extract the exact wavelength.

We overcome the problems of absolute power references and wavelength-dependent sensitivity by modulating the MZI using phase shifters on the arms. In this case, the phase shifters use reverse-biased PN-junction modulators, but they could also be implemented with heaters. We drive only one arm at a time, but both arms

have a modulator to balance the losses, which increases the extinction ratio and, therefore, the sensitivity of the measurement [31].

3.3.2.2 Working principle

The phase-shift principle is applied to the MZM to detect wavelengths. Phase-shift techniques are widely used for communication and metrology [32]. The same concept is adapted on the active asymmetric MZI. The transmission T_λ of a passive MZI is given by Eq. 3.14, where the phase term takes into account the resonance order o the filter.

$$T(\lambda) = \sin(\frac{\pi \Delta L}{\lambda} n_{eff}(\lambda) + 2\pi(m - \frac{n_{eff} \mid_{\lambda_0} \Delta L}{\lambda_0}))^2 \tag{3.14}$$

The period of the wavelength transmission (FSR) is proportional to the group index n_g while the phase depends on the resonance order and the n_{eff}. This means that the FSR of a filter depends on group index and other derivatives of this quantities. The position of the individual interferences depends on the effective index at that particular wavelength and the resonance order.

Each single input wavelength is considered as a tone. The optical output is coupled to a germanium photodiode: thus the optical signal is converted into an electrical one. The transmission of an MZI when the input is a pure tone is given by Eq. 3.15.

$$T_{\lambda_{in}} = \frac{1}{2} + \frac{1}{2}\sin(2\pi n_{eff}(\lambda_{in}, t)\frac{\Delta L}{\lambda_{in}}) \tag{3.15}$$

Basically, with a single wavelength input, the spectrum is sampled at a particular position. Eq. 3.15 proposes the response of the PIC under a new prospect: the output ceases to depend on the wavelength and now depends on the variable time t. This is because the phase shifters on the arms introduce a relation between the n_{eff}, and thus the peak position, and the time, and thus to the driving signal. The value of n_{eff} fixes the MZI transmission at a particular position of the spectrum. The range limitation of the device is the FSR of the passive filter Outside this range, due to the periodical transmission of the device, aliasing arises and thus, there is no longer a unique solution for the Eq. 3.15.

When we modulate the phase shifter, the spectral transmission response of the MZI shifts in wavelength. The n_{eff}, and thus the phase delay, depends linearly on the reverse bias applied (in first approximation). This assumption can easily be extended to non-linear relations. A schematic example of the working principle is given in Fig. 3.15, where the blue curve represents the passive response of the MZ. The transmission spectrum is shifted over time according to the green curve. The red arrow represents the unknown and constant input wavelength. The intrinsic limitation of the working range imposed by the FSR of the asymmetric MZI can

be visualized considering the case of the input peak either in the n^{th} or $(n^{th}+1)$ resonance order of the MZI response. Under this condition, the response will be identical.

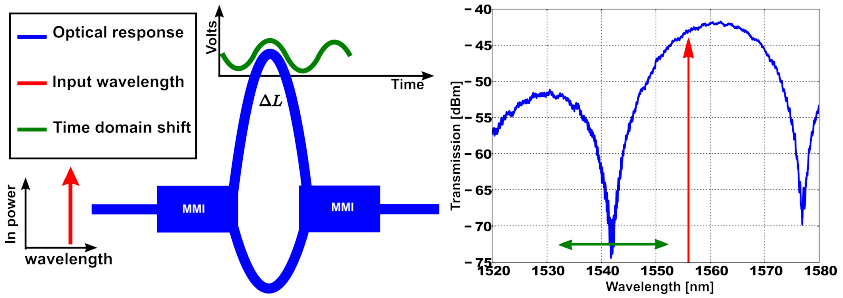

Figure 3.15: Schematic representation of the MZM wavelength meter: on the left there is the schematic of the device, optical and electrical driving respectively in wavelength and time domain, while on the right its wavelength response correlation.

3.3.2.3 Description of the PIC

The PIC is an asymmetric MZI modulator with carrier depletion phase shifters. The $3dB$ splitting and combining operation are performed with MMIs. The choice of the MMI over other splitting/combining devices is made for the bandwidth and fabrication tolerances (cf. Ch. 2). On the other hand, MMIs are both optically and electrically connected since silicon connects both the arms of the MZI. When the phase shifter of the arm is reverse biased, the reverse potential also affects the other arm, applying potential to one side of the PN junction, while its second contact is floating. This unwanted polarization is overcome by grounding to the electrodes of the unused phase shifter. This is possible since we only use one phase shifter at a time. The optical outputs of the MZI are connected to two germanium photodiodes, which perform the optoelectrical conversion for the read-out. The germanium photodiodes are symmetric devices, and they include two optical ports. One is used for the MZI output; the other ports is connected to an auxiliary grating coupler. The benefit of using auxiliary grating couplers is multiple. First they can be used as residual power output since the light not absorbed by the photodiode is forwarded to the grating couplers. Secondly, the output waveguide reduces the abrupt index change due to the discontinuity at the edge of the germanium device. Finally, the auxiliary grating coupler connected to the photodiode can be used for the characterization of the photodiode itself. Fig. 3.16 represents the microscope image of the device: in the green box a detail of the folded MZM is shown, while the red box is the microscope feature of the germanium photodiode. The blue box is the equivalent schematic of the circuit.

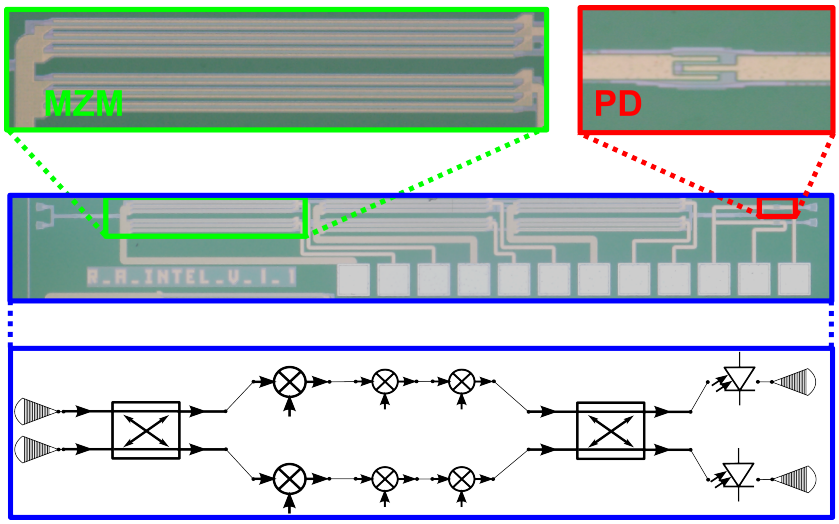

Figure 3.16: Microscope image and schematic of the spectrometer: the images in the blue square are respectively the microscope image and the relative schematic, the detail in the green square is the main folded modulation stage, while the detail in the red square is the Germanium photodiode.

3.3.2.4 Carrier depletion phase shifter

The phase shifters in both arms have a folded design, to reduce the footprint of the phase shifter. The full 1.5 mm length is divided into three sections of 0.5 mm, and each straight waveguide embeds an interdigitated PN junction. Electrically there are three PN junctions in parallel, biased with the same voltage, using an interdigitated metal line architecture. Optically speaking the three sections of the phase shifter are in series on the same optical path. Fig. 3.17(b) shows the phase shifter architecture qualitatively.

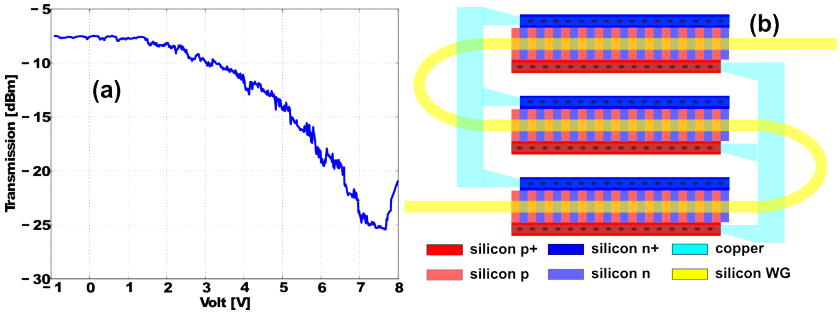

Figure 3.17: (a) Voltage light characteristic of a MZI in symmetric configuration, (b) schematic representation of the phase shifter present on each arm

To perform a measurement of the wavelength, we used low-speed driving equipment, and thus the performance of the MZM is significantly faster than our requirements. The circuit is driven by a carrier in the order of kHz and thus, at least, three orders of magnitude below the usual operation frequencies of the MZM. In series with the 1.5 mm, an extra mm of phase shifter is provided; in case a larger phase shift is required.

The performance metrics of the phase shifter are $V_\pi L_\pi$ and the IL. The efficiency $V_\pi L_\pi$ is extracted with a reverse bias sweep on a test MZI modulator, and is $\sim 1.05V \cdot cm$. The insertion loss of the actual modulator is difficult to estimate since the PIC always include the photodiode, and thus, one can only estimate the cumulative insertion loss of the cascaded elements: however the expected loss is $\sim 25\ dB/cm$ [23].

3.3.2.5 Germanium Photodetectors

Germanium photodetectors are monolithically integrated into our PIC [33]. The devices are based on a lateral p-i-n structure with "inverted rib" cross-section. The parameters of interest, in this case, are the responsivity R and the dark current I_{dark}. We used these specifications of the photodiodes for the design of the TIA, which we actually designed before the characterization of the optical circuit. We used the nominal value provided by the fab for the design of the amplifiers. We can also tune the gain of the TIAs, to avoid saturation or below-threshold conditions. The TIAs are interposed between the PD and the multichannel voltage reading.

3.3.2.6 Characterization of the device

The outcome of the characterization is a relation between the input wavelength and the measured wavelength. The setup used to characterize the PIC includes different configurations to accommodate the requirements of each of the characterization steps. The PIC is always kept at a constant temperature of $25°C$ with a Peltier element. The temperature stabilization is required since every thermal variation of temperature produces an unwanted shift in the MZI characterization. The direct consequence of this is a systematic offset in the device response. The first measurement is a passive characterization of the MZI. For this purpose, a tunable laser and a power meter are used for transmission measurement. The tunable laser triggers the data acquisition either from the powermeter or the voltage acquisition card. The two options for the acquisition depend on the reading out device: the auxiliary grating coupler or the photodiode. In case the auxiliary grating coupler is used, the measured transmission (not absorbed by the photodiode) is $40dB$. This measurement is used to extract the FSR of the device and the position of constructive and destructive interference. They correspond respectively to peaks and dips of the transmission.

After the passive characterization of the asymmetric MZI, a different measurement setup is used to evaluate the performance of the wavelength meter. The measurement setup used for this purpose includes an external tunable laser, a signal generator, and multiple channel oscilloscope. The tunable laser is used to emulate the unknown input wavelength. The CW signal is fed to the photonic integrated circuit input through the input grating coupler. The optical output power is monitored with the germanium photodiode responsible for the optoelectric conversion. Electrical probes are used to drive the modulators present on the arm of the MZI modulator, and to fix the potential to ground of the components not in used. A carrier frequency of 1.0 KHz is chosen and used for the phase shifter driving. The carrier is generated with an analog arbitrary signal generator. The experiment is iterated over the wavelength domain of interest. Fig. 3.18 represents on the right axis the driving signal, while on the left axis are represented both the electrical output signal and the relative fitting. The fitting is performed using a model for the ideal response of an asymmetric MZI modulator as target function and a non-linear least square algorithm as a fitting algorithm. The device is characterized with the setup shown in Par. A.7.

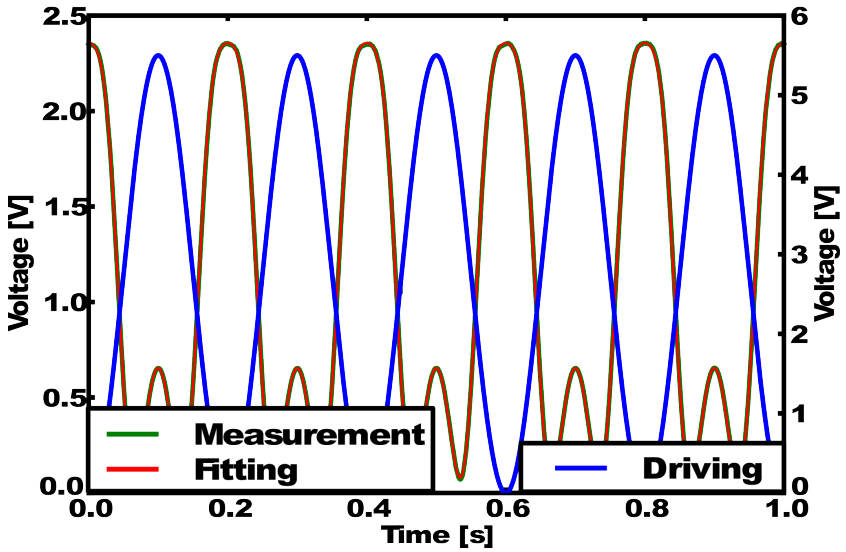

Figure 3.18: Time domain driving, measurement and fitting when the input is the laser line tuned at 1540 nm

3.3.2.7 Wavelength detection

The experimental characterization of our device is performed with a sinusoidal carrier signal. This choice is made considering the response of the MZI modulator

and the reading out perspective. The MZI modulator is carrier depletion based, thus in a first approximation the phase to voltage response can be assumed to be linear. The unknown input wavelength is represented by the optical source: in this case a continuous wave tunable laser. The characterization is performed from dip to dip. If the complementary output is used for the measurement(as the MMI is a 2×2 coupler), the characterization takes place from peak to peak, as there is a phase relation of π between the two outputs of the device. The fitting procedure is performed off-line after the full characterization. The least square optimization fitting algorithm is used to extract the phase of the electrical output signal. The target function for the fitting is

$$V(t) = V_{dc} + V_{ac}\sin(\sin(\omega t) + \Delta\phi) \tag{3.16}$$

and it is obtained from Eq. 3.15 when the carrier is sinusoidal. This fitting procedure, combined with the straightforward analytical model of the output signal, gives reliable fitting as represented in 3.18. The phase information $\delta\phi$ is then correlated with the input wavelength according to the 3.17. This expression is the theoretical relation between the electrical phase and the input wavelength. We can now determine an unknown wavelength by extracting the electronic phase delay ϕ from a time signal. The full FSR corresponds to π while the ϕ is linearly correlated to the in λ_{in}. A noticeable example is the case of $\phi_0 = 0$ which corresponds to λ_{in} equal to the wavelength of the dip of the MZI response. The proper wavelength recovery requires the peak transmission of the passive MZI to be known: any uncertainty in this quantity is transferred to wavelength recovery as an offset.

Iterating the fitting procedure for all the wavelength of interest, we obtain the characteristic response of the wavelength meter. It consists of measured electrical phase delay in function of the input wavelength. Fig. 3.19 represents the phase response. The ideal phase delay is represented in green while the measured is represented in blue. The x-axe represents the input wavelength generated by the CW laser. It is worth to mention that the solutions satisfying the analytical fitting formula are not univocal, and thus boundaries to the allowed solution are required. Referring to the Eq. 3.16 the amplitude of the argument sine has to be strictly positive or negative, this to avoid the redundant solution of the fitting procedure.

Normalizing the characteristic with the ideal response, we calculate the local accuracy. The local error is represented in Fig. 3.20 with the green dots. The result of the wavelength recovery shows a systematic error due to the non-linearity of the MZI response. This error reaches the maximum at the phase changing points. Namely where the MZI has the constructive and destructive interferences peaks and dips. The non-ideality under analysis is systematic, and thus it is possible to compensate it. Different approaches are possible to contain this systematic error. One solution is to use a more accurate model for the fitting. However, this can lead to a less robust convergence of the fitting. Another solution is to adopt a more

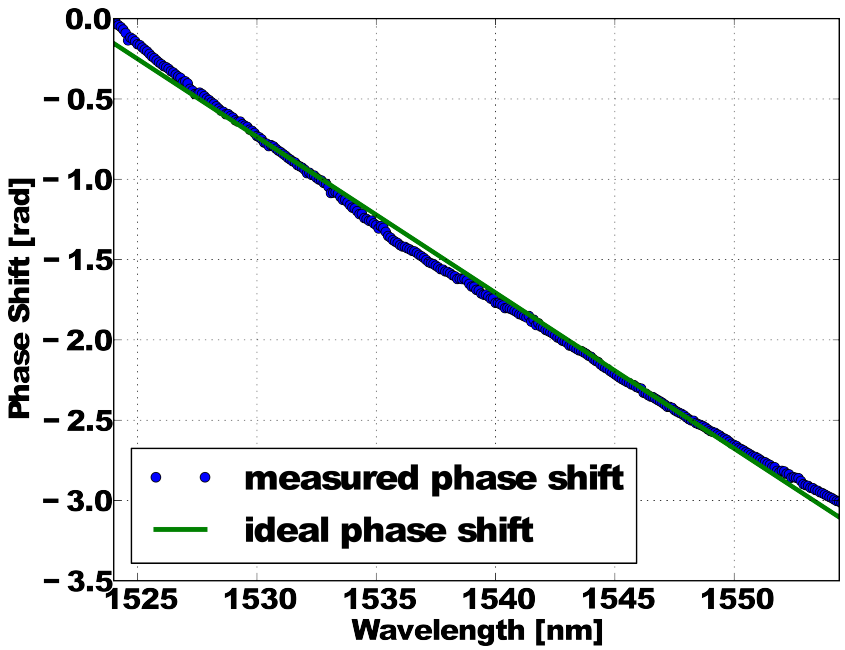

Figure 3.19: The plot represents the correlation that persists between the input wavelength and the extracted phase argument of Eq. 3.16

accurate driving carrier instead of the simple sinusoid, but this adds significant the complexity to the driving procedure. Instead, a Fourier-based normalization technique is used. As Fig. 3.19 shows the measured wavelength (blue dots), and the ideal curve (green line). Fig. 3.20 shows the difference between the measured and input wavelength. Fig. 3.20 (green dots) underlines the behavior of the accuracy error: it has a periodic triangular shape, larger at the resonance points. Since this curve is injective, it is possible to calibrate for it. We developed in Fourier terms the difference between the ideal and measured wavelength. Subsequently, we used this curve to normalize the response of the device. The result of such procedure is an accuracy response cleaned by strong systematic errors. The final result is shown in Fig. 3.20 (red dots). The measurement noise is still present.

It requires a one-time calibration (as the nonidealities are intrinsic to the circuit) and it is easy to apply this calibration to the measurements. The result of this normalization is represented by Fig. 3.20 with the red dots: the wavelength recovery error is substantially reduced, and the remaining error is due to fitting and measurement.

$$\Delta\phi = \frac{(\lambda_{res} - \lambda_{in})}{FSR} \tag{3.17}$$

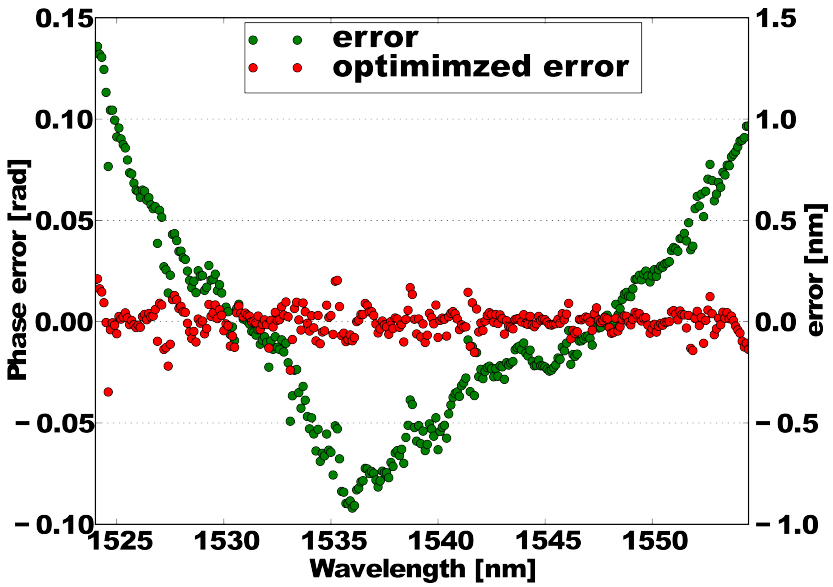

Figure 3.20: The accuracy relative to Fig. 3.19. The left axis represents the accuracy on the phase measurement , while the right axis represents the conversion of the phase accuracy in wavelength accuracy. The green and red dots are respectively the raw extraction and the calibrated results

3.3.2.8 MIZ wavelength meter: conclusions

An elegant way to use an asymmetric MZI modulator as a wavelength meter has been proposed, overcoming the intrinsic limitation of the same device in passive approach. The method is suitable for high-speed monitoring and low power consumption thanks to the high-speed depletion base modulator and the photodiode. The proposed approach shows a worst case and an average accuracy of 1.3 and 0.4 nm over the FSR that in this case is $\sim 30nm$, the maximum of the error are systematically situated at the constructive and destructive interference regions. With a simple calibration technique the worst case and average error is reduced to ~ 200 and ~ 64 pm. Future implementations can include homodyne detection and lock-in amplification. These electrical measurement techniques are very well suited for sinusoidal carriers and allow the use of relatively simple read-out electronics.

3.3.3 Conclusions

In this chapter active tuning and modulation techniques have been applied to optical filters to enhance their performance for wavelength interrogation purpose.

We introduced the modulation strategies and their working principles, together with some relevant examples. Using modulation and tuning techniques for rings,

we were able to simplify the structure of a ring based spectrometers significantly; one single thermo-optic tunable ring acted as an array of rings. Moreover, fabrication related misalignment where not anymore an issue since the ring was tuned dynamically. This device showed a resolution of 300 pm on an FSR of $\sim$ 10 nm.

Active modulation techniques have also been applied to an MZI asymmetric modulator based on carrier depletion effect. By itself, this device is not sufficient to interrogate its input spectrum, but we developed a phase shift technique to used this device as an accurate wavelength meter. We achieved that by monitoring an electrical phase delay between the driving and the output signal. We measured an average accuracy of 64 pm on the FSR of $\sim$ 30 nm measured for the passive device.

References

[1] S.K. Selvaraja, W. Bogaerts, P. Dumon, D. Van Thourhout, and R. Baets. *Subnanometer Linewidth Uniformity in Silicon Nanophotonic Waveguide Devices Using CMOS Fabrication Technology*. Selected Topics in Quantum Electronics, IEEE Journal of, 16(1):316–324, Jan 2010.

[2] Shankar Kumar Selvaraja, Peter De Heyn, Gustaf Winroth, Patrick Ong, Guy Lepage, Celine Cailler, Arnaud Rigny, Konstantin Bourdelle, Wim Bogaerts@ugent.be, Dries VanThourhout, Joris Van Campenhout, and Philippe Absil. *Highly uniform and low-loss passive silicon photonics devices using a 300mm CMOS platform*. In Optical Fiber Communication Conference, page Th2A.33. Optical Society of America, 2014.

[3] Sarvagya Dwivedi, Alfonso Ruocco, Michael Vanslembrouck, Thijs Spuesens, Peter Bienstman, Pieter Dumon, Thomas Van Vaerenbergh, and Wim Bogaerts. *Experimental Extraction of Effective Refractive Index and Thermo-Optic Coefficients of Silicon-on-Insulator Waveguides Using Interferometers*. J. Lightwave Technol., 33(21):4471–4477, Nov 2015.

[4] Sofie Lambert, Wout De Cort, Jeroen Beeckman, Kristiaan Neyts, and Roel Baets. *Trimming of silicon-on-insulator ring resonators with a polymerizable liquid crystal cladding*. Opt. Lett., 37(9):1475–1477, May 2012.

[5] J. Schrauwen, D. Van Thourhout, and R. Baets. *Trimming of silicon ring resonator by electron beam induced compaction and strain*. Opt. Express, 16(6):3738–3743, Mar 2008.

[6] Takayuki Mizuno, Yasuaki Hashizume, Takashi Yamada, Shinya Tamaki, Hirotaka Nakamura, Shunji Kimura, Mikitaka Itoh, and Hiroshi Takahashi. *Integrated 1.3/1.5 μm cyclic AWG router for λ-tunable WDM/TDM-PON*. Opt. Express, 20(26):B1–B6, Dec 2012.

[7] P. De Heyn, J. De Coster, P. Verheyen, G. Lepage, M. Pantouvaki, P. Absil, W. Bogaerts, J. Van Campenhout, and D. Van Thourhout. *Fabrication-Tolerant Four-Channel Wavelength-Division-Multiplexing Filter Based on Collectively Tuned Si Microrings*. Lightwave Technology, Journal of, 31(16):2785–2792, Aug 2013.

[8] S. Pathak, P. Dumon, D. Van Thourhout, and W. Bogaerts. *Comparison of AWGs and Echelle Gratings for Wavelength Division Multiplexing on Silicon-on-Insulator*. Photonics Journal, IEEE, 6(5):1–9, Oct 2014.

[9] S. Dwivedi, H. D'heer, and W. Bogaerts. *A Compact All-Silicon Temperature Insensitive Filter for WDM and Bio-Sensing Applications*. Photonics Technology Letters, IEEE, 25(22):2167–2170, Nov 2013.

[10] C.S.R. Murthy and M. Gurusamy. *WDM Optical Networks: Concepts, Design, and Algorithms*. Prentice Hall PTR, 2002.

[11] Ananth Z. Subramanian, Eva Ryckeboer, Ashim Dhakal, Frédéric Peyskens, Aditya Malik, Bart Kuyken, Haolan Zhao, Shibnath Pathak, Alfonso Ruocco, Andreas De Groote, Pieter Wuytens, Daan Martens, Francois Leo, Weiqiang Xie, Utsav Deepak Dave, Muhammad Muneeb, Pol Van Dorpe, Joris Van Campenhout, Wim Bogaerts, Peter Bienstman, Nicolas Le Thomas, Dries Van Thourhout, Zeger Hens, Gunther Roelkens, and Roel Baets. *Silicon and silicon nitride photonic circuits for spectroscopic sensing on-a-chip*. Photon. Res., 3(5):B47–B59, Oct 2015.

[12] Jose Capmany and Dalma Novak. *Microwave photonics combines two worlds*. Nat Photon, 1(6):319–330, Jun 2007.

[13] Richard A. Soref and B.R. Bennett. *Electrooptical effects in silicon*. Quantum Electronics, IEEE Journal of, 23(1):123–129, Jan 1987.

[14] Y. Kokubun, S. Yoneda, and S. Matsuura. *Temperature-independent optical filter at 1.55 mu;m wavelength using a silica-based athermal waveguide*. Electronics Letters, 34(4):367–369, Feb 1998.

[15] Jie Teng, Pieter Dumon, Wim Bogaerts, Hongbo Zhang, Xigao Jian, Xiuyou Han, Mingshan Zhao, Geert Morthier, and Roel Baets. *Athermal Silicon-on-insulator ring resonators by overlaying a polymer cladding on narrowed waveguides*. Opt. Express, 17(17):14627–14633, Aug 2009.

[16] A. Masood, M. Pantouvaki, G. Lepage, P. Verheyen, J. Van Campenhout, P. Absil, D. Van Thourhout, and W. Bogaerts. *Comparison of heater architectures for thermal control of silicon photonic circuits*. In Group IV Photonics (GFP), 2013 IEEE 10th International Conference on, pages 83–84, Aug 2013.

[17] Vittorio M. N. Passaro, Francesca Magno, and Andrei V. Tsarev. *Investigation of thermo-optic effect and multi-reflector tunable filter/multiplexer in SOI waveguides*. Opt. Express, 13(9):3429–3437, May 2005.

[18] F. Gan, T. Barwicz, M.A. Popovic, M.S. Dahlem, C.W. Holzwarth, P.T. Rakich, H.I. Smith, E.P. Ippen, and F.X. Kartner. *Maximizing the Thermo-Optic Tuning Range of Silicon Photonic Structures*. In Photonics in Switching, 2007, pages 67–68, Aug 2007.

[19] K. Okamoto. *Fundamentals of Optical Waveguides*. Electronics & Electrical. Elsevier, 2006.

[20] A. Boukabache and P. Pons. *Doping effects on thermal behaviour of silicon resistor*. Electronics Letters, 38(7):342–343, Mar 2002.

[21] S.M. Sze and K.K. Ng. *Physics of Semiconductor Devices*. Wiley, 2006.

[22] Hui Yu, W. Bogaerts, and A. De Keersgieter. *Optimization of Ion Implantation Condition for Depletion-Type Silicon Optical Modulators*. Quantum Electronics, IEEE Journal of, 46(12):1763–1768, Dec 2010.

[23] Hui Yu, Marianna Pantouvaki, Joris Van Campenhout, Dietmar Korn, Katarzyna Komorowska, Pieter Dumon, Yanlu Li, Peter Verheyen, Philippe Absil, Luca Alloatti, David Hillerkuss, Juerg Leuthold, Roel Baets, and Wim Bogaerts. *Performance tradeoff between lateral and interdigitated doping patterns for high speed carrier-depletion based silicon modulators*. Opt. Express, 20(12):12926–12938, Jun 2012.

[24] M. Pantouvaki, Hui Yu, M. Rakowski, P. Christie, P. Verheyen, G. Lepage, N. Van Hoovels, P. Absil, and J. Van Campenhout. *Comparison of Silicon Ring Modulators With Interdigitated and Lateral p-n Junctions*. Selected Topics in Quantum Electronics, IEEE Journal of, 19(2):7900308–7900308, March 2013.

[25] W. Bogaerts, P. De Heyn, T. Van Vaerenbergh, K. De Vos, S. Kumar Selvaraja, T. Claes, P. Dumon, P. Bienstman, D. Van Thourhout, and R. Baets. *Silicon microring resonators*. Laser Photon. Rev., 6(1):47–73, 2012.

[26] F. Gan, T. Barwicz, M.A. Popovic, M.S. Dahlem, C.W. Holzwarth, P.T. Rakich, H.I. Smith, E.P. Ippen, and F.X. Kartner. *Maximizing the Thermo-Optic Tuning Range of Silicon Photonic Structures*. In Photonics in Switching, 2007, pages 67–68, Aug 2007.

[27] Y. Sano and T. Yoshino. *Fast optical wavelength interrogator employing arrayed waveguide grating for distributed fiber Bragg grating sensors*. Lightwave Technology, Journal of, 21(1):132–139, Jan 2003.

[28] Inc. Lumerical Solutions. http://www.lumerical.com/tcad-products/fdtd/.

[29] Wim Bogaerts, Pieter Dumon, Patrick Jaenen, Johan Wouters, Stephan Beckx, Vincent Wiaux, Dries Van Thourhout, Dirk Taillaert, Bert Luyssaert, and Roel Baets. *Silicon-on-insulator nanophotonics*, 2005.

[30] R.G. Bartle. *The Elements of Real Analysis*. A Wiley Arabook. John Wiley & Sons, Incorporated, 1982.

[31] Po Dong, Long Chen, and Young kai Chen. *High-speed low-voltage single-drive push-pull silicon Mach-Zehnder modulators*. Opt. Express, 20(6):6163–6169, Mar 2012.

[32] B. Costa, D. Mazzoni, Mario Puleo, and Emilio Vezzoni. *Phase shift technique for the measurement of chromatic dispersion in optical fibers using LED's*. Quantum Electronics, IEEE Journal of, 18(10):1509–1515, Oct 1982.

[33] Hong Tao Chen, Peter Verheyen, Peter De Heyn, Guy Lepage, Jeroen De Coster, Philippe Absil, Gunther Roelkens, and Joris Van Campenhout. *High-Responsivity Low-Voltage 28-Gb/s Ge p-i-n Photodetector With Silicon Contacts*. J. Lightwave Technol., 33(4):820–824, Feb 2015.

4

Spectrometers based on actively modulated cascaded filters

In this chapter, we combine different kinds of spectral filters to overcome their individual limitations and enhance their performance when used as spectrometers. We propose architectures based on ring resonators and AWGs. Each of the optical filters introduced in Ch. 2 and Ch. 3 has its technical strengths and weaknesses. Relying on more complex architectures, we target to make the most use of the strengths and mitigate the weaknesses of the stand-alone optical filters. For example, rings have a high resolution properties thanks to the small FWHM achievable on SOI [1], and AWGs are suitable to use in a large wavelength range [2]. The work in this chapter focuses on these two devices and several architectures for different applications are explored.

The first proposed approach includes an array of AWGs, each of which is optically fed by the drop port of a microring resonator. This work is part of the European FP7 project SmartFiber [3] and it has been carried out in collaboration with Dr. Andrea Trita. The purpose of this project was to realize an integrated interrogator for FBG sensors [4]. The ring pre-filters the comb-like linewidths. The optical specifications of the rings and the AWGs are chosen in such way that the operation range of the spectrometer is equal to the FSR of the AWGs. The channel resolution is equal to the product of the number of AWG output channels and the number of rings/AWGs. The physical resolution is limited by the FWHM of the ring. Each resonance of the ring is fed to an individual AWG channel. The peak position of the rings is designed such that none of the rings have the same peak

position, but they are spaced by $\Delta\lambda_{res}$, thus, the resolution as shown in Fig. 4.1(a).

The second approach can be considered as both an advancement and a simplification of the previous approach. We cascade an AWG to a single ring resonator. Each resonance order of the ring falls into one channel of the AWG. The ring is used to select dynamically one wavelength in the range contained in a single AWG channel. First we demonstrate the device as a readout circuit for a ring-based sensor. We define the ratio of the ring FSR and the AWG channel spacing according to a Vernier scaling. The design approach overcomes the limitations imposed by the minimum measurable $\Delta\lambda$ valid for a single ring sensor. The gain factor induced by the resonance shift of the ring is proportional to the number of AWG output channels. This project has been carried out within a master thesis program in collaboration with Mr. José Juan Colás.

The same concept of cascading a single ring and an AWG is also experimentally demonstrated as a scanning spectrometer. The FSR of the spectrometer also, in this case, coincides with the FSR of the AWG. The resolution is limited by the transmission characteristic of the ring. Each resonance order of the ring is addressed to an AWG channel. The ring filters individual wavelengths and the AWG filters the resonance orders of the ring. The ring can be thermally tuned. The driving schemes adopted are both stepped and continuous, as already proposed of the single ring spectrometer of Ch. 3 as shown in Fig. 4.1(b).

4.1 Combining AWGs and rings

Rings and AWGs are individually powerful wavelength interrogation devices, but with limitations. In this chapter, we combine these two kind of filters, to realized large FSR and high-resolution spectrometers. Rings are extremely suitable devices for spectrometers. Indeed, a single ring resonator can provide a very small FWHM, and thus a high resolution. Thanks to the cross-talk properties of such a device, also the noise from other wavelength contributions is well suppressed with suppression ratio in the order of at least 20 dB [5]. On the other hand, one of the limiting factors of microring resonators is their relatively small FSR. Indeed, considering a strip waveguide and a bending radius of 5 um, the corresponding FSR is still at most $\lambda_0^2/n_g 2\pi r = 15nm$.

Another issue arises when thermo-optic tuning is required. Driving the same P_π for an FSR shift of a smaller ring leads to a larger required ΔT [6]. For small rings, this effect can lead to physical damage to the heater that is not able to sustain anymore the thermal power density needed.

AWGs, on the other hand, offer large FSR capability depending on other design parameters, with FSRs of 50 nm or more with overall good performances of crosstalk and insertion loss. For even larger FSR values, other layout approaches are available: instead of a classic U-shape AWG, an S-shape allows the designer

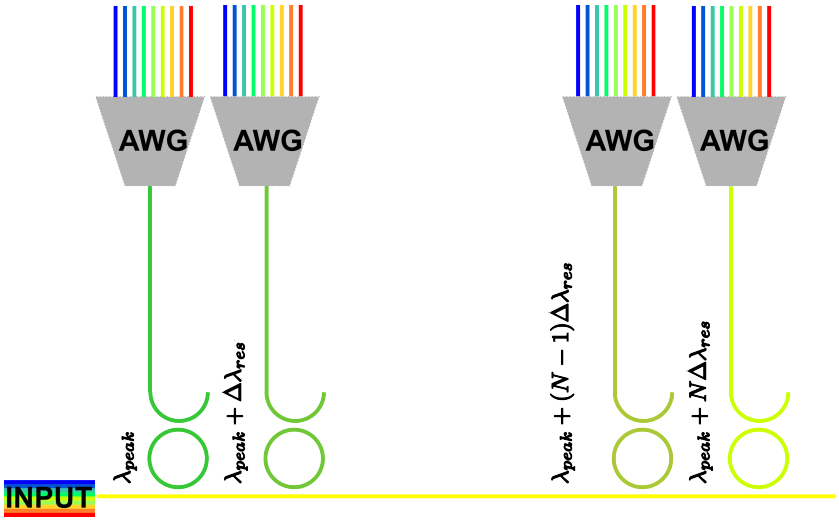

(a) Schematic representation of the multiple rings and AWGs cascaded system

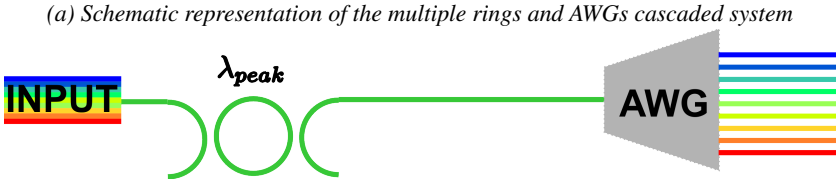

(b) Schematic representation of the single ring and AWG cascaded system

Figure 4.1: The schematic represents the basic block diagram of the photonic integrated circuits subject of this chapter

to overcome the minimum ΔL limit imposed by the U-shape layout [7]. For some applications in which a large FSR and a small channel count are required, PCGs will also be suitable. The limiting factor for AWGs is the channel spacing. The delay is inversely proportional to the channel spacing while the number of arms is proportional to the FSR/λ_{ch}, thus, a larger FSR with more channel spacing means more arms, but also a smaller ΔL. Hence, longer arms, as well as more arms, leads to more phase errors. Also, because more arms usually mean longer average length of the waveguides.

A larger footprint leads to a higher phase errors with consequent phase matching issues at the focusing output plane and a thus degradation of the crosstalk.

The main purpose of cascading AWGs and rings is to combine their individual strength, thus, use the high wavelength selectivity of the rings, and the large FSR capability of the AWGs. Such that we can have a large FSR and high-resolution spectrometer.

4.1.1 Multiple parallel AWGs and rings

The architecture of the spectrometer we discuss in this section consists of an array of sub-blocks. Each sub-block contains a ring and an AWG.

The FSR of the ring is designed to be identical to the channel spacing of the AWG, but with a different wavelength offset $\Delta\lambda_{res}$ for each subblock. The idea is to fill the empty wavelength gap between the n peaks of the ring.

4.1.1.1 Working principle

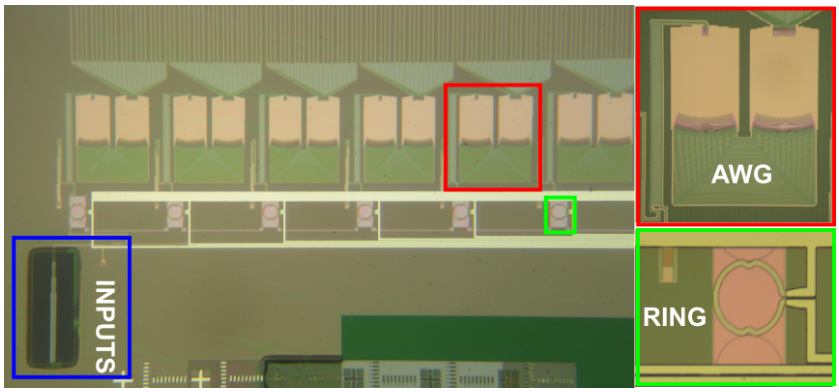

Figure 4.2: Microscope images of the PIC. The relevant sub-blocks are indicated: inputs, AWGs and rings

To understand how the device works, one can make the assumption that all of the sub-block behave according to the design specifications. In a second step non-idealities and the methodologies to compensate for them can be introduced. First of all the rings are assumed to have the designed FSR and wavelength peak position. Moreover, the rings are assumed to offer the required FWHM needed to provide the proper wavelength window selection. The FSRs of the rings in the array are designed to be the same and equal to the AWG channels spacing. Summarizing the FSR of the rings is equal to the AWG channel spacing, the wavelength of the rings resonances are the same of the AWG channels. Each of the sub-systems ring+AWG has a slightly shifted central wavelength, and they are equally spaced according to Eq. 4.1. If all of this conditions are satisfied, the PIC works as follow.

$$\lambda_{c,N+1} = \lambda_{c,N} + \frac{\Delta\lambda_{AWG,ch}}{N_{rings}} \tag{4.1}$$

The resolution is determined by the total number of channels, so $N_{AWG} * N_{out}/FSR_{AWG}$. Every channel of each AWG selects one resonance peak of the connected ring. This means that a Lorentzian window is applied to the spectrum

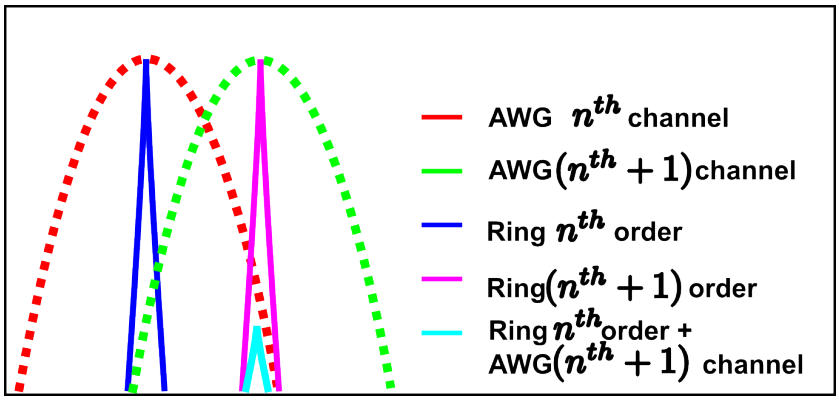

(a) Individual ring-AWG block working principle: only two channels are taken into account

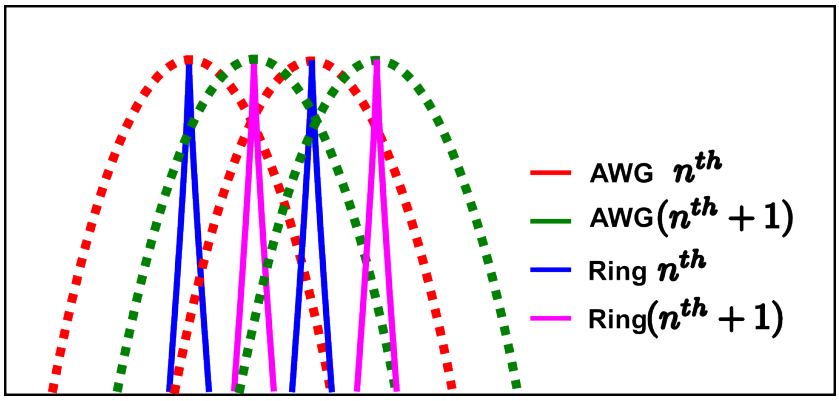

(b) Cascaded ring-AWG blocks: two consecutive blocks are taken into account

Figure 4.3: The images represent the simulation of one ring-AWG sub-block and of two consecutive ring-AWG sub-block. This to introduce the working principle of the circuit and how the individual sub-block contributes to the full PIC.

before it is sent to the AWG. For each AWG channel, the other ring resonance peaks are suppressed to the cross-talk level of the AWG. Fig. 4.3(a) shows the response of two neighboring AWG channels of the same ring-AWG sub-block. This plot also represents the suppression of the other ring peaks. As a result, only one of the ring resonance orders is transmitted.

Fig. 4.3(b) represents two consecutive ring-AWG blocks, and it gives a graphical interpretation of how two cascaded ring-AWG blocks are capable of filtering different wavelengths. The sequential shift in Eq. 4.1 of the sub-block increases the equivalent resolution, filling the wavelength gap between the peaks in Fig. 4.3(a).

Non-idealities, of course, affect the photonic integrated circuit. A global vari-

ation of the effective index and group index produces a shift of peaks resonances and variation of the expected channel spacing and FSR. But since it is a global variation, we can consider that the whole die has the same optical properties and thus compensation is possible. It can be realized by re-mapping (calibrating) the relation between physical output and measured wavelengths as introduced in Ch. 2. More complicated is the case of intra-die variations. Each ring and AWG can have wavelength grid misalignment of the peak and channel positions, respectively. Local variation causes fluctuations of the optical performance of the N subblocks on the same die. Compensation for this fluctuation is more complicated since it requires individual calibration for each of the rings and AWGs in the circuit. The tuning has to follow a proper passive characterization of the circuit.

4.1.1.2 Specifications and description of the PIC

The overall specifications of the final spectrometer are 48 nm of operation range and a 90 pm resolution. The FSR of the AWG is set to be 48 nm; it is equal to the operation range of the spectrometer. The AWGs have 20 output channels with a wavelength spacing of 2.4 nm. For proper channel roll-off, the AWGs have 60 arms, i.e. three times the number of output channels. The selected number of arms also guarantees a sufficiently low CT and a roll-off larger than what is required for communications purposes [8]. The center wavelengths of the AWGs are designed to be shifted by $\frac{\Delta\lambda_{AWG,ch}}{N_{rings}}$. Eq. 4.1 expresses the center wavelength shift of the $(N^{th}+1)$ compared to the N^{th}. The same design approach is used for the rings, such that every ring resonance is aligned with its AWG channels.

Fig. 4.4 shows the schematic representation of the photonic integrated circuit. The fiber-to-chip coupling is realized with an inverted taper [9]. To make testing easier, we also added grating couplers, combined using a 2 $\times$ 2 MMI that adds an intrinsic 3 dB loss. The bus channel of the MMI distributes the optical signal to the rings. Each of the rings has the drop port connected to the input of their respective AWG. The 20 output channels of the AWGs are arranged in a single row. The final target is to use an ROIC (Readout integrated circuit) with an integrated array of photodiodes. Fig. 4.2 represents the overall layout and the close-up microscope images of the circuit. The inverted tapers are realized with a SU8 3$\times$ 3 μm box cross-section [10]. The cross section used for the waveguides of the rings is a rib waveguide with 150 nm etch. This cross-section offers the advantage of being more robust against waveguide roughness [11, 12].

The reason for the better performance of rib compared to strip photonic wires lays in the optical mode shape. In the rib waveguide, the optical mode is more confined in the silicon and less intense at the interface, compared to strip waveguides. Since thermo-optic tuning will be required, heaters are processed on the rings with the fabrication process described in Par. 3.2.1.1. Titanium heaters with gold wiring

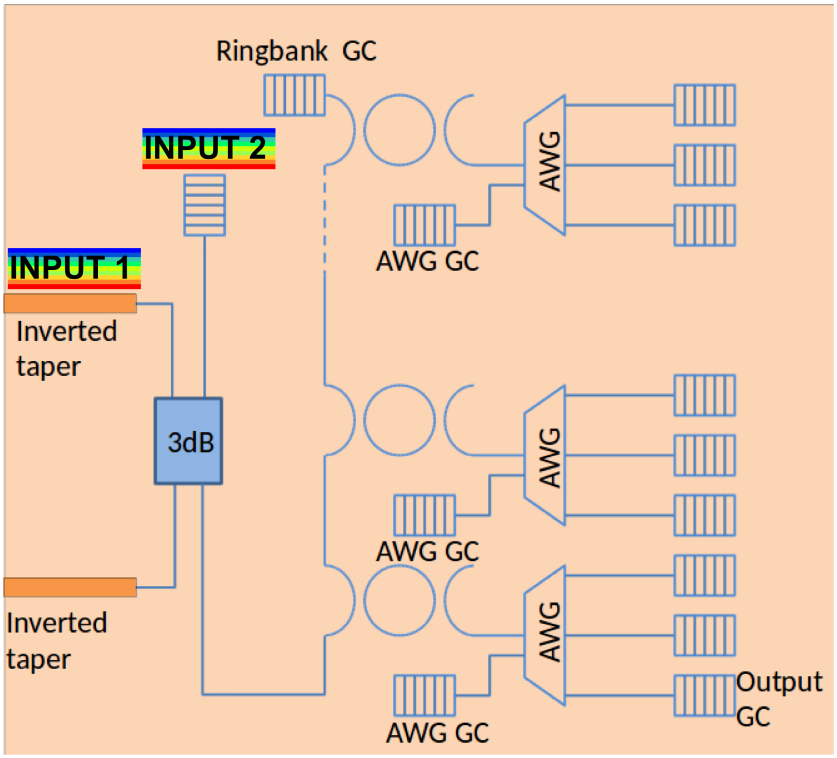

Figure 4.4: Schematic diagram of the spectrometer based on rings and AWGs array: the inputs are labeled according to the different use of the circuit.

and pads are deposited on top of the oxide cladding.

4.1.1.3 Characterization of the Cascaded system

The complexity of the PIC requires multiple characterization steps: the objective is to map the wavelength position of the AWGs channels and rings. Through active tuning, the rings have to be aligned to the spectrometer grid and the respective AWG channels. The first step toward the full characterization of the circuit is the individual sub-block measurements. For this purpose, the AWGs also have individual input test ports so they can be passively characterized without the presence of the ring. The auxiliary input port used for the characterisation is designed to have the same peak channel wavelengths but shifted with one or two channel spacings.

Fig. 4.5 represents the normalized response of the central AWG, measured through the test port. The normalization consists in the rescaling of the measurement taking into account the intrinsic losses of the coupling structures, in this case,

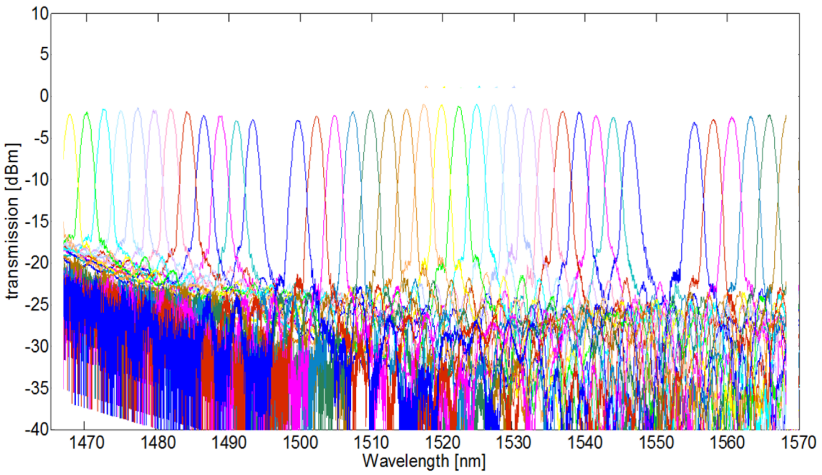

Figure 4.5: Transmission spectrum of the central AWG normalized with the test grating coupler. Three diffraction orders are in the range

grating couplers [13].

The target orders m and $(m \pm 1)$ are clearly distinguishable. Only the range of the center diffraction order is of interest. The AWG is designed to be centered at 1550 nm, while in the fabricated device it is clearly centered around $\sim$ 1525 nm. To compensate for this, the operation range of the device needs to be blueshifted to the center wavelength of the AWGs. The re-shift is required since the device does not utilize the entire FSR (the AWG is not cyclic), and thus, there is a gap in the wavelength transmission. In the gap, no wavelength analysis can be performed.

Fig. 4.6 shows the center channel wavelength in function of the AWG number (for a total of 26), while the different curves represent the output number of the different AWG (thus a total of 20). Analyzing the slope of one individual channel for each of the AWGs in the array, information about the wavelength shift can be obtained and compared with the design expectations. The plot in Fig. 4.7 shows the central channel wavelength of all the AWGs. The slope is quantified as 0.1 $d\lambda/dN_{awg}$. The slope is in line with the expected results. The scatter shown in the plot are partially due to die based variability, since the design is realatively large.

The rings have no auxiliary test port, so they have to be characterized through the main input of the circuit. Fig. 4.8 represents an example measurement of the system using the main input (in blue) and a comparison with the same ring/AWG sub-block measured with the auxiliary port (in green). Using the same optical input, we measure the array of output grating couplers sequentially with a semiautomatic setup. Fig. 4.8(a) and Fig. 4.8(b) represents two representative measurements: the first AWG and the third AWG at one of their outputs. When we use

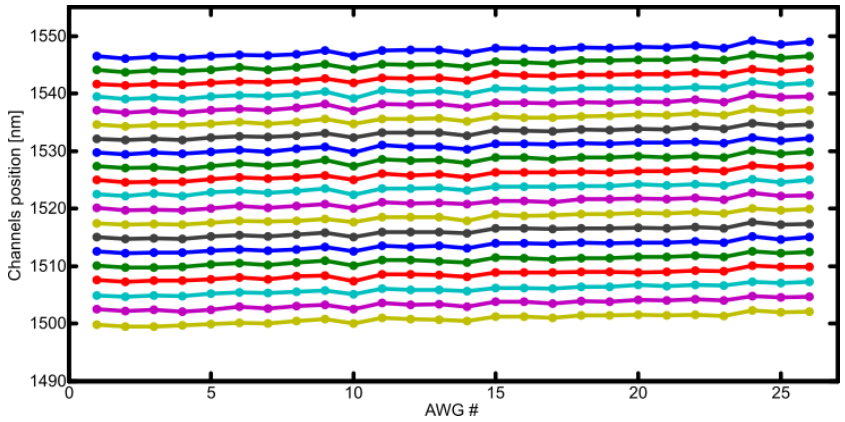

Figure 4.6: Central wavelengths of the 26 cascaded AWGs: the different curves represent the 20 outputs channels

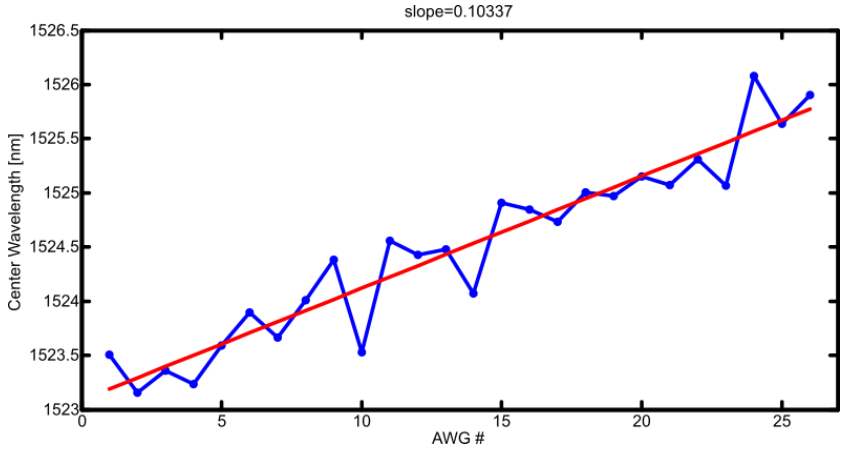

Figure 4.7: Channel wavelength position for the central output of the 26 AWGs. This is used to characterize the slope and thus the shift of the $\lambda_{out,n}$ in function of the AWG number

the auxiliary input, the measurement is adjusted to the different input wavelength shift. In these plots, the misalignment of AWG channel and ring peak is already evident and quantifiable. Compensation for this is possible since we provide the thermo-optic capability to each ring.

In Fig. 4.8(a) and Fig. 4.8(b) an overall power degradation between the first and third AWG is measured when we used the main input. The green curves represent the transmission the 1^{st} and 3^{rd} AWGs measured through the test ports, thus without using the main bus with the cascaded rings. The blue curves represent

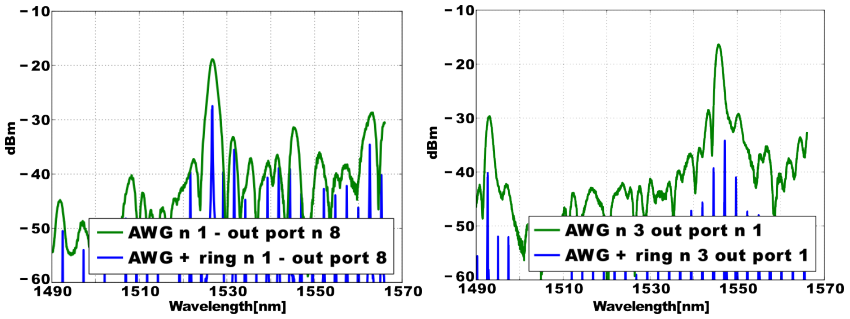

(a) First AWG and first ring cascaded with the AWG at the output port number 8

(b) Third AWG and Third ring cascaded with the AWG at the output port number 1

Figure 4.8: Example measurement of AWG through test ports and cascaded with the ring: The case of the auxiliary port the transmission is rescaled according to the input channel spacing

the same output ports of the same AWGs (1^{st} and 3^{rd}) when the main input is used, thus with the cascaded rings. The estimation of the loss is done comparing the peak power in the case of 1^{st} and 3^{rd} ring-AWG sub-blocks.

Fig. 4.9 represents the same outputs of four consecutive AWGs. Also, in this case, a misalignment from the expected grid can be noticed, but this is not the main issue. A power degradation in the order of $\sim$4 dB in each consecutive ring is measured. Furthermore, the FWHM is not sufficient for the required resolution of 90 pm. Due to the cascaded nature of the circuit, the ring transmission at the n^{th} stage will influence the Lorentzian of the following $n^{th} + 1$ and so on.

4.1.1.4 Array of rings and AWG: conclusion

After the demonstration of this device, work on this architecture in the Smartfiber project was discontinued. The low quality factor of the rings could not easily be overcome without increasing the bend radius beyond 15 μm, and thus decreasing the FSR. The rib waveguide would need a larger bending radius of at least 25 um. The current design intruded between 3 and 5 dB of additional loss each stage. When all the rings are cascaded the cumulative loss thus makes any stages beyond the 6^{th} practically unusable. Moreover a more fundamental problem regarding the matching the FSR_{ring} and the $\Delta\lambda_{AWG}$ is affecting this approach. However, the basic concept of the subblock with a cascaded ring and AWG is one we further explore in the next section.

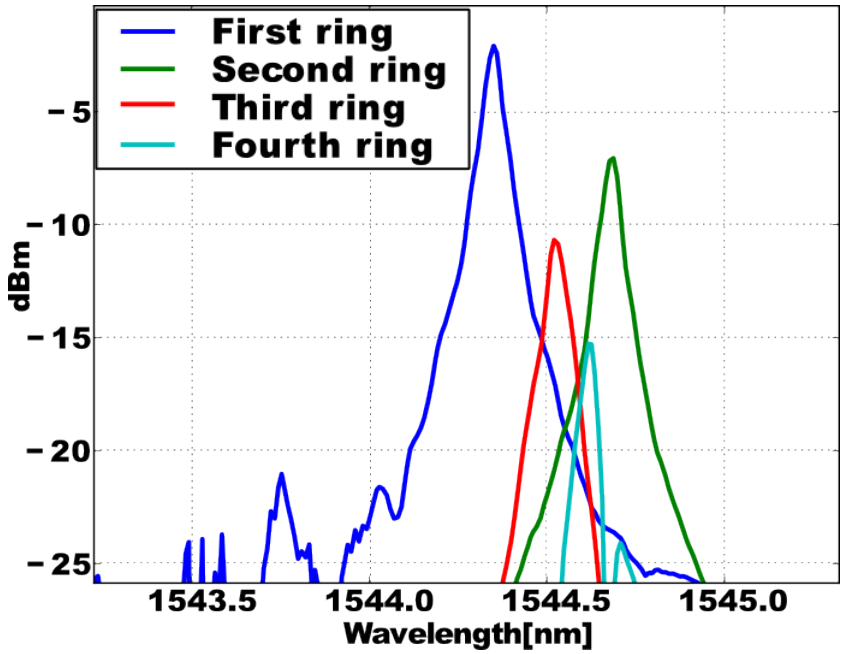

Figure 4.9: The plot represents the characteristic of the first four stages measured at the same output number

4.2 Combining a single ring and single AWG

In this section, we look deeper into the cascade of a single ring and a single AWG. We demonstrate the system as a ring sensing device with the AWG as a read-out spectrometer. We also demonstrate the same architecture as an actively driven scanning spectrometer. This configuration draws on the same strengths as the parallel array of AWGs and rings, but by choosing design parameters based on the Vernier principle, it becomes much more efficient. The ring can be tuned, and its wavelength interrogation property can be changed accordingly to the requirements in term of modulation speed and full FSR shift(cf. Ch. 3).

.

The fact that the device becomes actively modulated and thus consumes power is irrelevant compared when we consider that also the passive device in the previous section required active tuning to align the rings to the AWGs. In the case of driving with a sinusoidal carrier the ring, we need an RMS power of $P_\pi/\sqrt{2}$. If the previous design exhibits an average misalignment of the 26 ring of the 10%, we are going to need a DC power of $P_{pi} \cdot (26/10)$, thus, the power needed in the previous case is much larger that the design under test.

Fig. 4.10(b) shows the schematic of the of the basic structure. Fig. 4.10(a)

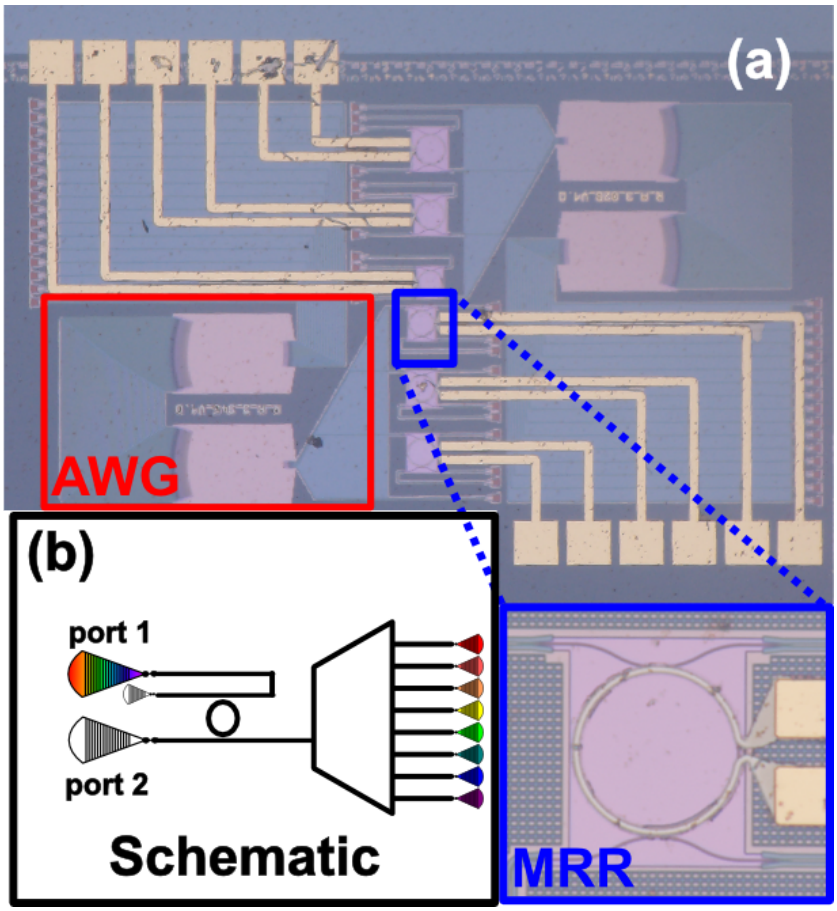

Figure 4.10: The image represents the microscope image of the PIC. In the blue box a particular of the microring resonator. In the red box a schematic of the PIC

shows a microscope image of the PIC: in the blue box there is a detail of the microring resonator while in the red box there is the AWG. The AWG has 16 output channels with 3.0 nm channel spacing. The FSR of the AWG covers the 48 nm. As the behavior of the AWG is not affected by adding more input ports (as long as they are not used simultaneously) we have added additional ring sensors with different FSR, as well as an input port for direct characterization. Multiple input rings are useful for several reasons. First of all the cross-section used for the AWG waveguides and the rings waveguides are different: the AWG uses strip waveguides while the second use rib waveguides [12].

The rings are connected to grating couplers in such a way that the optical port going to the AWG can be either the drop-port or the pass-port, by injecting light

into either port 1 or port 2 in Fig. 4.10(b). For operation as a spectrometer, we only send the drop port of the ring to the AWG. However, using the ring in 'pass' configuration is helpful to quantify precisely the channel responses of the AWG. The heater for tuning and modulation of the ring resonator is processed as explained in Par. 3.2.1.1: a titanium heater of 100 nm thick with gold wiring and pads.

4.2.1 AWG and ring: sensing interrogation

In a first experiment, we use the AWG and the ring as an effective index sensor system: the ring responds to local effective index changes, and the AWG operates as the integrated spectrometer. The FSR of the ring and the channel spacing of the AWG are scaled according to a Vernier factor. The cumulative envelope output shift have a large gain factor compare to the shift of the ring sensor in a stand-alone configuration.

We explore the capability of this architecture as an effective index variation ring sensor. The comb-like transmission spectrum response of the microring resonator exhibits peaks at the resonance wavelengths. They are spaced proportionally to the optical group roundtrip delay of the device, but the absolute position depends on the effective index and the resonance order. Anything that affects the effective index of the ring waveguide will affect the envelope of the resonances wavelengths. The change in the effective index can be induced by a change in the overcladding (like a fluid) or the binding of biological molecules [14]. To test the behavior of the interrogation system, we simply use the thermo-optic effect, instead of using a fluid overcladding. As the only effect of the heater is to induce a change in effective index, all conclusions also apply to index changes induced by other sensing methods.

The measurements performed with the tunable laser are always centered at 1510 nm, while all the broadband measurements are centered at 1550 nm, since this is the center wavelength of the SLED. This choice is made since the best performing wavelength range of the device is around 1510 nm(best ratio of ring FSR and AWG channel spacing), but the broadband source is centered at 1550 nm. This concept will be better exposed in the future sections.

The measurements are carried out with a tunable laser and a powermeter. Such measurement configuration guarantees high accuracy and reliability of measurement but is not extremely practical in case of real "field" application. This is because of the bulky aspect of the equipment and to the costs. Indeed, a broadband source is advisable [15], since we can build a photonic integrated circuit with integrated source and photo-detector.

4.2.1.1 System working principle

The AWG works as a spectrometer while the ring is the effective index variation sensor. Each output channel of the AWG exhibits a Gaussian-like wavelength transmission. Because the FSR of the ring is slightly larger than the channel spacing of the AWG, at most one resonance peak falls into the wavelength range of each AWG channel. The envelope output shows a Gaussian-like shape interpolated at the wavelength of the rings resonance peaks. The intensity of these points depends on the transmission of the AWG channel at the resonance wavelength.

The relation between the channel spacing of the AWG $\Delta\lambda_{awg,ch}$ and the FSR of the ring FSR_{ring} is designed using a Vernier scale:

$$FSR_{ring} = \Delta\lambda_{ch}\frac{N_{awg}}{N_{AWG} - m_{ver}} \tag{4.2}$$

The factor $N_{awg}/N_{AWG} - m_{ver}$ results in a Vernier effect in the transmission spectrum: for an N_{awg} channel AWG we get $n_{AWG} - mver$ ring resonances. As a result, the resonance peaks of the ring and the output channels of the AWG establish the envelope since the output is represented by the product of their transmission. The output power of each AWG channel can be written as

$$T = \sum_{m=0}^{M}(\sum_{n=0}^{N} L_{ring}(\lambda - \lambda_n))G_{AWG}(\lambda - \lambda_m) \tag{4.3}$$

where L is the Lorentzian-like response of the ring and G the Gaussian-like response of the AWG channel.

Referring to Fig. 4.11, when the FSR of the ring is equal to the AWG channel spacing, the output power collected at the AWG output channels will be the same for all channels. Shifting the ring peaks by a certain $\Delta\lambda_{n,ring}$ will also change the output intensity of all channels in the same way. But when a Vernier factor is introduced, a well-defined envelope over the channels of the AWG [16] will be obtained. A Vernier factor of $m_{ver} = 1$ is used. Different Vernier factors will give envelopes with multiple maximums. The concept is illustrated in Fig. 4.11 in the case of 0 and 1 Vernier factors.

4.2.1.2 Vernier sensor system characterization

We characterize the PIC in several steps to establish a relation between the electrical power driven in the heater and the envelope shift, which we can compare with the shift of the ring in a stand-alone configuration. The measurement is divided into different steps for passive, active and full system characterization. Finally, the system is tested with a broadband source.

The passive measurement of the PIC is carried out with a semiautomatic measurement setup [17].

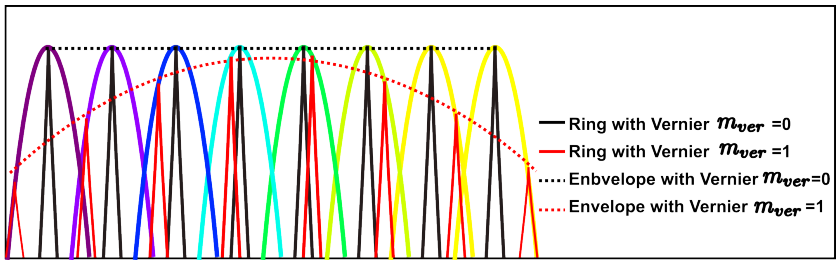

Figure 4.11: The image represents the working principle of the device: in particular it compares the $m_{ver} = 0$ and $m_{ver} = 1$ Vernier factor, thus zero envelope in black and one envelope in red

First the pass port and later the drop port output of the ring are used for the passive characterization. Fig. 4.12 represents the normalized spectrum of the full system when the ring is injected such that the pass port couples to the AWG (in Fig. 4.10(b) port 2). From this measurement, we can extract the AWG channels specifications, such as wavelength positions and cross-talk. To quantify the relative position of AWG center channel and ring peak wavelengths, we can monitor the transmission dip of the ring, which is superimposed on the AWG spectrum. As the dips and peaks are complementary, we also know the positions of the transmission peaks.

Moreover, we can use this measurement to calibrate the intensities when the drop port of the ring is fed to the AWG, hence, when port 1 on Fig. 4.10(b) is used.

For the experiment, we designed the FSR of the ring and the channel spacing of the AWG with a Vernier coefficient equal to 1. The dips of the ring are located in different relative positions compared to the center AWG channel wavelength.

Fig. 4.13 is the measurement of the same device but now with the light injected such that the drop port of the ring is connected to the AWG (in Fig. 4.10(b) port 1). The ring peaks' intensities are rescaled according to the maxima of the previous measurement. The envelope of the cumulative transmission spectrum is visible in Fig. 4.13: it has only one lobe since the Vernier coefficient chosen for this ring is $m/m - 1$.

Under these conditions, one FSR shift of the ring corresponds to a shift of Eq. 4.4 and so equal to the FSR of the AWG. This assumption is valid in ideal conditions and corresponds in our case to a gain factor of $\sim$16. The next step is the characterization of the thermo-optic tuner to exert the n_{eff} shift and thus the peaks shift. We stepwise increase the electrical power steps to the heater on top of the ring. For each power step, the CW laser is swept over the operation wavelength range. Fig. 4.14 represents three AWG channels while the heater is driven sequentially with three electrical powers. From this measurement, the thermo-optic efficiency is also extracted as P_π, which is found to be $\sim 30\ mW$.

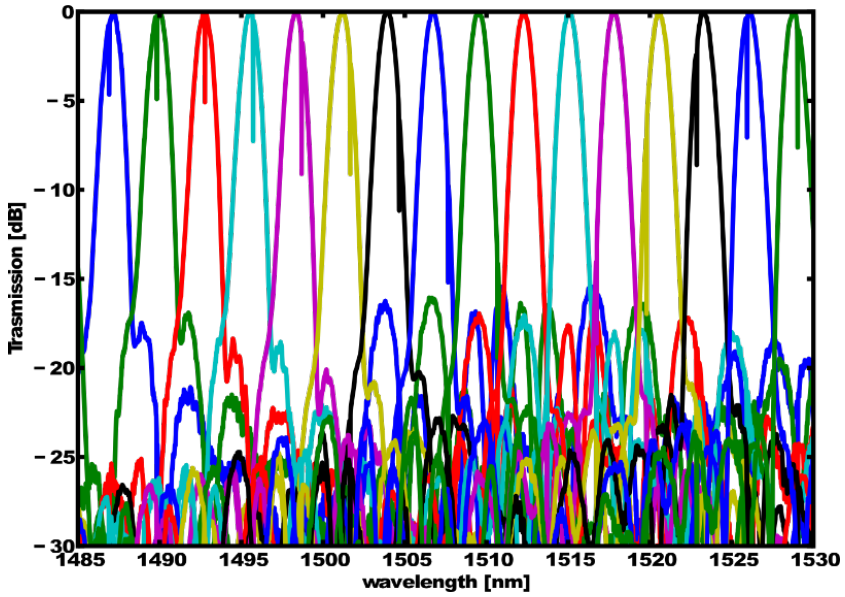

Figure 4.12: The transmission spectrum of the AWG when the pass port of the input ring is used: this configuration is used for test purpose

$$\Delta\lambda_{shift} = FSR_{ring} + AWG_{ch,sp} \cdot N_{out,ch} \tag{4.4}$$

The characterization performed with a tunable laser is used as a calibration for the actual measurements with a broadband source. The spectra obtained from the tunable laser scans are used by the data analysis software to extract the actual sensor shift, and the wavelength positions of the AWG channels are a fundamental input for the final device usage.

The characterization using the broadband source of the device as a sensing tool is demonstrated using a SLED centered around 1550 nm. The source has an emission spectrum of 100 nm and an integral power of 18 mW. The photonic integrated circuit is designed to work around 1550 nm, but due to fabrication variations, the wavelength range where the Vernier relation in Eq. 4.2 is properly respected has been shifted to $\sim$1510 nm: this condition is visible in Fig. 4.13 and in Fig. 4.12. This large shift in operation wavelength is because of the design choice of using two different waveguide types (rib and strip) for the ring and the AWG.

The consequences of working away from the best performing Vernier point is a smaller gain factor. Indeed, while in Fig. 4.13 and Fig. 4.12 a single envelope for the full FSR is present, this will not be the case in the experiment where we use the SLED centered at 1550.

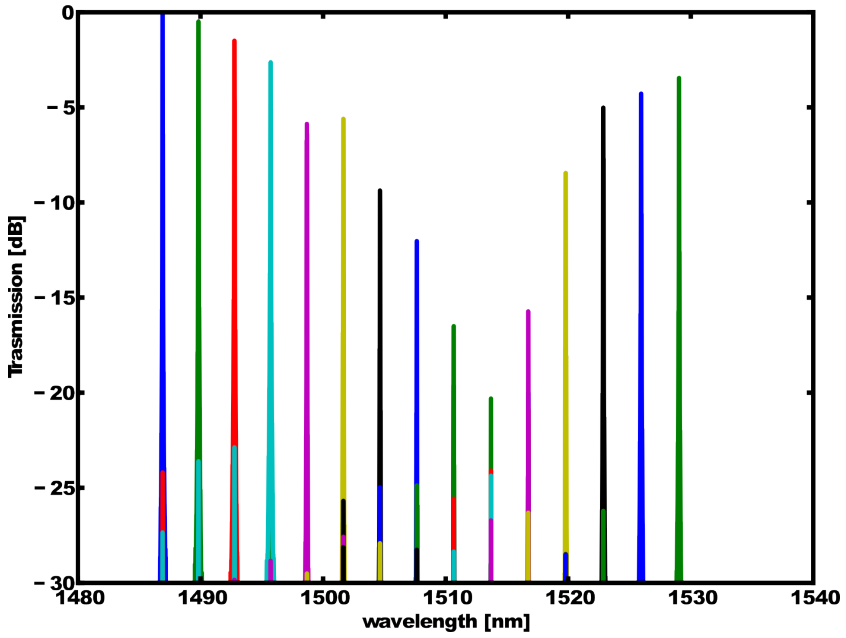

Figure 4.13: The transmission spectrum of the AWG when the drop port of the input ring is used: this configuration is the actual measurement of the circuit. In this case a tunable laser is used as source

We measure the device with an automated setup. It is capable of managing the optical and electrical measurements with programmable workflow. For the characterization of the circuit, first the electrical power is set, and then the PIC is optically characterized. This approach reduces the errors due to mechanical positioning variations. The alignments are actuated by automated mechanical stages.

With a broadband source, the output power is integrated over the entire wavelength domain. Thus, all the diffraction orders of the AWG will contribute to the integral output power. Unwanted diffraction orders of the AWG can cause different wavelength contribution to be collected by the powermeter. To limit the input to a single FSR, we apply a tunable filter and suppress the $m_{th} \pm 1$ orders to avoid multiple order collection. The filter window is centered around 1560 with a span of 48 nm. The final obtained correlation is between the electrical power biasing the heater (i.e. the change in n_{eff}) and the integral optical power collected in each of the N^{th} AWG outputs.

The device is characterized with the setup shown in Par. A.8, where the passive semi-automatic measurement setup is combined with an analog source and a broadband optical source.

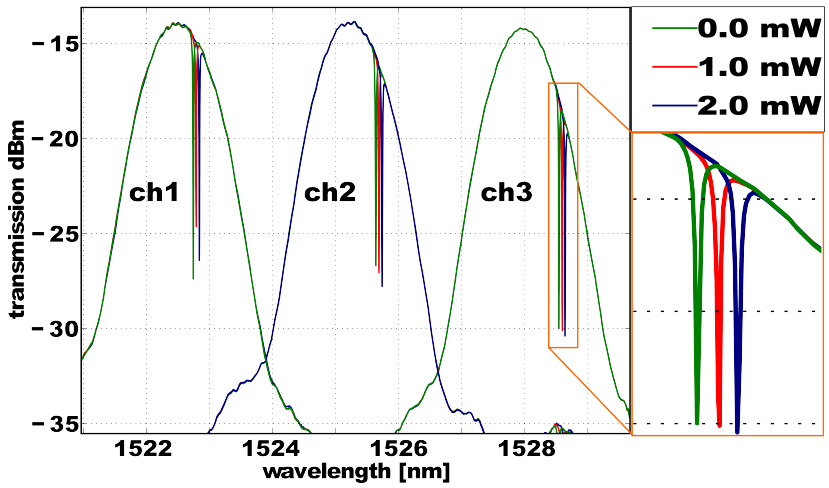

Figure 4.14: Three neighboring output channels when the pass port of the ring is coupled to the AWG input ;three electrical power steps are included to show the behaviour of the PIC.

4.2.1.3 Sensing system results

We compare the shift of the envelope vs. the electrical power with the shift of the ring sensor without the integrated spectrometer. Fig. 4.15 shows the wavelength shift of a single peak of the ring on the left. The right plot shows the same ring with the same electrical power applied, but when it is cascade with the Integrated AWG spectrometer and measured with the broadband source. The dots are the integral output power collected of the AWG outputs. They represent only a part of the outputs since one output channel in the red part of the spectrum are out of the filter window, and nine channels in the blue part of the spectrum are not usable for the envelope measurement. The shift of the envelope is 8.85 times larger than the shift of the ring in the stand-alone configuration. The measured gain shift factor is expressed in Eq. 4.5 as G, assuming the same equipment limitations. The gain factor is directly translated into *level of detection* (LOD) improvement. The LOD is defined as

$$LOD = \frac{\Delta\lambda_{min}}{G\frac{d\lambda}{dRIU}} \tag{4.5}$$

when the gain factor G is equal to 1. The LOD is the minimum measurable lambda shift λ_{min} divided by the variation of the wavelength as a function of the change in RIU (Refractive index unit) [1].

Eq. 4.5 expresses the LOD for the characterized device [18]. The envelope plot is obtained normalizing the spectrum to the wavelengths of the AWG channels.

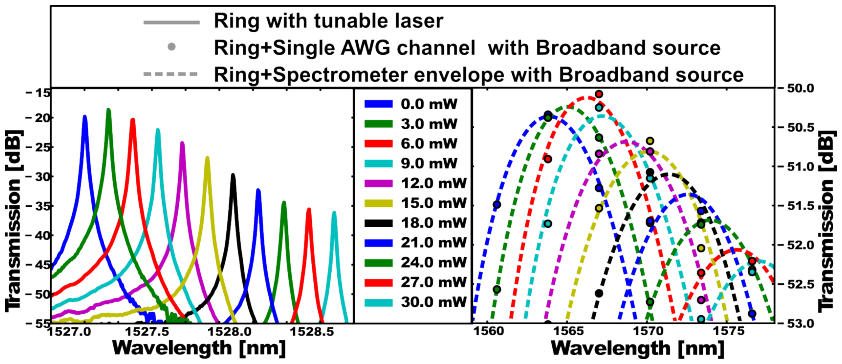

Figure 4.15: Comparison of the stand alone ring shift and the shift of the system under test: the same electrical power steps are applied. On the left there is the ring shift, while on the right there is the shift of the envelope of the ring+AWG sstem when a broadband source is used.

These wavelengths are obtained during the characterization phase. The normalization is required since we used a broadband source and no wavelength information is available when we measure the output power. The gain factor in smaller than what expected due to processing related variations of ring and AWG, and we operate away from the optimal Vernier configuration. Referring to the Fig. 4.13 the single Gaussian envelope is evident, while, in the case of the characterization with a broadband source, the slope has more than one peak, but only one is taken into account. The number of envelopes expressed in Eq. 4.2 as m_{ver} is not an integer and is smaller than one.

Worth to mention is that the noise that is affecting the measurement also has the same gain. However, the fitting error can be reduced with an optimization of the numerical fitting techniques(as a reference we can consider the approach proposed in Par. 2.5). Moreover, we can significantly improve on the design by using the same type of waveguide for both the ring and the AWG: this will make the device much less sensitive to fabrication variations, and will keep the device near the optimal Vernier regimen. Also, the gain can be boosted by increasing the number of channels on the AWG.

4.2.2 Ring-AWG scanning spectrometer

We also demonstrated the architecture proposed in Par. 4.2.1 as a spectrometer [19]. For this, we use the thermal tuner to scan the ring peak over a single AWG channel. The scanning concept applied can be considered as an extension of the scanning concept applied to a single ring in section 3.3.1.2, but hen cascaded with an AWG the operation range is no longer limited to a single FSR of the ring. And as the resolution is limited by the FWHM, and the FWHM itself is correlated to

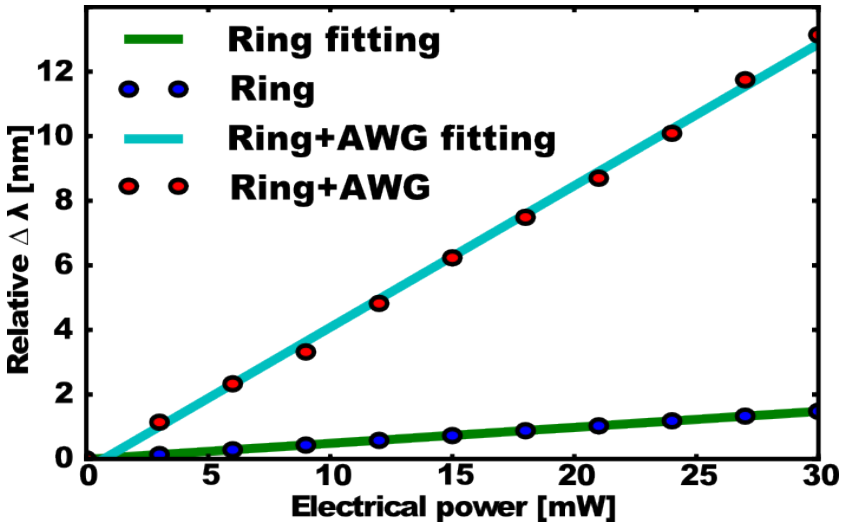

Figure 4.16: The plot compare the relative shift of the stand alone filter and the shift of the envelope associated to the ring-AWG system

the FSR [1], these two parameters have to be considered as trade-off features. In the case of the ring-AWG system, the ring has a smaller FSR (slightly larger than the AWG channel spacing) assuming the same critical coupling conditions as for the single ring, and therefore the ring can also have a smaller FWHM. Therefore, the resolution can be higher with the cascaded system.

For the experiment, we use the same chip as for the sensor configuration, so the measurement performed with the tunable laser are always centered at 1510 nm, while all the broadband measurements are centered at 1550 nm, since this is the center wavelength of the SLED.

4.2.2.1 Scanning spectrometer working principle

The main concept behind the scanning ring-AWG spectrometer is the capability of an AWG channel to isolate a single resonance peak of the ring, which is used to measure the wavelength range within a single AWG channel. The scanning procedure simultaneously affects all resonance peaks, and therefore all the output AWG channels. Fig. 4.18 shows the working principle on how a single resonance order of the ring scans the AWG channel.

The FRS of the ring needs to be larger than the bandwidth of the AWG channels, to avoid more than one peak in the same physical output channel. Two ring peaks into the same AWG channel wavelength would contribute to the same power integral (for instance if a photodiode is coupled to the optical output). If the FSR of the ring is larger than the AWG channel bandwidth, only one peak at the time

can contribute to the optical output in a significant way. The other ring peaks are suppressed down to the cross-talk level of the AWG, thus $\sim 20dB$. The ring is tuned with thermo-optic effect, and it is realized with titanium layer on top of the oxide cladding overlying the waveguide.

The spectrometer is experimentally demonstrated for stepped and continuous electrical driving. The procedure is similar as for the sensor, described in paragraph 3.3.1.2: first the FSR of the ring is stepped. The second experiment is realized modulating continuously in time domain scanning of the range of interest.

4.2.2.2 Stepped spectrometer characterization

We first characterize the passive optical circuit and the electrical circuit separately. This is because the performances of the spectrometer, in particular, the accuracy and repeatability, are strongly affected by the characteristic of the thermo-optic tuned ring and its stability. Each power driving step of the ring corresponds to the interrogation of a particular set of wavelengths, i.e. one wavelength per AWG channel.

The stability of the electrical circuit is essential for the reliable operation of the PIC as a spectrometer. If the thermo-optic characteristic changes over time, the uniqueness between the electrical power and the wavelength will be lost. Therefore, we have constructed an adaptive electrical driving scheme, which we use during the measurements. The measurement is managed both electrically and optically by the semi-automated measurement setup. For each scanning step, we first set the electrical power, and then the laser is swept over each one of the AWG output channels. In a first approximation, the thermo-optic efficiency (i.e. the conversion of electrical power to a change in n_{eff}) is assumed to be constant. Under this condition, the P_π is the only needed parameter for the proper driving of the heater [20]. For simplicity, we can also assume no second-order wavelength dispersion (n_g is constant), so the wavelength shift due to the thermo-optic effect is assumed to be constant $\Delta\lambda_{shift}/\Delta P_{heater} = c$ as well (this can easily be changed with an additional calibration measurement). If $\Delta\lambda_{shift}/\Delta P_{heater} \neq c$ each power step does not correspond to a constant $\Delta\lambda$. After a full heater characterization, two approaches are planned. The first requires the full heater performances characterization. A second order polynomial fitting of the resistance vs. voltage characteristic is used to linearized the heater response.

A second approach is a sequential driving. In this we control each voltage step with the following procedure:

$$V_{N+1} = \sqrt{(P_N + \Delta P) \cdot \frac{V_N}{I_N}} \tag{4.6}$$

We set the $(N^{th}+1)$ step, knowing the resistance from the driving voltage and current in the previous N^{th} step. This approach is missing the initial voltage step

since the resistance can not be calculated dynamically for the first step. Instead, we use the static value calculated in the previous iteration for the first step of Eq. 4.6. This driving scheme provides a linear shift $\Delta\lambda_{shift}$ for each voltage driving step. Worth to mention that with titanium heaters, the non-linearity of the resistance with the voltage is in most of the cases negligible.

Fig. 4.17 shows the zoom of a particular channel, the 11^{th} and the 12^{th}. From this plot, the achieved resolution can be estimated. Each single peak is spaced 50 pm from the neighboring peaks. Thanks to the low FWHM of the rings, even higher resolution sampling is feasible with this design. Particular attention has to be paid at the crossing point of the AWG channels. Indeed, the intensities of the two different contributions corresponding to the same wavelength have to be evaluated. The best performing peak in term of the signal to crosstalk ratio has to be used for that particular wavelength interrogation. The multiple choice in the crossing region of the AWG channels comes respectively from the N^{th} and $N^{th}+1$ channel of the AWG combined with the N^{th} and $N^{th}+1$ resonance order of the ring resonator.

The device is characterized with the setup shown in Par. A.9, where the passive semi-automatic measurement setup is combined with an analog source and a tunable laser.

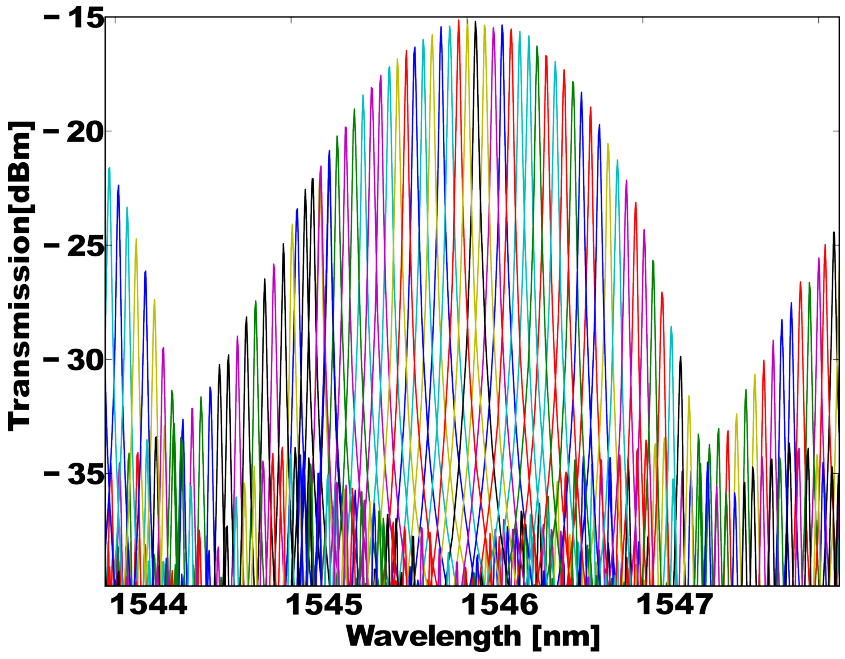

Figure 4.17: The plot represents one AWG output and the side neighboring channels. The closeup puts in evidence the resolution steps achieved

4.2.3 Time domain scanning and continuous driving

As in paragraph 3.3.1.2 for the individual ring, also this configuration can be driven with a continuous electrical carrier instead of a stepped driving. The operative range of the spectrometer is the same as in the case of the stepped driving. The ring is driven with a continuous time domain carrier. The output powers of the AWG are read out in the time domain. From these signals, an arbitrary spectrum can be reconstructed. Due to different initial conditions in term of ring peak and AWG channel wavelengths, a mapping of ring order and AWG channels needs to be performed. The resolution is correlated with the electrical driving carrier and the particular part of the spectrum. In particular, the resolution has worse performances at the AWG channels crossing regions. Noteworthy is the intrinsic advantage coming from the cascading of the ring and the AWG: in a case of the single ring, the FSR is $\sim 10\ nm$, and the resolution is limited to 300 pm, in this case, a smaller FSR is needed. Assuming for both rings the same finesse, the resolution of the present approach will be higher because of the higher FWHM of the ring combined with the smaller FSR.

4.2.3.1 Time domain scanning characterization

In this case, the measurement is carried out using of a broadband source combined with a waveshaper to construct arbitrary input spectra. The unknown spectrum generated with the waveshaper is then reconstructed with from the time signal of the AWG outputs. We also measured the resolution of the device is measured using two tunable lasers, as we did with the single ring in 3.3.1.2. The broadband source is a SLED with center wavelength at 1550 nm, a bandwidth of 100 nm and an output power of 18 mW. The wavelength range under test matches the central wavelength of the AWG passive response. A programmable wavelength filter is used to prevent influence from the neighboring diffraction orders of the AWG, but it is also used to define an unknown shape to reconstruct. The modulation scheme is a square-root sawtooth-like curve, such that for each period, a linear sweep of the scanned wavelength can be taken into account: each AWG output channel is scanned by a resonance order of the ring. We perform continuous electrical driving and acquisition: this allows us to collect with same trigger both the driving carrier and the electrical output voltage of the powermeter. The same optical reference level is used. The fixed reference level of the powermeter is set according to the maximum output signal. The requirement for the reference level is the non-saturation condition tested at the maximum transmission of the PIC. Since the reference level is set, also the dynamic range of the measurement is fixed. The dynamic range affects the AWG channel crossing region, limiting the resolution.

Fig. 4.18 shows the scanning operation of a single AWG channel graphically.

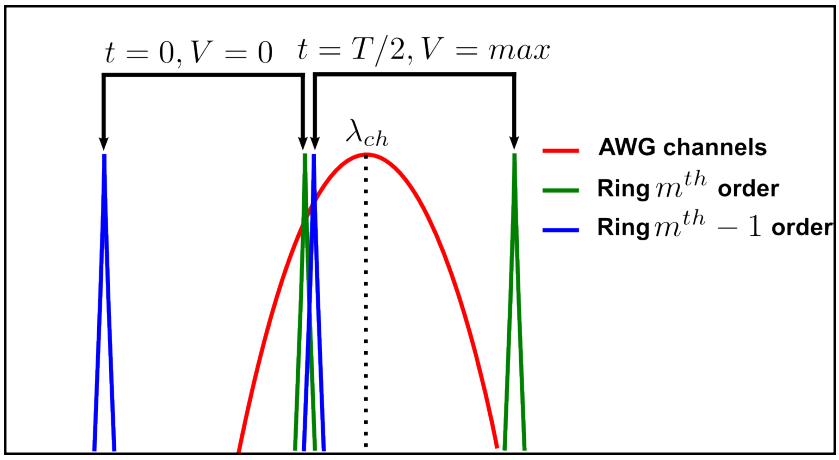

Figure 4.18: A graphic representation of the ring scanning operation required to cover the whole AWG channel of interest.

The scanning offset in the time domain depends on the default ring peak position with respect to the AWG channel center. One of the requirements to cover the entire spectrum of interest is that the full AWG channel needs to be covered by the wavelength scan. This is the case if $\lambda_{ring} > (\lambda_{ch} - \Delta\lambda_{AWG}/2)$, where $\Delta\lambda_{AWG}$ represents the bandwidth of the AWG channel calculated at the near channel crossing points, hence if the position of the ring is not at the blue border of the AWG channel. The part of the AWG channel that is not covered by resonance n will be covered by the $(n^{th} - 1)$ resonance order when it reaches the wavelength $(\lambda_{ch} - \Delta\lambda_{AWG}/2)$.

We scanned the ring with a scanning frequency as low as 100 Hz. The 'unknown' spectrum under test is a passband filter with center at 1550 nm and 30 nm bandwidth. The transmission is 0 dB in the passband and -40 dB elsewhere. Fig. 4.19 represents the coherent time-domain signals collected at the AWG outputs. The AWG channels are scanned by one of the resonance order of the ring at the time. In the plot, each m^{th} is the resonance order relative to the AWG channel. The circular zooms represent the beginning and the end of the passband filter. Indeed, as expected, since the channel spacing is 3 nm, for a 30 nm pass band filter, $\sim$10 channels show the Gaussian transmission. Since the FSR of the ring is larger than the AWG channel spacing, the different orders take part into the spectrum reconstruction. The starting point of the passband spectrum($\lambda_1 = 1535[nm]$ in Fig. 4.19) is on the edge of a channel of the AWG. For this reason, the beginning of the window is not clearly visible. This is due to the fixed dynamic range.

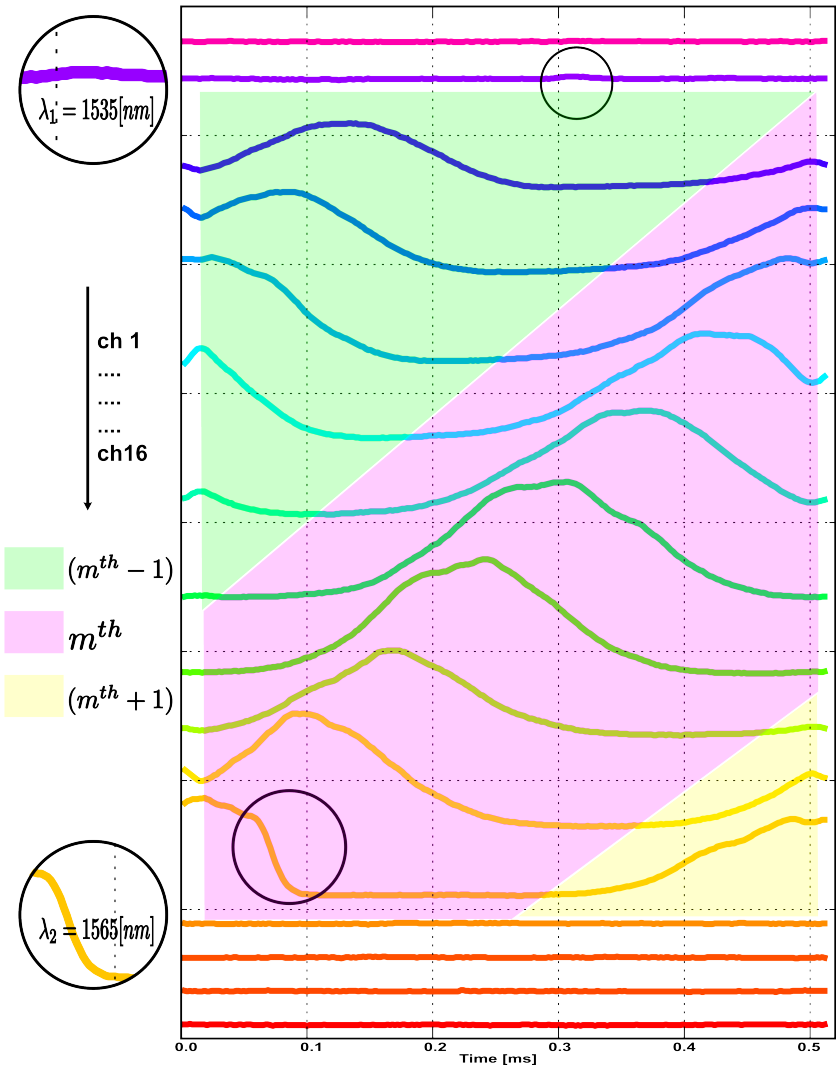

Figure 4.19: The simultaneous outputs of the 16 AWG channels when the ring is driven with a sawtooth-like carrier. The unknown spectrum is a passband filter centered at 1550: thus the side channel are not transmitting since they describe the stop-band part of the spectrum

Next, we characterize the resolution of this spectrometer. We monitor two tunable lasers which are tuned apart with a variable $\Delta\lambda$ and the time domain signal. When the two peaks are far enough apart to have 3 dB of extinction ratio, the relative peak distance is assumed to be the resolution. An exception is made for the resolution in the crossing range of two AWG channels where a more empirical

characterization is adopted.

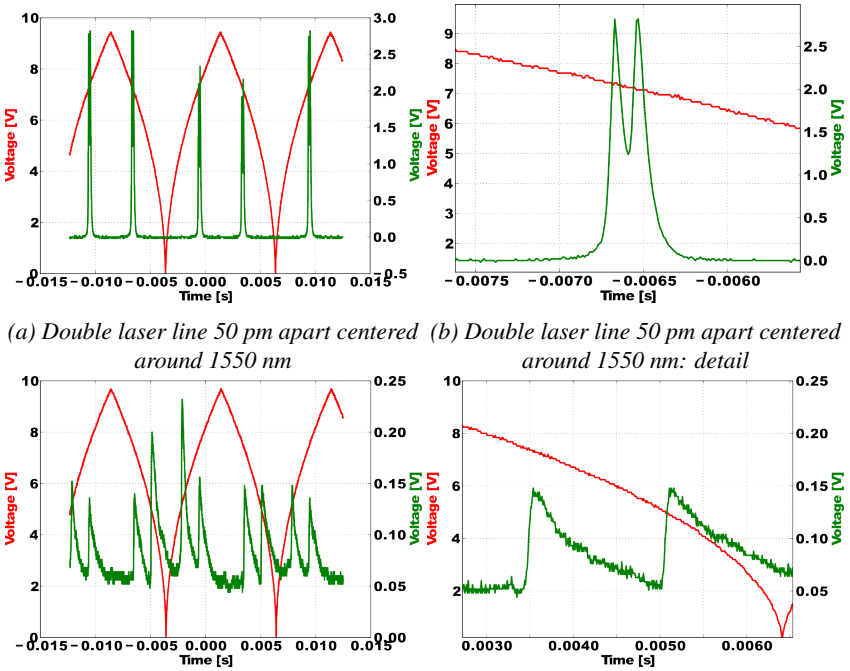

(a) Double laser line 50 pm apart centered around 1550 nm

(b) Double laser line 50 pm apart centered around 1550 nm: detail

(c) Double laser line 500 pm apart centered at the crossing point of two AWG channels

(d) Double laser line 500 pm apart centered at the crossing point of two AWG channels: detail

Figure 4.20: The plot represents the resolution mesued with the device at the center of the AWG channel in (a) and (b) and at the crossing point of two neighboring AWG channels in (c) and (d)

Fig. 4.20(a) and (b) show the time domain driving and read-out signals respectively in red and green. The measured resolution is 50 pm when the two laser lines are centered around 1549 nm. This quantity is in good agreement with the resolution measured with the stepped driving. Fig. 4.20(c) and (d) show the same experiment of the two laser lines but now close to the crossing point of two AWG channels and thus where the AWG insertion losses affect the measurement. The laser lines are centered around 1550 nm, at the crossing point of the 7^{th} and the 8^{th} AWG channels.

The IL and the crossing point require a lower reference setting of the powermeter. To be consistent with the previous experiments, the sensitivity of the powermeter is kept the same as the previous measurement. This forces the instruments to work near the limit of the measurable threshold: thus electrical parasitics and transients are affecting the quality of the signal reconstruction. The measurement

shows two laser lines 500 pm apart.

The final characterization we perform with this device is the full spectrum reconstruction. The unknown spectrum is generated with a broadband source and a tunable optical filter. We generate a triangle shape and two consecutive peaks of 2 nm bandwidth and separated by a dip of 1 nm. Fig. ‘4.21 shows the comparison of the input spectrum recovery in linear scale. The green curve is obtained with a commercial optical spectrum analyzer. The multicolor curve is obtained from the ouptus of the ring+AWG system, after the proper sectioning of the not needed time traces parts.

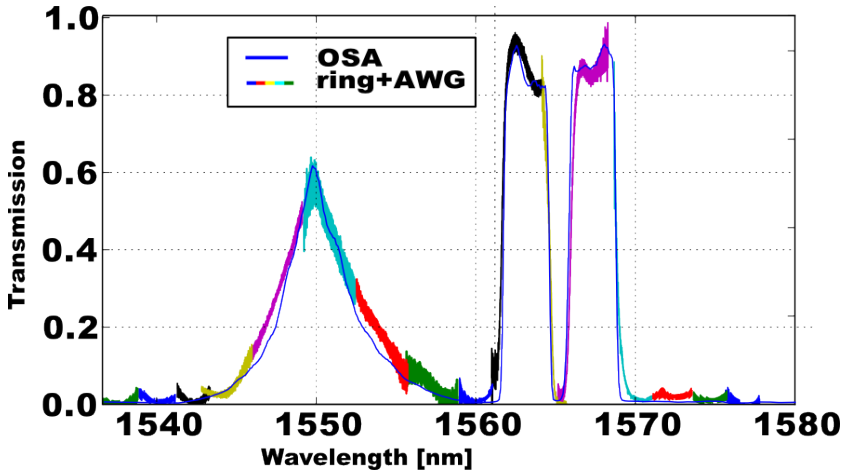

Figure 4.21: Random spectrum reconstruction: comparison of a commercial OSA and of the ring+AWG scanning spectrometer

The poor performance at the crossing point can be overcome by an improved design: it is possible for example to reduce the next channel cross-talk (i.e. make the roll-off less steep) such that the IL in this region is lower. This will limit the intrinsic dynamic range of the spectrometer. Fig. 4.22 shows the comparison of extinction between the center of the channel and the next channel crossing point. The dash lines represent the simulation of an AWG using an input MMI to flatted the channel shape [21]. In this case instead of $\sim$ 18 dB dynamic range, we are going to need only $\sim$ 8 dB of dynamic range. The drawback of this approach is the larger FSR required for the ring, since the bandwidth of the channel is larger, and thus we need a larger λ_{FSR} of the ring. This to make sure that only one resonance peak contributed to the wavelength sampling. This flat-top device is intrinsically lossier at the center of the channel, while on one side this is a drawback, on the other hand, it help to reduce the dynamic range needed since we measure it as the difference between the center channel and the crossing point of the neighbor channel.

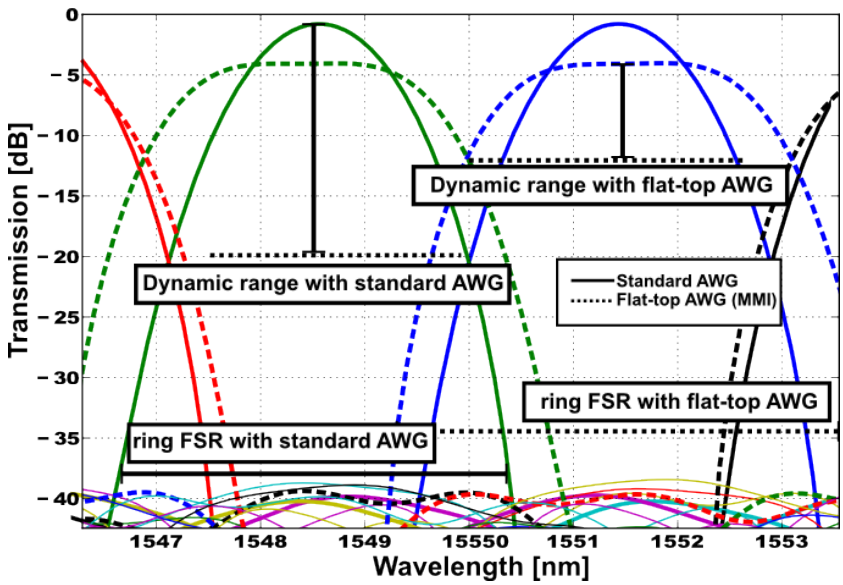

Figure 4.22: The plots show the comparison of classic AWG design (solid lines) used for this demonstrator and the simulation of a flat-top AWG (dash lines): the different dynamic range and ring FSR are represented.

The device is characterized with the setup shown in Par. A.3, using two tunable lasers for the resolution characterization and a broadband source combined with a tunable optical filter for the spectrum reconstruction. Furthermore, an external powermeter is used for the conversion of the time domain optical power to an electrical signal.

4.2.4 Conclusions

In this chapter, several approaches based on cascaded optical filters have been proposed and investigated. Combining filters with different properties significantly enhance the performance compared to their individual use. We combined AWGs and actively modulated rings demonstrating that the strength of the AWG and the ring can be combined. Even if the photonics level of complexity increased, the electronic readout does not become a bottleneck. The first architecture was based on many parallel cascades of AWGs and rings, but we discarded this concept because of a number of technical issues. Rather, we focused on improving the performance of a single ring and AWG cell, which we demonstrated for use in a ring sensor with an integrated interrogator. We found an experimental gain of ~ 9 in the LOD. The same architecture was then demonstrated as a spectrometer and tested with stepped driving and with continuous driving. In both cases, a resolution of 50

pm over 48 nm has been experimentally measured. Exception for the resolution is the crossing wavelength range of neighboring channels. Still further investigations are needed to overcome design limits such as the IL in the crossing point of the AWG channels. We proposed an alternative design strategy to overcome the limitation imposed my the crossing point insertion loss. We suggested using a flat-top AWG with an MMI at the input, such that the dynamic range needed to monitor the whole spectrum is smaller. To support this methodology, we implemented a comparison simulation.

References

[1] W. Bogaerts, P. De Heyn, T. Van Vaerenbergh, K. De Vos, S. Kumar Selvaraja, T. Claes, P. Dumon, P. Bienstman, D. Van Thourhout, and R. Baets. *Silicon microring resonators*. Laser Photon. Rev., 6(1):47–73, 2012.

[2] Shibnath Pathak, Dries Van Thourhout, and Wim Bogaerts. *Design trade-offs for silicon-on-insulator-based AWGs for (de)multiplexer applications*. Opt. Lett., 38(16):2961–2964, Aug 2013.

[3] FP7 SmartFiber. http://www.smartfiber-fp7.eu.

[4] Andrea Trita, Eli Voet, Jan Vermeiren, Danae Delbeke, Pieter Dumon, Shibnath Pathak, and Dries Van Thourhout. *Miniaturized Fiber Bragg Grating Interrogator based on an Arrayed Waveguide Grating in SOI platform*. In Frontiers in Optics 2015, page FTh3E.6. Optical Society of America, 2015.

[5] A. Vorckel, M. Monster, Wolfgang Henschel, P.H. Bolivar, and H. Kurz. *Asymmetrically coupled silicon-on-insulator microring resonators for compact add-drop multiplexers*. Photonics Technology Letters, IEEE, 15(7):921–923, July 2003.

[6] Adil Masood, Marianna Pantouvaki, Danny Goossens, Guy Lepage, Peter Verheyen, Joris Van Campenhout, Philippe Absil, Dries Van Thourhout, and Wim Bogaerts. *Fabrication and characterization of CMOS-compatible integrated tungsten heaters for thermo-optic tuning in silicon photonics devices*. Opt. Mater. Express, 4(7):1383–1388, Jul 2014.

[7] S. Pathak, P. Dumon, D. Van Thourhout, and W. Bogaerts. *Comparison of AWGs and Echelle Gratings for Wavelength Division Multiplexing on Silicon-on-Insulator*. Photonics Journal, IEEE, 6(5):1–9, Oct 2014.

[8] M.K. Smit and C. Van Dam. *PHASAR-based WDM-devices: Principles, design and applications*. Selected Topics in Quantum Electronics, IEEE Journal of, 2(2):236–250, Jun 1996.

[9] Jaime Cardenas, Kevin Luke, Lian Wee Luo, Carl B. Poitras, Paul A. Morton, and Michal Lipson. *High Coupling Efficiency Etched Facet Tapers in Silicon*. In Conference on Lasers and Electro-Optics 2012, page JW4A.10. Optical Society of America, 2012.

[10] Minhao Pu, Liu Liu, Haiyan Ou, Kresten Yvind, and Jrn M. Hvam. *Ultra-low-loss inverted taper coupler for silicon-on-insulator ridge waveguide*. Optics Communications, 283(19):3678 – 3682, 2010.

[11] L. Vivien, F. Grillot, E. Cassan, D. Pascal, S. Lardenois, A. Lupu, S. Laval, M. Heitzmann, and J.-M. Fdli. *Comparison between strip and rib {SOI} microwaveguides for intra-chip light distribution*. Optical Materials, 27(5):756 – 762, 2005. Si-based Photonics: Towards True Monolithic IntegrationProceedings of the European Materials Research Society Symposium {A1European} Materials Research Society 2004 Spring Meeting.

[12] Peter De Heyn, Diedrik Vermeulen, Thomas Van Vaerenbergh, Bart Kuyken, and Dries Van Thourhout. *Ultra-high Q and finesse all-pass microring resonators on silicon-on-insulator using rib waveguides*. In 16th European Conference on Integrated Optics, Abstracts, 2012.

[13] F. Van Laere, G. Roelkens, M. Ayre, Jonathan Schrauwen, D. Taillaert, D. Van Thourhout, T.F. Krauss, and R. Baets. *Compact and Highly Efficient Grating Couplers Between Optical Fiber and Nanophotonic Waveguides*. Lightwave Technology, Journal of, 25(1):151–156, Jan 2007.

[14] Katrien De Vos, Irene Bartolozzi, Etienne Schacht, Peter Bienstman, and Roel Baets. *Silicon-on-Insulator microring resonator forsensitive and label-free biosensing*. Opt. Express, 15(12):7610–7615, Jun 2007.

[15] Tom Claes, Wim Bogaerts, and Peter Bienstman. *Vernier-cascade silicon photonic label-free biosensor with very large sensitivity and low-cost interrogation*, 2011.

[16] Tom Claes, Wim Bogaerts, and Peter Bienstman. *Experimental characterization of a silicon photonic biosensor consisting of two cascaded ring resonators based on the Vernier-effect and introduction of a curve fitting method for an improved detection limit*. Opt. Express, 18(22):22747–22761, Oct 2010.

[17] Shibnath Pathak. *Silicon Nano-Photonics Based Arrayed Waveguide Gratings*. PhD thesis, University of Gent, Department of information technology, 2014.

[18] Katrien De Vos. *Label-Free Silicon Photonics Biosensor Platform with Microring Resonators*. PhD thesis, University of Gent, Department of information technology, 2010.

[19] Bernardo B. C. Kyotoku, Long Chen, and Michal Lipson. *Sub-nm resolution cavity enhanced micro-spectrometer*. Opt. Express, 18(1):102–107, Jan 2010.

[20] A. Masood, M. Pantouvaki, G. Lepage, P. Verheyen, J. Van Campenhout, P. Absil, D. Van Thourhout, and W. Bogaerts. *Comparison of heater architectures for thermal control of silicon photonic circuits*. In Group IV Photonics (GFP), 2013 IEEE 10th International Conference on, pages 83–84, Aug 2013.

[21] S. Pathak, M. Vanslembrouck, P. Dumon, D. Van Thourhout, and W. Bogaerts. *Optimized Silicon AWG With Flattened Spectral Response Using an MMI Aperture*. Lightwave Technology, Journal of, 31(1):87–93, Jan 2013.

5

Time domain multiplexed spectrometers

In this chapter, the concept of multi-domain multiplexing is introduced and applied to an AWG used as a spectrometer. Using multiple inputs of the AWG, we multiplex in the time domain different output wavelength channels on the same physical output waveguide of the AWG. The star coupler allows the AWGs to have multiple inputs and multiple outputs. We have already used this technique in Par. 4.1 and Par. 4.2, where we added additional inputs for testing and connecting multiple rings sensor devices. However, in that context, we only used one input during the normal operation of the device. Now we show how these inputs can be used simultaneously to improve the resolution of the AWG as a spectrometer.

AWGs and, in general, image based filters are among the most suitable demultiplexers for high channel counts. That's why we also use them as passive spectrometers. However, the resolution is still limited by the line-width of the filtering window (i.e. the ratio between the channel width and the FSR) [1]. For larger values of the FSR, the channels spacing is still larger than 1 nm, while for many spectroscopy applications a resolution on the picometer scale is required.

We overcome the resolution limit of a single AWG by combining multiple inputs and outputs. When the positions of the input and the output channels are properly designed, we can avoid the cyclic behavior of the AWG-based multiplexers. Instead, we use a Vernier scaling between the input and the output channel spacing. The principle is demonstrated with an AWG with five outputs and four inputs, each of which is connected to an MZI modulator. The concept is realized

on two different technology platforms: first the concept is tested on a passive chip with simple heaters added. We measured a resolution of 12 pm experimentally over the 20 nm FSR of the AWG. Then, to demonstrate the technology potential, a similar design was implemented on the active platform, using carrier depletion modulators, as well as germanium integrated photodiodes.

5.1 Vernier input multiplexed spectrometer: working principle

When the AWGs are used as multiplexer/demultiplexer or wavelength router, the input waveguides and output waveguides are symmetrically positioned on the input and output star coupler, respectively [2, 3].

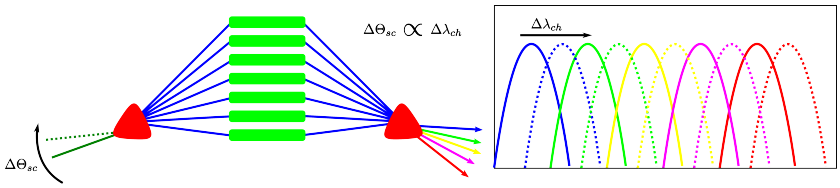

Figure 5.1: Vernier scaled AWG working principle: the transmission of the outputs shift in wavelength domain according to the insertion angle of the input waveguide

Because of that, the different input/output combinations will have the same set of channel center wavelengths, but shifted of a whole number of channel spacings. The set of allowed output wavelengths for all inputs are, in this condition, equal to the set of output wavelengths for a single input: $N_{\lambda ch} = N = M$.

A well define correlation persists between the input or output waveguides connection angle. The working principle is shown in Fig. 5.1. The image shows the correlation of angular waveguide connection in the input star coupler and spectrum shift. This principle is valid also for the output insertion angle.

However, if the symmetry between input and output star coupler is broken by repositioning the input waveguides, the output channels for each input will no longer peak at the same set of wavelengths. In this case, $N\lambda ch > M \neq N$. We can use Vernier scaling of the input and output channels to maximize the number of different peak wavelengths.

Te concept just described is graphically represented in Fig. 5.2: in Fig. 5.2(a) we see two symmetric star couplers, thus, shifting one of the inputs will produce a symmetric shift of the output spectrum of $\lambda_{in} = \lambda_{out}$. In Fig. 5.2(b) we shows a different condition in which the input and output waveguides have different physical distance, thus, the shift f the output spectrum, using another input, is $\lambda_{in} \neq \lambda_{out}$.

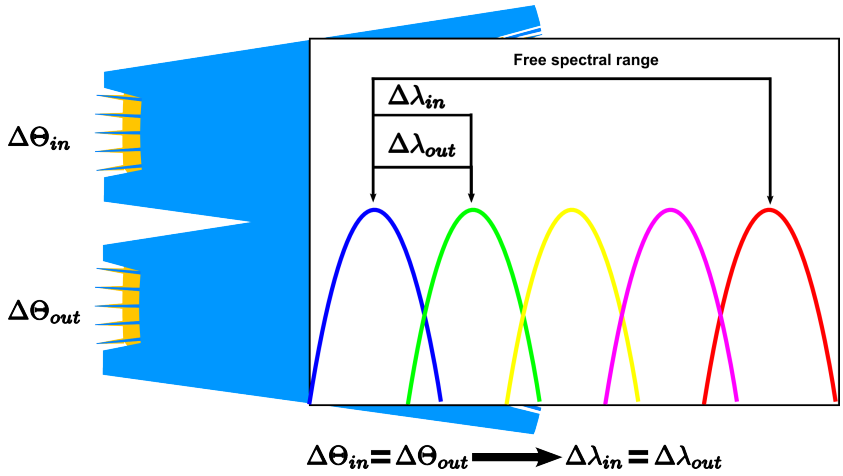

(a) The image correlates the input and output angular channel insertion of an AWG designed to have the same in/out spacing

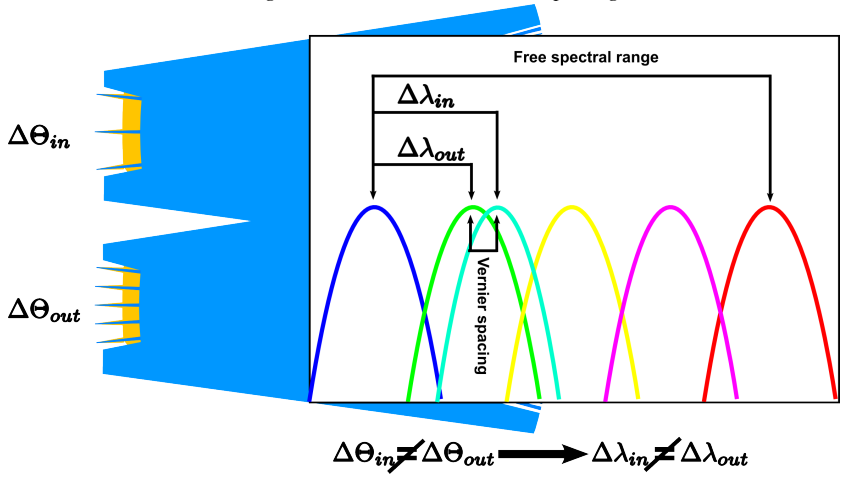

(b) The image correlates the input and output angular channel insetion of an AWG designed to have a Vernier in/out channel scaling

Figure 5.2: The drawings represent the input and output star coupler designs in case of router with same in and out channel spacing and in case of Vernier scaled AWG with different in out channel spacing

When we use a Vernier scaling, the number of inputs is chosen to be $N = M - m$, with usually $m = 1$. Fig. 5.2(b) describes the graphically the working principle of our device. When we proportionally position the input waveguides and the output waveguides, we will get a number of distinct channel peak wavelengths $N_{\lambda ch} = N.M/m$. As a result, the Vernier scaling gives an effective channel spacing smaller than the input or output channel spacing on their own. This design

strategy not only multiplies the resolution of the device, but it also removes the dead zones at the crossings between two adjacent AWG output channels.

However, if we use the different inputs together, contributions from the individual inputs will end up in the same output waveguides. A photodetector or power meter cannot distinguish between the contributions of the different inputs. Therefore, each input is equipped with a MachZehnder modulator to label the input in a unique way.

A schematic of the PIC is shown in 5.3. The full PIC has a single common optical input, from which the light is split into four waveguides and sent to a modulator for the labeling operation. The modulators are symmetric MZI interferometers with phase shifters on both arms (for balance), but we use only one at the time. Then the modulated optical signals are sent to individual AWG inputs. At the other end of the AWG, each output carries the combined modulated input contributions. The signals are recorded using a photodetector and then unraveled using signal processing techniques.

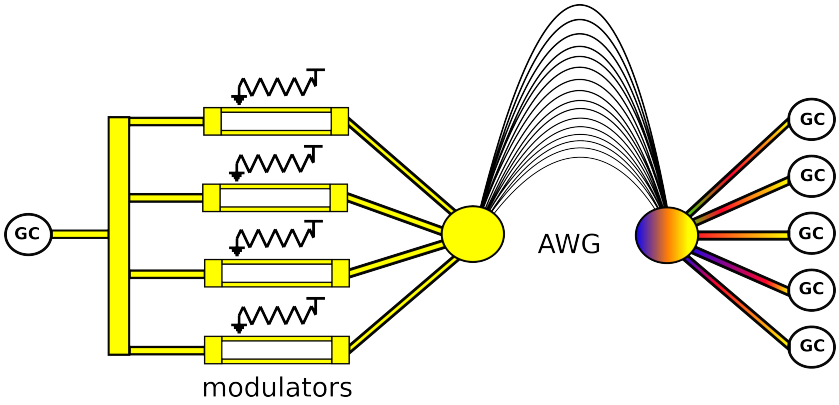

Figure 5.3: Schematic representation of the photonic integrated circuit

5.1.1 Description of the circuit

This optical circuit is realized in passive SOI technology of IMEC, in a CMOS-compatible pilot line [4].

The circuit contains a single AWG, and four symmetric MZIs, one for each input channel of the AWG. The 200mm SOI wafer substrates have a 2 μm buried oxide, and a 220nm silicon layer that is used for the waveguide patterning. On top, an additional 2 μm of oxide cladding is deposited. We used a curved grating coupler for the optical inputs and outputs [5]. The input light is divided into four branches using a binary splitter tree with standard 1×2 MMI (Multi-mode interferometer) splitters. Each branch has its MZI switch, with one input and out-

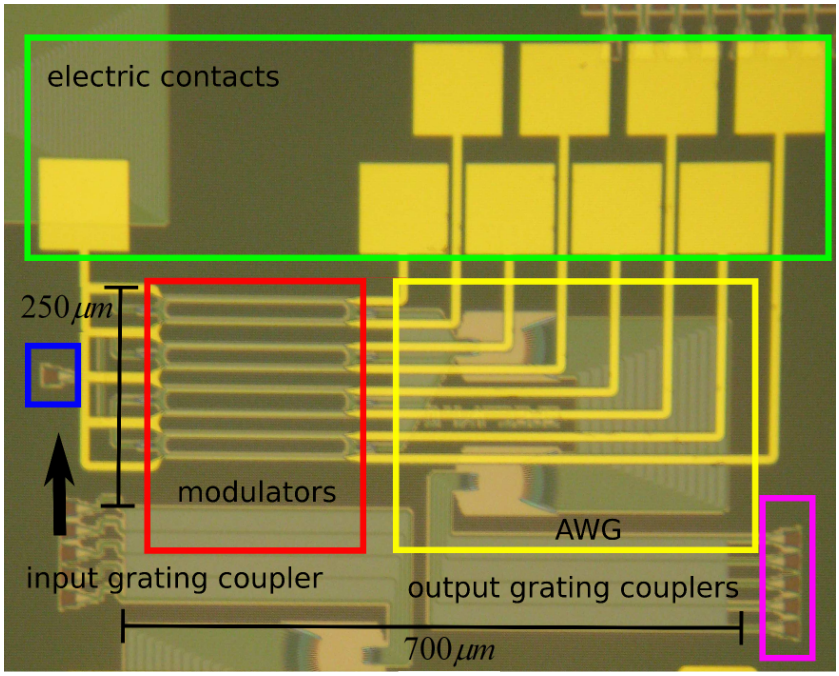

Figure 5.4: Microscope image of the photonic integrated circuit: the main sub-blocks and the footprint

put, using the same compact 1×2 MMI as a splitter and combiner. We deposit metallic heaters on the oxide cladding layers on top of the MZI arms waveguides, to make a set of 4 thermo-optic modulators or switches. The heaters are processed as in Par. 3.2.1.1. The output light from the AWG is extracted with an array of five grating couplers. Fig. 5.4 shows a microscope image of the PIC, and the sub-parts are indicated with colored boxes. The spectrometer part of the chip measures $700 \times 250 \mu m^2$, not counting the area occupied by the electrical pads and the grating couplers.

5.1.1.1 The arrayed waveguide grating

The AWG consists of two FPRs (Free Propagation Region) and an array of waveguides, with an equal path length difference between them. The longer the path length difference, the smaller the free spectral range (FSR) of the AWG. For a given number of waveguides in the array, a smaller FSR means a higher spectral resolution of the passive spectrometer and a better accuracy in wavelength detection. However, this is limited by the increase in phase errors induced by longer arms. With the current state of technology, this limits the channel spacing of the

silicon AWGs to around 1 nm or higher. For smaller channel spaces, the crosstalk will increase rapidly. Our AWG uses an input channel spacing of 5 nm and an output channel spacing of 4 nm. The inputs and the outputs channels are respectively 4 and 5. This satisfies the optimal Vernier condition of $N = M - 1$ and $N.\Delta\lambda_{in} = M.\Delta\lambda_{out}$.

The number of arms in the array is deliberately lower than in the case of WDM communication [6]. For a communication mux/demux design, the standard number of waveguides in the array is almost 3.5-4 times the number of wavelength channels: a number that ensures a sharp roll-off and sufficiently low crosstalk levels. The number of waveguides is fixed to 3 times the number of the output channels. The smaller number of arms reduces the crosstalk floor due to random phase errors, but also widens the channel transmission spectrum (less steep roll-off) and thus enlarges the overlap between neighboring channels. This design approach is useful for finding wavelength peaks that are located in the middle of two channels, but not a strict requirement in this case since the gap between channel is filled with the channel responses of the other inputs. The star couplers are laid out in a Rowland mounting, and the transition between the waveguides and the FPR is done using a deep and shallow etch, to reduce unwanted reflections. Fig. 5.5 shows how the inputs and outputs are configured in the two star couplers. Considering the spectral position of the AWG channels, the different combinations of M inputs and N outputs can be expressed as an $M \times N$ matrix (5.1).

$$P_{pos} = \begin{pmatrix} . & . & . & . & . \\ . & \lambda_{n-1,m-1} & \lambda_{n-1,m} & \lambda_{n-1,m+1} & . \\ . & \lambda_{n,m-1} & \lambda_{n,m} & \lambda_{n,m+1} & . \\ . & \lambda_{n+1,m-1} & \lambda_{n+1,m} & \lambda_{n+1,m+1} & . \\ . & . & . & . & . \end{pmatrix} \tag{5.1}$$

Each element in Eq. (5.1) represents the central wavelength of an input/output channels combination. Every row and column represent an input and an output, and the matrix elements are the peak wavelengths in the response from a given input to a given output. For a wavelength (de)multiplexer, this matrix would be a $1 \times N$ matrix. For a wavelength router, it would be an $N \times N$ matrix, where every element satisfies the condition

$$\lambda_{i,j} = \lambda_{(i,j)\pm 1} \tag{5.2}$$

Using the design approach introduce in Par. 5.1 for a Vernier scaled AWG much more spectral information can be obtained if we can read all these matrix elements individually. We can choose the input channels such that they are evenly spaced, and to have the same FSR as the output channels. As the FSR remains constant, the device has a cyclic behavior, similar to a wavelength router. The ratio

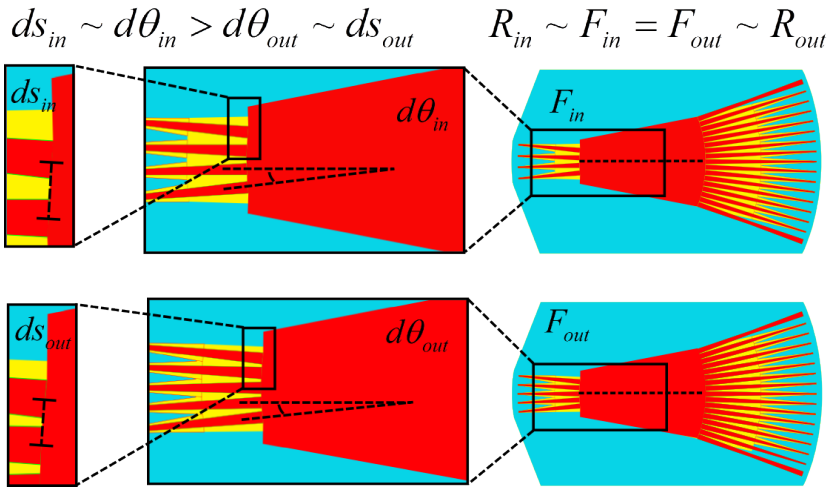

Figure 5.5: Input and output starcouplers of the Vernier scaled AWG: waveguide positioning.

between M and N is called the Vernier factor $n_{vernier}$ Eq. (5.3). The relation between the input and output channel spacing is obtained through the Eq. (5.4).

$$\frac{M}{N} = n_{vernier} \tag{5.3}$$

The Vernier scaling can be used to maximize the spectral information that can be extracted from an N-channel device. Fixing the Vernier factor $n_{vernier}$ (as the ratio of integer numbers) and the number of output channels N, the number of input channels M and the input channels spacing I_{chsp} can be calculated according to Eq. 5.4 where I_{chsp} and O_{chsp} are respectively input and output channel spacing.

$$I_{chsp} = \frac{O_{chsp}}{n_{vernier}} \tag{5.4}$$

5.1.1.2 Mach-Zehnder switch design

When using multiple inputs in an AWG at the same time, the intensities will add up incoherently in the photodetectors, and the additional spectral information will be

lost. Therefore, a mechanism is needed to disentangle the contributions of the different inputs. The disentanglement can be done by multiplexing: by electronically 'labeling' the different input signals, they can be separated with signal processing on the photodetector electrical output [7]. The simplest form of multiplexing that we can use here is time-domain multiplexing (TDM) [8]. By selectively switching on one input at a time, a sequential read out the signals from the different inputs is performed. For this, we can drive the heaters on one arm of the symmetric MZIs. All the heaters have a common ground, its contact pad is spaced from the arrays of signal pads, but aligned to the same grid for practical contacting reasons: both probe card and individual DC probes can be used. The MZI is symmetric: both arms have the same length of 200 um, chosen to guarantee a safe range of thermal driving power of the metallic heaters: the safe distance is assumed to be at least 50 um for the used metal width. Under these conditions, the passive response of each modulator is an all-pass device: all the inputs are in the ON state simultaneously: the ON state is valid in a range of $\pm five\%$. The thermo-optic effect is used to induce a π phase change in one of the arms, to drive the individual MZIs into destructive interference for the OFF state. The drawback of the thermo-optic effect is the low driving speed that is limited to few hundred μs. But compared to silicon modulators, the thermo-optic devices have a low insertion loss (cf. 3).

5.1.2 Use of the Device for Wavelength Peak Detection

A first application we want to use this device for is peak wavelength detection. This is useful for monitoring laser diodes, but also for sensing readouts of ring sensors or fiber-bragg gratings. The position of a wavelength peak can be estimated from the ratio of the channel outputs [9]. The limitation of accuracy and range for such a device is similar to the trade-off between channel spacing, the number of channels and FSR of WDM demultiplexer components. The wavelength range of the device is limited to the FSR of the AWG, in this case 20 nm. In the following algorithm, the wavelength response envelope of the channels is assumed to be Gaussian, but the reasoning holds for other spectral response shapes. Let us call the photodetector signal $S_{n,m}$ the integral (over all wavelengths) of the light that passes from input m to output n (assuming an ideal quantum efficiency of the photodetector), and an input signal that consists of a single wavelength peak $\delta(\lambda)$.

$$S_{n,m} = \int_{\lambda} G_{n,m}(\lambda)\delta_{peak}(\lambda)d\lambda, \tag{5.5}$$

Where the kernel function $G_{n,m}(\lambda)$ represents the pseudo-Gaussian response curve of each wavelength channel of the AWG. Of course, the actual signal S_n in the photodetector of output n consists of the multiplexed contributions from all M inputs:

$$S_n = \sum_{n=0}^{M} \int_{\lambda} \hat{G}_n(\lambda, t)\delta_{peak}(\lambda)d\lambda \tag{5.6}$$

The useful signals $S_{n,m}$ is extracted from the measured signals S_n by electronically disentangling them. When using time-domain multiplexing, S_n is a time-dependent signal 5.6, and so is the kernel function $\hat{G}_n(\lambda, t)$. At any given time, the measured value of S_n corresponds to one of the M signals $S_{n,m}$. For other multiplexing methods (e.g. *frequency division multiplexing* - FDM or *code division multiple access* - CDMA), the signals can be disentangled in a similar way. With time disentanglement, the extraction of $M \times N$ signals from the N photodetectors is done. This technique can now be used to estimate the wavelength position of the peak $\delta(\lambda)$. In a single input AWG wavelength detector, measurable signals for peak extraction are usually collected from only two neighboring channels. Using the Vernier scaling, more densely spaced spectral channels are available. A CoG (Center of Gravity) algorithm can be used to increase the accuracy of the device [10]. We assign an equivalent mass value to each channel intensity: the equivalent mass value is higher when the position of the peak is closer to the center of the channel. We take into account only the signal beyond a certain threshold: this selection is applied to filter out the noise. This approach gives an equivalence between the standard use of CoG and the wavelength detection used here. Considering the disentangled signals $S_{n,m}$ coming from the photodiodes, the CoG algorithm can be expressed as Eq. 5.7. The average accuracy of the spectrometer is evaluated according to the eq. 5.8.

$$\lambda_{meas} = \frac{1}{\sum_{n,m=1}^{N,M} S_{n,m}} \sum_{m=1}^{M} \sum_{n=1}^{N} \lambda_{n,m} S_{n,m} \tag{5.7}$$

$$S_{acc} = \frac{\sum_{n,m=1}^{N,M} \sqrt{(\lambda_{in} - \lambda_{meas})^2}}{N + M}, \tag{5.8}$$

$$\lambda_{calibrated} = \lambda_{meas} - F_{calibration}(\lambda) \tag{5.9}$$

In Eq. 5.7 $\lambda_{n,m}$ is the peak position of the channel of interest and $S_{n,m}$ in Eq. 5.5 the signal proportional to the photocurrent collected by the photodiode n. With this procedure the only calibration data used is a matrix containing the positions of the maxima belonging to each input/output channel combination of the AWG, in this particular case 20 elements. The error characteristic curve of the spectrometer shows that the CoG method generates a sawtooth-like error behavior. The stepping is due to each introduction of a new AWG channel and the removal of the previous one in the wavelength sweep. The channel introduction and removal is due to the threshold. The linear characteristic is due to the symmetric wavelength density of channels. Such stepped slope corresponds to a linear

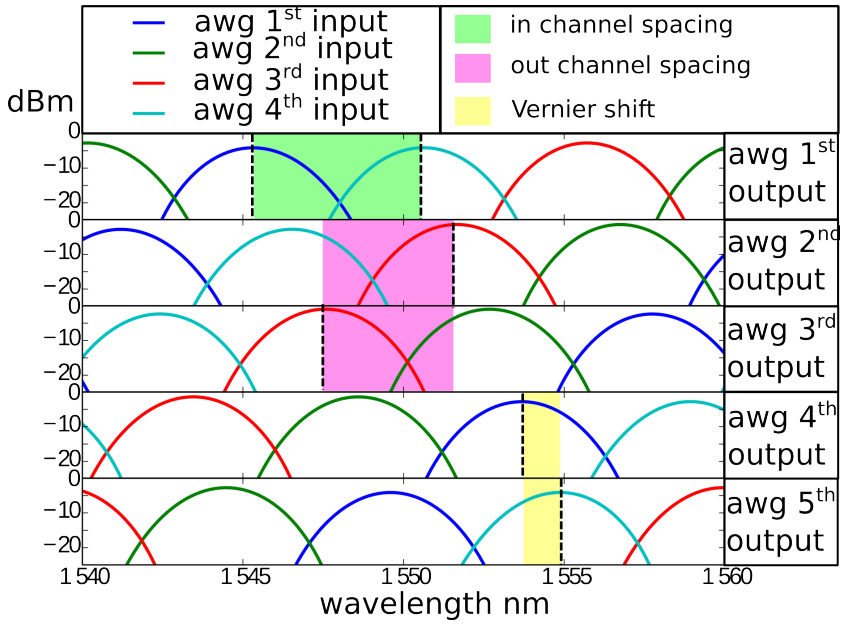

Figure 5.6: Spectral simulation of the spectrometer: all the in/out combination are delabeled with time domain demultiplexing techniques

behavior in the CoG algorithm. The slope mismatch is due to thresholding of the accepted signals and AWG non-idealities. If the function is injective [11], a complete calibration can be performed to take into account the intrinsic error of the device. With this approach, only the random part affects the measurement. Because of its sawtooth-like characteristic, the systematic error using the simple CoG algorithm can be analyzed and modeled. The resulting components of the Fourier series relative to the systematic error are used for a fine calibration of the device according to the Eq. 5.9, where a calibration function $F_{calibration}$ is used. This calibration leads to a "weighted" CoG algorithm. The wavelength peak we want to detect is assumed to be ideal as well. The ideality of the peak is a reasonable assumption as long as the $3dB$ bandwidth of the wavelength peak is, at least, $10\times$ narrower than the $3dB$ bandwidth of the AWG channel. The CoG algorithm can't be reliably used in a configuration with single-input AWG because each peak is collected with significant power by only one channel. In our configuration, this limitation is overcome because in every part of the spectrum there are multiple channels active. The wavelength positions for the calibration data are obtained by full characterization of the device. The approach used is valid only if the temperature is kept constant: with different temperatures the position of the channels and consequently the sawtooth-like curve change according to the new conditions

induced by the new thermal equilibrium. Indeed, in all of the used expressions temperature is a variable (the wavelength shift in the function of the temperature is around $0.1nm/^{\circ}C$). Since the temperature is kept constant at 25 $^{\circ}C$ ($< 0.5^{\circ}C$) using a TEC(Thermoelectric Cooler), it is not considered further in the analysis.

5.1.3 Simulation of the PIC

The simulation of the device is carried out with CAPHE circuit simulator by Luceda Photonics [12, 13]. For this, a circuit model for the individual building blocks is needed. For the waveguides (with heaters), splitters and combiners, an S-matrix model is defined. For the AWG, the model is calculated by breaking up the device into its separate parts and simulating those parts independently [14]. The coordination of these simulations is done with the IPKISS design framework [15]. Fig. 5.6 shows the results of the simulation of our photonic integrated circuit: each plot shows the M signals $S_{n,m}$ coming from all the M inputs, collected and de-labelled on one of the N outputs. In Fig. 5.6 the input channel spacing, the output channel spacing and the Vernier shifting of the relative channel position are also indicated. The simulated MZI switches include losses and 20-30dB ON/OFF suppression ratio.

5.1.4 Device characterization

The full characterization of the PIC is divided into two parts: for such purpose we use different setups. First we characterize the MZI modulators, finding the driving points to obtain full ON/OFF switching. Knowing the ON/OFF driving specifications, the wavelength domain response is estimated, and from that the optical crosstalk. The second part of the measurement performs the full TDM measurements and the wavelength recovery. For this purpose, free space optics and an IR camera are used for the simultaneous reading-out of the grating couplers array. This because without simultaneous reading of the output the experiment loose of relevance.

5.1.4.1 Device characterization: modulators specifications

The characterization of the four thermo-optic switches is done to determine the voltage required for full ON/OFF switching. The OFF Voltage corresponds to the first minimum in Fig. 5.7, marked with $\times$. In these points, with a single input channel in the OFF state, there is an integral power drop of approximately 25% (-1.5dB) that corresponds to one channel out of four in OFF state. However, some non-uniformity in the switching voltages for the four MZMs is found and listed in table 5.1. For this characterization, a broadband SLED (Superluminescent LED) centered at 1550nm is used, and the output light is collected from a single output

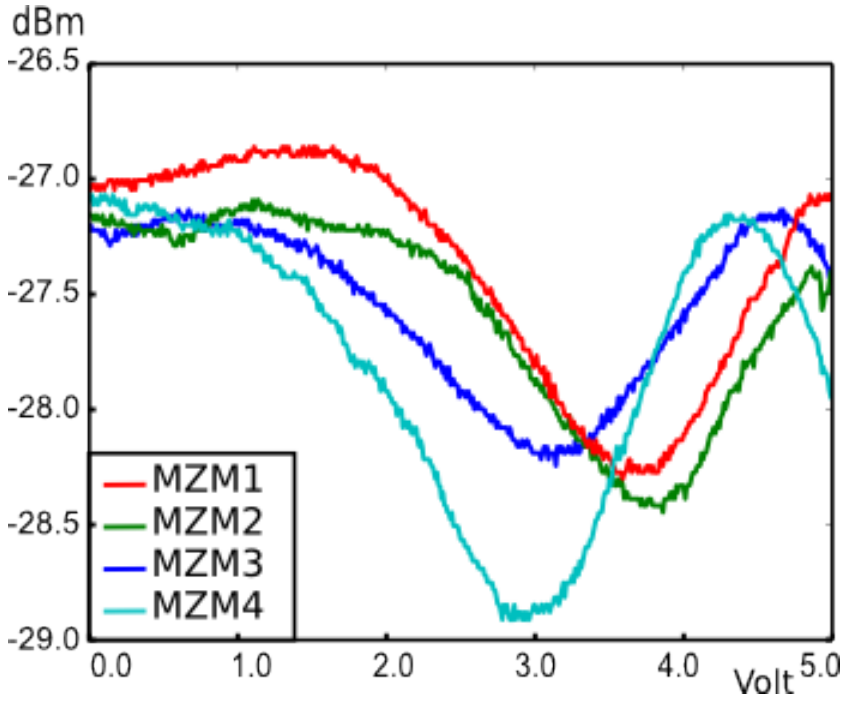

Figure 5.7: Optical output power sweeping the MZI voltage: this plot is used for the driving conditions of the modulators. At the zero derivative point a π shift is required

grating coupler through a fiber vertical coupling and redirected to an OSA. We used the OSA as a power meter of the integrated power in Fig. 5.7 and as a spectrum analyzer in Fig. 5.8, measuring the power spectral density. Fig. 5.8 shows the spectrum with the input channels switched alternatively off using the voltage values obtained in Fig. 5.7. A suppression ratio of 13-18dB is measured. The spectra in Fig. 5.8 also explain the non-uniformity in Fig. 5.7: as the AWG has a cyclic behavior, for some channels an additional AWG order is captured within the bandwidth of the SLED+grating coupler. The presence or absence of this additional spectral lobe will give a relatively larger or smaller change in the total power when that input is switched on or off.

To eliminate the effect of inter-channel crosstalk, a threshold filter method is applied before we use the CoG: we use a threshold of -10dB, which is above the worst extinction ratio of the switches (-13dB). By discarding all measurements below the threshold, non-idealities introduces by the switches will not affect the measurement. If some unwanted signal is for some reason higher than the threshold, its contribution will create an equivalent mass in the CoG in a wrong position (wavelength domain) shifting the estimated wavelength away from the actual po-

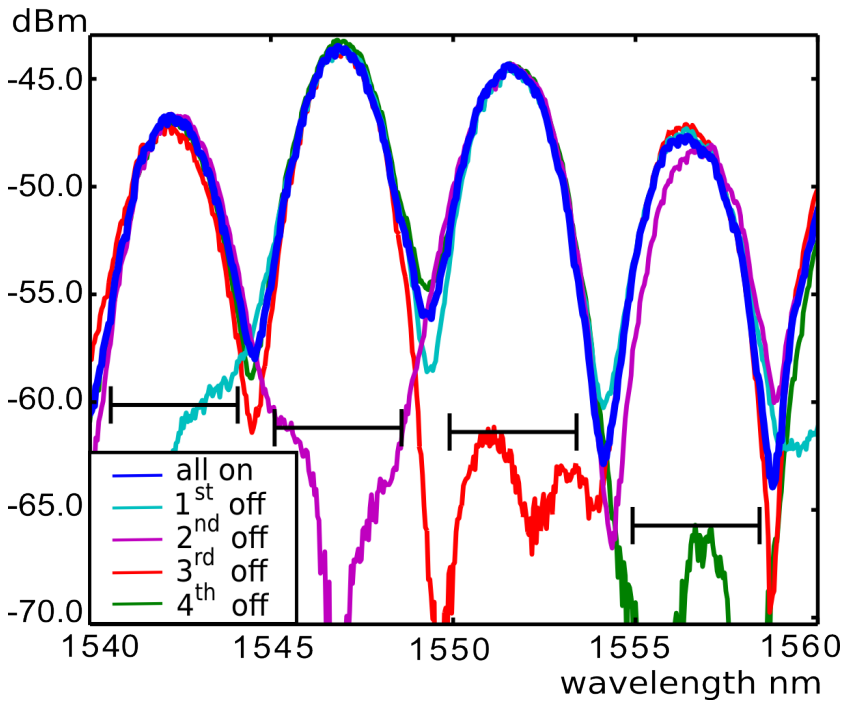

Figure 5.8: Individual suppression ratio of the four input channels when the modulators are sequentially switched off

sition. This part of the characterization is carried out with the setup shown in Par. A.4.

5.1.4.2 Device characterization and peak detection

For the full characterization of the spectrometer, a combination of optical and electrical instruments is used: thus another setup is built using optical transmission measurements and electrical multi-source driving. The optical outputs are read out with an IR camera: all the outputs can be measured simultaneously. We drive the array of thermo-optic switches with four independent voltage sources. All electrical grounds are connected to the common ground on our chip. The optical source used is a tunable laser, which can be considered the equivalent of a wavelength peak to be detected. In one camera frame, the intensity in different areas corresponding to the different grating couplers can be monitored. Fig. 5.9 shows a captured frame. The rectangles in it are the light spots coming out of the grating couplers. We perform an integration operation inside the selected areas, and thus a readout proportional to the power coming out of the grating couplers is obtained. The characterization is performed using a time division multiplexing scheme on

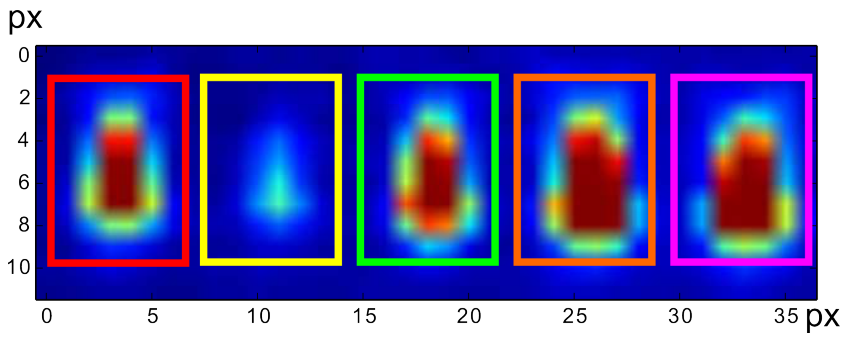

Figure 5.9: Frame captured by the IR camera showing the five output grating couplers and their transmissions

the switches: the MZIs are switched ON one at the time. Under this condition, only one of the inputs is optically connected to the AWG. A wavelength sweep with the laser is then performed. The IR collects frames at the output grating coupler for each wavelength and input driving combination. With a camera read-out, the signals from all outputs are collected simultaneously, instead of using a single fiber to read sequentially out the N outputs. Fig. 5.10 shows the result of the TDM measurement with all the input-to-output spectra disentangled. This corresponds well with the simulation result in Fig. 5.6. Due to deviations in the SOI fabrication process, the spectrum of the fabricated device is somewhat shifted compared to the design specifications. However, because the response is cyclic, the device can be calibrated in advance. This part of the characterization is carried out with the setup shown in Par. A.5, thus, an IR camera provides frames of the grating couplers, from which the optical output power is calculated integrating the signal of the pixel in the grating coupler area.

	Input 1	Input 2	Input 3	Input 4
Heater driving voltage	3.8	3.9	3.2	2.9
ON/OFF suppression ration	13dBm	18dbm	16dbm	18dBm

Table 5.1: MZMs characterization results

5.1.5 Experimental results

From the measured spectra an estimation of the position of the wavelength using the procedure described earlier can be performed. The resulting measured wavelength is plotted in Fig. 5.11 against the actual input wavelength as set on the tunable laser. The ideal response of the device would be a straight line where the measured wavelength is equal to the input wavelength. Fig. 5.12 shows the dif-

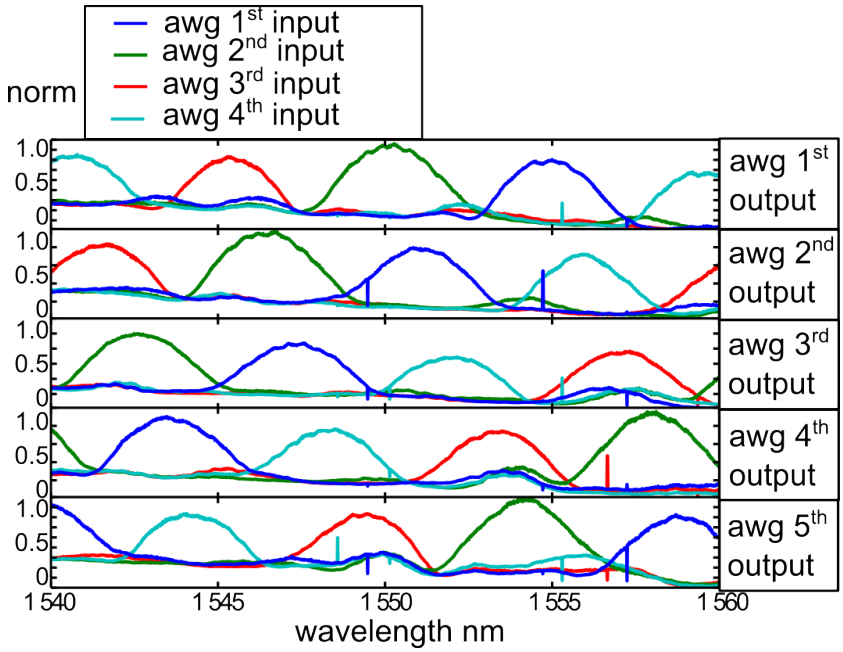

Figure 5.10: Spectral measurement of the spectrometer: all the in/out combination are delabeled with time domain demultiplexing techniques

ference between the measurement value and the straight line, which gives us the accuracy of the wavelength detection according to eq. 5.8. The raw measured accuracy of the CoG method is of the order of $\pm$ 0.5 nm while average accuracy is 180 pm and is evaluated according to Eq. 5.8. If the sawtooth-like behavior of the characteristic curve is taken into account (cf. Fig. 5.11 (zoom detail) and eq. 5.9) the worst case accuracy of the device is of the order of $\pm$ 0.2 nm, but the RMS accuracy is improved to 12 pm. Moreover, looking at Fig. 5.12 we see that few spikes have a low accuracy, most likely due to the thresholding procedure for the selection of the channel contributions.

The estimated dynamic range is approximately 20 dB, limited by the IR camera saturation level (between 10 and 13 dBm) and the threshold used for data selection (between -10 and -12 dBm). Fig. 5.11 (red curve), shows the local error using the "weight" CoG. It points out that the error is mainly caused by fast derivatives in the characteristic curve (cf. error zoom in Fig. 5.12), in other areas the average error is in the order of pm. More advanced fitting and calibration techniques can further improve the performance. Since the present work is a proof of concept, both peak accuracy, and average accuracy are mentioned. This because the spikes in the red curve of Fig. 5.12 can be eliminated.

To conclude, by using the Vernier effect and time-domain multiplexed mul-

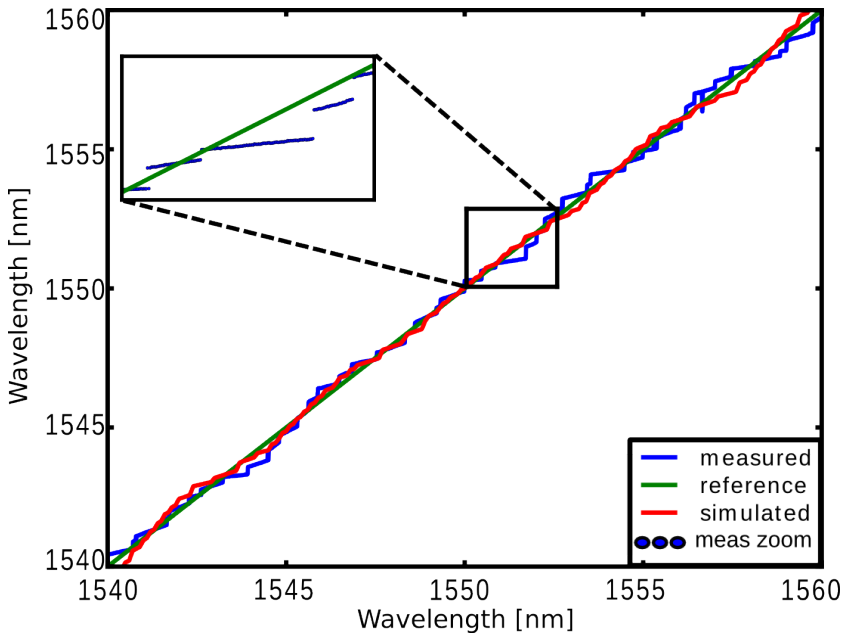

Figure 5.11: Absolute accuracy measured and simulated: in the particular there is the stepped behaviour of the characteristic curve

tiple inputs in our AWG, the peak detection accuracy is improved by a factor of $10\times$ compared to single input devices and $100\times$ if fine calibration procedure is performed. Moreover, such configuration offers more flexibility of use. Indeed, the PIC developed can detect peaks over its entire FSR with no unusable windows. The experimental performance demonstrated an average accuracy of 180 pm with standard CoG algorithm and 12 pm with the "weighed" CoG algorithm, across the FSR of the WDM device (20 nm).

5.2 Vernier input multiplexed spectrometer: active silicon and germanium on silicon design

The previous approach uses free space optics for the read-out of multiple output grating couplers and is not very appealing for practical use. Moreover, the thermo-optic switches limit the sampling rate of the final circuit to speed $<\sim 1KHz$. The first issue can be overcome using an on-chip optoelectronic converter such as a photosensor. The second problem can be solved opting for a faster modulating principle. The proposed solutions consist of using a CMOS fabrication process that includes doped silicon and germanium. The modulation technique has been

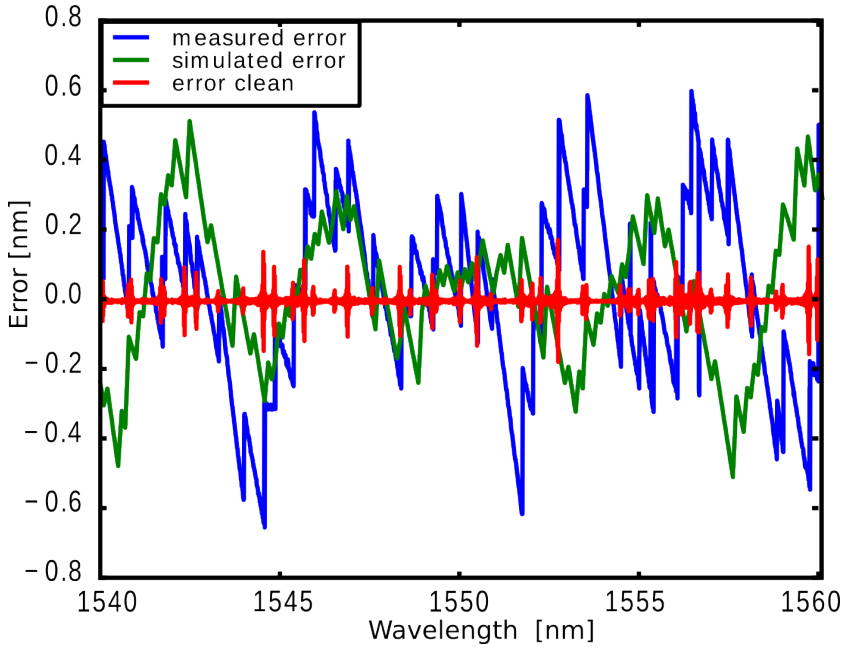

Figure 5.12: Measured local accuracy:comparison of simulation, measurement and measurement after the fine characterization

discussed in Ch. 3.

Thanks to the doped silicon, fast carrier depletion electro-optic modulators can be implemented [16]. While realizing doped germanium on the same SOI substrate, high efficiency and speed photodiodes can be obtained [17]. The photonic integrated circuit is fabricated with ePIXfab MPW ISIPP25G+ service in IMEC, Belgium. Integrated photodiodes give the advantage of reading out electrical signal on-chip instead of using grating coupler: We only need a single optical port to inject the spectrum of the light source.

5.2.1 Description of the circuit

The schematic block diagram of this design is similar to the previous in Fig. 5.3. The differences are mainly in the blocks used to perform the individual operations. Starting from the beginning: a curved grating coupler is used for the optical input driving, and then a more efficient splitter tree is used. Longer MMIs replaced the previous design; they guarantee better splitting ratio performances, within 5 $\%$ of tolerance both in amplitude and phase match between the outputs. With these MMIs, excitation ratio of the passive MZI $> 25dB$ have been measured, thus performances, in general, better than the values reported by the fab. Following the

power splitter tree, there is the array of modulators. Depletion effect PN junction modulators are implemented on each of the four channels.

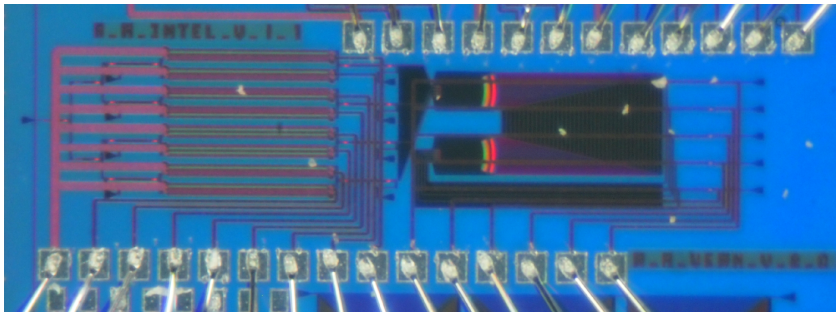

Figure 5.13: Microscope image of the fully integrated Vernier spectrometer after the wirebonding

Fig. 5.13 is a microscope image of the PIC after the wire bonding and custom packaging. Phase shifters are present on both arms, in the case of push-pull driving requirement. We use only one of them at the time since the phase shifters on one single arm reach π shift with $\sim 7\ V$. The carrier-mode interaction is achieved through transverse PN junction in interdigitated configuration. The length of the phase shifters is 1.5 mm, but to optimize the footprint of the MZMs, the same architecture used in Ch. 3 is adopted. The driving speed is limited by the speed of the measurement setup limit that is this case is 45 $kS/s/ch$ peak sampling rate of the electrical multi-channel signal generation and acquisition. The AWG is designed with similar in/out channels specifications as in the previous section. However, we used a larger number of arms to increase the roll-off, such that we can achieve a higher sensitivity. The design specifications are depicted in Fig. 5.14 where all the outputs using the same input and all the inputs using the same output are represented. In this case, the array of waveguides contains 40 elements. The output optical ports are connected to germanium photodiodes.

5.2.2 Characterization of the device

The photonic integrated circuit is characterized using the external optical source, a tunable CW laser. While for the electrical driving and reading a multi-channel electrical arbitrary signal generation and acquisition devices is used: the arbitrary signals generator drives the modulators, and the acquisition card collects the signals from the photodiodes. The germanium photodiodes generate a photocurrent proportional to the optical light absorbed in the intrinsic photodiode region. The responsivity is measured in the A/W and is the index of the efficiency of the device. For the photodiodes used in the present work, the fab declares a nominal responsivity of 0.7 A/W at -1 V. Since this quantity is a current, while with

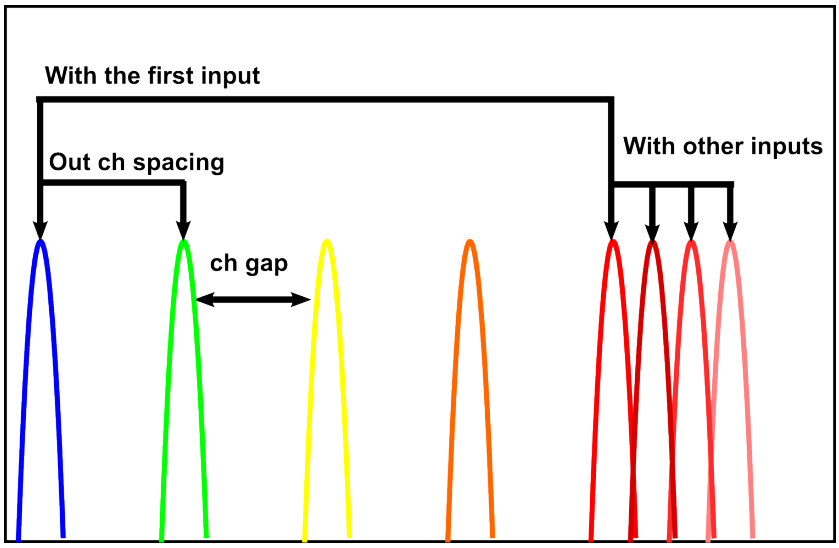

Figure 5.14: Working principle of the passive AWG: it represents the 5 outputs and the the channel space reached using all the inputs (one representative gap)

the setup in use we can sample only voltages, we design an array of tunable gain TIAs with an electrical cut-off of 3.6 KHz. We dimension the max speed at the minimum gain.

The main difference between the previous experiments is the electrical driving scheme. Thanks to the more advanced measurement setup and the use of much faster modulators, more sophisticated and efficient modulation schemes can be used. *Frequency division multiplexing* (FDM) [18] and *code division multiple access* (CDMA) [19] orthogonal function sets are tested. In the case of FDM, different carrier frequencies for each modulator are used, making sure that also higher order harmonics do not share spectral components. On the other hands, the maximum frequency in the electrical of the output needs to be below the electrical cut-off frequency of the analog TIA. The acquisition rate does not represent a bottleneck, since the generation-acquisition system, even if it communicates through an external clock(from the signal generator), has more stringent specifications for the generation. In this particular case, the speed bottleneck is the arbitrary multi-channel signal generator 45 $kS/s/ch$. According to this quantity, the working frequency and the working condition and the electronics have been defined.

Since there is, in theory, no negative voltage generated by the TIA pure CMDA is not realizable: two solutions are possible. The DC component can be subtracted from the driving and driven signals. The CDMA can be realized since we can create the orthogonal set of function. The second hypothesis is to find a set of orthogonal functions without negative values. Since the CDMA is less suitable

for amplitude detection, the following experiment is carried out with only use of FDM.

5.2.3 FDM modulation results

The experimental test of the device is carried out using an FDM modulation scheme. The driving clock is set by the multi-channel signal generator: in this case 45 $kS/s/ch$. Knowing this, four frequencies are selected such that there is no beating of spurious harmonics between them. In a real case, these quantities should be traded-off with the system speed requirements. Since this measurement is in an experimental phase, the driving speed is much lower than the integrated circuit capabilities.

We can write a generic expression for the modulating frequencies:

$$F_{ch}(n) = F_{base} + \sum_{0}^{N_{in}} \Delta F_{spacing} * n \tag{5.10}$$

F_{base} is the starting frequency for the first channel while $\delta F_{spacing}$ is the incremental electrical frequency shift to add to the input channels. For testing purpose, the selected base frequency is 0.5 KHz and the increment is $0.05KHz$.

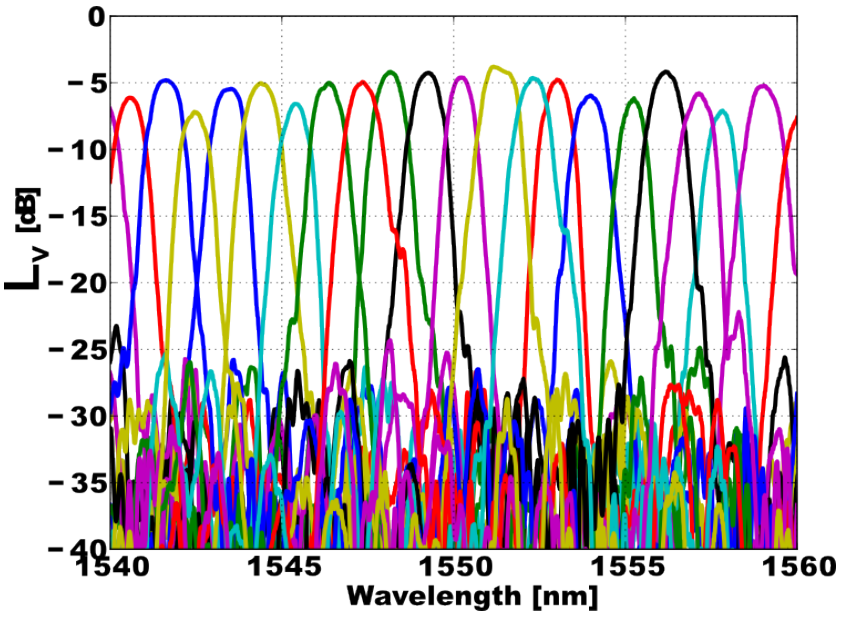

Figure 5.15: Spectral measurement of the spectrometer. IN his case FDM techniques is used for the labeling

Fig. 5.15 shows the reconstruction of the NxM input/output combination, thus a total of 20 channels. They are plotted in the level of signal $L_s\ dB$ since what is measured is the voltage coming from the bank of transimpedance amplifiers. The inhomogeneity comes mainly from the photodiodes responses and the gain of the TIAs. Compensation for these is possible in software, once individual characterization of both PDs and TIAs has been carried out.

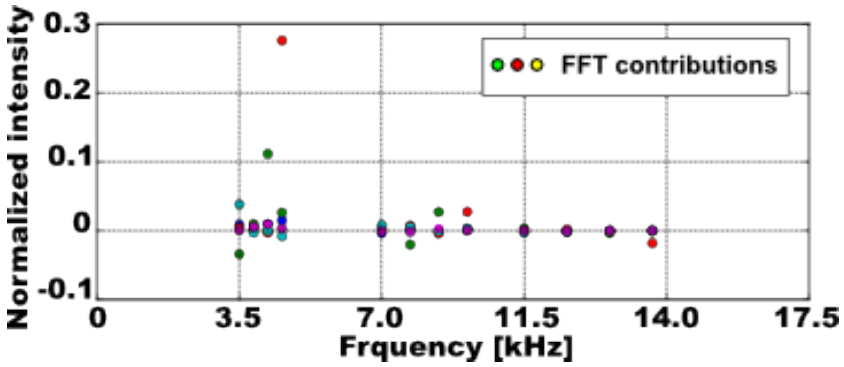

Figure 5.16: FFT spectrum of the outputs when the input wavelength is 1550 nm: these are the first, second and third harmonics

Fig. 5.16 shows the FFT domain of the collected signals coming from the five outputs of the AWG when the input laser is centered at 1550 nm. The discarded spectral contributions are not represented in the plot. The three groups of dots in the plot are the first, second and third order harmonics of the four carriers used for the modulators. These contributions are used to obtain the plot in Fig. 5.15 and in the following wavelength extraction.

This characterization is carried out with the setup in Par. A.6, where multiple analog sources for the modulators and multiple analog acquisition channels are sued simultaneously and synchronized by an external trigger generated by the arbitrary sources.

5.2.4 Gaussian fitting technique

We elaborate a more accurate wavelength extraction method, based on a Gaussian fitting. Center of gravity algorithm (CoG) is a robust technique to be used for wavelength recovery but is suffer from non-idealities related to the different application in gravitational fields and peak detection.

Indeed, when it is used for the calculation of masses center of gravity, it relies on the linearity relation between the actual mass and the distance from the origin. In the case of the wavelength recovery, the mass is associated with the power intensity of the output, while the distance is associated with the center wavelength

of the channel. Hence, since the intensity (transmission of the AWG channels) is not in a linear quantity (it has a Gaussian shape), the CoG does not perform ideally. We can extract a more accurate wavelength recovery technique based on the actual response of the system.

The transmission of the AWG can be written as

$$T_{AWG} = G_{ch}(\lambda) * \sum_{n=0}^{N} \delta(\lambda - \lambda_n) = \sum_{n=0}^{N} G_{ch}((\lambda - \lambda_n)) \tag{5.11}$$

The base Gaussian of the AWG channel is convolved with a train of Dirac centered at the AWG channel wavelengths. We assume G_{AWG} to describe all the channels of the AWG ideally. Assuming the input a pure wavelength,

$$T_{system} = \sum_{n=0}^{N} G_{ch}((\lambda - \lambda_n)) \cdot \delta(\lambda - \lambda_{in}) = \sum_{n=0}^{N} G_{ch}((\lambda_{in} - \lambda_n)) \tag{5.12}$$

This demonstrates that the output of the system is again a Gaussian centered at the input wavelength and sampled at the wavelengths of the AWG channels.

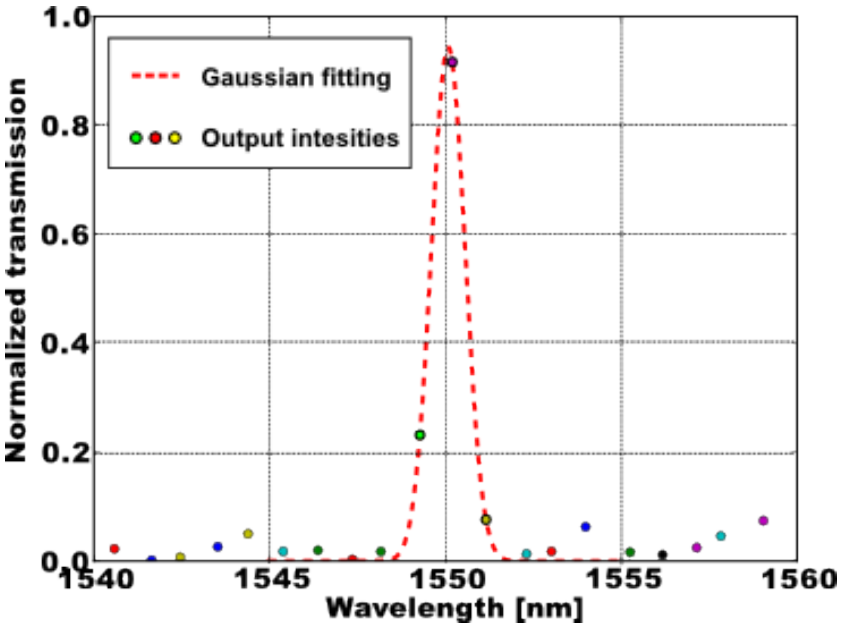

Figure 5.17: Gaussian advanced fitting for the wavelength recovery

Fig. 5.17 shows an example of this method applied to a wavelength measurement. The Gaussian fitting algorithm requires starting guessing value: to improve

the performances, we use a starting value equal to the wavelength of the AWG channel with the maximum intensity. The input wavelength, in this case, is 1550 nm. The standard CoG algorithm measured a wavelength of 1550.51 nm while the Gaussian fitting measured a wavelength of 1550.074 nm. Thus, a factor of ten improvement in accuracy compared to the raw CoG algorithm.

5.2.5 Conclusions

In this chapter, we used multi-domain multiplexing to enhance the performance of AWG-based spectrometers. This technique drastically improves the accuracy of an AWG-based spectrometer. The enhanced accuracy comes from the multiplexing of a larger and denser number of AWG channels, without the practical need of designing an AWG with dense channel spacing. With a relatively course channel spacing (4 nm), the accuracy obtained is in the order of tens of picometers (12 pm) on the whole FSR (20 nm). Passive photonics platform and active platform implementations (carried depletion modulators and integrated germanium photodiodes) have been tested. This last approach needs to be further investigated. In particular the fitting techniques, either CoG of a more advanced method such as the pseudo-inverse matrix method [20] or the generalized Gaussian method proposed in this works, can be optimized. Moreover, these methods have the property of the linearity, thus, multiple linewidths of the spectrum can be fit with a linear sum of the elementary function used for the fitting. A problem we faced with the fully integrated Vernier spectrometer was the low output power when broadband sources used.

References

[1] P. Cheben, J. H. Schmid, A. Delâge, A. Densmore, S. Janz, B. Lamontagne, J. Lapointe, E. Post, P. Waldron, and D.-X. Xu. *A high-resolution silicon-on-insulator arrayed waveguide grating microspectrometer with sub-micrometer aperture waveguides*. Opt. Express, 15(5):2299–2306, Mar 2007.

[2] C. Dragone. *An N*N optical multiplexer using a planar arrangement of two star couplers*. Photonics Technology Letters, IEEE, 3(9):812–815, Sept 1991.

[3] C. Dragone, C.A. Edwards, and R.C. Kistler. *Integrated optics N*N multiplexer on silicon*. Photonics Technology Letters, IEEE, 3(10):896–899, Oct 1991.

[4] *http://www.europractice-ic.com/*.

[5] F. Van Laere, G. Roelkens, M. Ayre, Jonathan Schrauwen, D. Taillaert, D. Van Thourhout, T.F. Krauss, and R. Baets. *Compact and Highly Efficient Grating Couplers Between Optical Fiber and Nanophotonic Waveguides*. Lightwave Technology, Journal of, 25(1):151–156, Jan 2007.

[6] M.K. Smit and C. Van Dam. *PHASAR-based WDM-devices: Principles, design and applications*. Selected Topics in Quantum Electronics, IEEE Journal of, 2(2):236–250, Jun 1996.

[7] Vittorio Passaro, Francesca Magno, and Andrei Tsarev. *Investigation of thermo-optic effect and multi-reflector tunable filter/multiplexer in SOI waveguides*. Opt. Express, 13(9):3429–3437, May 2005.

[8] J. Russell and R. Cohn. *Time-Division Multiplexing*. Book on Demand, 2012.

[9] Y. Sano and T. Yoshino. *Fast optical wavelength interrogator employing arrayed waveguide grating for distributed fiber Bragg grating sensors*. Lightwave Technology, Journal of, 21(1):132–139, Jan 2003.

[10] Charles G. Askins, Martin A. Putnam, and E. J. Friebele. *Instrumentation for interrogating many-element fiber Bragg grating arrays*, 1995.

[11] R.G. Bartle. *The Elements of Real Analysis*. A Wiley Arabook. John Wiley & Sons, Incorporated, 1982.

[12] Martin Fiers, Thomas Van Vaerenbergh, Joni Dambre, and Peter Bienstman. *CAPHE: Time-domain and Frequency-domain Modeling of Nonlinear Optical Components*. In Advanced Photonics Congress, page IM2B.3. Optical Society of America, 2012.

[13] *http://www.lucedaphotonics.com/en*.

[14] S. Pathak, E. Lambert, P. Dumon, D. Van Thourhout, and W. Bogaerts. *Compact SOI-based AWG with flattened spectral response using a MMI*. In Group IV Photonics (GFP), 2011 8th IEEE International Conference on, pages 45–47, Sept 2011.

[15] Wim Bogaerts, Yanlu Li, Shibnath Pathak, Alfonso Ruocco, Martin Fiers, Antonio Ribeiro, Emmanuel Lambert, and Pieter Dumon. *Integrated design for integrated photonics: from the physical to the circuit level and back*, 2013.

[16] Hui Yu, M. Pantouvaki, J. Van Campenhout, Katarzyna Komorowska, P. Dumon, P. Verheyen, G. Lepage, P. Absil, D. Korn, D. Hillerkuss, J. Leuthold, R. Baets, and W. Bogaerts. *Silicon carrier-depletion-based Mach-Zehnder and ring modulators with different doping patterns for telecommunication and optical interconnect*. In Transparent Optical Networks (ICTON), 2012 14th International Conference on, pages 1–5, July 2012.

[17] Hong Tao Chen, Peter Verheyen, Peter De Heyn, Guy Lepage, Jeroen De Coster, Philippe Absil, Gunther Roelkens, and Joris Van Campenhout. *High-Responsivity Low-Voltage 28-Gb/s Ge p-i-n Photodetector With Silicon Contacts*. Journal Lightwave Technol., 33(4):820–824, Feb 2015.

[18] K. Nosu, H. Toba, and Katsushi Iwashita. *Optical FDM transmission technique*. Lightwave Technology, Journal of, 5(9):1301–1308, Sep 1987.

[19] Jagdeep Shah. *Optical Code Division Multiple Access*. Opt. Photon. News, 14(4):42–47, Apr 2003.

[20] JooCarlosAlves Barata and MahirSaleh Hussein. *The MoorePenrose Pseudoinverse: A Tutorial Review of the Theory*. Brazilian Journal of Physics, 42(1-2):146–165, 2012.

6 Conclusion and perspectives

6.1 Conclusion

Active and passive optical filters were used individually and in combinations to develop spectrometers and wavelength meters of high resolution, small footprint and with no movable parts. Despite we chose to work in the telecom range (1.550 nm), the proposed architectures are flexible enough to work in any other range where optical waveguides and modulation techniques are available. Indeed, our approach avoided targeting a particular application, but focus on the methodologies to tackle a wide variety of problems.

Several demonstrators based on active modulation/tuning techniques applied to optical filters were reported. We used thermo-optic and electro-optic effects to modulate rings and MZIs found in our PICs. Such filters were also combined with AWGs. The outcome is a set of several different approaches capable of interrogating an unknown spectrum/wavelength.

Single stage filter active spectrometers

We applied modulation to a microring resonator and an asymmetric MZI. When a saw-tooth like carrier is applied to the ring, the wavelength range in between two resonance peaks (FSR) is scanned. Through the electro-optical characterization, we were able to reconstruct the correlation between the time scale and wavelength domain. In this case the resolution is only limited by the FWHM of the ring resonator, for our demonstrator a resolution of 300 pm has been measured within an

operation range of $\sim$10 nm.

Here a simple carrier depletion asymmetric MZI modulator has been demonstrated as a wavelength meter. The voltage signal applied to the modulator is a sinusoidal wave. Thanks to sinusoidal passive transmission of the device, we built a correlation between the electrical phase delay of driving and driven electrical signal. We achieved an average accuracy of $\sim$ 64 pm on the FSR of the passive MZI transmission of $\sim$ 30 nm.

Multi optical filters spectrometers

The level of complexity of our systems was increased by cascading different kinds of optical filters. This was realized by combining rings and AWGs to enhance their individual wavelength interrogation performances. In particular, an architecture base on a ring resonator feeding an AWG has been demonstrated as ring-based sensing device with an improvement of LOD of $\sim 9\times$.

Furthermore, the same architecture based on the ring-AWG system has been demonstrated as time-domain scanning spectrometer. Following our approach, each resonance peak of the ring scanned an individual AWG channel and showed a resolution of 50 pm over the FSR of the AWG of 48 nm.

Multi domain multiplexing spectrometers

Another concept explored was the multi-domain multiplexing. Together with wavelength division multiplexing, we combined time/frequency division multiplexing. An array of MZM labels in time domain its optical signal that was then fed to different inputs of the AWG. Different modulation techniques have been implemented. Electrical de-labeling was performed on the outputs, coherently with the electrical modulation techniques used for the labeling.

The design has been implemented in passive SOI photonics as well as in active SOI photonics platforms. The active design included integrated germanium photodiodes and carrier depletion based modulators. An accuracy of 12 pm was achieved on the 20 nm FSR of the AWG.

Future perspectives

The proposed architectures represent a viable solution to many of the current wavelength interrogation problems. Since no particular application has been targeted, the results remain of general purpose, but were obtained by taking into account the necessary trade-off between the operative range and the resolution/accuracy. Some of the proposed architectures targets a specific application. Indeed the device proposed in Par. 4.1.1 and Par. 5.1, are multi-peak oriented spectrometers,

thus, highly suitable for sensing application such as FBGs of ring sensors. The performances are not yet at the levels of commercial non-integrated products, but the improvement compared to integrated passive spectrometers is significant. The device proposed in Par. 4.2.1 is instead ring sensing oriented. The full system is an interrogator that integrates the sensor and the spectrometer. The LOD improvement is impressive compared to the use of the only ring sensor.

The performances in term of resolution and accuracy can readily applied to a large number of photonic applications, such as biosensing, environmental sensing, optical interconnects, etc.

From an experimental point of view, a second generation of devices using the feedback of the first fabricated chips remains however to be implemented in order to push to their limits the concepts explored in our work. Instead of a general purpose implementation, a much more custom approach can be adopted: knowing a particular application, the best solution proposed in this work can be selected and tailored to the requirements.

Practical examples of real applications for our architectures range over different fields. First of all sensing: extremely compact and reliable sensors for biological and environmental application can be integrated with our spectrometers on the same chip. The result would be a cheap, extremely compact and reliable integrated interrogation system. Space applications can also benefit from our results since no movable part are used. Hence, the susceptibility to gravity variation is reduced. The new frontiers of photonic communication could also make advantage of integrated spectrometers and wavelength meters integrated on the same chip: our device can indeed be used for laser or filters monitoring on-chip.

In conclusion, we proposed, implemented and tested a range of possible engineering solution to the most common wavelength interrogation requirements, ranging from sensing to optical networking. The implementation is carried out on a CMOS-compatible platform, enabling mass production of compact, low power consumption, integrated spectrometers. We provided a solution to the long-standing problem of mismatch in term of costs, footprint and complexity between the actual DUT (sensor, networking, etc.) and the interrogating device.

A

Measurement setups

A.1 Introduction

This appendix presents the schematic block diagram of the measurement setups used for this work. Besides the optical sources and readers, several electrical sources and readers are used, depending on the particular requirement in term of speed and counting of electrical channels. The optical sources used are divided into mainly two categories, basing on the characteristic of the generated light: namely tunable lasers and SLEDs. The first are narrowband while the others are broadband ($\sim$ 100 nm in out case). The optical reading out can be realized with powermeters or optical spectrum analyzers (OSAs). While the powermeter gives integral the optical power, the OSAs gives the optical power information in function of the wavelengths.

The software framework we used is an in-house developed library based on Python that is compatible with different communication protocols to synchronize and manage the measurements. The synchronization can take place software via (slower) of hardware via (faster) with an external clock wich synchronizes the instruments.

A.1.0.1 Common communication protocols

Here a brief introduction of the communication protocol is presented. The instruments use the GPIB (General Purpose Interface Bus) communication protocol. This standard is based on an 8-bit, electrically parallel bus and allows 15 devices

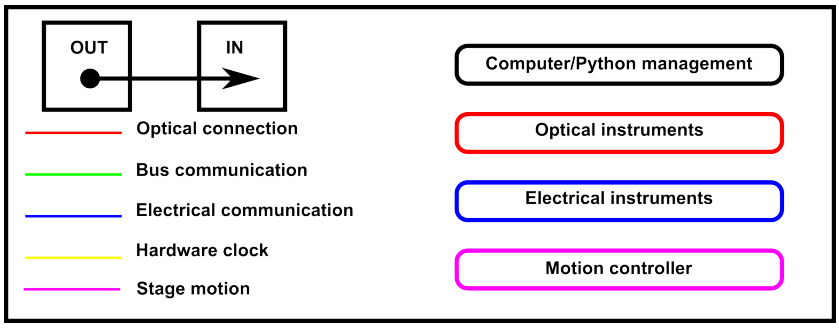

Figure A.1: Legend used for the representation of the measurement setup

to share a single physical bus. Another protocol used is the PXI(e) used of the multi-IO electrical chassis. PXI stands for PCI eXtensions for Instrumentation; it is based on the PCI technology.

The measurement can be automatized using motion controlled XYZ stages to manage the position of the fiber and using the optical output power as a feedback for the optimization of the position. The alignment starts with the manual positioning of the fibers in the proximity of a testing structure such as a straight waveguide. The position optimization is then obtained maximizing the transmission.

A.2 Passive optical transmission measurement

The passive optical transmission measurement is realize coupling light into the PIC with the source and reading the output: if the source is a laser, the reading out is realized with a powermeter.The two arrays of generated wavelength and read output powers are combined to build the transmission spectrum of the device under test.

If the source is broadband such as a SLED, the output spectrum is read with an OSA capable of measuring the correlation between wavelength and transmission.

A.2.1 Transmission measurement with arbitrary electrical carrier generation

The first setup explored in this appendix is used when an electrical modulation is required. The signal generator is used both to drive the electro-optic modulator and to start the acquisition trigger for the oscilloscope. A coaxial splitter is connected to the output channel of the arbitrary signal generator: one of the connector goes to the electrical connection of the DUT while the other goes to the oscilloscope reference channel. The optical source used in a tunable laser. The PC sets the parameters of the laser through GPIB and starts the oscilloscope acquisition. The

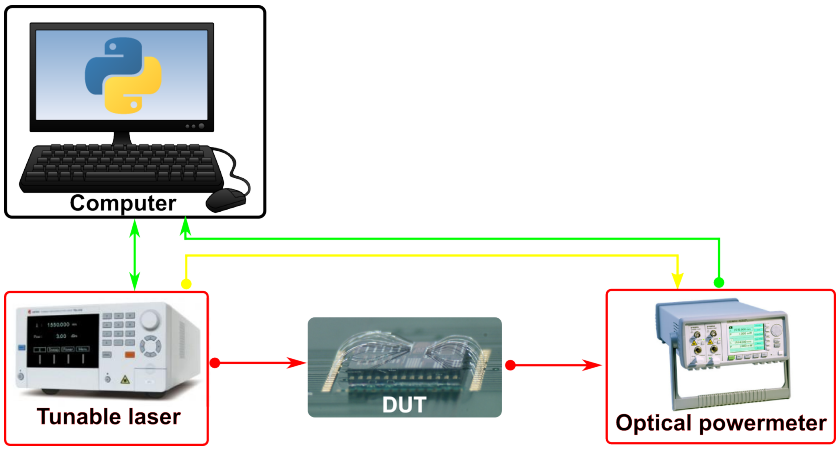

Figure A.2: Passive optical transmission setup

procedure is iterated over the spectrum of interest. Often, in this case, the electrical reading out is performed with the integrated photodiode, but when no on-chip photodiode is present, a grating coupler collects the output light and an external powermeter converts the optical power into a voltage signal.

A.2.2 Transmission measurement with electrical driving and broadband source

The setup described in this section is used when a broadband optical source and a multi-source electrical driver needs to be combined. Since a broadband source is used, the optical read-out is performed with an OSA. The triggering operation is needed for the electrical source and the OSA spectrum read-out. The process flow starts with the setting of the electrical driver: in this particular case, multiple channels are set at the user defined voltages. Each different voltage drives an individual active device. The OSA is then set up with the required settings such as bandwidth and resolution. Interrogation of the OSA is the conclusive step of the individual iteration. The procedure is repeated for the different voltages required.

A.2.3 Transmission measurement with electrical driving and tunable laser and IR camera

The setup described in this section is used when a combination of multi-source electrical driving and a tunable laser source is required. Moreover, the capability of simultaneous output grating coupler reading is provided through an IR camera. The IR camera collects the frames containing the image of the grating couplers. The diagram flow is organized as follow: the multi-electrical source is set to the

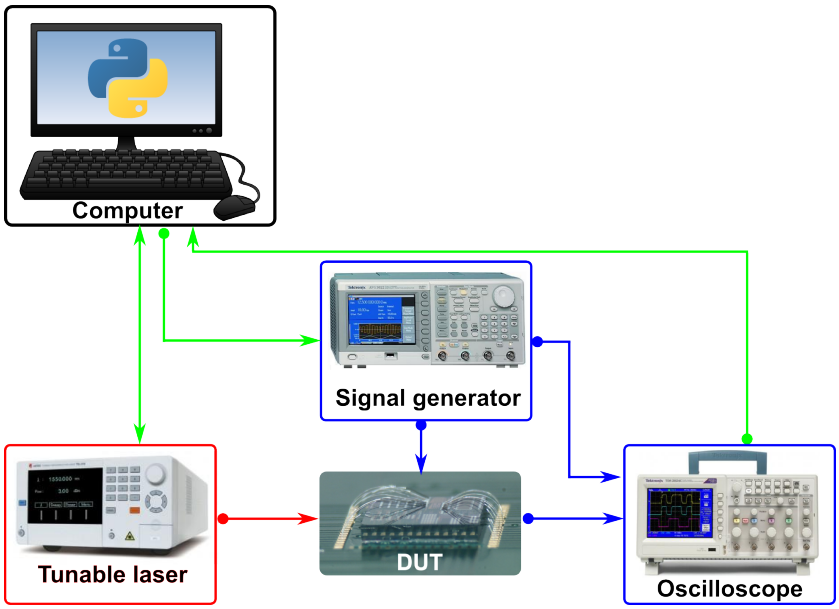

Figure A.3: Electro-optic measurement setup with synchronous analog electrical signal generation and collection

used defined voltages. Following the tunable laser is set at the required wavelength. The final step of this procedure is the collection of the IR camera frame associated with the input wavelength and voltage driving settings. This steps flow is iterated over the wavelengths of interest.

A.2.4 Transmission measurement with integrated modulators and photodiodes: electrical driving

This setup is used for electro-optic characterization of PIC with integrated modulators and photodiodes. The tunable laser is set through GPIB port to the required wavelength. The multi-IO analog device is set through PXIe port. The synchronization of electrical IN/OUT is realized with a hardware clock trigger generated and followed by the same hardware. The germanium photodiodes integrated on-chip use the TIAs (Transimpedance amplifier); this is because the analog sampling card reads-out the voltages and not the currents. The procedure is iterated over the wavelength domain of interest.

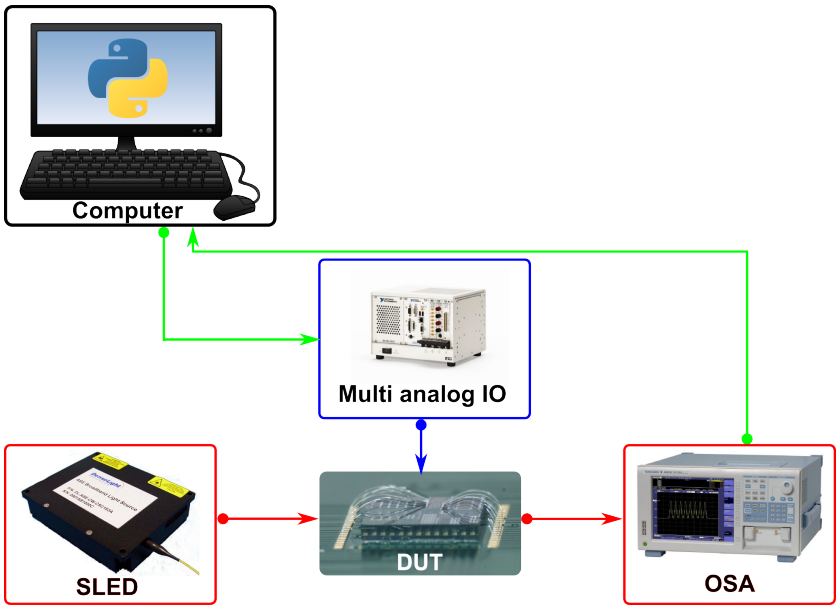

Figure A.4: Electro-optic measurement setup with multiple input DC voltages: reading out with OSA

A.2.5 Transmission measurement with integrated modulators and photodiodes: optical sweep

The setup exposed in this paragraph is used for the characterization of PICs with integrated photodiodes, when the main target of the measurement is a sweep in the wavelength domain. A PXIe trigger sets the analog read-out in ”listening mode”. The GPIB port is used to start the sweep of the tunable laser. The hardware trigger of the laser synchronizes the acquisition of the analog read-out. The outcome of the measurements is the transmission of the PIC represented as wavelength versus voltages.

A.2.6 Electro-optic semi-automatic measurement with broadband source

This setup differs from the previous because the optical fiber to grating coupler is managed with automated micrometer stages. The analog output of an auxiliary powermeter is used to provide a correlation between the optical output in the optical fiber and the position. The hardware communication between the auxiliary powermeter and the motion controller is independent of the PC. The measurement proceeds as follow: the (x,y) coordinates of the in/out grating coupler are the start-

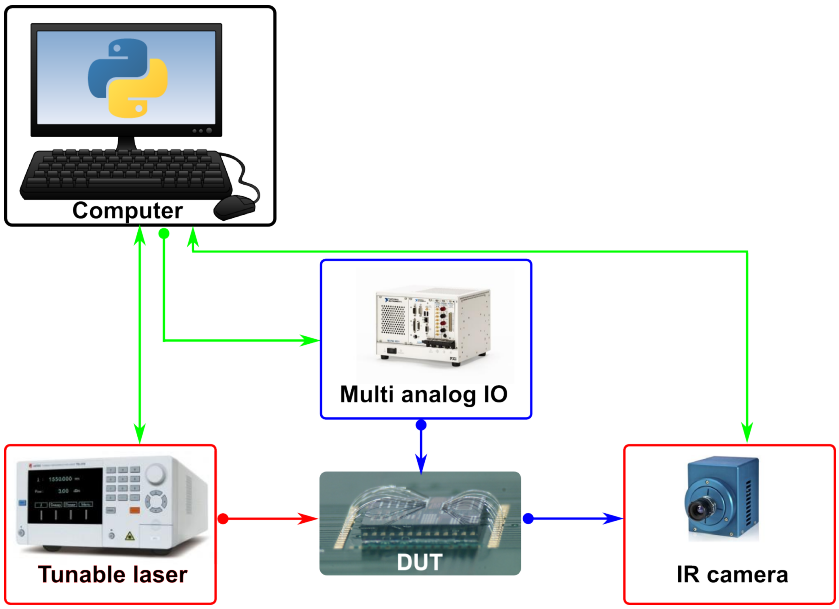

Figure A.5: Electro-optic measurement setup with multiple input DC voltages: IR camera free space optical reading-out

ing point for the alignment. The motion controller follows predefined path around the (x,y) of the grating coupler, first for the input and then for the output. The motion controller records the correlation between the coordinates and voltages. Once the maximum is found, the fiber is shifted accordingly.

At this point, the electrical source performs the sweep as required for the measurement and synchronously the optical powers are recorded. The procedure is iterated for all the inputs. Instead of sweeping the electrical source, it would be possible to set the electrical power and measure all the optical outputs. This process flow has been avoided to reduce the optical alignment inhomogeneity, since less optical alignment are required ($N_{al} = AWG_{out,ch}$, instead of $N_{al} = N_{el,steps} * AWG_{out,ch}$).

A.2.7 Electro-optic semi-automatic measurement with tunable laser

This measurement setup follows the same procedure of the previous, but a tunable laser is used as the optical source. The alignment procedure is similar to the previous setup configuration. One difference persists: since the tunable laser emits a single wavelength, it can happen that this wavelength is in the stopband of the device under test. To overcome this limitation, a rough alignment at 1550 nm

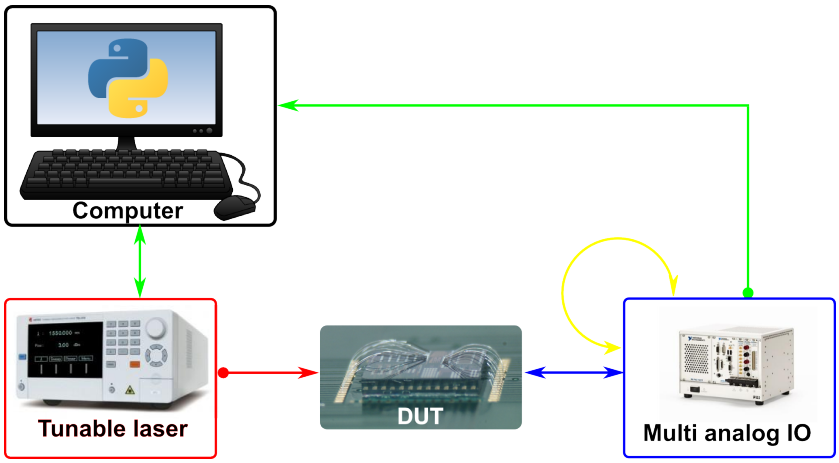

Figure A.6: Electro-optic measurement setup with synchronous multi analog electrical signal generation and collection

is followed by a laser sweep. This step returns the wavelength with maximum transmission. The maximum transmission wavelength is used for a fine alignment. When in and out fiber are aligned, the electrical source is set to the desired value. A tunable laser measures the transmission of the device in function of the wavelengths and for the defined input voltage. The laser sweep is repeated for each voltage value to be tested. The procedure is iterated on all the optical inputs and outputs.

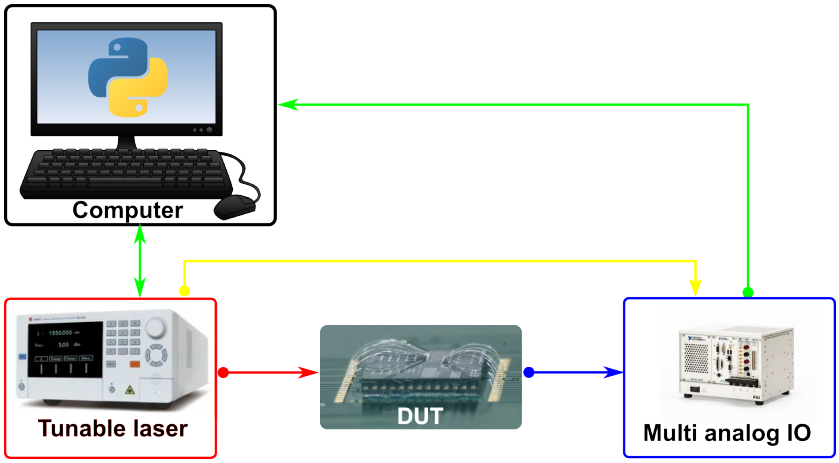

Figure A.7: Electro-optic measurement setup with synchronous multi analog electrical signal collection

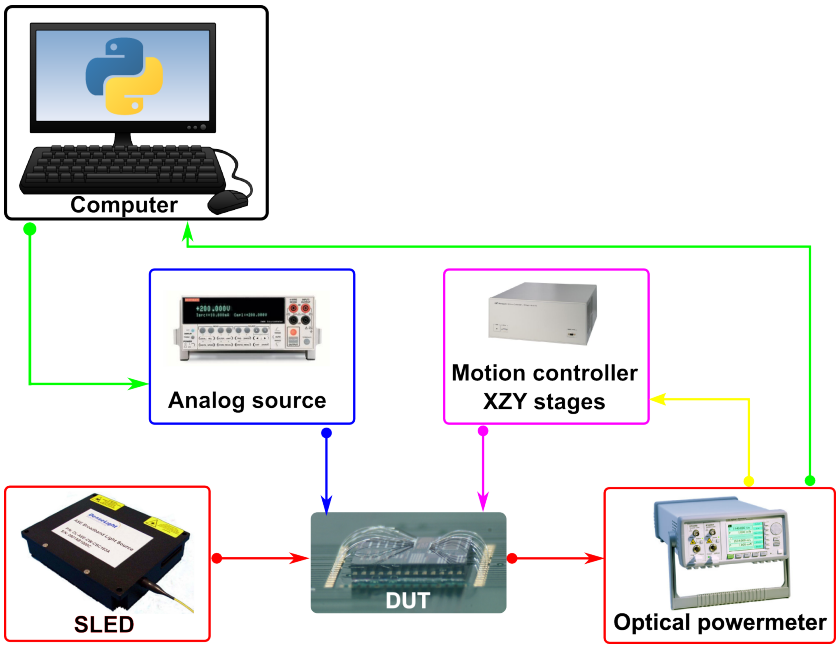

Figure A.8: Semi-automatic electro-optic measurement setup with analog DC electrical driving and broadband source

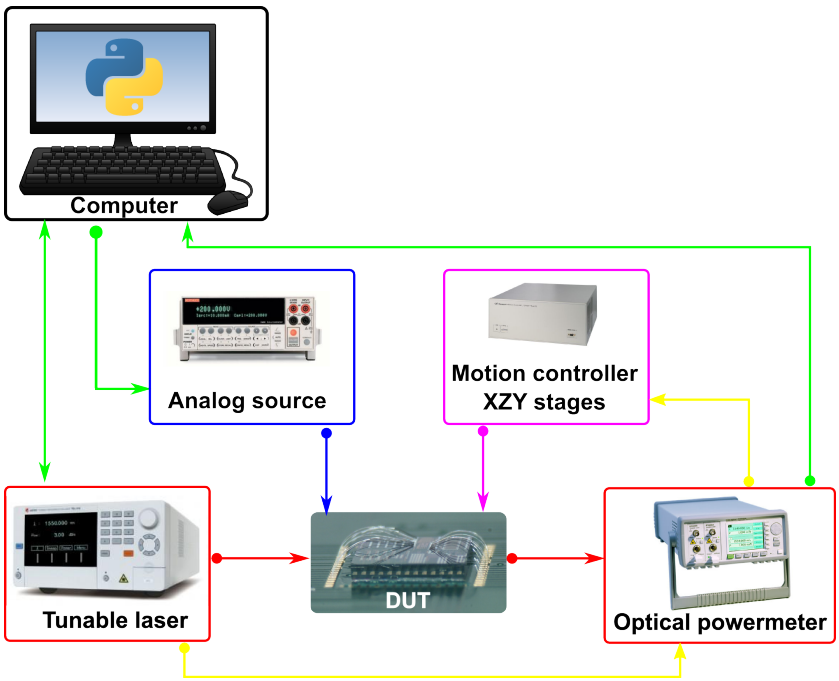

Figure A.9: Semi-automatic electro-optic measurement setup with analog DC electrical driving and tunable laser

B

Electronics and packaging

B.1 Introduction

In this appendix, the design of the TIAs used for the germanium photodiodes is briefly introduced. The individual TIA is replicated 8 times on the same custom PCB. The same hardware is used for multiple photodiodes of the same photonic chip. The second part of the appendix describes the design of the PCB used for the wirebonding and packaging of the photonics integrated circuits.

B.1.1 Transimpedance amplifiers

The germanium integrated photodiodes used in the present work are photocurrent generators. In most of the cases, as well as in our case, the lab instruments sample voltages. Thus, a transimpedance amplifier is required. The easier example of such device with a the I to V conversion property is a resistance. However, using a load as transimpedance amplifier has the drawback of offering a non-zero input impedance.

We designed and implemented a bank of transimpedance amplifiers based on operational amplifiers. Fig. B.1(a) represents the schematic of the basic TIA with the main components specifics. The basic TIA building is replicated eight times on the same PCB.

An IC containing four operational amplifiers is used to replicate four times the basic TIA. Moreover, the macro cell is replicated twice on the PCB. The IC used is the Texas Instruments TLV2474 [1], which is a quad low-power rail-to-rail

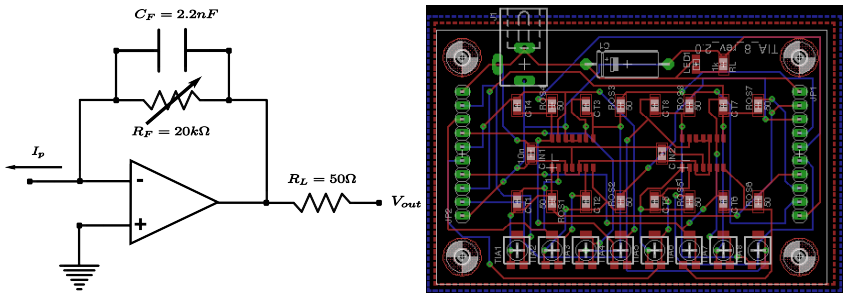

(a) Schematic of the TIA element *(b) Schematic of the TIAs PCB*

Figure B.1: Schematic of the TIA element and the Double metal layer PCB

operational amplifiers included in the same package. Fig. B.1(b) shows the PCB board sent for fabrication.

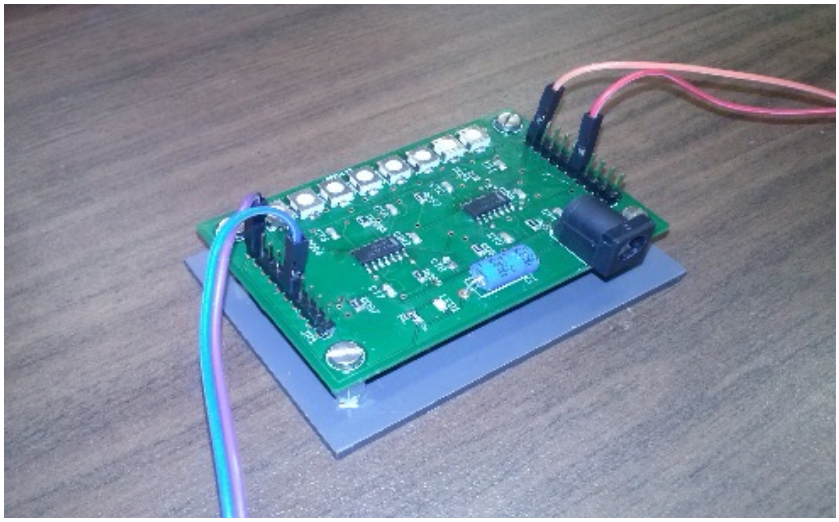

Figure B.2: Photo of the TIAs boards ready to use

We work at low frequency compared to the IC TLV2474 cut-off limits, thus, we assume that the loop gain $V_{OL}\beta$ in much larger than 1. In this condition, the gain of the device is represented in Eq. B.1. The cut-off frequency is calculated according to Eq. B.2 where we assumed negligible the equivalent capacitance of the photodiode [2].

$$V_{out} = -\frac{I_p R_F}{1 + \frac{1}{A_{OL}\beta}} \simeq -I_p R_F \tag{B.1}$$

$$f_{cut-off} = \frac{1}{2\pi C_F R_F} \tag{B.2}$$

Fig. B.2 is a photo of the final TIAs board. Clearly visible a couple of ICs containing the operation amplifiers and the array of variable feedback resistances for the tuning of the gain.

B.1.2 Packaging and wirebonding

The number of contacts in our PIC under test became large. Thus, we designed an affordable low-speed packaging solution. We designed a PCB capable of accommodate 72 wires on the four sides of the photonic chip. Of the four sides, only two were simultaneously wirebonded. Fig. B.4(b) shows the PCB board sent for fabrication.

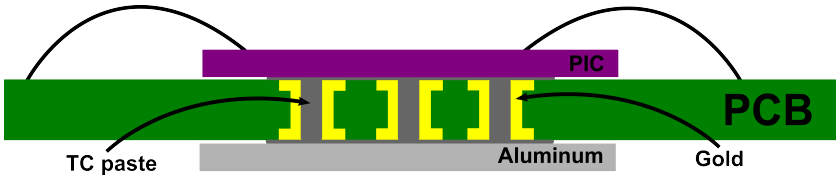

Figure B.3: Cross-section of the thermal channels connecting the two sides of the PCB

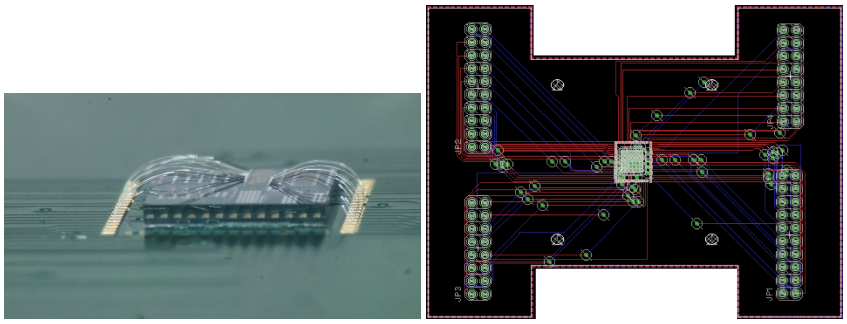

(a) Photo of the photonic integrated circuit after the wirebonding

(b) Schematic of the PCB used for the wirebonding(upper side)

Figure B.4: Images of the PIC after the wirebonding and the packaging

To facilitate the thermal control of the circuit, we provided thermal metal vias to the board. Following a thermoconductive paste (as well as glue) creates the thermal channel between the photonic substrate and a plate of aluminum in contact with the Peltier thermo-controlled chuck. Fig. B.3 shows a schematic of the cross-section underneath the photonic integrated circuit. The image shows the uncovered metal channels thermally contacting the upper and lower part of the PCB.

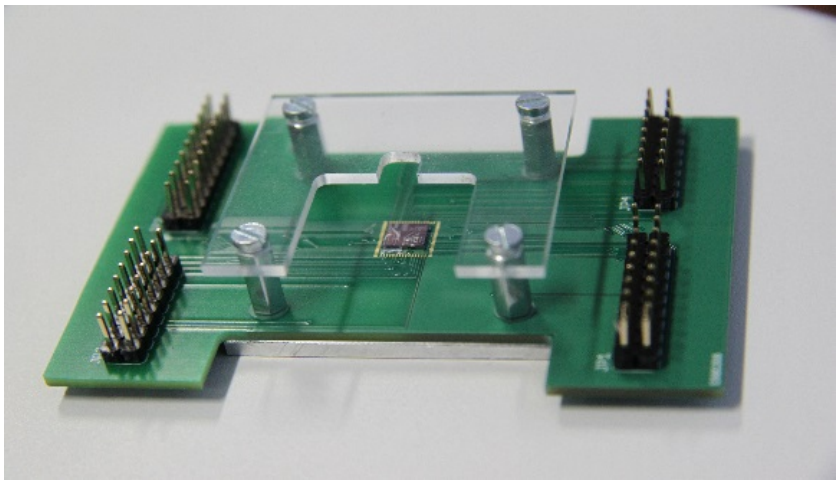

Figure B.5: Photo of the packaged PIC

Fig. B.4(a) and Fig. B.5 show respectively the a close-up of the wirebonded chip and a photo of the final packaged. In the bottom part, the aluminum plate to be contacted to the heat-sink is visible. A Plexiglas cage protects the integrated photonic chip from mechanical damage. One side of it is still accessible for the optical input.

References

[1] *http://www.ti.com/*.

[2] P. Horowitz and W. Hill. *The Art of Electronics*. Cambridge University Press, 2015.